Semi-Autonomous Guidance and Control of a Saab SeaEye Falcon ROV

by

Alison A. Proctor
B.S. Embry-Riddle Aeronautical University 2000
M.S. Georgia Institute of Technology 2004
A Dissertation Submitted in Partial Fulfillment of the
Requirements for the Degree of

DOCTOR OF PHILOSOPHY

in the Department of Mechanical Engineering

University of Victoria

Semi-Autonomous Guidance and Control of a Saab SeaEye Falcon ROV

by

Alison A. Proctor
B.S. Embry-Riddle Aeronautical University 2000
M.S. Georgia Institute of Technology 2004

Supervisory Committee

Dr. C. Bradley, Co-Supervisor
(Department of Mechanical Engineering)

Dr. B. Buckham, Co-Supervisor
(Department of Mechanical Engineering)

Dr. P. Agathoklis, Outside Member
(Department of Electrical Engineering)

ABSTRACT

Supervisory Committee
Dr. C. Bradley (Department of Mechanical Engineering)
Co-Supervisor
Dr. B. Buckham (Department of Mechanical Engineering)
Co-Supervisor
Dr. P. Agathoklis (Department of Electrical Engineering)
Outside Member

For decades, Remotely Operated underwater Vehicles (ROVs) have been helping mankind explore the depths of the ocean, and build and maintain infrastructure on the seafloor. Since the first ROV was developed in 1953, the number of uses for these vehicles has exploded. They are now an essential part of maintaining the world's energy resources, collecting scientific data about our oceans, and performing underwater search and recovery.

This research will discuss guidance, navigation, and control algorithms for use as a low-level position controller for ROVs, which will enable semi-autonomous behaviour for the vehicle. Semi-autonomous behaviour is when the pilot issues high-level position commands and the low-level controller handles station keeping and maneuvering between the commanded positions. In this configuration, the low level controller compensates for the environmental disturbances and unknown dynamics (such as current and tether dynamics), allowing the pilot to focus on other aspects of the task (such as manipulator control).

In this work, the design, implementation, and testing of a complete guidance, navigation, and control system is presented. A Saab Sea-Eye Falcon ROV is augmented with a suite of navigation instruments. The augmented vehicle is characterized and a dynamic model is developed. This model is used in an extended Kalman filter, which will be shown to produce a position estimate for the vehicle with an error of less than ± 6 cm. The navigation system is combined with a guidance system and adaptive controller to enable semi-autonomous behaviour. With this suite of software, the ROV can operate semi-autonomously. The resulting ROV system is a research platform, from which the underwater community can continue research into algorithms for optimal control, remote operations, and other performance enhancing technologies.

Contents

List of Tables

List of Figures

ACKNOWLEDGEMENTS

I would like to thank my supervisory committee: Colin Bradley, Pan Agathoklis, and Brad Buckham for their dedicated support to this research. You provided funding, technical guidance, emotional support, and unendless patience and understanding. Brad, the SWAT has been an invaluable tool for this work. Thank you for supporting the development of that facility, both financially and with your energetic enthusiasm for this work. Pan, thank you for all your time and patience. No matter what crazy idea I brought to your office, you always managed to set me back onto the path of reason. Lastly, I would especially like to thank Colin, who, in addition to his duties as supervisor, has spent the last few years teaching me about research philosophies, project management, grant writing, politics, work ethics, and so much more. You have helped shaped the person that I am today.

The people at the Ocean Technology Laboratory (Amos Buchanan, Jeff Kennedy, Darryl Gamroth, Emmett Gamroth and Lori Muck) have given me the tools and hands-on support that I needed to realize this work. Amos Buchanan has spent many nights in the SWAT pushing the ROV around, while I tried to figure out why my measurements weren't quite perfect. Jeff Kennedy was responsible for most of the mechanical modifications that were required for the Falcon. Darryl Gamroth provided endless advice and help with electronics design and repair. Emmett Gamroth was responsible for implementing much of the Labview software that ran on on the ROV. Lori provided administrative support and always had time to listen to my frustrations. Thank you all.

I would also like to thank Serdar Soylu and Jonathan Zand, my predecessors in the SWAT facility. Not only did I gain expertise from your research, but I was able to learn from the hardships that you faced in the SWAT, and help to turn it into the research facility that it has become.

Last, but not least, I would like to thank my friends and family. Mom, Dad, Stacy and Paula - thank you for putting up with this for so many years; this has been a really long time coming and you never once doubted me. I would also like to thank Lenore Newman - you never stopped being supportive even though you clearly thought that I was taking a ridiculously long time to finish my thesis. And lastly, I would like to thank my roller derby family. You have provided me with friendship, understanding, support, and an outlet for all my pent up anxiety. You guys are the best.

DEDICATION

To Kelly for helping me finish, Natalie for helping me start, and my dog, Lily, for sitting patiently at my feet throughout it all.

Nomenclature

Roman letters

B	Biases
$I_{x,y,z}$	Mass Moment of Inertia along the x, y, or z-axis
IF	Interference Factor
J_0	Advance Number
K_T	Thrust Coefficient
p	Roll Rate of the Vehicle in the Body Frame
q	Pitch Rate of the Vehicle in the Body Frame
r	Yaw Rate of the Vehicle in the Body Frame
u	Longitudinal Velocity of the Vehicle in the Body Frame
v	Lateral Velocity of the Vehicle in the Body Frame
V_a	Thruster Advance Speed (m/sec)
w	Vertical Velocity of the Vehicle in the Body Frame
w_T	Wake Number
x	Longitudinal Position of the Vehicle in the Navigation Frame
y	Lateral Position of the Vehicle in the Navigation Frame
z	Vertical Position of the Vehicle in the Navigation Frame
CB	Centre of Buoyancy
CG	Centre of Gravity

Greek letters

χ	Guidance Command (subset of η)
η	Position and Attitude States
ν	Velocity and Angular Rate States
Ω	Propeller Speed (rad/sec)
ϕ	Euler Angle about the Body x-axis (roll angle) (rad)
θ	Euler Angle about the Intermediate y-axis (pitch angle) (rad)
ζ	Guidance Velocities and Rates (subset of ν)

Vectors and matrices

$\boldsymbol{\delta}$	Control Inputs
$\boldsymbol{\eta}$	Earth Fixed Position and Attitude (NRF)
$\boldsymbol{\nu}$	Body Fixed Velocity and Angular Rates (BRF)
$\boldsymbol{\omega}$	Angular Rate Vector $[p\ q\ r]^T$
$\boldsymbol{\tau}$	Forces and Moments Due to Control Surfaces and Propulsion Systems
$\hat{\mathbf{x}}^-$	A Priori Estimate of Process State
$\hat{\mathbf{x}}$	Estimate of Process State
$\mathbf{A}$	Jacobian of the Process Model
$\mathbf{a}$	Acceleration Vector
$\mathbf{B}$	Thruster Input Matrix

$\mathbf{C}$	Coriolis and Centripetal Force and Moment Matrix
$\mathbf{D}$	Hydrodynamic Force and Moment Matrix
$\mathbf{f}$	Process Model
$\mathbf{G}$	Forces and Moments due to Gravity and Buoyancy
$\mathbf{H}$	Jacobian of the Measurement Model
$\mathbf{h}$	Measurement Model
$\mathbf{J}$	Transformation Matrix between $\boldsymbol{\nu}$ and $\dot{\boldsymbol{\eta}}$
$\mathbf{K}$	Kalman Gain
$\mathbf{M}$	Mass Matrix
$\mathbf{m}$	mass (kg)
$\mathbf{n}$	Arbitrary Vector or Ray
$\mathbf{P}$	EKF Covariance Matrix
$\mathbf{Q}$	Quaternion Operator
$\mathbf{Q}_P$	Process Model Covariance Matrix
$\mathbf{R}$	Rotation Matrix
$\mathbf{R}_M$	Measurement Covariance Matrix
$\mathbf{s}$	Quaternion Describing the Inertial to Body Transformation
$\mathbf{T}$	Thrust Vector
$\mathbf{v}$	Process Noise
$\mathbf{w}$	Measurement Noise
$\mathbf{z}$	Measurement

Subscripts and Superscripts

$\hat{(\cdot)}$	Estimate
$\widetilde{(\cdot)}$	Skew Symmetric Matrix constructed from Vector $\in \Re^3$
B	Body Reference Frame
$B \rightarrow N$	Body to Navigation transformation
$H \rightarrow N$	SWAT to Navigation transformation
k	Discrete Sample at Time k
N	Navigation Reference Frame
$N \rightarrow B$	Navigation to Body transformation
S	Sensor Reference Frame

Acronyms

AHRS	Attitude Heading Reference System
AIC	Auxiliary Interface Container
AUV	Autonomous Underwater Vehicle
BRF	Vehicle Body Reference Frame
CRF	Camera Reference Frame
DCM	Direction Cosine Matrix
DOF	Degree of Freedom
DP	Dynamic Positioning
DVL	Doppler Velocity Log
EKF	Discrete Extended Kalman Filter
FIR	Finite Impulse Response
GNC	Guidance, Navigation, and Control
GPS	Global Positioning System
HRF	SWAT Reference Frame
IC	Integrated Circuit
IMU	Inertial Measurement Unit
INS	Inertial Navigation Systems

LBL	Long BaseLine
LORAN	LOng RAnge Navigation System
MEMS	Micro-Electro-Mechanical Systems
MOCAP	Motion Capture Camera System
MRF	Measurement Reference Frame
MRU	Motion Reference Unit
NN	Neural Network
NRF	North East Down Reference Frame
OTL	Ocean Technology Lab
PF	Particle Filter
ROV	Remotely Operated underwater Vehicle
ROVM	ROV-Manipulator
SBL	Short BaseLine
SCU	Surface Control Unit
SRF	Sensor Reference Frame
SSC	SubSea Controller
SWAT	Shallow Water Acoustic Test
UKF	Unscented Kalman Filter
USBL	Ultra Short Baseline acoustic System
UUV	Unmanned Underwater Vehicle
UVic	University of Victoria
WMM	World Magnetic Model

Chapter 1

Introduction

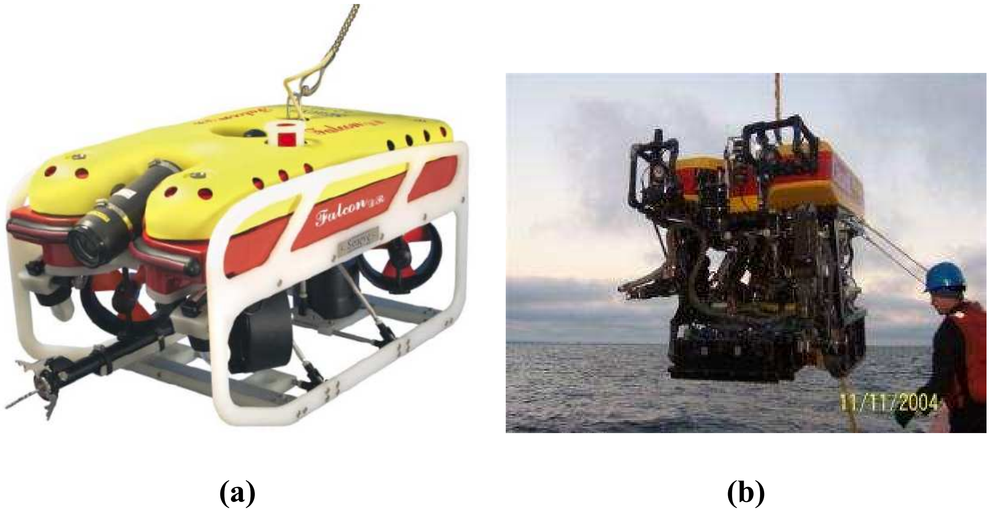

(a) **(b)**

Figure 1.1: Modern ROVs: a) Observation Class ROV - the Saab SeaEye Falcon b) Work Class ROV - ROPOS

For decades, Remotely Operated underwater Vehicles (ROVs) have been helping mankind explore the depths of the ocean, and build and maintain infrastructure on the seafloor. The first ROV, an archeological vehicle named POODLE, was developed by Dimitri Rebikoff in 1953. The US Navy soon recognized the utility of the ROV and begun development on a vehicle of their own. They wanted to use the vehicle to recover lost torpedoes from the sea floor. By the 1960s, the Navy had a fully operational vehicle called the Cable-

Controlled Underwater Research Vehicle (CURV). The ROV soon assumed a vital role in the military, completing important missions, such as retrieving a lost atomic bomb and rescuing stranded crew members in a damaged manned submersible [13]. Over the next few decades, advances in underwater engineering made ROVs more reliable and commercially viable. By the 1980s, ROV technology was being extensively used by offshore industries to work at otherwise unattainable depths [71]. ROVs, like those depicted in Figure 1.1, are now being used for underwater applications such as: mining, logging, environmental sampling, welding, and drilling.

There are three main classes of ROV:

Observation Class: The primary purpose of these vehicles is to deliver a camera (or other sensor) to a site of interest and relay video (or other sensor data) back to the surface support team. They are typically smaller vehicles with limited ability to manipulate objects in their environment. This class of vehicle can often be deployed with a small crew from a vessel of opportunity.

Work Class: These are larger vehicles, specifically designed to carry heavy duty underwater equipment and tooling. These vehicles are typically very large and have an abundance of power to support hydraulic tools and manipulators. This class of vehicle normally has an extensive top-side support system and requires a large ship to facilitate operations.

Special Purpose: These vehicles come in all configurations, ranging from small vehicles built for academic purposes to large vehicles built for highly specialized tasks, such as subsea cable burial.

ROV operations require a highly skilled team. At all times the team must be:

1. monitoring the position of the boat, tether, and vehicle;

2. adjusting flight plans for changing wind, tides, and current;
3. managing the amount of tether that is in the water;
4. piloting the boat;
5. piloting the ROV;
6. operating manipulators or ROV mounted tooling; and
7. collecting mission data.

Small observation class vehicles require upward of three people for a typical mission; more sophisticated work class vehicles require a full crew for the support ship, plus a 4-6 person ROV team, including: an ROV pilot, a navigator, one or more manipulator operators, and one or more mission specialists. Since ROV operations often run 24 hours a day (two shifts), when going to sea, two crews of people will be required to keep the vehicle working.

As new applications for ROVs emerge, the demand for ROVs continues to increase. According to a summary of the World ROV Report $2013 - 2017$[1], the annual expenditures by the oil and gas industry on ROV operations will likely be $\$9.7$ billion for this five-year period, an 80% increase over expenditures during the previous five year period. Shortages in skilled operators have caused the day rates for ROV operational personnel to increase, a trend that will only be exacerbated by the projected growth in the industry.

1.1 Research Motivation

Given the continued growth in the ROV industry and the work load currently experienced by ROV crews, there is an imminent need for new technologies that can simplify ROV operations and automate low level vehicle control; in other words, enable semi-autonomous

---

[1] The World ROV Report is an industry market report published yearly by Douglas-Westwood

capabilities. In a semi-autonomous configuration, the human pilot is given a supervisory role, providing high-level position commands instead of directly controlling the vehicle's propulsion system. Therefore, it is the controller that corrects for forces and moments due to currents, tether drag, and the non-linear vehicle dynamics, thereby allowing the pilot to focus on the work being performed. In the marine industry, the systems that enable this type of semi-autonomous behaviour are called Dynamic Positioning (DP) systems[2].

The semi-autonomous approach has the following benefits:

Reduction in Pilot Work Load: The pilot assumes a high-level supervisory role, as compared to the traditional role of directly controlling the thrusters via a joystick. This enables the following:

- A pilot can ignore low-level requirements, such as holding position against a current, and can focus on the duties required to complete the task (i.e. manipulator control).
- A low-level controller can enable vehicle behaviours that a typical ROV pilot cannot perform, for example, it could perform precise manoeuvres in high currents, where human pilots cannot react fast enough to disturbances.

Remote Piloting with High Latency: Latency[3], or time delays, injected into the control loop can limit the bandwidth or performance of a controller. If the pilot is controlling the thrusters directly, then he/she must respond to environmental disturbances. Consequently, the amount of latency that can exist in the control loop (pilot to vehicle and

---

[2] The term "Dynamic Positioning (DP)" system was coined in reference to modern autopilot systems for ships. On a ship with a DP system, the helmsman can control the position and orientation of the ship with a joystick (or similar input device) and a low-level autopilot manages the ships primary propulsion and bow thrusters to achieve the desired position and heading. The low-level autopilot is designed to maintain station in wind, waves, and current. Many modern ships are equipped with this system including Coast Guard ships, cable laying ships, ROV support ships, survey ships, tankers, etc.

[3] In control theory, latency refers to a time delay inserted into the control loop. This has a destabilizing effect on the closed-loop system. Franklin et al. provide a complete description of latency and its effects on system dynamics in [22].

back) has an upper bound that depends on the dynamics of the environment, and is typically quite small. By locating a low-level controller on the vehicle, the system latency is reduced, as the high latency part of the communication loop is removed. This allow the pilot to be further removed from the ROV, enabling pilots to remotely control the vehicle over high-latency jittery mediums, such as satellite communication or the Internet.

Optimal Control Techniques: Adding a low-level controller allows use of optimal control techniques in the controller design. Human pilots are not very good at optimizing the thrust vector when trying to compensate for a current or tether drag. However, a low-level controller could be designed to minimize thruster power. This would allow the vehicle to operate in heavier currents and would minimize the vehicle's power consumption.

In summary, the motivation for this research is to develop a low-level control scheme that can enable ROVs to be used in a wider variety of applications in a more efficient and effective manner; these are not new concepts. More than 20 years ago, as part of an educational program, the JASON ROV was operated remotely over a satellite link[4] [77]. More recently, in [61], Soylu investigated the concept of a unified ROV-manipulator (ROVM) system. With an ROVM system, the pilot flies the end effector of the manipulator, and the pose of the vehicle and manipulator arm are determined and maintained through an autonomous control system. In the last few years, industry has also come onboard: several sonar based DP systems for workclass ROVs have come on the market [66, 1] and, most recently, SeaByte has developed a video-based DP system for observation class ROVs called the CoPilot [53]. It is clear that semi-autonomous ROV capabilities are not just an interesting idea, but, given the limited resources available, there is a need for these technologies to increase the productivity of ROV operations.

---

[4] In the JASON project, a round trip latency of nearly one second was observed and managed.

1.2 Thesis Overview

This thesis is divided into 7 chapters, with Chapter 1 being this introduction. Chapter 2 describes the research facilities that were used to conduct the research contained herein, including the Falcon ROV, and the modifications that were made to the vehicle to support this research. Chapter 3 starts out by describing a theoretical dynamic model for the vehicle and thrusters, and concludes by presenting experimentally derived model parameters. Chapter 4 presents the design and implementation of an extended Kalman filter, which implements the dynamic model that is described in Chapter 3. Chapter 4 also includes a discussion about sensor characterization and modelling. Chapter 5 discusses the implementation of a Lyapunov based guidance algorithm that is used to guide the vehicle between waypoints. Chapter 6 presents a full 6 degree of freedom simulation of the vehicle, using the model described in Chapter 3; then continues, by using the simulation to evaluate two different control strategies. The two controllers are used in conjunction with the navigation system from Chapter 4 and the guidance system from Chapter 5. The conclusions and future work are then summarized in Chapter 7. The beginning of each chapter contains a literature review and background information relevant to the contents.

There are 6 appendices to this document. Appendix A describes the mathematical notation used in this document. Appendix B provides a detailed description of modifications that were made to the ROV to support this research. Appendix C describes the extended Kalman filter that was used to process the motion capture camera data from the tracking system described in Section 2.2.1. Appendix D describes Euler angles, quaternions, and the associated math. Appendix E presents the derivation of the Jacobians for the extended Kalman filter presented in Chapter 4, as well as the initial values for the extended Kalman filter matrices. Lastly, Appendix F is an in-depth discussion on the types of navigation sensors that are available, as well as their advantages and disadvantages.

1.3 Contributions

The primary contributions from this work include:

Vehicle Design (Chapter 2 and Appendix B): This work describes the design and implementation of a novel vehicle architecture that enables low level dynamic control to be performed on the vehicle, allowing the operator to command position and attitude, instead of controlling the thrusters directly and having to compensate for environmental disturbances. This method allows the pilot to effectively control the vehicle from a remote location.

System Identification (Chapter 3): A 6 DOF model of the Saab SeaEye Falcon ROV and an associated navigation sled was developed that improves upon previously available models by adding: a physics-based thrust model, a pitch and roll model that include cross coupling, and a realistic estimate of the rigid body inertia.

Navigation (Chapter 4): A novel method of calibrating and characterising the onboard sensors using a camera based motion capture system is described. This method allowed all of the sensors to be accurately located and oriented with respect to the vehicle reference frame and for the compass to be calibrated with respect to the navigation reference frame. The calibrated sensors were used to implement an extended Kalman filter with a position error of less than 5 cm.

Simulation (Chapter 6): A high fidelity Matlab simulation has been developed that includes the aforementioned vehicle model, as well as sensor models, which include discretization, noise, and latency.

Control (Chapter 6): A neural network-based control system, previously used on helicopters, has been adapted and implemented. This control system is shown to increase tracking performance in the face of external disturbances and modelling errors, such as those errors created by the ROV tether.

Chapter 2

Research Facilities and Experimental Setup

Figure 2.1: Saab Sea Eye Falcon ROV operated by the OTL

The work presented here is demonstrated experimentally using a Saab SeaEye Falcon ROV; an observation class ROV, shown in it's nominal configuration in Figure 2.1. The data collected in this work was primarily obtained through the use of UVic's shallow water acoustic test facility (SWAT) located at Van Isle Marina and a small test tank located at

UVic's Marine Technology Centre, both located in Sidney, B.C. The SWAT facility is a floating laboratory that has been developed and instrumented to facilitate research on ROVs and to enable the collection of dynamic ROV data. To this end, the SWAT is equipped with a short baseline (SBL) underwater acoustic positioning system which delivers positioning data for the ROV with centimetre level accuracy at approximately 1 Hz. The SWAT also has a high speed motion capture (MOCAP) camera for tracking the motion of objects above the surface. The MOCAP operates at more than 100 Hz and can track objects within it's field of view at millimetre level accuracy. The two tracking systems are described in more detail in Section 2.2.1.

2.1 Marine Technology Centre

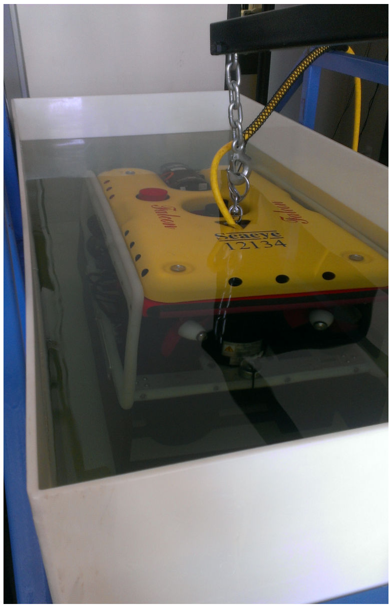

Figure 2.2: The ROV shown inside of the MTC test tank

The Marine Technology Centre (MTC) is industrial warehouse space managed by UVic and utilized by the ocean technology community. At the MTC, the OTL has a small bay that was used for development, as well as assembling and testing the Falcon ROV used in this research. The bay contains a small salt water test tank, Figure 2.2, large enough for the Falcon. The salinity of the water in the test tank was varied such that the density of the water in the tank closely matched the density of the water at the SWAT facility. Since the water at the two locations are different temperatures, the salinity of the two locations will not be the same. This allows the tank to be used for ballasting and taking measurements, as well as troubleshooting groundfaults and verifying the sensor configurations.

2.2 Shallow Water Acoustic Test Facility (SWAT)

The SWAT facility, shown in Figure 2.3-a, is a fully instrumented floating laboratory for underwater vehicle research. The facility is a converted boathouse moored at the Van Isle Marina in Sidney, B.C.; there is a work deck, walkways, and control room for protecting electronics. The boathouse is a better environment for acoustic instrumentation than a normal test tank or pool, because it doesn't have any sides. In a pool or test tank, the acoustic signals bounce off the bottom and walls causing multipath problems, which can degrade the accuracy of the measurements. The SWAT floats on the water's surface, attached to a dock, so the sides underneath are open to the ocean, mitigating multipath issues by allowing acoustic signals to escape into the ocean. Depending on the tide, the water at the SWAT is between 3 and 5 m deep, and the primary test area is approximately 5.25 m long and 3 m wide. The opening is used to launch and recover the ROV and for making measurements, however, once underwater, the ROV can venture outside of these boundaries.

2.2.1 Tracking Systems

The SWAT has two tracking systems for measuring the position of objects inside the testing arena: the VZ3000 VisualEyez surfaced-based MOCAP system from PhoeniX Technologies Incorporated, and a SouthStar SBL system from Desert Star, for tracking motion under-

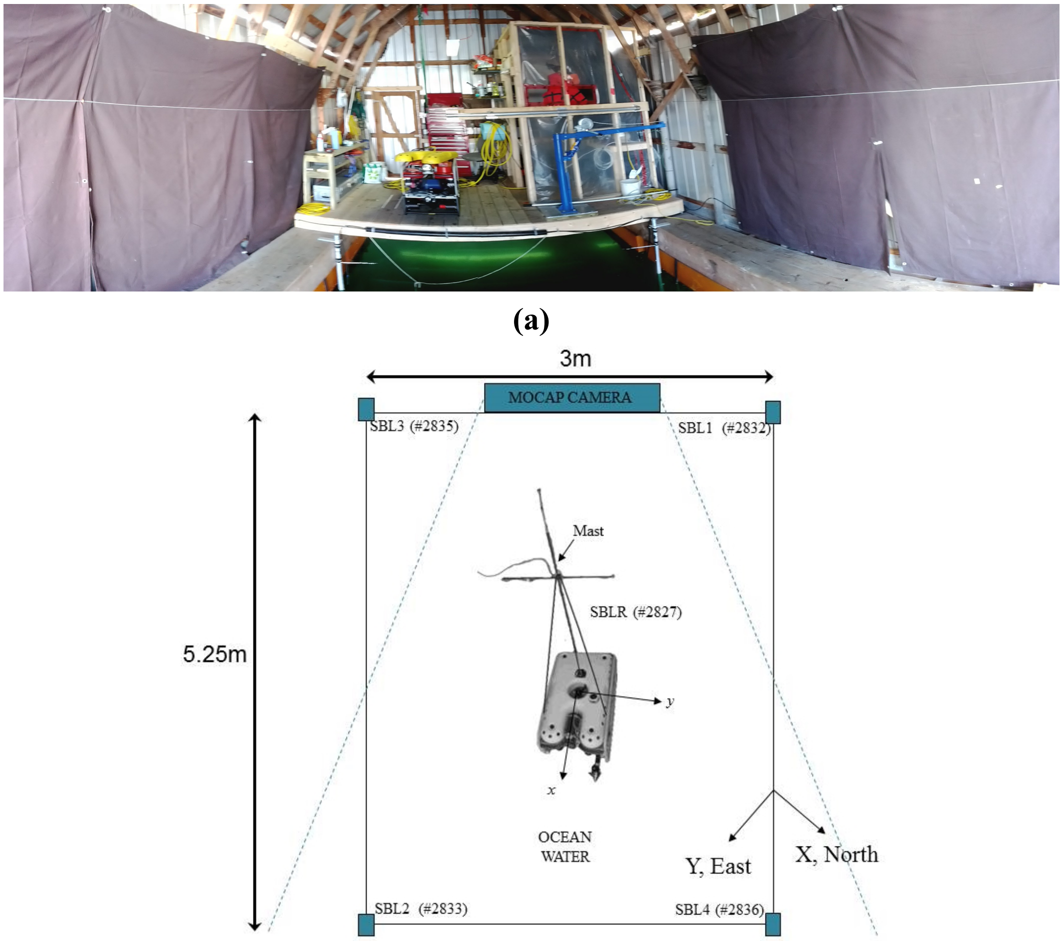

(a)

(b)

Figure 2.3: Shallow Water Acoustic Test Facility (SWAT) located at Van Isle Marina: (a) image showing deck area and launch area (b) schematic showing the layout of the primary test area

water. The MOCAP can provide millimetre accuracy at over 100 Hz for objects above the surface of the water. The SBL provides subsea position updates with centimetre accuracy at 1 Hz.

The MOCAP system is used to map the location of objects within the boathouse and to generate "truth" data for verifying the position and orientation of the ROV. The camera unit is mounted in such a way that it can capture a wide swath of the water surface, as shown in Figure 2.3-b. The camera contains three high-speed high-resolution imaging sensors that can estimate the position of a set of optical markers within their field of view and up to 7 m away from the camera. The MOCAP can be used to track the location of the ROV through the use of a mast that sticks up above the water. To use the MOCAP system to track the vehicle while it is underwater, a mast is employed that holds the tracking LEDs out of the water while the vehicle manoeuvres below the surface. The mast is further described in Section 2.3.

The SBL system has four acoustic transceivers (receiving stations) mounted in each corner of the SWAT facility as shown in Figure 2.3-b. The transceivers are located approximately 0.8 m below the surface of the water. The location of the receiving stations are surveyed using the MOCAP system. This method can provide a position for each acoustic element with respect to the boathouse to within a few centimetres. The ROV carries a roving transceiver (rover), which emits an acoustic ping that is detected by the receiving stations. The receiving stations and the rover are all cabled to the main control box on deck, with the rover cable being routed up the vehicle's tether. The cabled configuration permits synchronized timing between the rover and the receiving stations, enabling a precise measurement of the range between the rover and each receiving station from the time of flight of the acoustic ping. Using trilateration, the four different ranges can be used to determine the position of the rover and, thereby, the position of the vehicle. The most accurate positioning is obtained inside the boathouse in the plane containing the reference stations. The positioning information from the SBL is available outside of the boathouse as well, but the accuracy of the estimate decreases as the vehicle moves away from the receiver array.

2.3 Falcon Remotely Operated Underwater Vehicle

The work presented herein utilizes a Saab Sea Eye Falcon ROV, a highly maneuverable 'open frame' observation class ROV, which has been manufactured using polypropylene and other composite materials. The nominal mass of the vehicle is approximately 55 kg

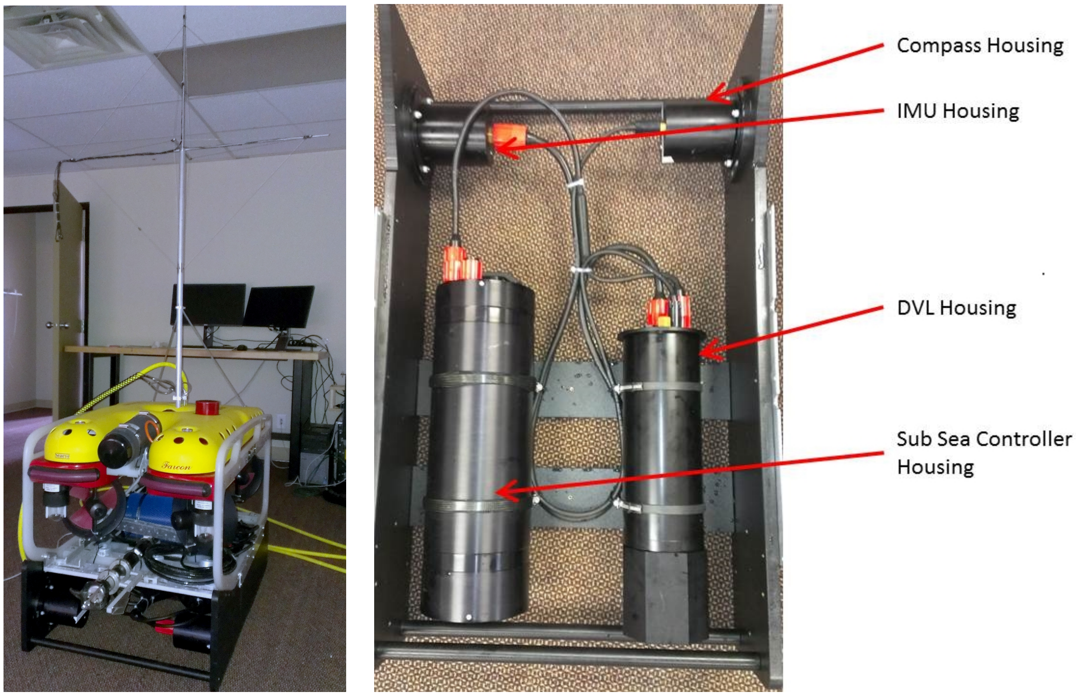

(a) **(b)**

Figure 2.4: The Falcon configured for research: (a) the modified vehicle showing mast and sled attached, and (b) the layout of the instruments on the navigation sled (shown from top).

and it is powered by five magnetically coupled thrusters (four in the horizontal plane and one for vertical motion), each capable of achieving 13 kgf thrust or a combined forward thrust of approximately 50 kgf. The ROV's design makes it rugged and powerful enough to work in moderate currents and manipulate sizable objects underwater. The vehicle has an upper and lower mounting surface. The lower surface, located at the bottom of the vehicle, is an open frame structure for mounting ballast and tooling; the upper mounting surface is a solid red block, near the top of the ROV, to which all the thrusters, cameras, lights, and instruments are mounted. All the equipment on the ROV, including the thrusters, are controllable through RS-485 communication protocol, this is one of the key features that makes the Falcon a suitable platform for this research.

The off-the-shelf Falcon ROV is equipped with a pressure sensor and compass for navigation. These two instruments alone cannot be used to produce a sufficiently accurate estimate of the vehicle's position and attitude. Therefore, for the purposes of this research, the OTL Falcon has been modified, as shown in Figure 2.4-a, with an auxiliary interface container (AIC) (in blue, mounted to the centre of the vehicle) and a navigation sled. The navigation sled, shown in Figure 2.4-b, is mounted to the lower surface of the vehicle. The sled holds an inertial measurement unit (IMU), a doppler velocity log (DVL), and a Sub-Sea Controller (SSC). It also has an additional compass and pressure sensor that provide improved accuracy and resolution over the instruments that come with the Falcon. The navigation sled was designed as a stand alone addition to the ROV so that it could easily be installed or removed from the ROV depending on the requirements of a mission.

The base Falcon vehicle was also upgraded such that it was able to interface with the navigation sled. The AIC, which is a permanent addition to the Falcon, provides power, Ethernet communication, and a means for communicating on the Falcon's RS-485 communication buss. The AIC is a multi-purpose interface that can be used to install third party hardware on the Falcon. On the OTL Falcon, the AIC supports the navigation sled, a high-definition camera, and a forward looking sonar. A detailed description of the hardware that was developed to support this project is located in Appendix B.

2.4 Reference Frames and Methodology for Making Measurements

The following reference frames are used throughout this work.

North, East, Down Reference Frame (NRF): This is the navigation frame and, for the purpose of this work, is also considered to be an inertial frame[1]. For this work the

---

[1] An inertial frame is reference frame where Newton's laws are considered to be valid. For high-speed aircraft and space craft, the Earth's rotation and curvature have an impact on the equations of motion and a reference frame attached to a fixed position on the Earth cannot be considered an inertial frame; for this work, however, the vehicle speeds are very slow and the distances travelled are quite small compared to the scale of the Earth. As such, one can assume that the Earth is flat in the operating region and that the contribution

NRF is attached to a reference datum in the boat house and has the x-axis pointing north, the z-axis pointing down, and the y-axis pointing east.

Vehicle Body Reference Frame (BRF): This frame is defined with the origin at the centre of gravity of the vehicle, the x-axis pointing forward along the longitudinal axis of symmetry, parallel to the ROV's upper mounting surface, the y-axis in the same plane, perpendicular to the x-axis pointing towards the starboard side of the vehicle, and the z-axis is perpendicular to both x-axis and y-axis pointing down.

SWAT Reference Frame (HRF): This is an intermediate frame attached to the SWAT facility and is used to orient all of the objects in the boathouse with respect to each other, including cameras and SBL towers. This reference frame is mounted to the wall of the SWAT. The x-axis points along the axis from SBL1 to SBL4, the y-axis points down and the z-axis points out towards the port side, forming a right hand coordinate system.

Camera Reference Frame (CRF): This is the native frame attached to the MOCAP camera. This frame is not used explicitly, rather, data is collected in this frame and then immediately transformed into either the BRF or HRF.

Measurement Reference Frame (MRF): This is an intermediate frame, attached to the vehicle, and used to measure the location of all the pertinent points on the vehicle using the MOCAP. The MRF exists because it is not always possible to know the location and orientation of the BRF in the CRF when taking measurements of the vehicle. The MRF was selected such that it's location and orientation are visible to the MOCAP system from many different angles and located such that the LEDs that define it could be mounted to the vehicle in a repeatable fashion. Since the transformation between the CRF and the MRF can always be measured and the transformation

---

that the Earth's rotation makes to the vehicle dynamics is negligible. This allows us to define an Earth-fixed reference frame at any arbitrary point and call it an inertial frame.

between the BRF and the MRF is a measurable constant, the MRF can always be used to transform positions from the CRF into the BRF.

Sensor Reference Frame (SRF): This frame is attached to the centre of gravity (CG) of the specific sensors. Each sensor is oriented differently on the vehicle and the rotation matrix between the sensor frame and the vehicle frame is unique for each one.

2.4.1 SWAT Reference Frame (HRF)

The HRF is a reference frame that is permanently fixed to the SWAT and can be used to relate different camera reference frames with the NRF. Since the MOCAP cameras are put up and taken down regularly, the relationship between the NRF and the CRF also changes regularly. The HRF is established by securing three LEDs to the side of the boathouse test area as shown in Figure 2.5. After the MOCAP camera is mounted, the position of the LEDs in the camera frame are captured. With this information, a transformation between the CRF and HRF can be established and used to create a transformation between the camera and the NRF.

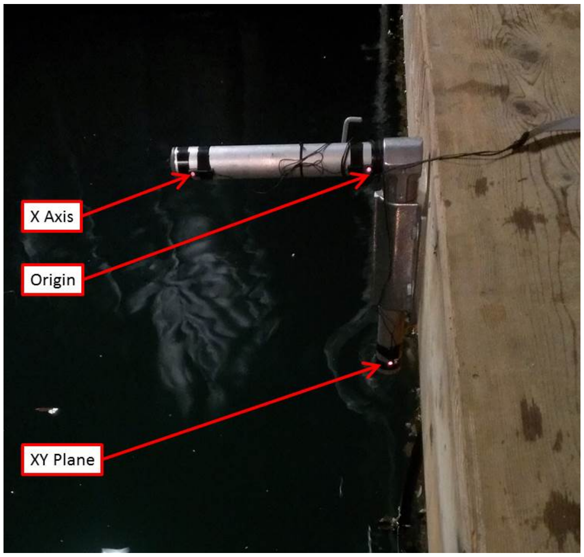

Figure 2.5: SWAT Reference Frame (HRF) fixed to the boathouse on the starboard side of the test area.

The HRF and NRF have a fixed relationship. This was determined by measuring the direction of gravity and the heading relative to true north in the boathouse frame. The origin of the NRF is set to be coincident with the origin of the HRF. The rotation matrix that relates the HRF and NRF is as follows:

$$R^{H\rightarrow N} = \begin{bmatrix} 0.96460 & -0.00951 & -0.26356 \\ -0.26334 & 0.01953 & -0.96451 \\ 0.01432 & 0.99976 & 0.01633 \end{bmatrix} \tag{2.1}$$

2.4.2 Mast for Motion Capture System

Figure 2.6: The arrangement of the Falcon mast.

The MOCAP can be used to measure the position and attitude of the vehicle with respect to the HRF (and by extension to the NRF), but the MOCAP LEDs can only be used above the surface of the water. In order to use the MOCAP to estimate the position and orientation of the vehicle while it is underwater, markers were affixed to a lightweight mast and mounted to the ROV as shown in Figure 2.4-a. Since the mast is rigidly mounted to the vehicle, the position and orientation of the vehicle underwater can be directly inferred from the position and orientation of the mast. Therefore, the position of the optical markers on the mast can be used to calculate the position and orientation of the ROV while it performs manoeuvres up to 1 m below the surface of the water. The mast is installed on the top of the vehicle aft of the vertical thruster, right next to the vehicle's lifting point. The mast is 1.4 m tall and has a cross member 0.4 m from the top. The mast carries 12 optical markers, one cluster of two on the top, another cluster half way down to the cross member, another at the intersection point, one on each end of the cross member, and then two single markers pointing aft mid way down the cross member. Figure 2.6 shows the marker locations on the mast.

The locations of the LED markers in the BRF are given in Table 2.1. As long as four of the markers are visible to the camera, the orientation of the BRF with respect to the NRF can be uniquely determined using a non-linear least squares minimization algorithm (described in Section 2.4.2). The mast has twelve markers, which provide redundancy for determining the orientation of the BRF. Having markers pointing forward and aft at each point makes it more likely at least one marker for each pair will be visible to a camera at any given time.

Determining the Position and Orientation of the Vehicle Using the Mast

Since the marker LEDs visible to the camera are constantly changing, it is not practical to define a reference frame using specific markers. Two methods of deriving state information about the vehicle from the mast were derived. The first was a generalized non-linear optimization, which estimated the position and orientation of the mast using 4 or more LEDs. The second was an EKF, similar to the one designed for the vehicle navigation in Chapter 4.

The generalized non-linear optimization algorithm utilizes the fact that the location of each LED is known in the body frame (Table 2.1) and minimizes the following cost func-

Table 2.1: Mast LED Locations in the Body Frame

LED	X	Y	Z
1	-0.05523	0.01295	-1.27840
2	-0.28817	0.00740	-1.27340
3	-0.15688	0.45266	-1.26852
4	-0.17723	0.45209	-1.26794
5	-0.17998	0.02586	-1.74386
6	-0.20050	0.02512	-1.74247
7	-0.16516	-0.43204	-1.28365
8	-0.18800	-0.43211	-1.28468
9	-0.17060	0.02263	-1.50774
10	-0.19118	0.02136	-1.50879
11	-0.18186	0.28964	-1.26754
12	-0.18633	-0.20329	-1.28059

tion:

$$F = \sum_{i=1}^{n} \mathbf{X}^{N}{}_{i} - \left(\mathbf{R}^{B\rightarrow N}\left(\mathbf{s}\right)\mathbf{X}^{B}{}_{i} + \mathbf{T}^{N}\right) \tag{2.2}$$

where n is the number of LEDs that are visible, $\mathbf{X}^{B}{}_{i}$ is the known location of LED$_i$ in the BRF, $\mathbf{R}^{B\rightarrow N}(\mathbf{s})$ is the rotation matrix from the BRF to the NRF derived from the attitude quaternion, **s**, and $\mathbf{X}^{N}{}_{i}$ is the measured location of LED$_i$ in the NRF frame[2]. This minimization estimates the attitude quaternion, **s**, and the translation vector between the origin of the BRF and the NRF expressed in the NRF, and $\mathbf{T}^{N}$, subject to the constraint $||\mathbf{s}|| = 1$. The 125 Hz update rate for the MOCAP frame is relatively fast compared to the vehicle dynamics, with maximum translational and rotational speeds of 1.5 m/s and $50°$/s, the maximum amount of expected rotation and translation per MOCAP cycle is $0.4°$ and 1.2 cm. Therefore, the processing time for the optimization can be minimized by using the solution from the previous iteration as the initial guess.

The above approach generates a very precise estimate of the position and attitude of the vehicle, but doesn't provide any information about velocity or angular rates. Numerically differentiating the position and attitude generates predictably noisy results. Since this work

---

[2] The transformation from the Camera Reference Frame (CRF) to the NRF is a known static quantity and can be applied before the optimization

relies on the MOCAP data to validate the sensor measurements and navigation estimates, which includes velocity and rate information, an EKF method was also derived that provided a better method of estimating rates. The EKF derivation can be found in Appendix C.

Effect of the mast on the vehicle dynamics

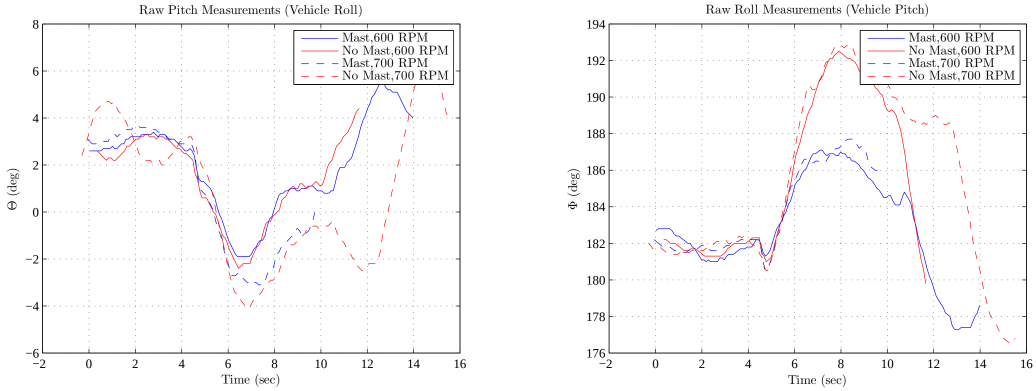

(a) **(b)**

Figure 2.7: Comparison of the (a) pitch and (b) roll angles for high speed forward motion with and without the mast .

While the mast allows the vehicle to be tracked, it also changes it's mass and buoyancy characteristics slightly. The mast is made of a sealed light weight aluminum tube that adds buoyancy as it is submerged. The additional drag from the mast will be negligible compared to the drag from the rest of the vehicle. However, since the mast adds weight more than a meter above the centre of buoyancy, it can be expected to affect the vertical stability margin and change the inertial properties. A comparison of the roll and pitch dynamics with and without the mast are shown in Figure 2.7. Here it can be seen that the overall effect of the mast is to increase the roll and pitch stability slightly during high-speed forward motion (i.e. smaller roll and pitch angles are seen), with the vehicle pitch being affected most. This is indicative of a larger separation between the center of buoyancy and the center of gravity.

Chapter 3

Dynamic Model

A dynamic model of the Falcon ROV is an important part of obtaining an accurate estimation of the vehicle state vector and of testing potential control systems. In this chapter, a dynamic model for the thrusters is presented, followed by a discussion on the vehicle kinematics and the equations of motion. In the second half of the chapter, the parameters of the two models are identified through a series of system identification tests performed at the SWAT and MTC facilities.

3.1 Background

Researchers have been trying to characterise the dynamics of ROVs since the US Navy first developed CURV in the 1960's. Dynamic models can be used for guidance, navigation and control systems (as is presented here), developing simulators for training, and optimising mechanical designs to improve performance. Conventional dynamic modelling identifies the primary physical phenomenon (the physics) and conducts some experimental parameter estimation (PE) experiments. With roots in system identification methods for ships and aircraft, parameter estimation for ROVs has historically involved the use of a tow tank, where the vehicle (or a scale model) would be carefully instrumented and then pulled through the water in an attempt to isolate and excite the different dynamic modes and measure the response. A conventional ROV dynamic model framework includes entrained mass, added mass, rigid body dynamics, a quadratic drag model, and has 288 different parameters to be identified [20]. Identifying all of these parameters is an expensive and time-consuming task, fraught with error. This makes exceptionally accurate dynamic models prohibitively expensive to develop. They are specific to a particular vehicle configuration, and, as soon as the vehicle configuration changes (which often occurs between ROV deployments), the hydrodynamic characteristics change and the model becomes obsolete [14]. As a result, many work-class ROVs are designed without consideration for their hydrodynamic properties, which generally ensures a high level of uncertainty in the vehicle's performance characteristics. Typical ROV operations rely on visual feedback to a human pilot to overcome these uncertainties.

Despite the 288 parameters in a conventional ROV model, there are several limitations to the approach: 1)it will never be able to capture the more intricate higher order dynamics that occur when a complex body moves arbitrarily through a viscous fluid, 2) it will not account for the dramatic changes in local water velocity that occur in the vicinity of thrusters, 3) it will not account for the dynamics imparted on the vehicle by the tether. While attempts have been made to model these extraneous phenomena [8, 3, 11], estimating the contributions of these effects to the ROV motion in real-time on a working vehicle is not realistic [10]. As such, we are left with a model where dynamic uncertainties can outweigh the predictable physical factors.

The best approach for generating a dynamic model depends on the application. For example, when creating a simulation, one will want to insert some realistic tether dynamics. These dynamics can be somewhat contrived, as the intent is to provide the pilot with a realistic ROV operating experience, not to exactly model what will occur on a specific mission. For the purpose of navigation and control, the most important thing is to realistically model the input/output dynamics. In Clark et al. [14], the authors present a method for identifying system parameters during sea trials using onboard sensors instead of using a test tank. The results produce a model of similar accuracy albeit less detailed. This methodology is further explored by Caccia, Indiveri and Veruggio in [11], where they included the introduction of a thruster interference factor to account for interference from system integration on the thrust output. The system identification method used in this work differs only slightly from that presented by Caccia, Indiveri and Veruggio. They used a least squares optimization on the steady-state velocities to determine the thrust factor and the drag coefficients; in this work, the least squares optimization uses data taken during both the acceleration and steady-state phases to determine the drag coefficients, the added mass coefficients, and the thruster interference factor simultaneously.

3.2 Theoretical Model of the Dynamics and Kinematics

3.2.1 Thruster Model

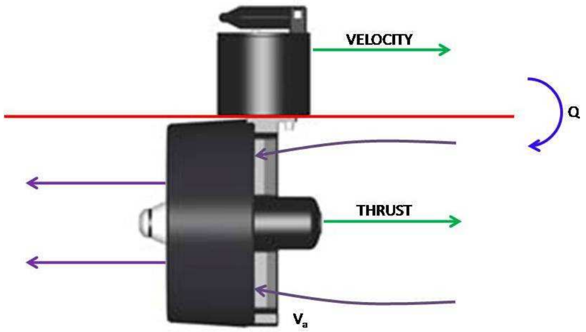

Figure 3.1: Diagram showing the relationship between the vehicle velocity, advance speed, and thrust for a negative command (clockwise propeller rotation).

The thrusters are modelled using the bi-linear thruster model in Eq. 3.1, which is a first order approximation of the torque developed about the thruster axis, and the corresponding thrust developed using the lift-force calculations for a single-screw propeller [20]. For this work, the motor dynamics are being neglected as are effects from varying angles of attack of the thruster. A more sophisticated thruster model that includes these additional effects is concurrently being developed in the OTL, but will not be used here.

Using the sign conventions shown in Figure 3.1, the thrust model can be expressed using the following:

$$T = \rho D^4 K_T \left(J_0\right) |\Omega| \Omega \tag{3.1}$$

where ρ is the density of water, D is the diameter of the propeller, Ω is the propeller speed, and $K_T \left(J_0\right)$ is the thrust coefficient. The thrust coefficient is a function of the advance number, J_0. The advance number is the following non-dimensional coefficient:

$$J_0 = V_a/(\Omega D) \tag{3.2}$$

where V_a is the thruster advance speed (the speed of the water as it enters the thruster).

In general, the advance speed is not the same as the vehicle velocity. A ship's propeller provides a relatively simple example: the propeller is usually at the stern of a ship and located inside of the ships wake; as such, the speed of water at the propeller is less than the speed of the ship. Traditionally, the advance speed has been related to the vessel velocity by the following relation:

$$V_a(V) = (1 - w_T)V \tag{3.3}$$

where w_T is the wake fraction number (typically a constant between 0.1 and 0.4). ROV systems encounter this same phenomenon, but with much less predictability. When moving forward, the advance speed for the forward thrusters will be relatively close to the free stream velocity, but the aft thrusters will be in the wake of the forward ones and the advance speed will likely be dramatically different from the free stream velocity. This is an important concept, as it can lead to variability in the output thrust at any given command.

The physics of the thruster, as described in [40], suggests that K_T should be quadratic in J_0 instead of linear as suggested in [20]. In Section 3.3, measurements will show that a quadratic function is a reasonable assumption for the Falcon. This allows the following approximation to be used:

$$K_T(J_0) = \alpha J_0^2 + \beta J_0 + \gamma \tag{3.4}$$

Eq. 3.1 through Eq. 3.4 result in a simple method for estimating the thrust over a wide range of operating conditions. First the advance speed, V_a, and advance number, J_0, are found, then the thrust coefficient, K_T can be determined. Once K_T is known, then the estimated thrust can be calculated using Eq. 3.1.

3.2.2 Vehicle Model

The rigid body dynamics of an ROV with six degrees of freedom (DOFs) can be described by the following equation:

$$\dot{\boldsymbol{\eta}} = \mathbf{J}(\boldsymbol{\eta})\boldsymbol{\nu} \tag{3.5}$$

where $\boldsymbol{\eta} = [x \ y \ z \ \mathbf{s}]^T \in \Re^7$ and $\boldsymbol{\nu} = [u \ v \ w \ p \ q \ r]^T \in \Re^6$. x, y, and z are the three components that make up the position of the vehicle in the NRF and $\mathbf{s} = [s_0 \ s_1 \ s_2 \ s_3]^T$ is attitude quaternion[1]. u, v, and w are the velocities and p, q, and r are the angular rates, both expressed in the BRF. Finally, $\mathbf{J}(\boldsymbol{\eta})$ is the transformation matrix which maps the velocities expressed in the BRF to the NRF. $\mathbf{J}(\boldsymbol{\eta})$ is block diagonal, and can be broken down as follows:

$$\mathbf{J}(\boldsymbol{\eta}) = \begin{bmatrix} \mathbf{J}_1 & \mathbf{0}^{3\times 3} \\ \mathbf{0}^{4\times 3} & \mathbf{J}_2 \end{bmatrix} \tag{3.6}$$

In this definition, $\mathbf{J}_1$ is a rotation matrix transforming a vector in the BRF to the NRF. As per the derivation for Eq. D.19 in Appendix D, using the quaternion representation, $\mathbf{J}_1$

---

[1] The use of quaternions to represent orientation is further described in Appendix D.

can be written as:

$$\mathbf{J}_1(\boldsymbol{\eta}) = \begin{bmatrix} s_0^2 + s_1^2 - s_2^2 - s_3^2 & 2(s_1 s_2 - s_0 s_3) & 2(s_1 s_3 + s_0 s_2) \\ 2(s_1 s_2 + s_0 s_3) & s_0^2 - s_1^2 + s_2^2 - s_3^2 & 2(s_2 s_3 - s_0 s_1) \\ 2(s_1 s_3 - s_0 s_2) & 2(s_2 s_3 + s_0 s_1) & s_0^2 - s_1^2 - s_2^2 + s_3^2 \end{bmatrix} \tag{3.7}$$

Similarly, $\mathbf{J}_2$, the mapping from p, q, r to $\dot{\mathbf{s}}$, can be written as:

$$\mathbf{J}_2(\boldsymbol{\eta}) = \begin{bmatrix} -s_1 & -s_2 & -s_3 \\ s_0 & -s_3 & s_2 \\ s_3 & s_0 & -s_1 \\ -s_2 & s_1 & s_0 \end{bmatrix} \tag{3.8}$$

Eq. 3.7 and Eq. 3.8 highlight one of the advantages of quaternions, the elimination of computationally expensive trigonometry functions in the transformation matrices. The primary advantage of quaternions, however, is the avoidance of singular conditions, often called "gimbal-lock", that occur with Euler angles, a complete discussion of the quaternions and Euler angles is given in Appendix D.

The time-evolution of $\boldsymbol{\nu}$ can then be predicted as follows [20]:

$$\dot{\boldsymbol{\nu}}\left(\boldsymbol{\delta}, \boldsymbol{\nu}, \boldsymbol{\eta}\right) = \mathbf{M}^{-1}\left(\boldsymbol{\tau}_E + \boldsymbol{\tau} - \mathbf{C}\left(\boldsymbol{\nu}\right)\boldsymbol{\nu} - \mathbf{D}\left(\boldsymbol{\nu}\right)\boldsymbol{\nu} - \mathbf{g}\left(\boldsymbol{\eta}\right)\right) \tag{3.9}$$

where $\mathbf{M}$ is the mass matrix, $\mathbf{C}$ is the coriolis and centripetal matrix, $\mathbf{D}$ is the hydrodynamic contribution, $\mathbf{g}$ is the buoyancy and gravitational contributions, and $\boldsymbol{\tau}$ and $\boldsymbol{\tau}_E$ are the forces and moments from the actuators and the environment respectively. Each of these components will be discussed in-depth in the following sections.

Inertial Properties

The inertial properties of the vehicle can be divided into the rigid body mass matrix and the added mass matrix. The rigid body mass matrix comes from the kinematic equations and can be expressed as:

$$\mathbf{M}_{RB} = \begin{bmatrix} m\mathbf{I}^{3\times3} & -m\tilde{\mathbf{r}}_{CG} \\ m\tilde{\mathbf{r}}_{CG} & \mathbf{I}_0 \end{bmatrix} \tag{3.10}$$

where m is the mass of the vehicle, $\mathbf{r}_{CG}$ is the vector from the origin of the BRF to the CG of the vehicle, and $\mathbf{I}_0$, the body's inertia tensor, which is defined as:

$$\mathbf{I}_0 \triangleq \begin{bmatrix} I_x & -I_{xy} & -I_{xz} \\ -I_{yx} & I_y & -I_{yz} \\ -I_{zx} & -I_{zy} & I_z \end{bmatrix} \tag{3.11}$$

For this work, the origin of the BRF is the CG ($\mathbf{r}_{CG} = \mathbf{0}$). Under this assumptions, Eq. 3.10 results in the following:

$$\mathbf{M}_{RB} = \begin{bmatrix} m & 0 & 0 & 0 & 0 & 0 \\ 0 & m & 0 & 0 & 0 & 0 \\ 0 & 0 & m & 0 & 0 & 0 \\ 0 & 0 & 0 & I_x & -I_{xy} & -I_{xz} \\ 0 & 0 & 0 & -I_{yx} & I_y & -I_{yz} \\ 0 & 0 & 0 & -I_{zx} & -I_{zy} & I_z \end{bmatrix} \tag{3.12}$$

Coriolis and Centripetal Forces and Moments

The coriolis and centripetal terms in the ROV dynamics come from the $\omega \times v$ and the $\omega \times (\omega \times r_{CG})$ terms that appear when you derive Newton's second law in terms of kinematic variables defined in the rotating BRF. Several skew symmetric parameterizations of these terms are presented in [20]; recalling that $\mathbf{r}_{CG} = \mathbf{0}$ this parameterization can be simplified as:

$$\begin{aligned}\mathbf{C}_{RB} &= -\mathbf{C}_{RB}^T = \begin{bmatrix} m\widetilde{\boldsymbol{\nu}_2} & -m\widetilde{\boldsymbol{\nu}_2}\widetilde{\mathbf{r}_{CG}} \\ m\widetilde{\boldsymbol{\nu}_2}\widetilde{\mathbf{r}_{CG}} & -\widetilde{\mathbf{I}_0\boldsymbol{\nu}_2} \end{bmatrix} \\ &= \begin{bmatrix} m\widetilde{\boldsymbol{\nu}_2} & 0 \\ 0 & -\widetilde{\mathbf{I}_0\boldsymbol{\nu}_2} \end{bmatrix}\end{aligned} \tag{3.13}$$

where $\boldsymbol{\nu}_2 = [p\ q\ r]^T$.

Added Mass

Added mass can be often misunderstood, according to Fossen [20]:

> Added (virtual) mass should be understood as pressure-induced forces and moments due to forced harmonic motion of the body which are proportional to the acceleration of the body.

For completely submerged vehicles, one can assume the added mass coefficients are constant. For a more thorough understanding, it can be noted that for a vehicle to accelerate into a stationary fluid, the fluid must move aside and then close up behind the vehicle. Therefore, the motion of the vehicle imparts a kinetic energy into the fluid, which it would otherwise lack if the vehicle was not in motion. Since this kinetic energy comes from the vehicle, it must be accounted for in the vehicles equation of motion.

Added mass can be accounted for be adding an additional term to the mass and coriolis matrices in Eq. 3.9, such that:

$$\begin{aligned}\mathbf{M} &\triangleq \mathbf{M}_{RB} + \mathbf{M}_A \\ \mathbf{C} &\triangleq \mathbf{C}_{RB} + \mathbf{C}_A\end{aligned} \tag{3.14}$$

where $\mathbf{M}_A$ is the added inertia matrix and $\mathbf{C}_A$ corresponds to the centripetal and coriolis components that are added from these same hydrodynamic sources. For a complete derivation of the added mass dynamics from the kinetic energy of the fluid, one can refer to [20].

For low speed applications, one often assumes that there is relatively little cross coupling between the DOFs so the added inertia matrix can be considered to be diagonal; this assumption will not be made in this work. Therefore, the added inertia matrix for the two systems can be defined as:

$$\mathbf{M}_A \triangleq - \begin{bmatrix} X_{\dot{u}} & X_{\dot{v}} & X_{\dot{w}} & X_{\dot{p}} & X_{\dot{q}} & X_{\dot{r}} \\ Y_{\dot{u}} & Y_{\dot{v}} & Y_{\dot{w}} & Y_{\dot{p}} & Y_{\dot{q}} & Y_{\dot{r}} \\ Z_{\dot{u}} & Z_{\dot{v}} & Z_{\dot{w}} & Z_{\dot{p}} & Z_{\dot{q}} & Z_{\dot{r}} \\ K_{\dot{u}} & K_{\dot{v}} & K_{\dot{w}} & K_{\dot{p}} & K_{\dot{q}} & K_{\dot{r}} \\ M_{\dot{u}} & M_{\dot{v}} & M_{\dot{w}} & M_{\dot{p}} & M_{\dot{q}} & M_{\dot{r}} \\ N_{\dot{u}} & N_{\dot{v}} & N_{\dot{w}} & N_{\dot{p}} & N_{\dot{q}} & N_{\dot{r}} \end{bmatrix} \tag{3.15}$$

Using the SNAME notation, the hydrodynamic added mass force X_A along the x-axis due to an acceleration $\dot{w}$ along the z-axis would be calculated by $X_A = X_{\dot{w}}\dot{w}$, where $X_{\dot{w}} \triangleq \frac{\partial X}{\partial \dot{w}}$. Note that for fully submerged vehicles M_A will always be strictly positive[2] [20].

From Fossen[20], one can always parameterize $\mathbf{C}_A(\boldsymbol{\nu})$ such that it can be written as:

$$\mathbf{C}_A(\boldsymbol{\nu}) = \begin{bmatrix} 0 & 0 & 0 & 0 & -a_3 & a_2 \\ 0 & 0 & 0 & a_3 & 0 & -a_1 \\ 0 & 0 & 0 & -a_2 & a_1 & 0 \\ 0 & -a_3 & a_2 & 0 & -b_3 & b_2 \\ a_3 & 0 & -a_1 & b_3 & 0 & -b_1 \\ -a_2 & a_1 & 0 & -b_2 & b_1 & 0 \end{bmatrix} \tag{3.16}$$

---

[2] The matrix M_A will be strictly positive. The individual elements of M_A are not necessarily positive.

where the equations for a_1, a_2, a_3, b_1, b_2, and b_3 are given by the following[3]:

$$\begin{aligned}
a_1 &= X_{\dot{u}}u + X_{\dot{v}}v + X_{\dot{w}}w + X_{\dot{p}}p + X_{\dot{q}}q + X_{\dot{r}}r \\
a_2 &= Y_{\dot{u}}u + Y_{\dot{v}}v + Y_{\dot{w}}w + Y_{\dot{p}}p + Y_{\dot{q}}q + Y_{\dot{r}}r \\
a_3 &= Z_{\dot{u}}u + Z_{\dot{v}}v + Z_{\dot{w}}w + Z_{\dot{p}}p + Z_{\dot{q}}q + Z_{\dot{r}}r \qquad (3.17) \\
b_1 &= K_{\dot{u}}u + K_{\dot{v}}v + K_{\dot{w}}w + K_{\dot{p}}p + K_{\dot{q}}q + K_{\dot{r}}r \\
b_2 &= M_{\dot{u}}u + M_{\dot{v}}v + M_{\dot{w}}w + M_{\dot{p}}p + M_{\dot{q}}q + M_{\dot{r}}r \\
b_3 &= N_{\dot{u}}u + N_{\dot{v}}v + N_{\dot{w}}w + N_{\dot{p}}p + N_{\dot{q}}q + N_{\dot{r}}r
\end{aligned}$$

Potential and Hydrodynamic Damping

With ocean going vessels, hydrodynamic forces can typically be filed into four categories: potential damping $\mathbf{D}_P$, wave damping $\mathbf{D}_W$, skin friction $\mathbf{D}_S$ and vortex shedding $\mathbf{D}_M$ [20]. The total hydrodynamic drag on the vehicle is defined as:

$$\mathbf{D}\left(\boldsymbol{\nu}\right) \triangleq \mathbf{D}_P\left(\boldsymbol{\nu}\right) + \mathbf{D}_W\left(\boldsymbol{\nu}\right) + \mathbf{D}_S\left(\boldsymbol{\nu}\right) + \mathbf{D}_M\left(\nu\right) \qquad (3.18)$$

Potential damping, otherwise known as wave or radiation induced damping, occurs when a body moving through water creates waves (such as a body bobbing up and down). These waves transport energy away from the system, which in turn dampens the eliciting motion. This type of damping is generally negligible for underwater vehicles operating at depth, as they are not affected by wave action and typically don't exhibit much oscillatory motion. Wave damping, the added resistance that a ship experiences when cutting through waves, is also negligible when operating at depth. However, while these two components do not factor in significantly at depth, they do impact the vehicle while it is on the surface or operating near the surface, and when neglected will add to the dynamic uncertainties.

---

[3] The equations for a_1, a_2, a_3, b_1, b_2, and b_3 are incorrect in [20]. They have been corrected in the subsequent version of this book. The equations presented here are the corrected equations

Skin friction is the combination of the drag produced by the laminar boundary layer in response to low frequency motion through a viscous medium and the drag produced by the turbulent boundary layer in response to high frequency motion. Laminar drag is linear in ν and the turbulent drag due to high frequency motion is quadratic.

When a viscous fluid flows past an object with sufficient speed, vortices form in the fluid behind the trailing edge of the object. This phenomenon is often referred to as a wake, and it occurs because, with the frictional forces present in a viscous fluid, the system (fluid and vehicle) does not conserve energy. This vortex shedding produces an additional quadratic damping force on the vehicle.

Therefore, in six DOF, the total drag from skin friction and vortex shedding can be calculated using a linear and a combined quadratic component:

$$\mathbf{D}(\boldsymbol{\nu}) = \mathbf{D}_L\boldsymbol{\nu} + \begin{bmatrix} |\boldsymbol{\nu}|^T \mathbf{D}_{Q_u}\boldsymbol{\nu} \\ |\boldsymbol{\nu}|^T \mathbf{D}_{Q_v}\boldsymbol{\nu} \\ |\boldsymbol{\nu}|^T \mathbf{D}_{Q_w}\boldsymbol{\nu} \\ |\boldsymbol{\nu}|^T \mathbf{D}_{Q_p}\boldsymbol{\nu} \\ |\boldsymbol{\nu}|^T \mathbf{D}_{Q_q}\boldsymbol{\nu} \\ |\boldsymbol{\nu}|^T \mathbf{D}_{Q_r}\boldsymbol{\nu} \end{bmatrix} \tag{3.19}$$

where $\mathbf{D}_L \in \Re^{6\times 6}$ is the linear drag matrix, and $\mathbf{D}_{Q_i}\quad i = u, v, w, p, q, r$ are 6 quadratic drag matrices, are all contained in $\Re^{6\times 6}$. In a model where all 6 DOFs are decoupled, the quadratic drag matrices have only a single non-zero element on the diagonal which corresponds to the DOF in question: for example, the $(1, 1)$ element of $\mathbf{D}_{Q_u}$, the $(2, 2)$ element of $\mathbf{D}_{Q_v}$ etc. This allows one to replace the 6 individual matrices with a single diagonal matrix instead. This assumption will not be made in this work, and the 6 quadratic matrices will be kept separate to support cross coupling terms.

While in theory all of the coefficients can be populated for this model, only those with significant effect will be measurable in the system ID testing, and the majority will be zero. This is particularly true with the quadratic drag matrices, which will be very sparsely populated.

Gravitational Forces and Moments

The gravitational and restoring forces and moments are different than other forces that have been previously discussed in that their natural frame of reference is the NRF as opposed to the BRF. This means that, in the BRF, the expression for the gravitational and restoring forces will involve $\mathbf{J_1}\left(\boldsymbol{\eta}\right)$. The two forces in question are the force of gravity, acting at the CG, and the buoyancy force, which acts at the centre of buoyancy (CB); using simple statics the force equation can be written as:

$$\mathbf{g}\left(\eta\right) = -\begin{bmatrix} \mathbf{f}_G\left(\eta\right) + \mathbf{f}_B\left(\eta\right) \\ \mathbf{r}_{CG} \times \mathbf{f}_G\left(\eta\right) + \mathbf{r}_{CB} \times \mathbf{f}_B\left(\eta\right) \end{bmatrix} \tag{3.20}$$

where $\mathbf{r}_{CB}$ is the location of the CB in the vehicle body frame, the location of the CG is $\mathbf{r}_{CG} = 0$, and

$$\mathbf{f}_G\left(\eta\right) = \mathbf{J}_1^T\left(\eta\right)\begin{bmatrix} 0 \\ 0 \\ mg \end{bmatrix} \qquad \mathbf{f}_B\left(\eta\right) = -\mathbf{J}_1^T\left(\eta\right)\begin{bmatrix} 0 \\ 0 \\ \rho g \nabla \end{bmatrix} \tag{3.21}$$

where ρ is the water density, g is the gravitational acceleration, and ∇ is the displacement of the vehicle. Define $W \triangleq mg$ and $B \triangleq \rho g \nabla$ then Eq. 3.20 can be expanded to be:

$$\mathbf{g}(\eta) = -\begin{bmatrix} (W-B)\cdot 2\left(s_1 s_3 - s_0 s_2\right) \\ (W-B)\cdot 2\left(s_2 s_3 - s_0 s_1\right) \\ (W-B)\cdot\left(1 - 2\left(s_1^2 + s_2^2\right)\right) \\ (-y_B B)\cdot\left(1 - 2\left(s_1^2 + s_2^2\right)\right) - (-z_B B)\cdot 2\left(s_2 s_3 - s_0 s_1\right) \\ (-z_B B)\cdot 2\left(s_1 s_3 - s_0 s_2\right) - (-x_B B)\cdot\left(1 - 2\left(s_1^2 + s_2^2\right)\right) \\ (-x_B B)\cdot 2\left(s_2 s_3 - s_0 s_1\right) - (-y_B B)\cdot 2\left(s_1 s_3 - s_0 s_2\right) \end{bmatrix} \tag{3.22}$$

Thruster and Environmental Forces and Moments

The forces and moments imparted on the vehicle by the environment and the thrusters, are denoted by $\boldsymbol{\tau}_E$ and $\boldsymbol{\tau}$, respectively. $\boldsymbol{\tau}_E$ is a result of unknown forces applied to the vehicle by the environment; this includes, but is not limited to, forces and moments from the tether, hitting the seafloor, and unmodelled wave action. Since these forces are unknown they cannot be accounted for in the model. Representative environmental forces and moments can, however, be added to a simulation to create a realistic environment.

The forces and moments from the thrusters are more deterministic. For the Falcon, who has 5 thrusters, the effect of the thrusters on the CG of the vehicle can be calculated using the following equation:

$$\begin{aligned} \boldsymbol{\tau} &= \begin{bmatrix} \mathbf{D}_{T_1}^B & \mathbf{D}_{T_2}^B & \mathbf{D}_{T_3}^B & \mathbf{D}_{T_4}^B & \mathbf{D}_{T_5}^B \\ \widetilde{\mathbf{X}}_{T_1}^B \mathbf{D}_{T_1}^B & \widetilde{\mathbf{X}}_{T_2}^B \mathbf{D}_{T_2}^B & \widetilde{\mathbf{X}}_{T_3}^B \mathbf{D}_{T_3}^B & \widetilde{\mathbf{X}}_{T_4}^B \mathbf{D}_{T_4}^B & \widetilde{\mathbf{X}}_{T_5}^B \mathbf{D}_{T_5}^B \end{bmatrix} \begin{bmatrix} T_1 \\ T_2 \\ T_3 \\ T_4 \\ T_5 \end{bmatrix} \\ &= \mathbf{BT} \end{aligned} \tag{3.23}$$

Table 3.1: Thruster location summary

Location	Description	Units
Front Port	$\mathbf{X}_{T_1}^B = \left[\begin{array}{ccc} 0.24765 & -0.18203 & -0.05528 \end{array} \right]^T$	m
	$\mathbf{D}_{T_1}^B = \left[\begin{array}{ccc} 0.79744 & 0.60316 & -0.01717 \end{array} \right]^T$	N/A
Rear Stbd	$\mathbf{X}_{T_2}^B = \left[\begin{array}{ccc} -0.35850 & 0.17351 & -0.04623 \end{array} \right]^T$	m
	$\mathbf{D}_{T_2}^B = \left[\begin{array}{ccc} 0.86426 & 0.50287 & -0.01291 \end{array} \right]^T$	N/A
Front Stbd	$\mathbf{X}_{T_3}^B = \left[\begin{array}{ccc} 0.24572 & 0.17422 & -0.05315 \end{array} \right]^T$	m
	$\mathbf{D}_{T_3}^B = \left[\begin{array}{ccc} 0.81275 & -0.58236 & -0.01725 \end{array} \right]^T$	N/A
Rear Port	$\mathbf{X}_{T_4}^B = \left[\begin{array}{ccc} -0.35251 & -0.18466 & -0.04844 \end{array} \right]^T$	m
	$\mathbf{D}_{T_4}^B = \left[\begin{array}{ccc} 0.82701 & -0.56102 & -0.03623 \end{array} \right]^T$	N/A
Vertical	$\mathbf{X}_{T_5}^B = \left[\begin{array}{ccc} -0.01796 & -0.00835 & -0.35058 \end{array} \right]^T$	m
	$\mathbf{D}_{T_5}^B = \left[\begin{array}{ccc} 0.0 & 0.0 & 1.0 \end{array} \right]^T$	N/A

where $\mathbf{X}_{Ti}^B$ is the position of each thruster in the BRF, $\mathbf{D}_{T_i}^B$ is the direction of thrust, $\mathbf{B} \in \Re^{6\times 5}$ is the thruster input matrix and $\mathbf{T} \in \Re^{5\times 1}$ is the a vector of the thrust from each thruster in Newtons. The location and the direction of the thrust vector for each thruster, denoted by $\mathbf{X}_{T_i}^B$ and $\mathbf{D}_{T_i}^B$ respectively, was measured using the MOCAP camera system, and are given in Table 3.1.

Figure 3.2: Image of the thruster test apparatus mounted in the UVic Flume tank for the work done by Amos Buchanan.

3.3 System Identification for the Thruster Model

The system identification for the thrusters on the Falcon was done using the apparatus shown in Figure 3.2 as part of a Masters project by Amos Buchanan [7]. The thruster was mounted to a shaft, suspended from the top of the apparatus, and allowed to rotate freely about the attachment point. The shaft was then constrained to be vertical using four force sensors. When a force is exerted by the thruster, the reaction force on the sensor can be measured. The test apparatus was installed in the UVic flume tank. A flume tank is much like a wind tunnel, and circulates the water past the thruster in a predictable and controllable way. This allows one to measure the thrust at different advance speeds.

3.3.1 Propeller Speed as a Function of Command

The Falcon thrusters have an open loop control system for regulating the speed of the propeller for an input command. The thruster accepts inputs between -100 and 100 with -100 being full speed clockwise rotation of the propeller (moves vehicle in the forward or up direction). The transient response is shown in Figure 3.3, one can see that the internal Falcon control system does not implement an internal controller for propeller speed. When a step input is given where the command increases the propeller speed or changes direction of the propeller, the rise time is approximately 350ms for 0 to 100% step command; however,

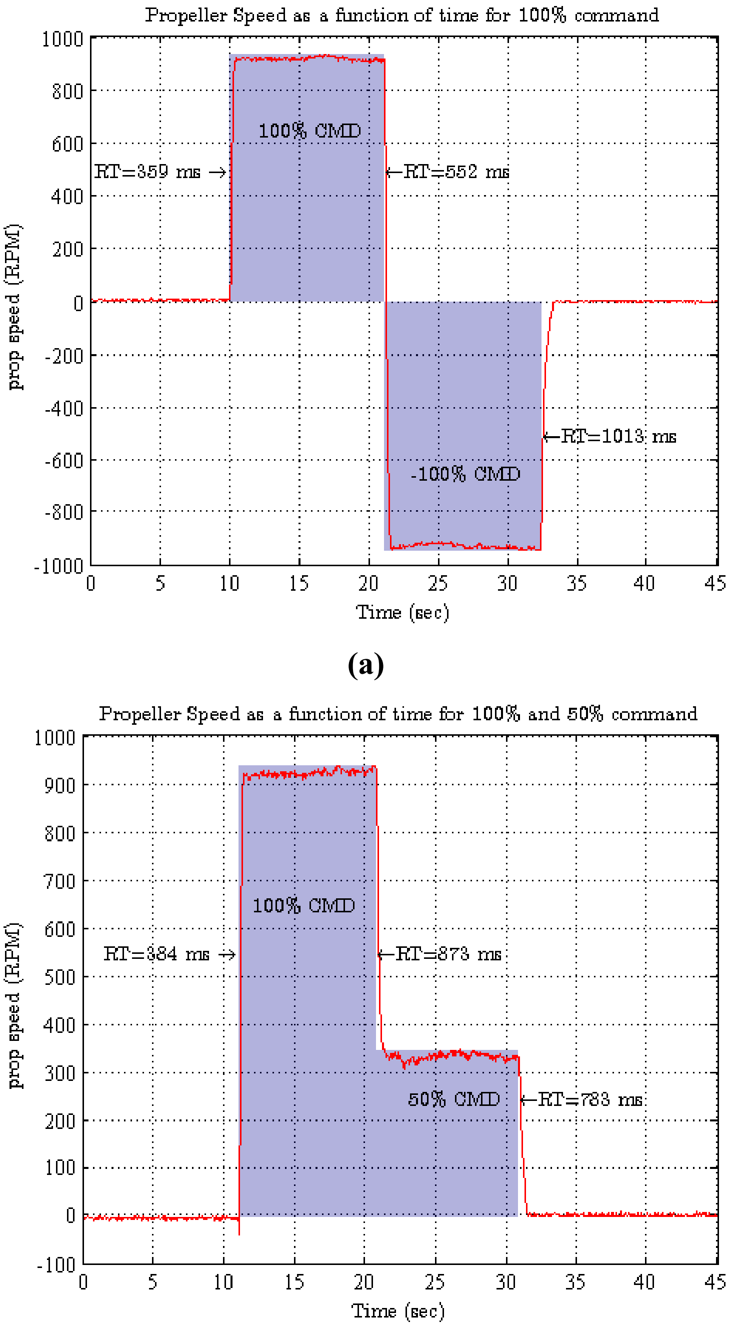

(a)

(b)

Figure 3.3: Propeller speed as a function of time for an input command with the rise time (RT) indicated for each step.

when a command is given to decrease the propeller speed, the decay time is significantly longer (approximately 1 second for a 100 to 0% step). This is indicative of the propeller slowing due to drag and friction, as opposed to being driven to a specific propeller speed. The latency between when a command is sent to the thruster and when the thruster begins to respond is between 30 and 50 ms.

Since the thruster is operating with an open loop velocity controller, an input command will result in different propeller speeds for different advance speeds, as is seen in Figure 3.4-a. With an open loop controller, the propeller speed will also vary between thrusters, as different units will have different amounts of wear and friction. As a result, for any given command the propeller speed could vary by 50 rad/sec or more.

When the SSC, described in Chapter 2 and Appendix B, is in control of the vehicle feedback on the propeller speed for each thruster is available, however, when the surface control unit (SCU) is in control, it is not[4]. When measurements of the propeller speed are not available, the estimated propeller speed with zero advance speed is used[5]. This relationship is shown in Figure 3.4-b and is characterized by the following equations:

$$\begin{array}{ll} \delta = -100 \rightarrow -60 & \Omega = 0.013827\delta^2 + 3.667122\delta + 130.533044 \\ \delta = -60 \rightarrow 0 & \Omega = 0.661971\delta \\ \delta = 0 \rightarrow 60 & \Omega = 0.650779\delta \\ \delta = 60 \rightarrow 100 & \Omega = -0.015015\delta^2 + 3.844637\delta - 136.578499 \end{array} \tag{3.24}$$

where δ is the thruster command in input percent and Ω is the propeller speed in rad/s.

---

[4] See Appendix B for details on the hardware configuration and difference between piloting the ROV through the SCU and the SSC.

[5] Estimating the propeller speed assuming zero advance speed could lead to error in the propeller speed and thrust predictions.

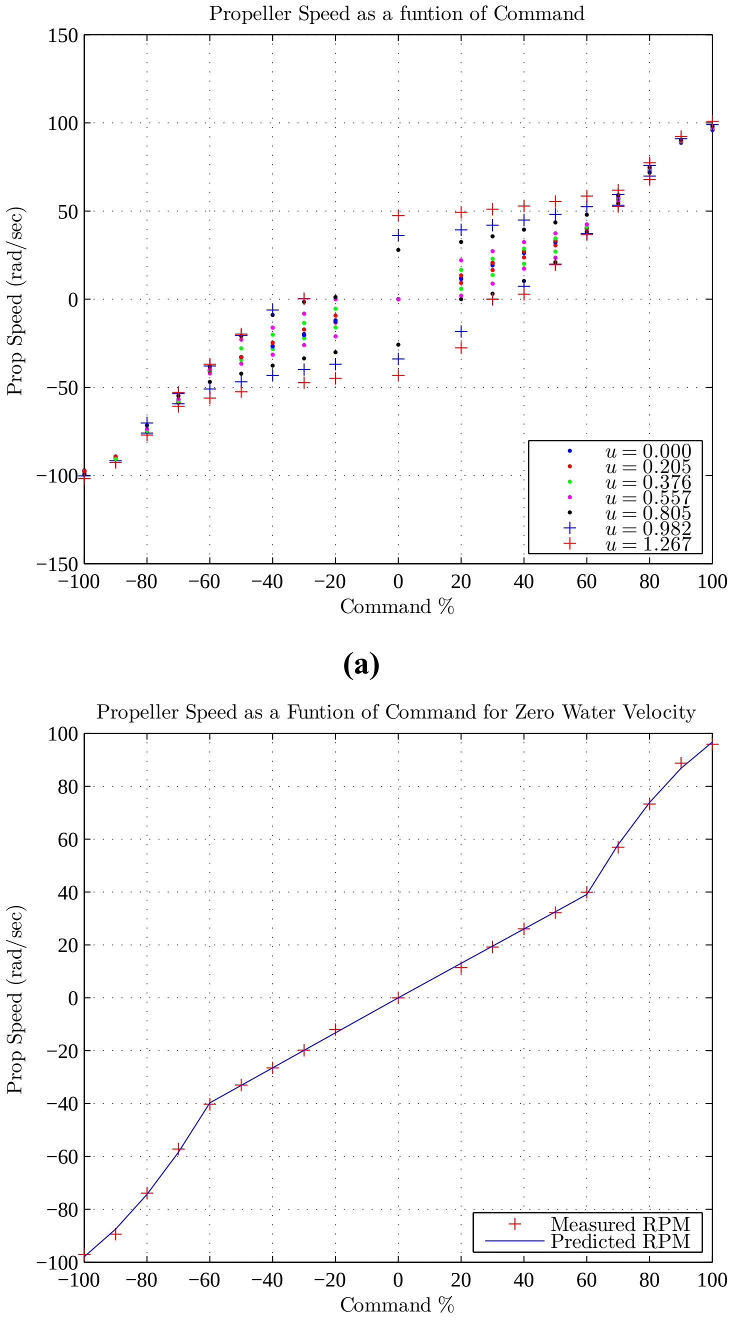

(a)

(b)

Figure 3.4: Propeller speed as a function of input command (a) for different water speeds (advance speeds) and (b) for zero water speed. Negative deviations in propeller speed occur when the water is flowing against the thruster and positive deviations occur when the water is flowing with the thruster (recall that a negative command gives forward thrust).

3.3.2 Thrust as a Function of Propeller Speed and Advance Speed

The thrust output at a given propeller speed is heavily dependant on the advance speed, V_a of the thruster. Eq. 3.1 shows that the output thrust is a function of the square of the propeller speed and K_T which is a function of the advance number, J_0. Figure 3.5 shows a plot of K_T versus J_0 for the data collected in the flume tank.

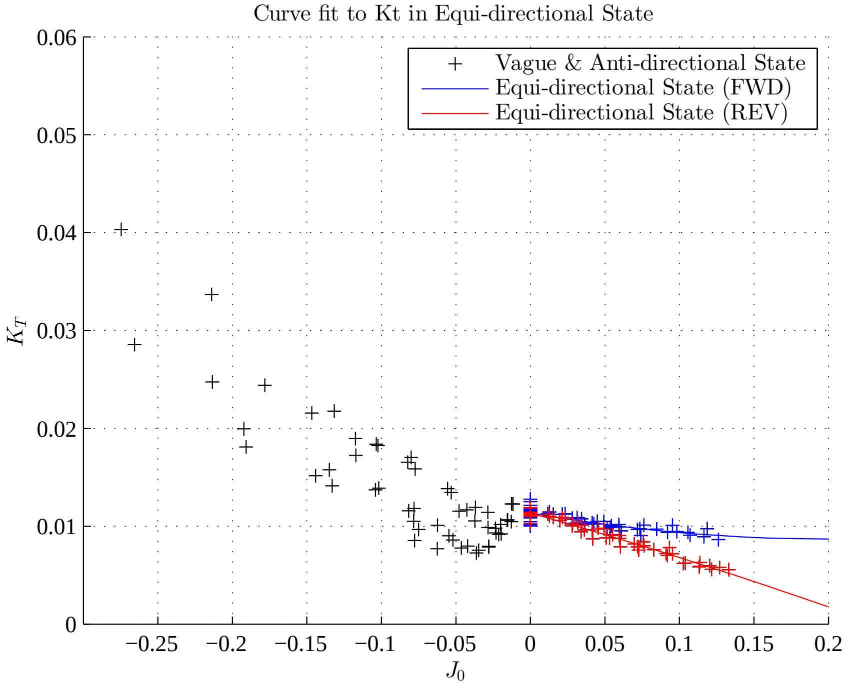

Figure 3.5: Thrust coefficient, K_T, as a function of advance number,J_0.

According to [40], there are three different operating regimes for the thruster: 'equi-directional', 'anti-directional', and 'vague-directional'. In the equi-directional regime the ambient water flow is in the same direction as the flow of water through the thruster nozzle; in the anti-directional regime, the thruster is fighting the water and the flow is in the opposite direction of the flow through the thruster nozzle. In the vague-directional regime, the desired flow through the nozzle is opposite in direction to the ambient flow, but the thruster is not spinning fast enough to overcome the ambient flow and the flow in the nozzle is unpredictable. Therefore, the equi-directional state would be normal operation, the anti-directional state would be similar to braking, where the thrusters are providing force opposite to the direction of travel, and the vague-directional state would be similar to braking but without using enough force to be effective. For this research, it will be assumed that the thruster is always operating in the equi-directional state. As previously mentioned in Section 3.2.1, the OTL is developing a more complete model that will address all three states.

Since the thruster is not completely symmetric, one would expect that the relationship between K_T and J_0 would be different for the two directions, and this has proven to be true. Figure 3.5 show the K_T values corresponding to the equi-directional state for forward and reverse in blue and red, respectively. The vague- and anti-directional states are shown in black. The quadratic curve fits to the data result in the following equations:

$$\begin{aligned} \delta > 0: \qquad & K_T = -0.025089 J_0^2 - 0.042911 J_0 + 0.011350 \\ \delta <= 0: \qquad & K_T = -0.067853 J_0^2 - 0.026903 J_0 + 0.011369 \end{aligned} \tag{3.25}$$

Using the value of K_T from Eq. 3.25, Figure 3.6 shows the thrust predicted by Eq. 3.1-Eq. 3.4 for several different water velocities and compares it to the thrust that was measured in the flume tank experiment. Since only the equi-directional state is being considered, the thrust for positive propeller speed is measured with the water flowing with the thruster. The negative propeller speed is measured in separate runs with the thruster turned around in the flume tank so that the water flows in the opposite direction.

3.3.3 Determining J_0

In order to use this model, an advance number, J_0, must be determined for each thruster. During operations, the advance speed, V_a, is not known, as the thrusters are often in the shadow of another object which deflects the flow of water and causes the local water veloc-

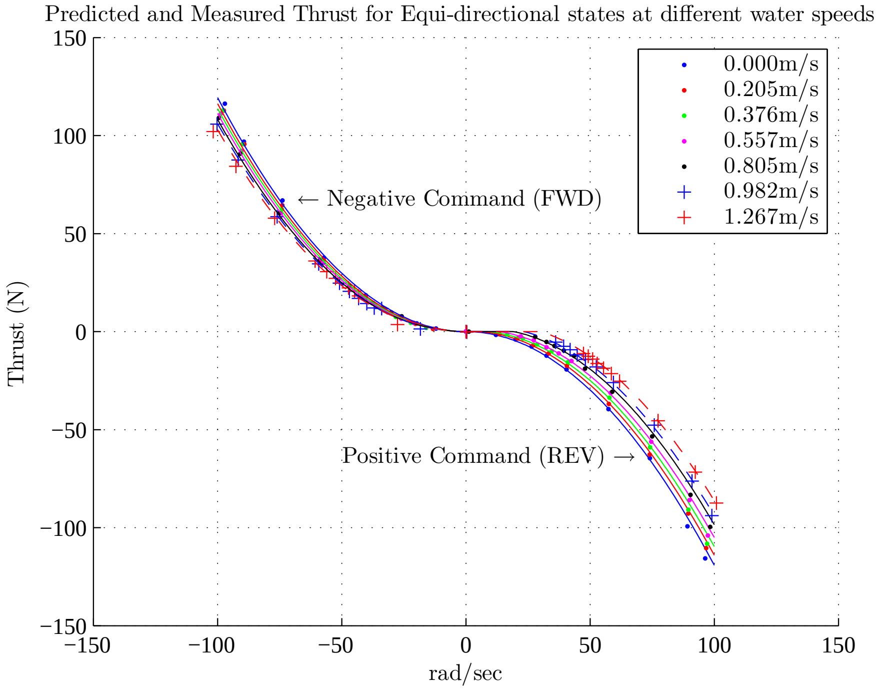

Figure 3.6: Predicted thrust compared to the measured thrust for different water speeds as measured in the flume tank experiment.

ity to deviate from the ambient water velocity. In ship design, this is often captured using a wake number, w_t, as described in Eq. 3.3. For an ROV, this effect is constantly changing and different for each thruster, and cannot be sufficiently captured by a constant. As such, the local water velocity with respect to the vehicle will be used directly to estimate the advance speed, with the knowledge there will be modelling errors due to wake effects.

Since the vehicle is undergoing translational and rotational motion, each thruster will experience a unique advance speed. For the vehicle pictured in Figure 3.7, thrusters 2 and 3 will see an increase in velocity due to rotation, while thrusters 1 and 4 will see a decrease. Assuming that vertical thruster is only effected by vertical speed, the the advance speed for the 5th thruster is $V_{a_5} = w$. For the horizontal thrusters, the total water velocity, $\mathbf{V}_T$, observed by the thruster will be a combination of the horizontal vehicle velocity and the yaw rate. This will be given by:

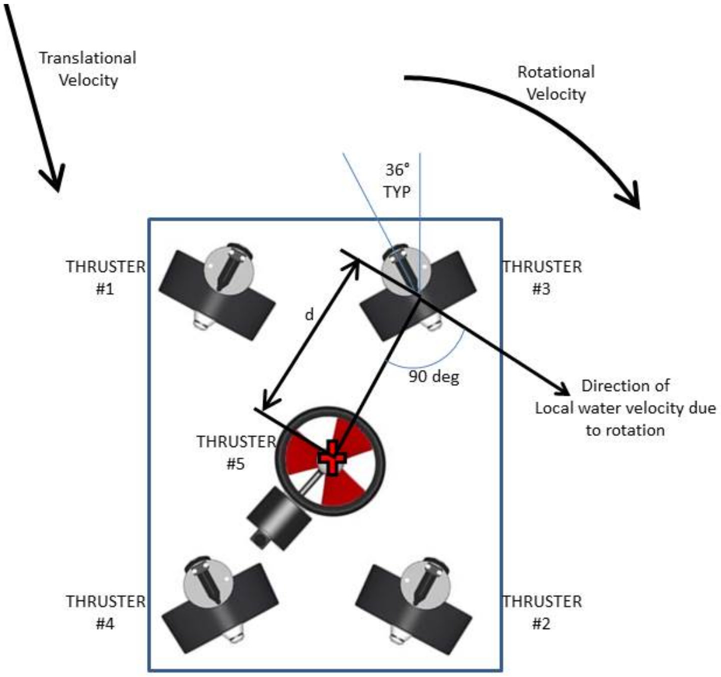

Figure 3.7: Schematic showing the components of the advance speed, V_a

$$\mathbf{V}_T = [u\ v\ w]^T + r \cdot d \frac{\widetilde{\mathbf{e}}_3 \mathbf{X}_{T_i}^B}{\|\mathbf{X}_{T_i}^B\|} \tag{3.26}$$

where $[u \quad v \quad w]$ is the water velocity due to vehicle translation, r is the yaw rate, d is the radial distance between the centre of thrust and the CG, as shown in Figure 3.7, $\mathbf{e}_3$ is a unit vector in the direction of the z-axis of the BRF, and $\mathbf{X}_{T_i}^B$ is the location of the thruster in the BRF. Then V_a can be found by determining the component of the velocity vector that is aligned with the thrusters x-axis.

$$V_{a_i} = V_{T_i}(1)cos\left(\gamma\right) + V_{T_i}(2)sin\left(\gamma\right) \tag{3.27}$$

where γ is the angle of the thruster with respect to the x-axis of the BRF, and $V_{T_i}(1)$ and $V_{T_i}(2)$ are the elements of the total relative water velocity in the x and y directions of the BRF, respectively.

3.3.4 Model Errors

This thruster model was developed with a stand alone test thruster, and produced very repeatable and accurate measurements for the ideal thruster. However, in the field the thruster will not be ideal. Once it is mounted in the vehicle, there will be turbulent flow and interference that will diminish the performance of the thruster and, therefore, degrade the accuracy of the model.

Motor Dynamics and Imparted Moments

In Section 3.2.1 it was stated that the motor dynamics of each thruster will be neglected. Figure 3.3 shows the transient in the propeller speed from a $0 - 100\%$ step input. The measured latency between when a command was issued and when the propeller speed began to change is between 30 and 50 milliseconds. The rise time for the step up to 100% is approximately 350 ms and the step back down to 0 is approximately 1 second. In order for these dynamics to be negligible, the controller must provide a suitably stable command.

As the propeller spins and pushes water it imparts a moment onto the vehicle in the opposite direction. This is most clearly seen when the vertical thruster causes the vehicle to yaw. For this work, these moments will be neglected.

3.4 System Identification for the Vehicle Model

To determine the coefficients for the vehicle model described in Section 3.2, a series of dry land and wet system identification tests were performed. The wet tests were performed in a small test tank and at the SWAT facility, described in Section 2.2. These tests use the MOCAP system, along with the sensors on the navigation sled to capture the dynamic response of the vehicle to a range of thrust inputs. The MOCAP and navigation sensor data are all synchronized to within 1 ms, allowing them to be used together to establish an augmented estimate of the vehicles attitude and position.

3.4.1 Mass, Inertia, Buoyancy, and Vehicle Body Frame

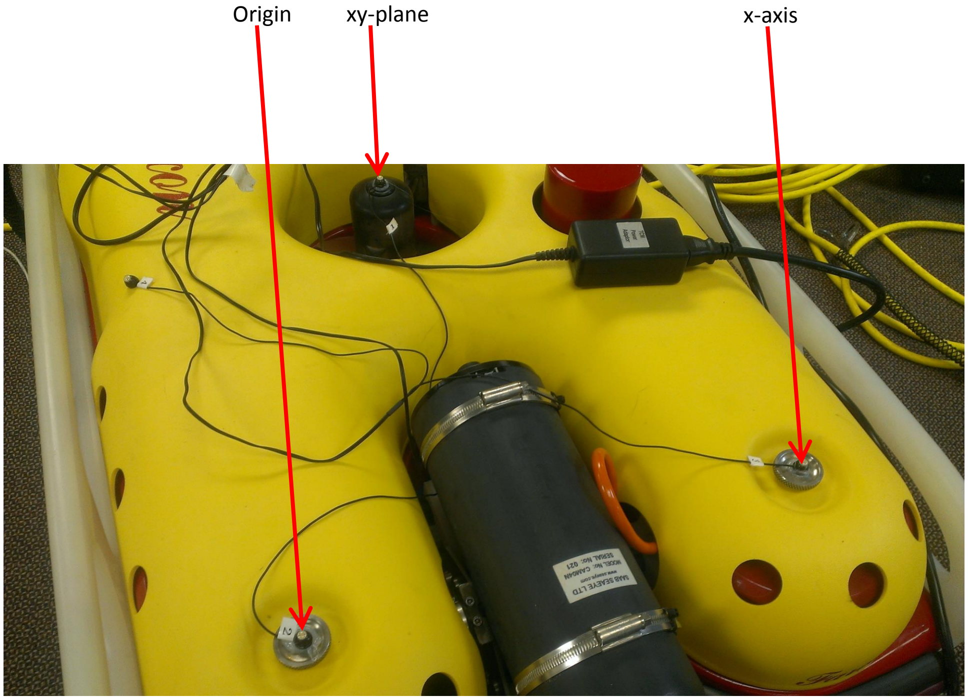

Figure 3.8: The LED locations for the measurement reference frame (MRF) on the ROV

Mass and Vehicle Body Frame (BRF)

The vehicle sled combination has a mass of 116.0kg and has approximately 0.2 kg of positive buoyancy, when the sled is removed 2.5 kg of ballast is added to the ROV to compensate for the change. In order to locate the BRF on the vehicle and calculate the location of the CB, it is first necessary to find the location of the vehicle CG.

The MRF was established so that items could be measured in a consistent reference frame using the MOCAP. The MRF was chosen so that it was visible from most camera angles and provided the most repeatable measurements. The MRF is defined using 3 LEDs as shown in Figure 3.8; the first LED is the origin, then second LED defines the direction of the x-axis, and the third LED defines the xy-plane. With this scheme, a rotation matrix between the native camera frame and the measurement frame can be created as follows:

$$\begin{aligned}
\mathbf{O} &= P_{LED_O} \\
\mathbf{X} &= \frac{P_{LED_X} - P_{LED_O}}{\|P_{LED_X} - P_{LED_O}\|} \\
\mathbf{XY} &= \frac{P_{LED_Y} - P_{LED_O}}{\|P_{LED_Y} - P_{LED_O}\|} \\
\mathbf{Z} &= \frac{\mathbf{X} \times \mathbf{XY}}{\|\mathbf{X} \times \mathbf{XY}\|} \\
\mathbf{Y} &= \frac{\mathbf{Z} \times \mathbf{X}}{\|\mathbf{Z} \times \mathbf{X}\|}
\end{aligned} \tag{3.28}$$

where $\mathbf{X}$, $\mathbf{Y}$, $\mathbf{Z}$ are the basis vectors for the measurement frame. The rotation matrix between the measurement frame and the camera frame can then be created using Eq. D.1:

$$\mathbf{R}^{M \to C} = \begin{bmatrix} \mathbf{X} \cdot \mathbf{e}_x & \mathbf{X} \cdot \mathbf{e}_y & \mathbf{X} \cdot \mathbf{e}_z \\ \mathbf{Y} \cdot \mathbf{e}_x & \mathbf{Y} \cdot \mathbf{e}_y & \mathbf{Y} \cdot \mathbf{e}_z \\ \mathbf{Z} \cdot \mathbf{e}_x & \mathbf{Z} \cdot \mathbf{e}_y & \mathbf{X} \cdot \mathbf{e}_z \end{bmatrix} \tag{3.29}$$

where $\mathbf{e}_x = [1\ 0\ 0]^T$, $\mathbf{e}_y = [0\ 1\ 0]^T$ and $\mathbf{e}_z = [0\ 0\ 1]^T$. Once a vehicle fixed measurement frame is established, then all of the other points of interest can be measured in that frame and translated/rotated into the BRF.

The BRF was then established by measuring the location of the CG, then determining a direction for the x-axis and y-axis. The CG was located by sliding the vehicle back and forth on a thin metal bar and finding the point where it balanced. This was done on all three axes (longitudinal, lateral, and vertical), which allowed all three of the components of the CG position to be determined in the measurement frame. The BRF was constructed, as shown in Figure 3.9, with the origin at the aft end of the vehicle, the x-axis running along the port side frame and the xy-plane defined towards the starboard side of the vehicle. Knowing

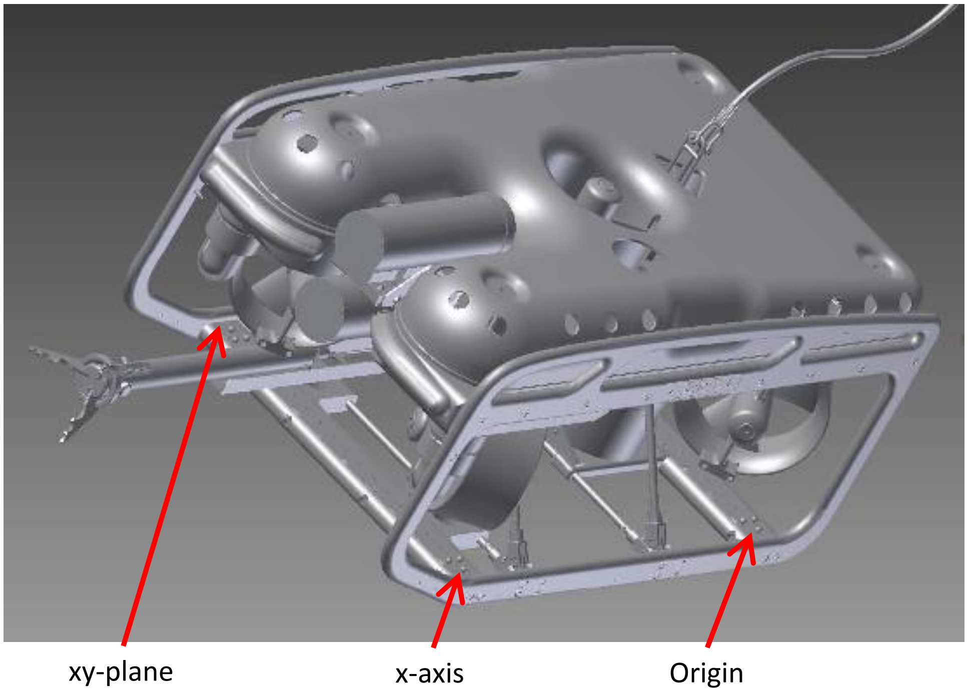

Figure 3.9: The LED locations for the vehicle reference frame on the ROV

the location of these three LEDs in the measurement frame allows one to create a rotation matrix between the measurement frame and the vehicle body frame using the equations in Eq. 3.28. The frame was then translated such that the origin was at the CG instead of the origin LED at the aft end of the vehicle.

Buoyancy

Once the vehicle reference frame was established, it was possible to locate the CB using a simple lever test to measure the restoring moment of the vehicle; in order for the test to be accurate, the vehicle must be completely submerged. A diagram showing the test setup is shown in Figure 3.10. Using the test tank at MTC, the vehicle was suspended from overhead using an inline scale. A weight was then added to the front or side of the vehicle so that the vehicle was negatively buoyant and completely submerged at some pitch or roll angle. Once the vehicle was in an equilibrium state, the roll angle, pitch angle, and the suspension

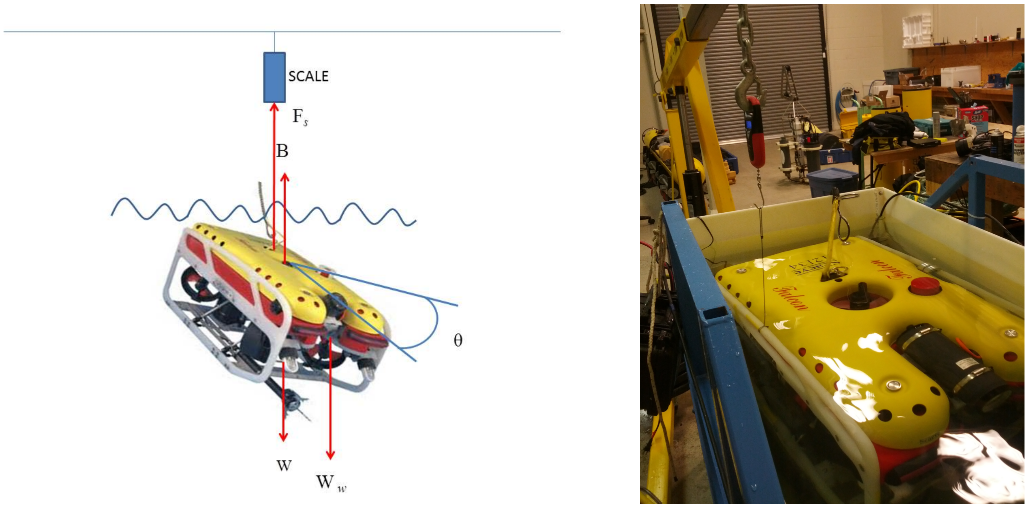

(a) **(b)**

Figure 3.10: Test setup for determining the CB a) Test diagram showing the forces contributing to the moments b) photo showing the vehicle configured to measure the CB using the roll axis

force were recorded. The steps for the test are as follows:

1. **Determine the buoyancy force:** Small calibration weights were placed at the centre of the vehicle until the vehicle was neutrally buoyant. The net force from these weights (gravitational minus buoyancy) is equal to the excess buoyancy force.
2. **Ensure the vehicle sits flat:** Ensure the vehicle is correctly ballasted and sitting as flat as possible in the water. If it is not then the CB is not over top of the CG.
3. **Suspend the vehicle:** Suspend the vehicle from the lifting point using a small scale - the scale will only need to be able to support a few kilograms.
4. **Pitch the vehicle forward:** Put a ballast weight, that is heavier than vehicle's excess buoyancy, on the front of the vehicle. Once the vehicle stabilizes record the pitch angle and the suspension force.
5. **Roll the vehicle sideways:** Repeat the previous step putting the ballast weight on the side of the vehicle and recording the roll angle and the suspension force.

The accuracy of the measurement can be confirmed by repeating the last two steps for several different weights. Assuming that the CB and the CG are aligned in the xy-plane, the restoring arm for the buoyancy force can be calculated by summing the moments about the CG.

$$\begin{aligned} \sum \mathbf{M} &= \sum \mathbf{r} \times \mathbf{f} = 0 \\ &= \big(\widetilde{\mathbf{R}^{B\to I}\mathbf{r}_{CB}}\big)\mathbf{f}_B + \big(\widetilde{\mathbf{R}^{B\to I}\mathbf{r}_W}\big)\mathbf{f}_W + \big(\widetilde{\mathbf{R}^{B\to I}\mathbf{r}_S}\big)\mathbf{f}_S \\ \big(\widetilde{\mathbf{R}^{B\to I}\mathbf{r}_{CB}}\big)\mathbf{f}_B &= -\left[\big(\widetilde{\mathbf{R}^{B\to I}\mathbf{r}_W}\big)\mathbf{f}_W + \big(\widetilde{\mathbf{R}^{B\to I}\mathbf{r}_S}\big)\mathbf{f}_S\right] \\ &= \mathbf{M}_f \end{aligned} \tag{3.30}$$

Designate the right hand side of the equation as $\mathbf{M}_f$, where $\mathbf{f}_B$ is the buoyancy force of the vehicle, $\mathbf{f}_W$ is the force being exerted by the ballast weight, and $\mathbf{f}_S$ is the suspension force. The position vectors for the weight and suspension point, expressed in the BRF, are designated as: $\mathbf{r}_W = [x_W \ y_W \ z_W]^T$ and $\mathbf{r}_S = [x_S \ y_S \ z_S]^T$. The rotation matrix from the BRF to the NRF, designated by $\mathbf{R}^{B\to I}$, is obtained using ether the measured pitch and roll angle, setting the other angles to zero.

At this point, it is important to realize that the cross product transformation, $\widetilde{(\cdot)}$, is not linear and that $\mathbf{f}_B = [0 \ 0 \ B]^T$. Thus $\mathbf{f}_B\mathbf{f}_B^T$ has a rank of 1, meaning that it is not invertible and Eq. 3.30 can only be solved for one independent parameter. However, since it is being assumed that the CB is vertically in line with the CG then only one parameter is needed, $\mathbf{r}_{CB} \approx [0 \ 0 \ z_{CB}]$. If the ballast weight and lifting force both act on the vehicle along the x-axis for the pitch tests (i.e. $y_W = y_S = 0$) then Eq. 3.30 can be reduced to a single scalar moment equation about the y-axis. Similarly if $x_W = x_S = 0$ for the roll tests then Eq. 3.30 reduces to a single scalar moment equation about the x-axis.

Therefore, for the pitch test:

$$\begin{aligned}
\left[\left(\mathbf{R}^{B\to I}\mathbf{r}_{CB}\right)\right]\times\mathbf{f}_B &= \left(\begin{bmatrix} cos(\theta) & 0 & sin(\theta) \\ 0 & 1 & 0 \\ -sin(\theta) & 0 & cos(\theta) \end{bmatrix}\begin{bmatrix} 0 \\ 0 \\ z_{CB} \end{bmatrix}\right)\times\begin{bmatrix} 0 \\ 0 \\ -B \end{bmatrix} \\
&= \begin{bmatrix} 0 \\ sin(\theta)z_{CB}B \\ 0 \end{bmatrix} = \mathbf{M}_F \\
z_{CB} &= = \frac{M_{Fy}}{sin(\theta)B}
\end{aligned} \tag{3.31}$$

Similarly for the roll test:

$$\begin{aligned}
\left[\left(\mathbf{R}^{B\to I}\mathbf{r}_{CB}\right)\right]\times\mathbf{f}_B &= \left(\begin{bmatrix} 1 & 0 & 0 \\ 0 & cos(\phi) & -sin(\phi) \\ 0 & sin(\phi) & cos(\phi) \end{bmatrix}\begin{bmatrix} 0 \\ 0 \\ z_{CB} \end{bmatrix}\right)\times\begin{bmatrix} 0 \\ 0 \\ -B \end{bmatrix} \\
&= \begin{bmatrix} sin(\phi)z_{CB}B \\ 0 \\ 0 \end{bmatrix} = \mathbf{M}_F \\
z_{CB} &= = \frac{M_{Fx}}{sin(\phi)B}
\end{aligned} \tag{3.32}$$

Table 3.2: Centre of Buoyancy Measurements

Test no.	f_W	f_S	ϕ	θ	z_{CB}
Pitch 1	$5.67\ N$	$5.30\ N$	N/A	$-3.2°$	$-0.043\ m$
Pitch 2	$8.50\ N$	$7.75\ N$	N/A	$-5.0°$	$-0.041\ m$
Pitch 3	$11.34\ N$	$11.67\ N$	N/A	$-6.9°$	$-0.039\ m$
Roll 1	$5.67\ N$	$5.00\ N$	$-3.4°$	N/A	$-0.044\ m$
Roll 2	$8.50\ N$	$6.67\ N$	$-4.8°$	N/A	$-0.044\ m$
Roll 3	$11.34\ N$	$9.91\ N$	$-6.5°$	N/A	$-0.046\ m$

The experimental results are summarized in Table 3.2, using Eq. 3.30 to determine z_{CB}, where $\mathbf{f}_W = [0, 0, -f_W]^T$, $\mathbf{f}_S = [0, 0, f_S]^T$ and $B = 1140.41$ N. The location of the ballast weight and suspension point for the pitch tests are $\mathbf{r}_W = [0.472, 0.0, -0.237]^T$ and $\mathbf{r}_S = [-0.023, 0.0, -0.361]^T$ m; the locations for the roll test are $\mathbf{r}_W = [0.0, -0.277, -0.341]^T$ and $\mathbf{r}_W = [0.0, -0.275, 0.351]^T$ m. The final value of z_{CB} was obtained by averaging the results from Table 3.2.

z_{CB} is the length of the moment arm for the buoyancy force. In reality, it is not possible to guarantee that the CB is directly above the CG in the BRF, which may not be perfectly aligned with the vehicle. To find the location of the CB in the BRF, the vehicle was fully submerged in the SWAT and the neutral attitude, where the CB is directly above the CG, was recorded. The location of the CB in the BRF can then be calculated as:

$$\mathbf{X}_{CB}^{B} = R^{N \to B} \begin{bmatrix} 0 \\ 0 \\ -0.043 \end{bmatrix} \tag{3.33}$$

The result was $\mathbf{X}_{CB}^{B} = [-0.00045 \quad -0.00128 \quad -0.04298]^T$ m.

Rigid Body Inertia Matrix

Estimating the inertia matrix for the vehicle can be challenging. As seen in the derivation of the dynamic model in Section 3.2, the overall dynamics depend on the inertia matrix plus an added mass matrix. Therefore, the inertia matrix cannot be identified directly from the system dynamics in water. In order to get an estimate of the inertial and the added mass contributions to the mass matrix, the inertia must be estimated separately. A bifilar torsional pendulum experiment is one method of determining the mass moment of inertia for a complex object [33].

Figure 3.11 shows the ROV setup for measuring the moment of inertia using a bifilar

(a) **(b)**

Figure 3.11: Bifilar pendulum setup for determining the mass moment of inertia a) about the x-axis (roll) b) about the z-axis (yaw)

pendulum. In Figure 3.11-a the vehicle is suspended with the x-axis of the BRF pointing up. The two cables are attached to the vehicle such that they are aligned with the y-axis of the BRF and the CG is situated between them. This configuration will give the mass moment of inertia about the x-axis. The inertia is estimated by rotating the vehicle slightly about the x-axis, letting it go and recording the resulting rotational motion. With a bifilar pendulum, rotating the vehicle will cause a change in height, therefore giving the vehicle some potential energy. Once released the vehicle will oscillate back and forth trading potential for kinetic energy. The frequency of the oscillations is related to the inertia of the vehicle. In Figure 3.11-a the MOCAP camera is shown in the foreground. LEDs are mounted to the upper surface of the vehicle and the camera is able to capture the oscillatory motion. Figure 3.11-b shows the vehicle mounted to measure inertia about the z-axis, where the pendulum wires are attached to the vehicle along the y-axis with the z-axis pointing up. The setup for the y-axis (not shown) has the vehicle tipped onto its side with the two wires attached at either end of the vehicle along the x-axis with the y-axis pointing up.

For this work the linearized equation of motion shown in Eq. 3.34 of the bifiliar pendulum was used.

$$\ddot{\theta} + \left[\left(\frac{K_D}{I}\right)\left(\frac{8A}{3\pi}\right) + \frac{C}{I}\right]\dot{\theta} + \left(\frac{mgD^2}{4Ih}\right)\theta = 0 \tag{3.34}$$

where K_D and C are quadratic and linear damping terms, A is the average oscillation amplitude, D is the distance between the pendulum wires, h is the length of the pendulum wires, m is the mass of the assembly, g is gravity, and I is the mass moment of inertia about the axis of rotation. Since the linearized equation of motion uses small angle approximations, the amplitude of the rotations were kept small to minimize the error.

Since Eq. 3.34 is in the form of a simple second order linear system, one can also write:

$$\ddot{\theta} + 2\zeta\omega_n\dot{\theta} + \omega_n^2\theta = 0 \tag{3.35}$$

and deduce that

$$\omega_n^2 = \left(\frac{mgD^2}{4Ih}\right) \Rightarrow I = \frac{mgD^2}{4h\omega_n^2} \tag{3.36}$$

where $\omega_d = \omega_n\sqrt{1-\zeta^2}$ relates the natural frequency, ω_n, to the damped natural frequency. The frequency of the oscillations was measured to get ω_d and the damping ratio, ζ, was determined by comparing the amplitude of subsequent peaks using the logarithmic decrement method.

$$\zeta = \frac{\delta}{\sqrt{(4\pi^2+\delta^2}}; \quad \delta = \frac{1}{n}ln\left(\frac{\theta(t)}{\theta(t+n\Delta T)}\right) \tag{3.37}$$

where $\theta(t)$ is the amplitude at one peak and $\theta(t+n\Delta T)$ is the amplitude n peaks later.

The calculated ω_n and ζ parameters were then used as an initial guess for a least squares optimization that minimized the error between the measured angle and the angle predicted by (3.35). The optimized ω_n and ζ were then validated by comparing the predicted angle from Eq. 3.35 against all of the data runs.

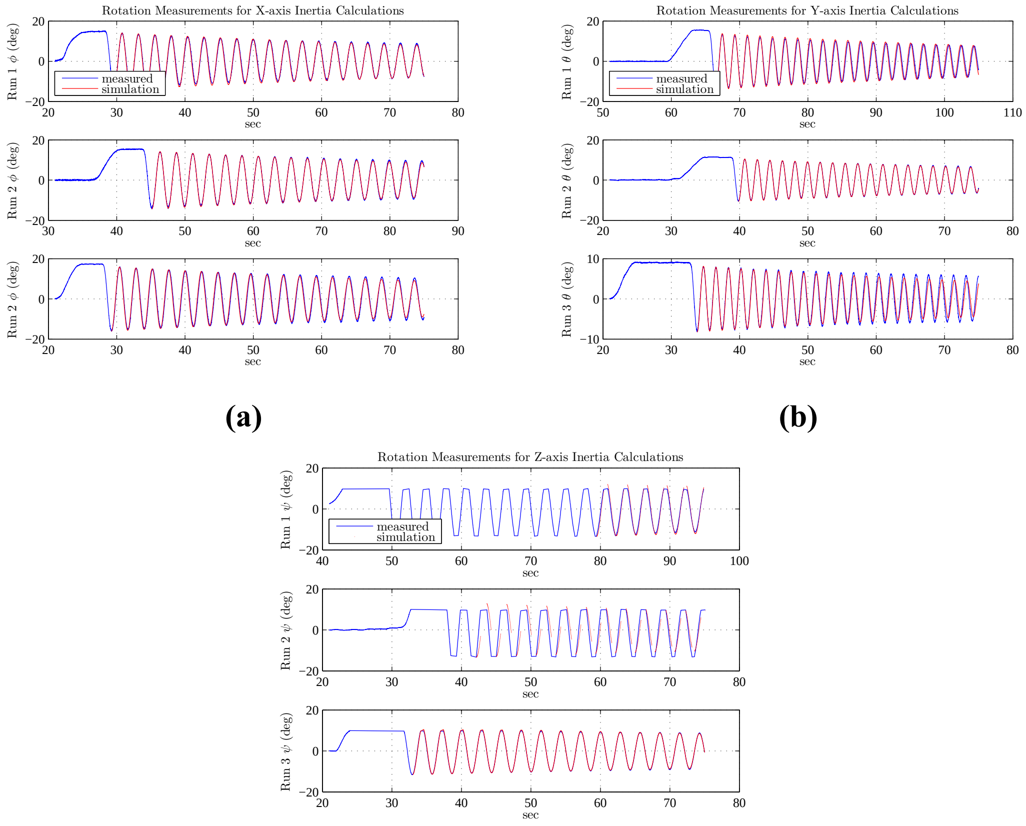

(a) **(b)**

(c)

Figure 3.12: Measured and simulated rotation angle as a function of time for the bifilar pendulum experiment about the x-axis (a), y-axis (b), and z-axis (c)

Three runs were done on each axis, the data in the first x-axis run is questionable due to problems with the lighting that LED to increased noise in the MOCAP output. The first two z-axis runs were also compromised due to occlusion of the LEDs at rotation angles greater than $+10$ degrees. This problem can still be seen in the first couple of peaks of the third run (shown in Figure 3.12) but it was still possible to get a reasonable solution from the data. Table 3.3 shows the mean error between the predicted angles using the optimized coefficients for (3.35). For the data runs that were not compromised, the maximum error is 0.034 radians or approximately 2 degrees, which is sufficient for this estimation. Note also that a small phase shift, or slight errors in ω_n will cause significant changes in the magnitude error being reported here.

Table 3.3: Inertia Measurements

Axis	ω_n	ζ	I	$\bar{e}_1(rad)$	$\bar{e}_2(rad)$	$\bar{e}_3(rad)$
X	2.61996	0.00484	9.30079	0.01540	0.00527	0.02677
Y	3.41806	0.00440	14.91636	0.03485	0.00491	0.02184
Z	2.20642	0.00339	13.11394	0.01729	0.09787	0.00463

Summary

Table 3.4 summarizes all of the rigid body mass, inertia, and buoyancy properties of the Falcon vehicle and sled combination.

Table 3.4: Weight and Balance Summary

Description	Value	Units
Vehicle Mass	116.0	kg
Vehicle Buoyancy [6]	116.2	kg
Vehicle Displacement	0.114	m^3
Moment of Inertia about x-axis	9.30079	$kg\ m^2$
Moment of Inertia about y-axis	14.91636	$kg\ m^2$
Moment of Inertia about z-axis	13.11394	$kg\ m^2$
CG in MRF	$\begin{bmatrix} 0.164 & 0.368 & -0.351 \end{bmatrix}^T$	m
CB in BRF	$\begin{bmatrix} -0.00045 & -0.00128 & -0.04298 \end{bmatrix}^T$	m

3.4.2 Hydrodynamic Coefficients

The added mass and drag coefficients described in Section 3.2.2 were obtained by collecting sensor data during a series of system identification manoeuvers. In these tests, the vehicle

---

[6] Buoyancy was measured using water with a density of $1022.4 kg/m^3$; this is the average density of seawater at the SWAT facility.

was given a step input of command (forwards, lateral, up/down, or spin) and the response was measured. The drag coefficents are obtained by observing the steady state velocity at a given thruster command. The added mass coeffiencts can then be deduced from the acceleration profile.

To isolate the drag effects, the vehicle was flown at a steady state velocity (i.e. $\dot{\nu} = 0$) while exciting only one DOF at a time. While in practice it is not possible to 100% isolate the indiviual DOFs, the extraneous motion can be minimized to such an extent that the coriolis effect is negligible. By further minimizing the environmental forces and moments as much as possible, the system dynamics can be reduced to the following simplified equation of motion:

$$\begin{aligned} 0 &= \boldsymbol{\tau}\left(\boldsymbol{\delta}\right) - \mathbf{D}\left(\boldsymbol{\nu}\right)\boldsymbol{\nu} - \mathbf{g}\left(\boldsymbol{\eta}\right) \qquad (3.38) \\ \mathbf{D}\left(\boldsymbol{\nu}\right)\boldsymbol{\nu} &= \boldsymbol{\tau}\left(\boldsymbol{\delta}\right) - \mathbf{g}\left(\boldsymbol{\eta}\right) \end{aligned}$$

Since $\mathbf{D}\left(\boldsymbol{\nu}\right)$ is a linear function in $\boldsymbol{\nu}$ and it is multiplied by $\boldsymbol{\nu}$ in the equations of motion, one would expect that plotting $\boldsymbol{\tau}\left(\boldsymbol{\delta}\right) - \mathbf{g}\left(\boldsymbol{\eta}\right)$ as a function of $\boldsymbol{\nu}$ for different levels of thrust would result in a quadratic curve with a zero intercept.

Similarly, when the vehicle first begins to accelerate and $\boldsymbol{\nu}$ is still very small, one can neglect the drag component allowing the added mass can be estimated as follows:

$$\mathbf{M}\dot{\boldsymbol{\nu}} = \boldsymbol{\tau}\left(\boldsymbol{\delta}\right) - \mathbf{g}\left(\boldsymbol{\eta}\right) \qquad (3.39)$$

Therefore, by plotting $\boldsymbol{\tau}\left(\boldsymbol{\delta}\right) - \mathbf{g}\left(\boldsymbol{\eta}\right)$ as a function of $\dot{\boldsymbol{\nu}}$ for different levels of thrust, one should obtain a linear relationship with a zero intercept and a slope of M.

The challenge with this procedure is determining a valid estimate for the thruster forces. The model presented in Section 3.3 is valid for a single detached thruster, it does not take into account the interference that occurs when the thruster is mounted onto the vehicle. This

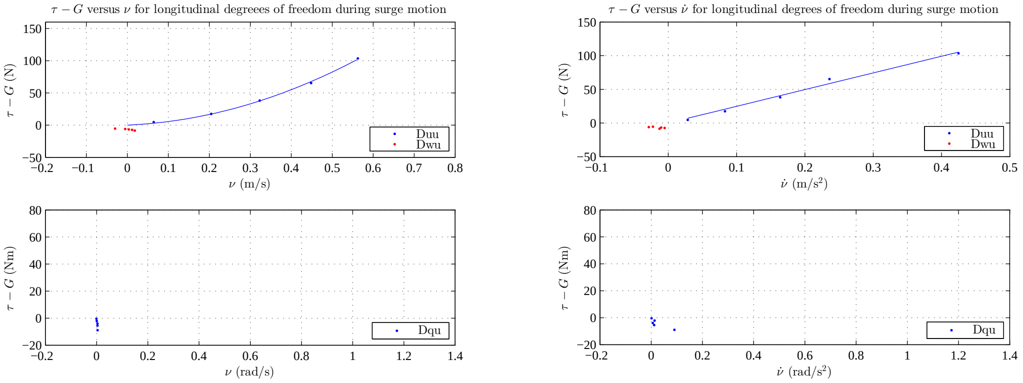

(a) **(b)**

Figure 3.13: Hydrodynamics coefficient estimates for surge: a) drag profile and b) mass profile.

uncertainty is handled by introducing an interference factor, IF, that allows for a degradation in the thrust due to interference effects. The value of the interference factor, drag coefficients and added mass coefficients can all be determined simultaneously using a least squares optimization routine.

Surge Coefficients

Figure 3.13-a, shows the quadratic drag curve that was anticipated from the theory. The top graph shows the translational longitudinal DOFs and the bottom graph shows the rotational DOF. The y-axis shows $\tau - G$ for each of the different directions, which are effectively the input forces, and the x-axis shows velocities. This shows that the surge DOF is primarily being excited during these step tests and that the data fits a quadratic drag profile very well. There is also a small amount of heave that occurs due to surge without there being any input forces in this direction. Since these graphs show angular rates instead of angles, pitch due to surge cross coupling will not show up here but will be discussed later in this chapter. The results for the estimation of M is shown in Figure 3.13-b, as expected the relationship is linear.

Figure 3.14-a shows estimates of the surge velocity using the measured coefficients.

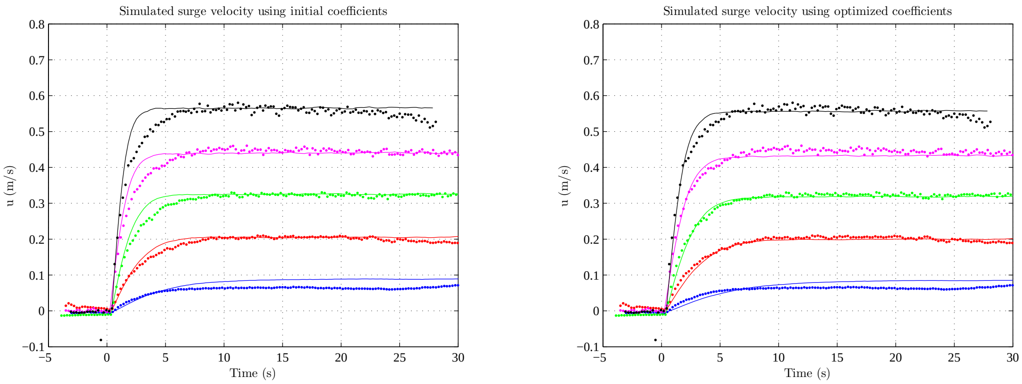

(a) **(b)**

Figure 3.14: Estimated velocities in surge using a) measured coefficients and b) optimized coefficients.

This estimate is good but the vehicle accelerates more quickly in the simulation then was measured. This effect is even more prevalent on other DOFs (such as sway), and is likely due to overestimating the thrust being produced by the thrusters (ie not taking into account the interference effect as described in [11]). By applying an interference factor (IF) to the thrust, the curves can be corrected to more accurately follow the measured velocity. To determine the IF an optimization was performed that minimizes the least squares error between the simulated velocity and the measured velocity while allowing the mass, drag and IF to vary. The result is shown in Figure 3.14-b.

Even with an optimization, the thrust curves will not be a perfect prediction as they do not take into account environmental effects, including tether drag. This effect can be substantial. There are floats attached to the tether to make it neutrally buoyant near the vehicle. Depending on the depth, the vehicle may be dragging these floats across the surface of the water or pulling them down through the water column, causing changes in the drag profile and gravitational forces between and during runs.

A summary of the measured and optimized coefficients for surge are shown in Table 3.5 along with the IF. In the surge direction the IF was 0.87 which is a reasonable number given that the vehicle and thruster orientations are optimized for forward motion. The surge coefficients were only measured in the forward orientation. While it is possible to take measurements with the vehicle operating in reverse, the measurements are highly corrupted by tether disturbances and add little value. From the vehicle symmetry, one can expect the hydrodynamic coefficients to be very similar whether the vehicle is travelling forward or reverse.

Table 3.5: Hydrodynamic Coefficient Summary for Surge

Coefficient	Measured Value	Optimised Value	Units
$m + X_{\dot{u}}$	248.0	283.6	kg
$D_{L_{uu}}$	27.9	26.9	kg/s
$D_{Q_{u11}}$	273.6	241.3	kg/m
IF_u	N/A	0.87	N/A

Sway Coefficients

The results of mass and drag estimates for the sway direction are shown in Figure 3.15. These plots are similar to the surge plots with the lateral translational DOFs shown on top and the rotational ones shown on the bottom. In these plots, both drag and mass curves fit the expected profiles very well. There is a small amount of yaw due to sway, and a small rolling moment that is applied to the vehicle from the thrusters. Roll due to sway cross coupling will not show in these graphs but will be discussed along with the other cross coupling effects will be discussed later in this section.

In the sway direction, the acceleration profile in the simulated results is significantly different from the acceleration profile in the measured velocities, Figure 3.16-a. This is undoubtedly due to the IF as the vehicle is not optimized for travel in this direction. The simulation results that use the optimized coefficients fits the measured velocities much better,Figure 3.16-b.

Environmental effects were also more noticeable while taking data in the sway direction, this is primarily due to the way that the tether is pulled when travelling laterally. In

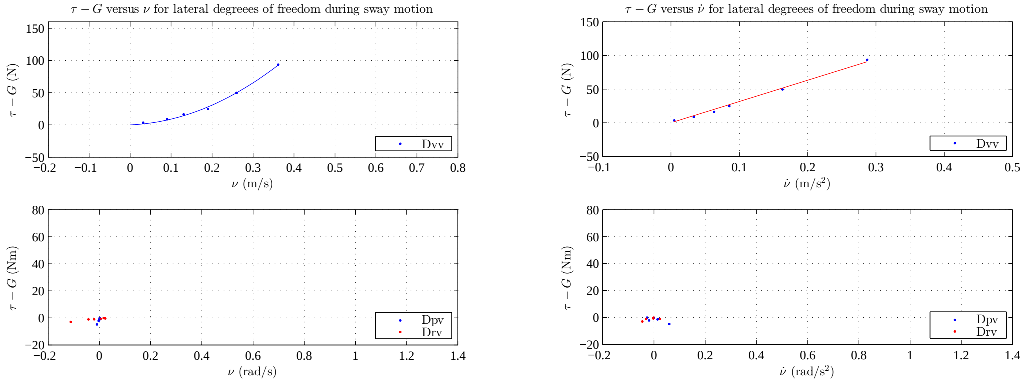

(a) **(b)**

Figure 3.15: Hydrodynamics coefficient estimates for sway: a) drag profile and b) mass profile.

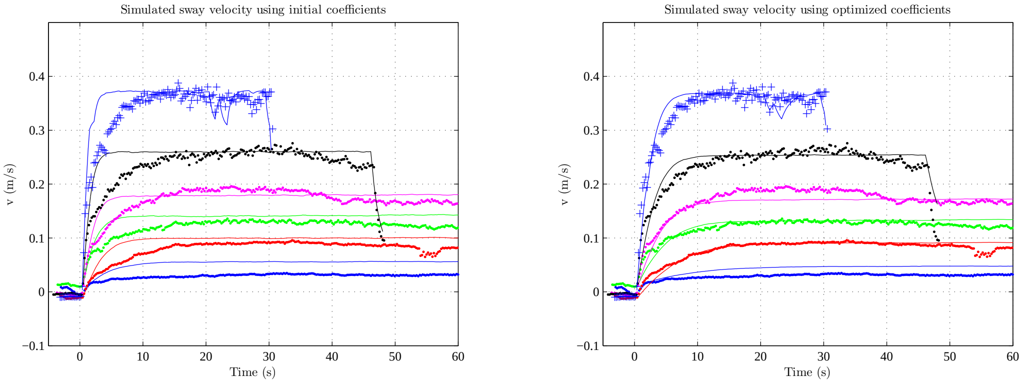

(a) **(b)**

Figure 3.16: Estimated velocities in sway using a) measured coefficients and b) optimized coefficients.

practically every run, the steady state velocity decreased by a noticeable amount once the vehicle started to pull a loop of tether through the water. This limits the accuracy to which one can estimate the coefficients for this DOF.

A summary of the measured and optimized coefficients for surge are shown in Table 3.6 along with the IF. In the sway direction the IF was 0.83. Note that the added mass and drag forces are higher in the sway direction than in surge, this is to be expected given the profile of the vehicle. As with surge, the sway coefficients were only measured in one direction, but again due to vehicle symmetry, one can expect the hydrodynamic coefficients to be very similar whether the vehicle is travelling to the port or starboard side.

Table 3.6: Hydrodynamic Coefficient Summary for Sway

Coefficient	Measured Value	Optimised Value	Units
$m + Y_{\dot{v}}$	315.7	593.2	kg
$D_{L_{vv}}$	24.8	35.8	kg/s
$D_{Q_{v22}}$	642.0	503.8	kg/m
IF_v	N/A	0.83	N/A

Heave Coefficients

Obtaining measurements for the heave DOF was difficult, as there is only a few metres between the surface and the seafloor in the SWAT facility. This issue is exacerbated by the fact that the DVL loses bottom lock and stops providing velocity measurements when it is less than one metre above the seafloor. In heave, one can expect significantly different responses in the positive and negative directions. This is partially due to the addition of the AIC below the vertical thruster and partially due to the fact that top of the vehicle has a smooth hydrodynamic fairing, while the bottom of the vehicle is open and can trap large amounts of water.

The results of mass and drag estimates for the yaw direction are shown in Figure 3.17. The measured coefficients for heave are not nearly as accurate as were seen in either surge or sway. This is due to the difficulties in obtaining steady state motion as well as the challenges in identifying the initial acceleration. When the vehicle starts on the surface, the vertical thruster can take a few seconds before it starts to bite the water and descend. When the vehicle is on the bottom it is practically impossible to capture the initial acceleration from a stand still because the DVL cannot measure speed when it is close to the bottom. As a result, the measured mass and drag characteristics are questionable at best and in some cases generated non-physical values. Fortunately, the optimization method still works and generates reasonable coefficients for both directions.

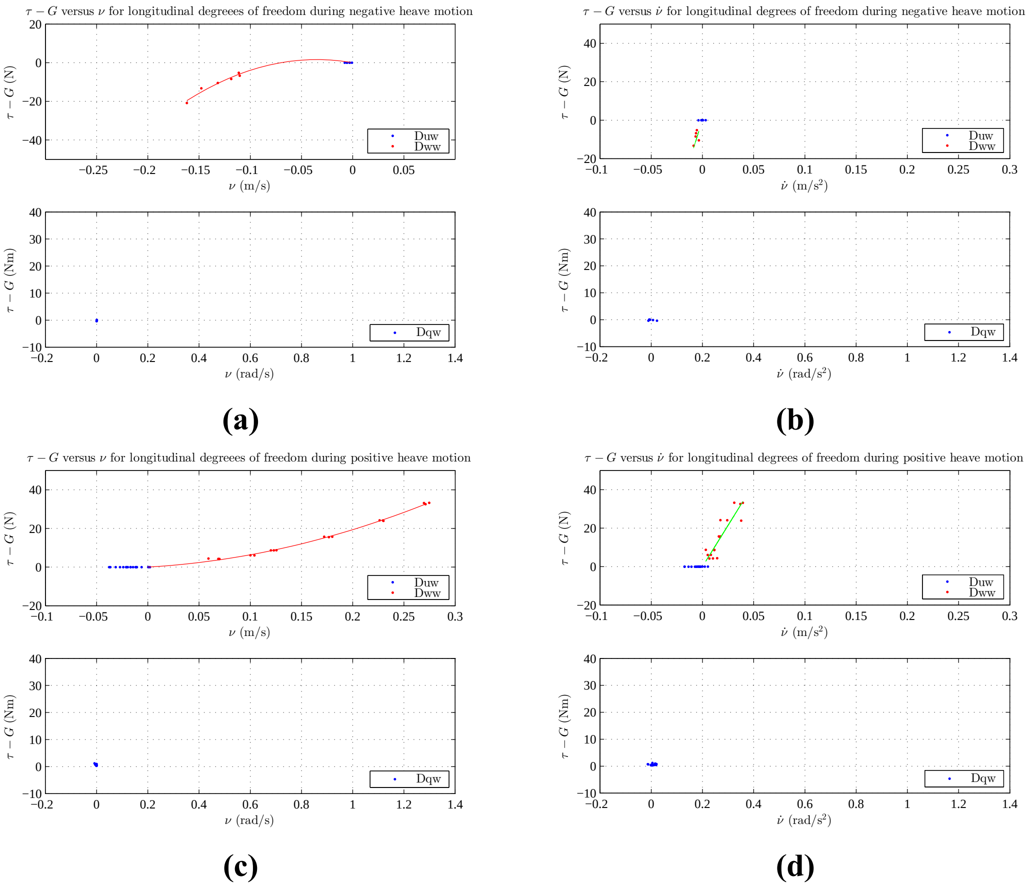

(a) **(b)**

(c) **(d)**

Figure 3.17: Hydrodynamics coefficient estimates for heave: a) drag profile for negative heave command b) mass profile for negative heave command, c) drag profile for positive heave command d) mass profile for positive heave command (NOTE: positive heave command is down).

The simulated responses for both positive and negative heave motion are shown in Figure 3.18 and the optimized coefficients works very well. As expected, the positive and negative directions are significantly different, with larger added mass and drag coefficients in the down direction. The IFs also differ significantly with the a modest factor of 0.65 for downward motion (when the thruster is exhausting up) and a factor of 0.15 for upward motion (when the thruster is exhausting downwards into the AIC). While extreme, these values are not unexpected and match what the performance that was observed while operating the vehicle. A summary of the measured and optimized coefficients for heave are shown in Table 3.7 along with the IF. Also notable in Figure 3.17 is the lack of q as a result of w; this

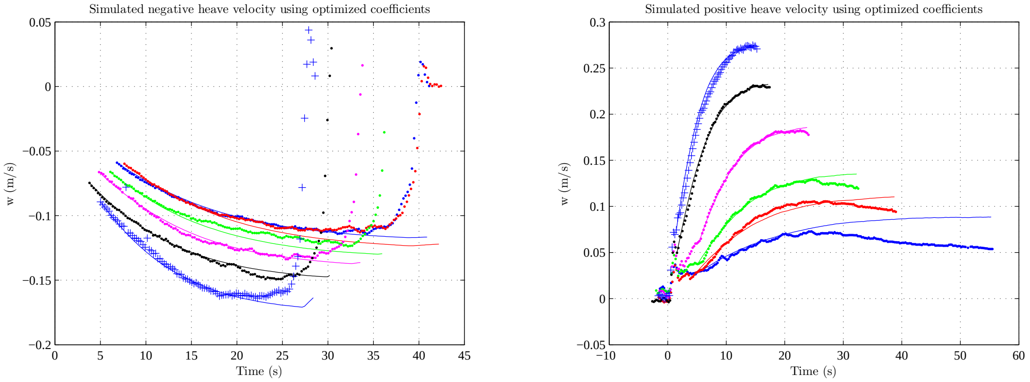

(a) **(b)**

Figure 3.18: Estimated velocities in heave using the optimal coefficients for: a) a negative command and b) a positive command.

suggests that the cross coupling between q and w is negligible.

Table 3.7: Hydrodynamic Coefficient Summary for Heave

Direction	Coefficient	Measured Value	Optimised Value	Units
DOWN	$m + Z_{\dot{w}}$	859.6	499.0	kg
	$D_{Z_{ww}}$	30.6	0.0	kg/s
	$D_{Q_{w33}}$	330.7	265.6	kg/m
	IF_w	N/A	0.65	N/A
UP	$m + Z_{\dot{w}}$	N/A	351.7	kg
	$D_{Z_{ww}}$	N/A	6.2	kg/s
	$D_{Q_{w33}}$	N/A	119.1	kg/m
	IF_w	N/A	0.15	N/A

Yaw Coefficients

For the yaw DOF, it is relatively easy to collect data in both the positive and negative directions without introducing significant data corruption from tether disturbances. One would expect the dynamics in the two directions to be similar, and this provides a double check on the validity of the the parameters and methods. The results of mass and drag estimates for the yaw direction are shown in Figure 3.19, with all four curves fitting the expected profiles very well.

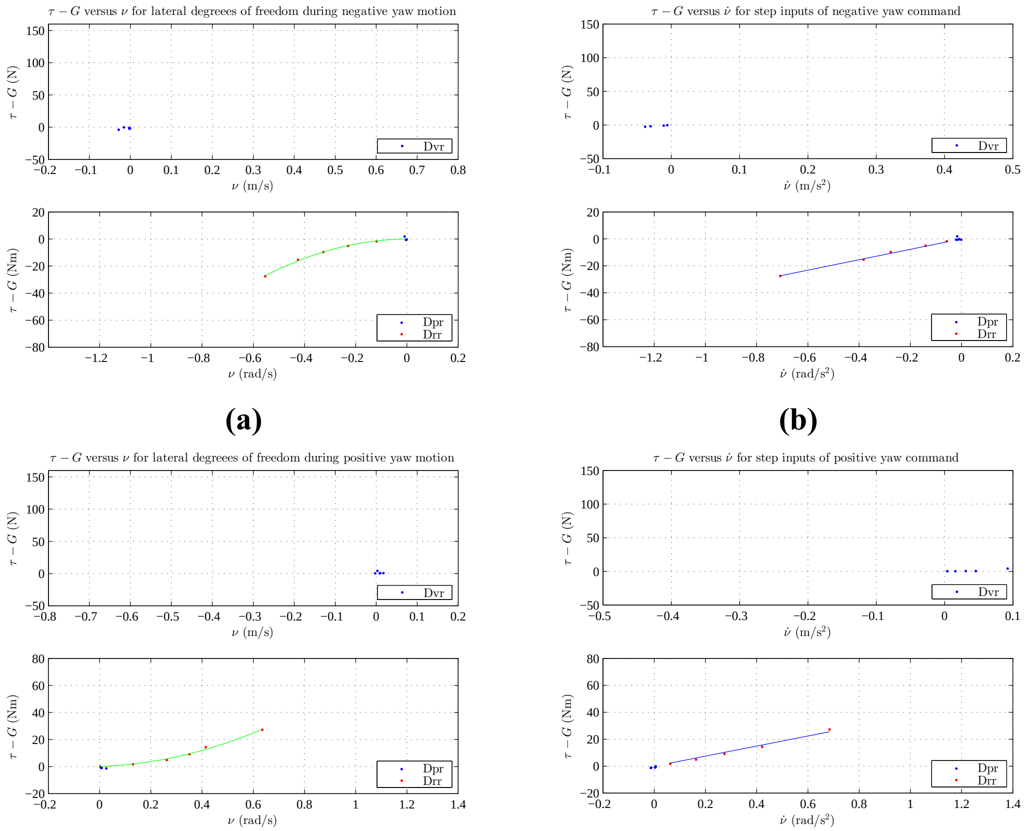

(a) (b) (c) (d)

Figure 3.19: Hydrodynamics coefficient estimates for yaw: a) drag profile for negative yaw command b) mass profile for negative yaw command, c) drag profile for positive yaw command b) mass profile for positive yaw command.

The simulated responses for both port and starboard, shown in Figure 3.20, fit very well and the optimized coefficients ended up being very close in value for the two directions (which is to be expected). A summary of the measured and optimized coefficients for yaw are shown in Table 3.8 along with the IF. Since the final values were so close, the mean value of the two directions were used and no differentiation is made between the two directions.

Pitch and Roll Coefficients

Since neither roll nor pitch are controllable DOFs, it is not possible to excite or control these dynamics using the thrusters. As such, the pitch and roll dynamics are often ignored

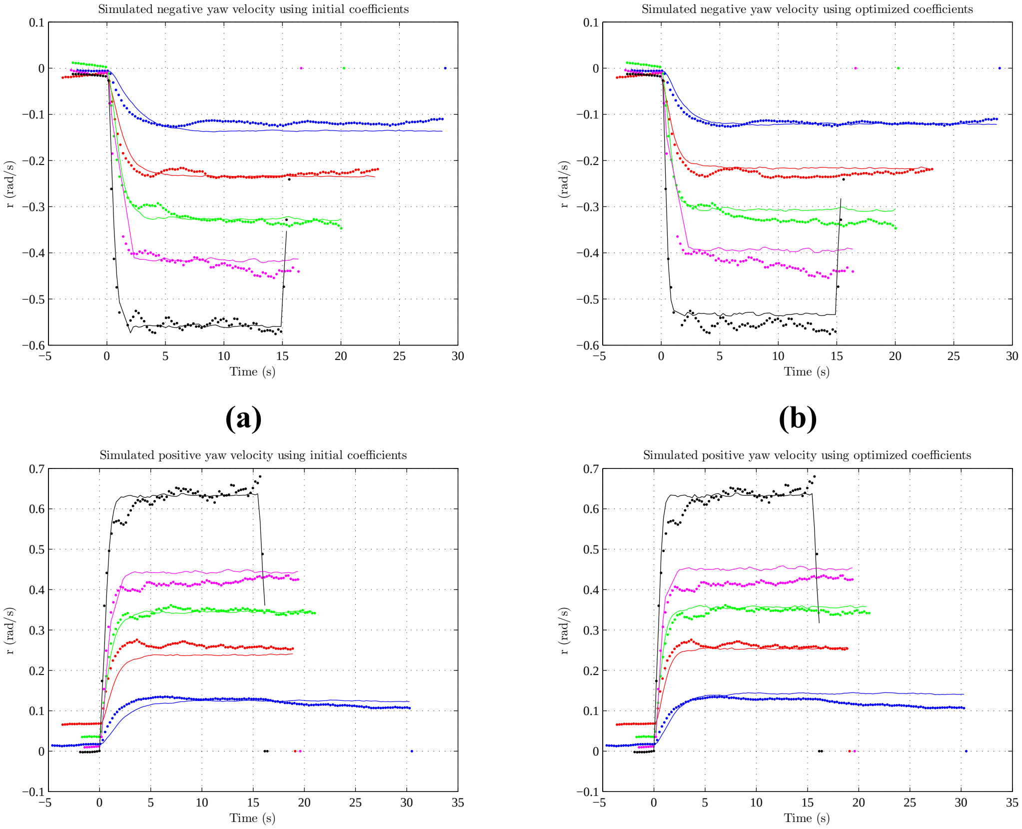

(a) **(b)**

(c) **(d)**

Figure 3.20: Estimated velocities in yaw using: a) measured coefficients for the negative command, b) optimized coefficients for negative command, c) measured coefficients for the positive command, d) optimized coefficients for positive command.

Table 3.8: Hydrodynamic Coefficient Summary for Yaw

Direction	Coefficient	Measured Value	Optimised Value	Units
STBD	$I_z + N_{\dot{r}}$	37.3	28.9	$kg \cdot m^2$
	$D_{L_{rr}}$	6.97	3.2	$kg \cdot m^2/s$
	$D_{Q_{r66}}$	57.4	63.3	$kg \cdot m^2$
	IF_r	N/A	0.95	N/A
PORT	$I_z + N_{\dot{r}}$	38.6	29.0	$kg \cdot m^2$
	$D_{L_{rr}}$	1.34	3.83	$kg \cdot m^2/s$
	$D_{Q_{r66}}$	86.2	90.5	$kg \cdot m^2$
	IF_r	N/A	1.06	N/A

completely, and designers rely on the inherent stability of the vehicle to manage the pitch and roll motion. However, for some applications, such as work in high flow environments, and when trying to accurately position a manipulator in real-time [61], identifying these parameters can be important.

To measure these dynamics, the vehicle was submerged at some angle and then released, producing oscillations due to the trade off between vehicle angle and restoring forces. The angle of the vehicle was measured during these oscillations and used to determine the added mass and drag characteristics. To measure the single DOF dynamics, it is necessary to produce pitching or rolling motion while imparting as little surge or sway velocity as possible. Since the vehicle is positively buoyant, there will always be some amount of heave velocity when the vehicle is submerged. However, looking at the layout of the ROV, the centre of pressure for pure heave motion will be relatively close to the z-axis of the BRF; therefore, the moment contribution due to pure heave motion should be negligible. The tether also ends up in a quasi-static state during this type of motion, minimizing the tether contribution.

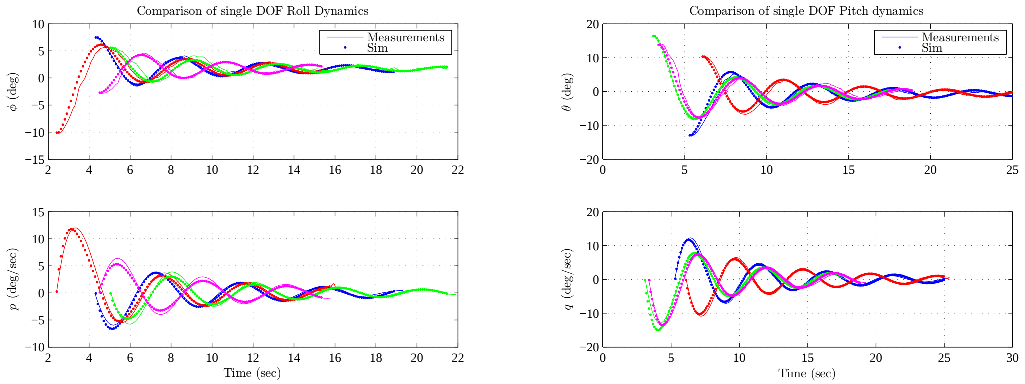

(a) **(b)**

Figure 3.21: Estimated and measured angular rates (with negligible translational velocity) for a) roll and b) pitch.

Figure 3.21 shows the decoupled rolling and pitching dynamics. The pitch and roll characteristics were measured on two different occasions several weeks apart and the results were obtained using a mix of data from both days. The coefficients for the model were determined using a least squares optimization between the measured angular rate and the simulated one. The runs chosen for inclusion in the optimization were selected based on the following criteria:

- The translational velocity in the horizontal plane was as small as possible.
- The oscillations were measured and undisturbed for a sufficiently long time to adequately determine the quadratic drag.
- The were no noticeable disturbances due to the tether or other external influences.

More than 40 data sets of roll and pitch motion were collected over the two days, with 4 data sets being chosen for inclusion in each optimization. The primary reason for excluding data sets was excessive translational velocity. Several data sets were also excluded because oscillatory motion stopped prematurely leading to inconclusive values for the quadratic damping (this occurred when the vehicle was not deep enough and came to the surface too quickly). The results of the optimization are validated using the data sets shown in Figure 3.21; these data sets are a combination of runs that were selected for inclusion in the optimization and runs that were rejected. While there is some discrepancy between the measured data and the simulation at the beginning the period and amplitude of the oscillations as they decay are captured well. The modelling error at the beginning of the run is understandable given that: 1) there is typically some small amount of surge or sway motion at the beginning of the run which quickly dies out, and 2) environmental disturbances (primarily from the tether) are more likely to occur at the beginning of the run before the system is able to settle into a pseudo-steady state condition. The coefficients for the single DOF model are listed in Table 3.9. All of the parameters obtained are in line with expectations given the coefficients previously obtained for yaw.

While the model captures the dynamics well for the case when there is no translational velocity, it does not accurately predict the angles during translational motion. This can be seen by comparing the single DOF model with the measurements of pitch and roll that were

Table 3.9: Hydrodynamic Coefficient Summary for Pitch and Roll

Direction	Coefficient	Value	Units
ROLL	$I_x + K_{\dot{p}}$	20.9	$kg \cdot m^2$
	$D_{L_{pp}}$	3.0	$kg \cdot m^2/s$
	$D_{Q_{p44}}$	101.6	$kg \cdot m^2$
PITCH	$I_y + M_{\dot{q}}$	30.4	$kg \cdot m^2$
	$D_{L_{qq}}$	4.9	$kg \cdot m^2/s$
	$D_{Q_{q55}}$	59.9	$kg \cdot m^2$

taken during the surge and sway system ID tests presented in the previous sections. the results are shown in Figure 3.22, it is clear that the pitch and roll angles are not accurately predicted. It turns out that cross coupling effects due to translational velocities are an important part of the pitch and rolling dynamics. This is not an unexpected result. The addition of the sled to the ROV, added a large flat panel below the centre of gravity; during sway motion water pushing against this surface will impart a significant positive rolling moment to the vehicle. Similarly, during surge motion, the water pushing against the frontal area of the ROV will likely also be a source of pitching dynamics. It should also be pointed out that the cross coupling terms from the added mass component of the **C** matrix also play a significant role in the roll and pitch dynamics while the vehicle is underway. The $\mathbf{C}_A$ matrix contribution is kinematic but is contingent on the accuracy of the previously determined coefficients and estimation of the rigid body mass and inertia to accurately predict motion.

In order to determine the contribution of surge and sway to pitch and roll, a second least squares optimization was done. For this optimization,the single DOF coefficients for roll and pitch were fixed and only the cross coupling components were allowed to vary. The results are shown in Figure 3.23. The results are excellent given the complexity of the dynamics and all of the potential sources of error (including errors in previously determined coefficients). The model predicts some level of oscillation which is on par with what was seen on the vehicle and the steady state angle is also predicted well. The resulting coeffi-

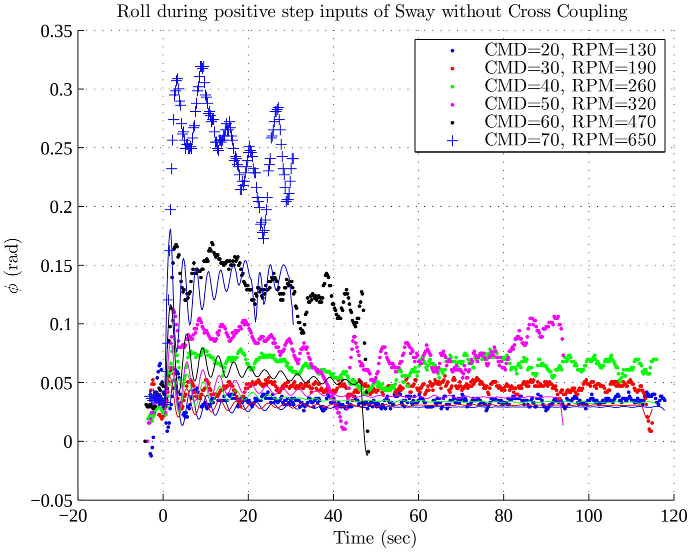

(a)

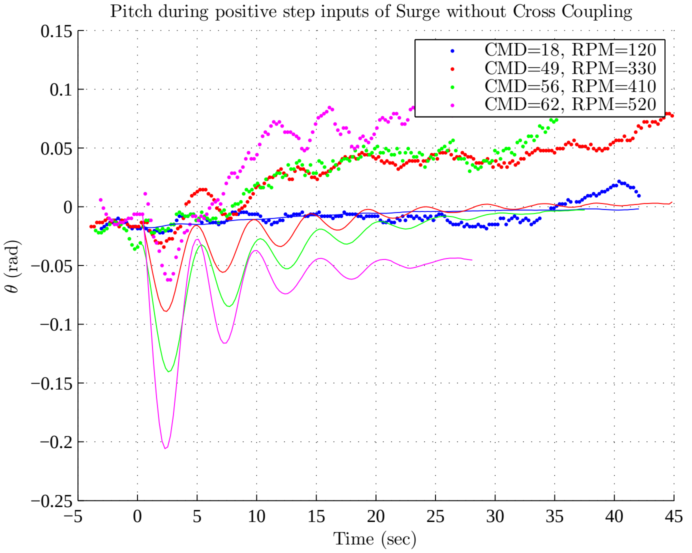

(b)

Figure 3.22: The predicted and measured angles using a single DOF model for a) roll and b) pitch when translational velocity is present.

cients are presented in Table 3.10.

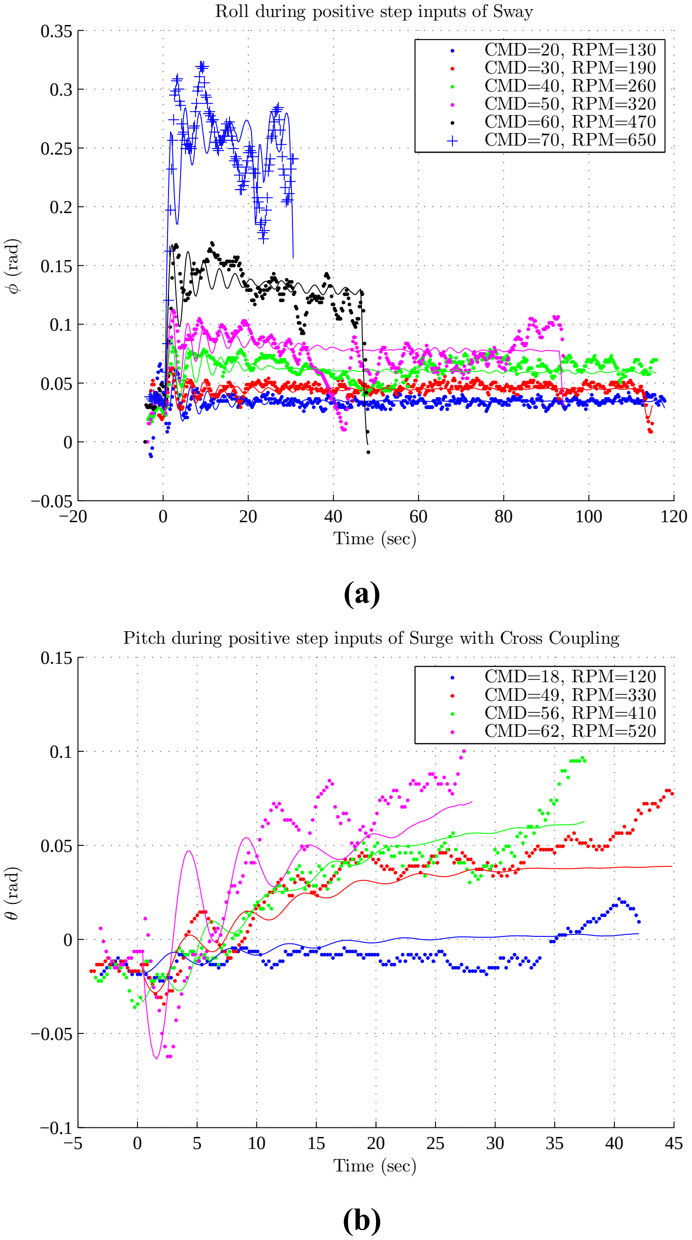

Figure 3.23: Estimated and measured angles using a cross coupled model for a) roll and b) pitch when translational velocity is present.

Hydrodynamic Summary

This section summarizes the results of the system identification for the hydrodynamic parameters of the dynamic model. Statistics on the quality of fits were purposely not presented, as they can be deceiving in the face of large environmental disturbances primarily due to

Table 3.10: Hydrodynamic Cross Coupling Coefficient Summary for Pitch and Roll

Direction	Coefficient	Value	Units
ROLL	$K_{\dot{v}}$	-22.8	$kg \cdot m^2$
	$D_{L_{pv}}$	-3.5	$kg \cdot m^2/s$
	$D_{Q_{p22}}$	-46.4	$kg \cdot m^2$
PITCH	$M_{\dot{u}}$	-15.3	$kg \cdot m^2$
	$D_{L_{qu}}$	-1.5	$kg \cdot m^2/s$
	$D_{Q_{q11}}$	-13.7	$kg \cdot m^2$

the tether. The graphs provide a better means of interpreting the results.

Table 3.11: Interference Factor Summary

Dir.	Interference Factor
Surge	0.87
Sway	0.83
Heave (DN)	0.65
Heave (UP)	0.15
Yaw	1.0

Table 3.11 summarizes all of the IFs determined during the system identification tests. These factors will be applied to the thruster force and moment vector τ, to create a more accurate prediction of the vehicle dynamics. The different heave factors will be applied to the vertical thrust depending on the direction of motion. A summary of all the hydrodynamics properties of the vehicle are presented in Table 3.12.

3.5 Conclusion

In this chapter, a comprehensive vehicle and thruster model was developed. The thrust model was developed through measurements taken using a test stand. These measurements produced consistent repeatable results for an ideal stand-alone thruster. The thruster model was then used to determine the forces and moments on the vehicle during a series of system

Table 3.12: Hydrodynamic Coefficient Summary

Dir.	Rigid Body & Added Mass	Linear Drag	Quadratic Drag
Surge	$m + X_{\dot{u}} = 283.6\ kg$	$D_{L_{uu}} = 26.9\ kg/s$	$D_{Q_{u11}} = 241.3\ kg/m$
Sway	$m + Y_{\dot{v}} = 593.2\ kg$	$D_{L_{vv}} = 35.8\ kg/s$	$D_{Q_{v22}} = 503.8\ kg/m$
Heave(DN) Heave(UP)	$m + Z_{\dot{w}} = 499.0\ kg$ $m + Z_{\dot{w}} = 351.7\ kg$	$D_{L_{ww}} = 0.0\ kg/s$ $D_{L_{ww}} = 6.19\ kg/s$	$D_{Q_{w33}} = 265.6.1\ kg/m$ $D_{Q_{w33}} = 119.1\ kg/m$
Roll	$I_x + K_{\dot{p}} = 20.9\ kg\ m^2$ $K_{\dot{v}} = -22.8\ kg\ m^2$	$D_{L_{pp}} = 3.0\ kg\ m^2/s$ $D_{L_{pv}} = -3.5\ kg/s$	$D_{Q_{p44}} = 101.6\ kg\ m^2$ $D_{Q_{p22}} = -46.4\ kg$
Pitch	$I_y + M_{\dot{q}} = 30.4\ kg\ m^2$ $M_{\dot{u}} = -15.3\ kg\ m^2$	$D_{L_{qq}} = 4.9\ kg\ m^2/s$ $D_{L_{qu}} = -1.5\ kg/s$	$D_{Q_{q55}} = 59.9\ kg\ m^2$ $D_{Q_{q11}} = -13.7\ kg$
Yaw	$I_z + N_{\dot{r}} = 29.0\ kg\ m^2$	$D_{L_{rr}} = 3.5\ kg\ m^2/s$	$D_{Q_{r66}} = 76.9\ kg\ m^2$

identification tests. The system identification tests were used to determine the hydrodynamic coefficients for the vehicle model. The final coefficients for the model were determined using a least squares optimization, which incorporated a thruster interference factor. The identification of the pitch and roll dynamics was done in two steps. The first step was to identify the single DOF dynamics by isolating the pitching and rolling motion. Once the single DOF dynamics were identified, additional cross-coupling coefficients due to surge and sway were obtained using the full 6 DOF model. With the addition of the cross-coupling coefficients, the pitch and roll model agreed well with the dynamics that were measured during surge and sway motion.

Deriving an accurate dynamic model for an ROV is a difficult task. There are a lot of coefficients that need to be estimated at the same time, and it is often difficult to validate the data. Even if it was easy to obtain system identification data that doesn't contain noise and environmental disturbances, the quadratic drag model that is being used is only an approximation. It is unlikely that a simple quadratic drag model will precisely predict the drag profile for a complex body, such as an ROV, as it twists and turns through the water. Despite these complexities, the model presented here is comprehensive and consistent.

Chapter 4

Navigation

The art of navigation has been evolving for millennia; even the very first humans needed a way of describing where they were relative to important land marks. Seafarers pushed the boundaries of navigation, travelling further away from known landmarks in attempts to discover new parts of the world. Remarkable feats of navigation have been recorded as early as 350-BC [6]. These early mariners navigated without the use of compasses or sextants, or any of the other instruments we typically consider to be essential tools for even the most rudimentary ocean navigation. Things have changed and, in modern times, we rely heavily on instruments such as compasses, IMUs, and GPSs. When discussing navigation for autonomous vehicles, one is typically referring to the fusion of information from multiple sensors in some kind of optimal way to estimate the state vector of the vehicle. The state vector is a collection of variables which completely defines the condition of each independent degree of freedom of the body. This estimation is normally done using an observer or parameter estimator. The output of the navigation system provides feedback to the controller. Therefore, the accuracy of the navigation system will directly impact the design of the control system.

Precise underwater state information is often difficult to obtain. Highly accurate position data is challenging to acquire, due to the difficulties in communicating information through water. This makes the accuracy and stability of the inertial sensors more important. Extraneous unmodelled forces, such as tugs on the tether or collisions with the bottom or other subsea infrastructure, provides an additional challenge as these forces can dwarf the more subtle hydrodynamic and propulsion forces inherent in the vehicle. However, the density of water does provide one advantage - underwater vehicle dynamic motion is well damped. Transient dynamics die out and maintaining a sideslip or non-trimmed angle of attack requires the application of a constant force. Therefore, under a suitably stable controller the vehicle should remain in a quasi steady-state condition and follow a model relatively well.

In this chapter, an extended Kalman filter (EKF) will be developed to estimate the state vector of the Falcon ROV. The EKF will use the results from Chapter 3 for a the process model, and measurement models will be developed for all the sensors described in Appendix B. The resulting EKF will be validated using the MOCAP tracking system described in Chapter 2.

4.1 Background

As remotely operated and autonomous vehicles have become more prevalent, navigation has become an increasingly more important topic; through this, the Kalman filter, first described in 1960 by R.E. Kalman [37], has remained the dominant estimator in the field. The Kalman filter, also know as the linear quadratic estimator, minimizes the H_2 norm of the error between sensors measurements and an estimate of what those measurements would be, given an estimate of the position and orientation (state) of the sensors. The original Kalman filter was a linear estimator, but was extended to address non-linear plants. The EKF simply linearizes the non-linear models and applies the linear Kalman update equations [69]. This approach has been successfully applied to many different robotic applications from aircraft, to ground vehicles, to underwater vehicles.

While the EKF has dominated the navigation market, it does have some draw backs [17]. The biggest being that it relies heavily on the accuracy of the covariance matrices for the process model and measurement models for ensuring the optimality of the estimate. If these matrices are wrong then the estimate can be very inaccurate and the problem may even become ill conditioned. This has provided researchers with incentive to find better solutions to the nonlinear filtering problem. In 1993, Gordon, Salmond and Smith first proposed the 'bootstrap' filter as a rival to the EKF [25]; this filter has subsequently become known as the Particle Filter (PF). A PF exploits the Bayesian characteristics of the model and uses Monte Carlo sampling to obtain an optimal estimation. For a sufficiently well behaved problem, a PF with superior accuracy and equivalent computationally efficiency can be designed. However, for problems with high degrees modelling uncertainty, the computational cost can increase dramatically making the PF accuracy sub-optimal given the constraints of real-time computing. Never the less, over the last two decades, there has been an abundance of research on PFs and methods of augmenting them. In 1997, the unscented Kalman filter (UKF) was proposed [36]. The unscented filter is more stable and predictable in the face of non-linearities, as it bypasses the need to linearize the process and measurement models by using the "unscented transformation". Finite impulse response (FIR) filters have also been used for navigation, with comparable results to an EKF [49]. Research into the design and implementation of exact non-linear filters (much like the KF is exact for linear systems), have also been broached but they are complex and can be prohibitively expensive computationally. That being said, an exact solution which can produce optimal estimates to the nonlinear filtering problem is the holy grail of navigation. Research in this area is occurring[1], but there is still much work to be done in this area [17].

---

[1] Research on exact non-linear filters is presented in [18, 5]

Despite the advances in nonlinear filters in the literature, the discrete EKF was chosen for this work. It has a proven reliability for underwater applications, builds on previous work in at UVic [61, 78, 64], and is computationally inexpensive. Since the software is running on a small embedded processor, computational efficiency is an important quality.

4.2 Discrete Extended Kalman Filter

All of the Kalman filters have a few common components:

1. A process model which describes the dynamics of the system,
2. A measurement model which describes the output of the sensors given the state of the process model,
3. A set of propagation equations which propagates the process model given the error between the actual and estimated measurements.

The process and measurement models are given by Eq. 4.1 and Eq. 4.2, respectively.

$$\mathbf{x}_k = f(\mathbf{x}_{k-1}, \boldsymbol{\delta}_{k-1}, \mathbf{w}_{k-1}) \tag{4.1}$$

$$\mathbf{z}_k = h(\mathbf{x}_k, \mathbf{v}_k) \tag{4.2}$$

where $\mathbf{x}_k$ is the model state vector, $\boldsymbol{\delta}_k$ are the control inputs, $\mathbf{z}_k$ are the measurements and $\mathbf{w}_k$ and $\mathbf{v}_k$ are the process and measurement noise respectively, which are assumed to be from independent normally distributed white noise sources. It isn't possible to know the values of the white noise, $\mathbf{w}_{k-1}$ and $\mathbf{v}_k$, at a given time step, but one can use these models to estimate x and z. The estimates are denoted by $(\hat{\cdot})$. In this case we have used the symbol $\mathbf{x}$ as a generic state vector; it will be neither $\boldsymbol{\eta}$ nor $\boldsymbol{\nu}$ but a superset which includes both. A full derivation of the Kalman equations is presented in [69]. The following will just introduce the discrete EKF and discuss the formulation that is used for this work.

Given the process and measurements models, an optimal estimate of the state variables can be obtained using the process outlined in Figure 4.1. In this diagram, **P** is a covariance matrix for the EKF and **K** is the Kalman Gain. $\hat{\mathbf{x}}$ and $\hat{\mathbf{z}}$ are estimates of the state and measurement vectors, derived from **f** and **h**. **z** is the vector of actual measurements, $\mathbf{Q}_P$ is the covariance matrix for the process model and $\mathbf{R}_M$ is the covariance matrix for the measurement model. Finally, **A** and **H** are the Jacobians of the process and measurement models respectively.

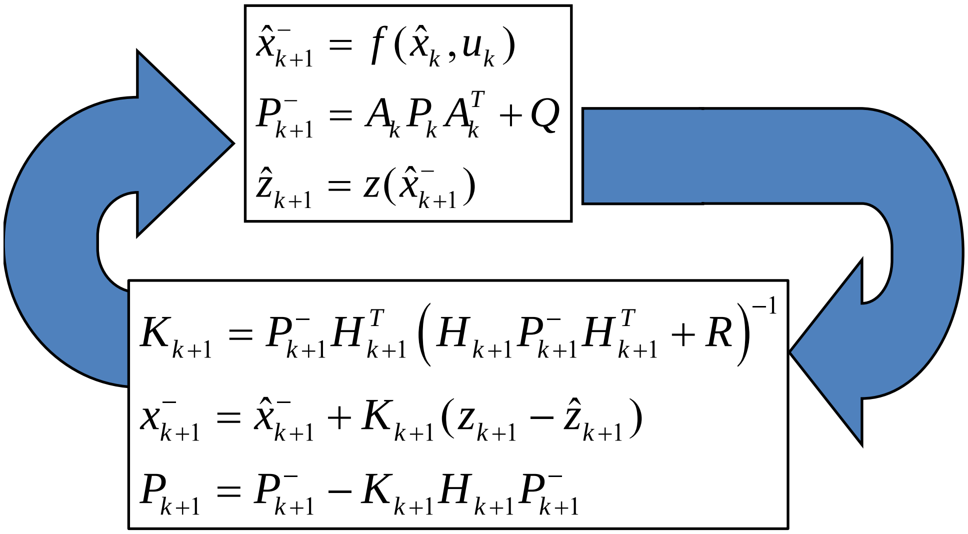

$$\hat{x}_{k+1}^{-} = f(\hat{x}_k, u_k)$$

$$P_{k+1}^{-} = A_k P_k A_k^T + Q$$

$$\hat{z}_{k+1} = z(\hat{x}_{k+1}^{-})$$

$$K_{k+1} = P_{k+1}^{-} H_{k+1}^T \left(H_{k+1} P_{k+1}^{-} H_{k+1}^T + R \right)^{-1}$$

$$x_{k+1}^{-} = \hat{x}_{k+1}^{-} + K_{k+1}(z_{k+1} - \hat{z}_{k+1})$$

$$P_{k+1} = P_{k+1}^{-} - K_{k+1} H_{k+1} P_{k+1}^{-}$$

Figure 4.1: Process for Iterating an Extended Kalman Filter

In the first step of this process, the state and measurements are predicted using the process and measurement models and an interim value of **P** is calculated; the predicted value of **x** is denoted by the superscript $\hat{\mathbf{x}}^{-}$. In the second step, the Kalman gain, **K**, is calculated. This is then used along with the predicted estimates to determine a final value for the state estimate, $\hat{\mathbf{x}}$, and estimate covariance, **P**. The following sections describe the process and measurement models; the lengthy derivatives required for the **A** and **H** matrices can be found in Appendix E.

4.2.1 Process Model

For this work, the process model is the dynamic model described in Section 3.2. With underwater vehicles, the accuracy of the process model is important. The measurements from the SBL come at approximately 1 Hz (as opposed to terrestrial systems like the Global Positioning System (GPS) which operates at around 10 Hz), so without an accurate process model the estimate can drift substantially between SBL updates. In general, to ensure a rapid convergence the process model should be as simple as possible while still capturing all of the dominant dynamics. In the past, it has been noted that including oscillatory higher order terms in the model can degrade the accuracy of the solution by causing what is essentially a limit cycle in the process model; when tuning the EKF, it is essential to look at the higher order terms and determine which ones are helpful and which ones are not. The Jacobian of the process model, $\mathbf{A}$, and the a description of which components were neglected is described in Appendix E.

In addition to the process model and its Jacobian, the initial estimate and error covariance matrices must be defined. The initial estimate is the best guess for the state vector given the available information. When starting the EKF for the first time, a few things are known:

- The vehicle is likely at rest on the surface,
- The vehicle is probably inside the boathouse,
- The vehicle is likely sitting level with minimal pitch and roll angle.

From this, we can pick an initial estimate for the position, quaternion, angular and translational rates as well as the accelerometer and rate gyro biases. The value for $\mathbf{x}_0$ used in this work is listed in Appendix E. The initial estimate for $\mathbf{P}$, denoted by $\mathbf{P}_0$, reflects the confidence in $\mathbf{x}_0$. For example, an estimate of the maximum error in the initial estimate of position will be a function of the size of the boathouse, which is only 3 m wide and 6 m long. Poor choices of values for $\mathbf{P}_0$ won't stop the estimate from converging, but will affect the speed at which it converges. The values used for $\mathbf{P}_0$ in this work are also listed in Appendix E.

The last matrix to be defined in the process model is $\mathbf{Q}_P$, the process model covariance matrix. $\mathbf{Q}_P$ should capture the noise in the process model itself. The values of $\mathbf{Q}_P$ were determined through trial and error using vehicle data that was recorded while the MOCAP was running. By comparing the estimated state with the MOCAP measurements, it was possible to manipulate the process model covariance matrix such that the EKF gave consistent performance under a variety of scenarios. The values used for $\mathbf{Q}_P$ in this work are listed in Appendix E.

4.2.2 Sensors and the Measurement Model

The sensors used for this research are mounted on the navigation sled as described in Appendix B. This sled is a removable addition to the Falcon; the sled can be affixed when precise positioning is required and then easily removed as a unit when a more compact vehicle configuration is necessary. Keeping the entire ensemble together as a single unit is advantageous because it eliminates the need to survey the locations of all the instruments each time the vehicle is reassembled.

In an EKF, each of the sensors are modelled such that one can predict the measurement based on the output of the process model. The difference between the measurements and the estimated measurements are called the residuals, and are used to produce the final state estimate. The better the measurement model, the more accurate the residuals will be which will lead to a more accurate state estimation.

The measurement model includes several components:

1. $z(\hat{x})$: an equation that describes the measurement in terms of the state vector,

2. Δt: the latency between the time the measurement is taken and the time that it is processed by the EKF,
3. R_M: the mean variance of noise in the measurements.

Since both the IMU and MOCAP are low latency systems operating at high frequency (125 Hz and 100 Hz respectively) with respect to the system dynamics, it can be assumed that their latency is negligible. The latency in the command loop is obtained by comparing the time stamp from when the thrust command is initiated with the time stamp from the first acceleration that is detectable by the IMU. This will indicate the time delay between when a command is issued and when the action is initiated (i.e., the thrusters fulfill the command). Each of the sensors will also have their own separate latency between the time that a measurement is observed and when it is delivered to the control computer. Since the sensors are measuring position and velocity, this latency is most easily measured by comparing the sensor output with the motion logged by the MOCAP camera system. The Jacobian of the measurement model, **H**, is described in Appendix E.

Inertial Measurement Unit

The inertial measurement unit used here is the Epson M-G350-PD11, a quartz-MEMS IMU. Quartz-MEMS units are high-end MEMS IMUs, providing superior stability and sensitivity to other MEMS devices without a significant increase in price; this sensor outputs acceleration and angular rates for all three body axes. See Appendix F for a more complete discussion on different types of IMUs.

The IMU is mounted as shown in Figure 4.2; note that the IMU is shown with the x-axis pointing away from the opening for the rip cord (indicated by two small silver posts on the left hand image), the z-axis pointing away from the black endcap and the y-axis forming a right had coordinate system. The IMU housing is mounted to the port side of the sled,

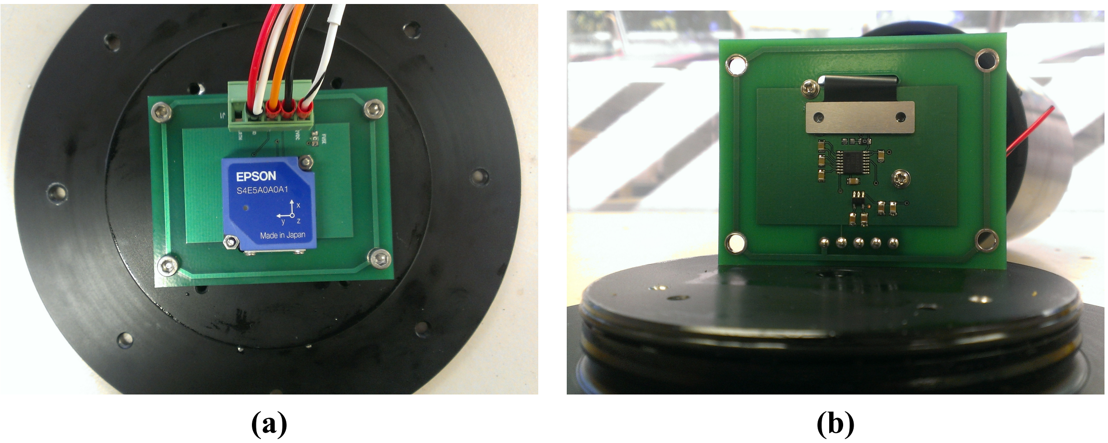

Figure 4.2: Inertial Measurement Unit: (a) sensor as mounted in the housing (b) custom interface board

Table 4.1: IMU Sensor Location Summary

Description	Value	Units
$R^{S\to B}$	$\begin{bmatrix} 0 & -1 & 0 \\ 0 & 0 & 1 \\ -1 & 0 & 0 \end{bmatrix}$	N/A
X_i^B	$\begin{bmatrix} 0.37644 \\ -0.26550 \\ 0.25732 \end{bmatrix}$	m

with the rip cord opening facing downwards. The transformation matrix from the SRF to the BRF as well as the location of the sensor in the BRF are shown in Table 4.1.

In the IMU documentation, the noise density is quoted to be ± 0.1 mG/$\sqrt{\text{Hz}}$ for the accelerometers and ± 0.004 (°/sec)/$\sqrt{\text{Hz}}$ for the rate gyros. Given a sampling rate of ± 125 Hz, which has a Nyquist frequency of ± 62.5 Hz, the static variance for white noise can be calculated to be the square of the noise density times the bandwidth of the signal (which is the Nyquist frequency). Therefore, the expected variance for the acceleration and angular rate measurements are ± 0.625 (mG)^2 and ± 0.001(°/s)^2 respectively. Static testing of the instrument confirmed this with values of ± 0.263630 (mG)^2, ± 0.300581 (mG)^2, and ± 0.165441 (mG)^2 for the three accelerometers. Similarly, the static variance for the three

Table 4.2: IMU Measurement Summary

Description	Unit	Biases	Static Variance	Dynamic Variance	Latency (sec)
Acceleration $(\ddot{x}, \ddot{y}, \ddot{z})$	mG	N/A	0.625	900	0
Angular Rate (p, q, r)	°/s	N/A	0.001	0.5625	0

rate gyros was ± 0.000553(°/s)^2, ± 0.000714(°/s)^2 and ± 0.000706(°/s)^2. In practice, however, when the vehicle is moving the variance will be higher due to vibration in the vehicle from the thrusters and hydrodynamic forces. The dynamic variance of the measurements was determined by studying the noise in the sensors during the system ID tests. This is most readily measured on the off-axes and when the system is moving in a steady state condition.

Determining all of the sensor biases exactly can be impossible and can result in conflicting information from the sensors; for example, the rate gyros could have a small bias and indicate that the roll angle is changing while the compass indicates that the angle is unchanging. Conflicting sensor information will artificially increase the error covariance in the P matrix and can drive the EKF to instability. This is especially critical on the low level sensors in the IMU, where small biases get integrated and can have a large impact on higher level states. To mitigate this situation, the accelerometer and rate gyro biases are estimated dynamically in the EKF. This approach has two benefits: 1) it eliminates the need to try and figure out accurate biases for the IMU (accelerometer and rate gyro biases are highly sensitive to power cycling and environmental changes) and 2) it stabilizes the EKF by providing an outlet for other sensor misalignments that create conflicting information.

The acceleration measured by the IMU will be a function of where it is mounted with respect to the CG of the vehicle. Newton's second law for acceleration of a particle in a rotating reference frame, whose position with respect to the origin of the rotating frame is given by $\boldsymbol{r}$, can be described as follows:

$$\begin{aligned}
\dot{\boldsymbol{r}} &= \boldsymbol{v} + \boldsymbol{\omega} \times \boldsymbol{r} \\
\ddot{\boldsymbol{r}} &= \frac{d}{dt}\left(\boldsymbol{v} + \boldsymbol{\omega} \times \boldsymbol{r}\right) \\
&= \dot{\boldsymbol{v}} + \dot{\boldsymbol{\omega}} \times \boldsymbol{r} + \boldsymbol{\omega} \times \dot{\boldsymbol{r}} \\
&= \boldsymbol{a} + \boldsymbol{\omega} \times \boldsymbol{v} + \dot{\boldsymbol{\omega}} \times \boldsymbol{r} + \boldsymbol{\omega} \times \left(\boldsymbol{v} + \boldsymbol{\omega} \times \boldsymbol{r}\right) \\
&= \boldsymbol{a} + 2\boldsymbol{\omega} \times \boldsymbol{v} + \dot{\boldsymbol{\omega}} \times \boldsymbol{r} + \boldsymbol{\omega} \times \left(\boldsymbol{\omega} \times \boldsymbol{r}\right)
\end{aligned} \tag{4.3}$$

where $\ddot{\mathbf{r}}$ is the measured acceleration vector, **a** is the BRF translational acceleration vector (ie the acceleration of the vehicle CG), **v** is the vehicle velocity vector and $\boldsymbol{\omega}$ is the angular rate vector. Lastly accelerometers measure specific force (or the acceleration with respect to free fall) [26]. This means that when an object is at rest an accelerometer will show an acceleration of approximately 9.8 m/s^2 in the direction opposite of gravity. As previously mentioned, there will also be time varying biases in the accelerometers, which will be estimated in the EKF. Therefore, the total measured acceleration will be:

$$\begin{aligned}
\boldsymbol{h}_a(\mathbf{x}) &= \mathbf{R}^{B\to S}\left(\ddot{\boldsymbol{r}} + \mathbf{sa}\right) + \mathbf{B}_a \\
&= \mathbf{R}^{B\to S}\left(\ddot{\boldsymbol{r}} + \mathbf{R}^{N\to B}\begin{bmatrix} 0 \\ 0 \\ -g \end{bmatrix}\right) + \mathbf{B}_a
\end{aligned} \tag{4.4}$$

where $\mathbf{R}^{B\to S}$ is the rotation matrix from the body to sensor frame, shown in Table 4.1.

Modelling the measurements from the rate gyros is more straight forward. The roll, pitch and yaw rate measurements, p, q, and r, as well as the IMU rate biases will also be estimated directly in the EKF. Figure 4.3 shows IMU measurements versus predicted measurements from the EKF.

$$\boldsymbol{h}_g(\mathbf{x}) \quad = \quad \mathbf{R}^{B\to S}\boldsymbol{\omega} + \mathbf{B}_g \tag{4.5}$$

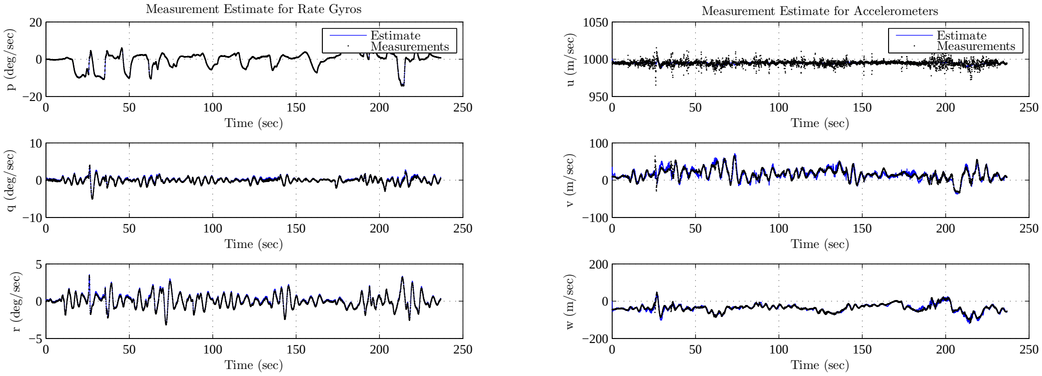

(a) **(b)**

Figure 4.3: IMU measurements: (a) rate gyros (b) accelerometers.

Pressure Sensor

Ambient water pressure is closely related to depth and a pressure transmitter can be used to determine the depth of the vehicle. The pressure transmitter used here is a Series 30 Preciseline pressure sensor from Keller America. It was chosen primarily for its stability as opposed to it's absolute accuracy and repeatability. Knowing exact depth from pressure requires additional sensors on the surface, as the atmospheric pressure (which is constantly changing), will also contribute to the total pressure that is measured at any particular depth. For the purposes of this research the most important attribute for a depth sensor is to give a steady output at a given depth, so that when the vehicle is trying to hold a stable vertical position it is getting consistent feedback. More information on pressure sensors can be found in Appendix F.

The pressure sensor is mounted in the SSC as shown in Figure 4.4-a, the sensing diaphragm exposed to ambient pressure through the end cap of the SSC. The location of the

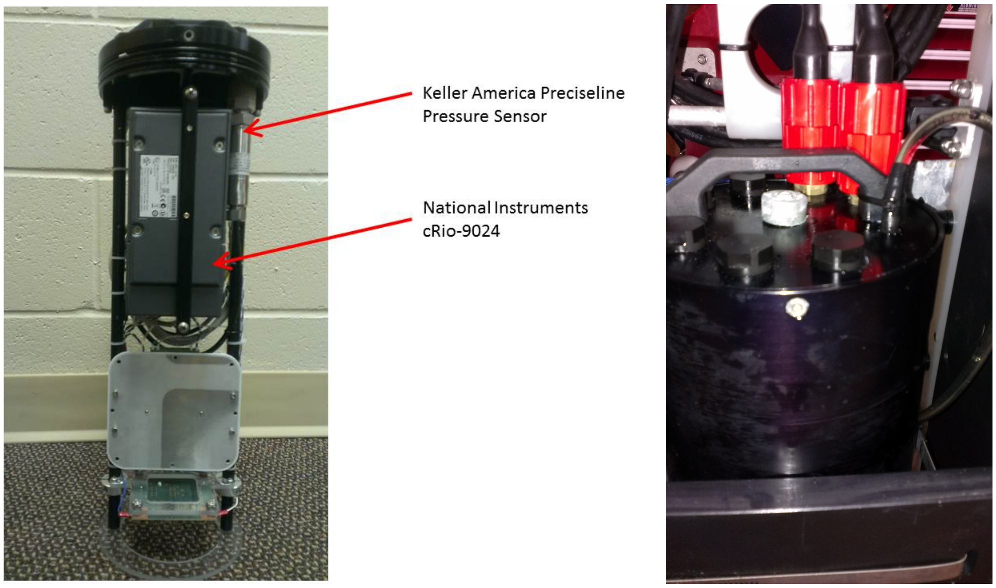

(a) (b)

Figure 4.4: Keller America Pressure Sensor: (a) picture of the Keller America Preciseline sensor inside the SSC (b) image showing the tube connecting the pressure sensor and the oil filled bladder

Table 4.3: Pressure Sensor Location Summary

Description	Value	Units
$R^{S \to B}$	N/A	N/A
X_p^B	$\begin{bmatrix} 0.10130 \\ -0.22116 \\ 0.26171 \end{bmatrix}$	m

diaphragm in the vehicle body frame is summarized as Table 4.3.

The measured static variance for the pressure sensor is $\pm 4.0 \times 10^{-8}$ bar^2. As with the other sensors, in practice when the vehicle is moving the variance will be higher due to pressure variations in the water. Pressure variations can be caused by the vehicle motion causing moving water to push against the sensor membrane; pressure changes can also occur due to the flow of water around the vehicle structure. The ambient water pressure will be the sum of the atmospheric pressure, the pressure from the water column, and the dynamic effects. The predominant effect will be from the vehicle velocity.

An oil-filled bladder was attached to the inlet of the sensor, as shown in Figure 4.4-b; the primary reason for the oil filled bladder is to isolate the sensor from seawater and also protect it from crevasse corrosion. Dynamic pressure (the pressure resulting from moving water pushing against the membrane) is given by $q = 1/2\rho V^2$; given the density of saltwater ($\rho \approx 1025$ kg/m^3) and a maximum vehicle velocity of $V = 2$ m/s^2, the dynamic pressure on an exposed flat face could result in pressure fluctuations up to 2050 Pa or 0.02 bar. In shallow water, if this isn't taken into account it could result in an error of as much as 25 cm in the depth estimate. It isn't possible to completely eliminate pressure fluctuations due to the hydrodynamics and vehicle motion, but they can be mitigated by keeping the oil filled bladder inside the ROV so that it is protected from the water flow.

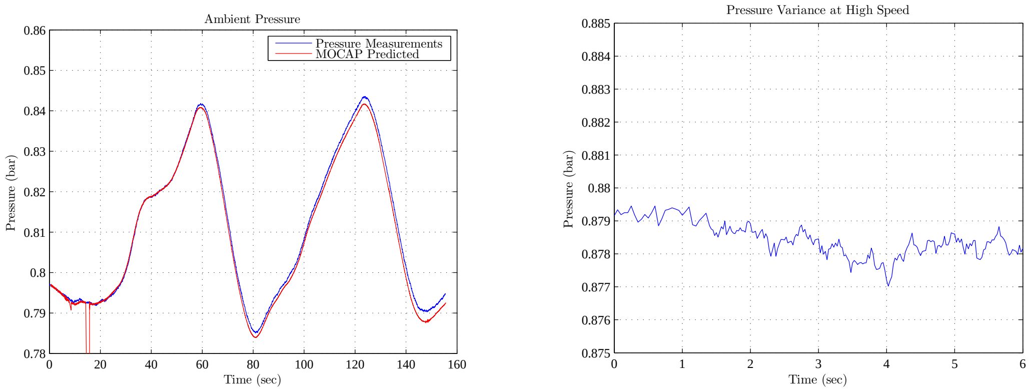

(a) **(b)**

Figure 4.5: Pressure Sensor: (a) plot showing the sensor measurements compared to the estimated pressure based on the MOCAP measurements of depth (b) variance of the measurement at high speeds.

Dynamic variance measurements were preformed by flying the vehicle forward at the surface of the water at high speed (Figure 4.5-b), which should produce the maximum amount of pressure variability. There is very little noise in this sensor with the dynamic variance being 6.25×10^{-8}, which is only one order of magnitude larger than the measured static variance, Table 4.4. The most significant issue with the pressure sensor is drift in the bias. As shown in Figure 4.5-a, the pressure sensor tracks the vertical motion very well

Table 4.4: Pressure Measurement Summary

Description	Unit	Biases	Static Variance	Dynamic Variance	Latency (sec)
Pressure	bar	$\approx 0.7- > 1.05$	4×10^{-8}	6.25×10^{-8}	≈ 0.0

but shows a drift of 0.0027 bar over a 150 seconds. This is likely due to poor performance with the internal temperature compensation algorithm. Given the time line of this research, changing to a new pressure sensor was not an option. Therefore, to mitigate this issue, all tests were kept to less than 1.5 minutes long so that the sensor drift doesn't significantly impact the navigation solution. Since this sensor runs at the same speed as the navigation filter (20 Hz), there can be no latency compensation as the latency will always be less than one time step.

The pressure measurements are modelled using the depth-pressure formulas given by Leroy and Parthiot in [43]. The necessary equations are summarized as follows:

$$\begin{aligned}
g &= 9.7803(1 + 5.3 \times 10^{-3} sin(\Phi)^2) \qquad (4.6)\\
k &= (g - 2 \times 10^{-5} z_p)/(9.80612 - 2 \times 10^{-5} z_p)\\
h_{45} &= 1.00818 \times 10^{-2} z_p + 2.465 \times 10^{-8} z_p^2 - 1.25 \times 10^{-13} z_p^3 + 2.8 \times 10^{-19} z_p^4\\
\delta h &= \frac{.01 z_p}{z_p + 100} + 6.2 \times 10^{-6} z_p\\
P &= 10(h_{45} \cdot k - \delta h) + B_p
\end{aligned}$$

where P is the pressure in bars, Φ is the latitude in radians and z_p is the depth of the sensor. In this case, the bias, B_p, will be a static constant and will be approximately equal to the atmospheric pressure in bars. This constant should be updated at the being of each data collection period and periodically throughout day if the atmospheric pressure is changing significantly. Note that the exact depth of the sensor will be dependant on the depth of the vehicle and on the attitude of the vehicle and the location of the sensor in the vehicle frame.

$$z_p = z + \mathbf{R}^{B \to N} \mathbf{X}_p^B(3) - Z_s \tag{4.7}$$

where $\mathbf{R}^{B \to N} \mathbf{X}_p^B(3)$ is the third element in the vector resulting from $\mathbf{R}^{B \to N} \mathbf{X}_p^B$ and Z_s is the vertical location of the water surface in the NRF.

Compass

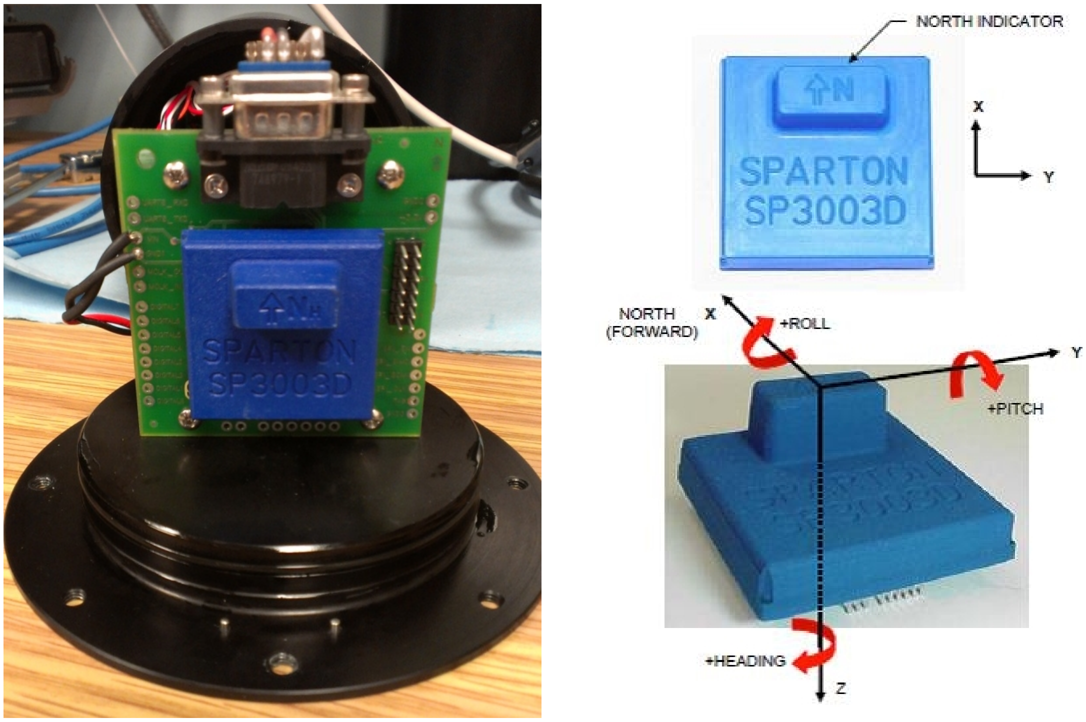

(a) **(b)**

Figure 4.6: Spartan Compass: (a) sensor as mounted in the housing (b) sensor orientation diagram

The compass chosen for this work is the Sparton SP3003D Digital Magnetic Compass; this sensor outputs roll, pitch and heading and has proven to be a reliable instrument with built-in calibration algorithms that can mitigate the effects of hard and soft iron distortions. The sensor uses the tilt-measurements obtained by measuring the direction of the Earth's gravitational vector to compensate the heading measurement for the sensor orientation.

The compass is mounted as shown in Figure 4.6; note that the compass is shown with the z-axis pointing away from the opening for the rip cord (indicated by two small silver posts on the left hand image), the x-axis pointing away from the black endcap and the y-axis forming a right hand coordinate system. The compass housing is mounted to the starboard side of the sled with the rip cord opening facing downward. The sensor is not perfectly aligned inside the housing and has roll, pitch and yaw alignment errors of approximately $-1.21°$, $1.43°$, and $7.0°$ respectively. Secondly, the compass uses accelerometers to measure pitch and roll angles. Therefore, the measurements will describe the direction of gravity, not euler angles. Since θ is defined in an intermediate frame, it is not the same as the pitch angle.

In order to simplify the H matrix, the measurements were used to calculate the euler angles for the vehicle and then the euler angles were used in the EKF instead of the raw measurements. Firstly, the roll, pitch and heading measurements in the body frame can be derived as:

$$\begin{aligned} \alpha &= (\beta_C + B_\alpha)\frac{\pi}{180} \\ \beta &= (180 - \alpha_C + B_\beta)\frac{\pi}{180} \\ \gamma &= (\gamma_C + 90 + B_\gamma)\frac{\pi}{180} \end{aligned} \tag{4.8}$$

where α, β, and γ are the measured roll, pitch and magnetic heading angles, and B_i are the respective misalignment angles. θ can then be calculated by creating a unit vector in the direction described by α and β.

$$\mathbf{u} = \frac{\begin{bmatrix} tan(\alpha) & tan(\beta) & 1 \end{bmatrix}^T}{\|\mathbf{u}\|} \tag{4.9}$$

Table 4.5: Compass Sensor Location Summary

Description	Value	Units
B_α	-1.21	deg
B_β	1.43	deg
B_γ	-7.0	deg
X_c^B	$\begin{bmatrix} 0.36716 \\ 0.16087 \\ 0.27544 \end{bmatrix}$	m

The euler angle θ can then be found by rotating **u** by the roll angle, α, such that it is in the intermediate frame, and taking the arctangent of the new angle.

$$\begin{aligned} \mathbf{u}_I &= \mathbf{R}_x\left(\alpha\right)\mathbf{u} \\ \theta &= atan\left(\frac{u_{I_1}}{u_{I_3}}\right) \end{aligned} \tag{4.10}$$

where $\mathbf{R}_x$ is the rotation matrix for rotations about the x-axis, and u_{I_1} and u_{I_3} are the first and third components of the vector $\mathbf{u}_I$. Since the roll, α, and heading,γ, are measured in the proper reference frames for euler angles, ϕ and ψ_M are simply:

$$\begin{aligned} \phi &= \alpha \\ \psi_M &= \gamma \end{aligned} \tag{4.11}$$

The transformation matrix from the sensor reference frame to the BRF as well as the location of the sensor in the BRF are shown in Table 4.5.

In the compass documentation, the quoted covariance for the static heading, roll, and pitch measurements are ± 0.04 deg^2, ± 0.04 deg^2 and ± 0.25 deg^2, respectively. Static testing of the instrument confirmed this with values of ± 0.02 deg^2, ± 0.03 deg^2 and ± 0.07 deg^2 for the three measurements. When the vehicle is moving the variance will increase due, primarily, to two factors:

- Unmodelled magnetic fields from electromagnetic interference due to thrusters and other electronics, hard and soft iron fluctuations from being in proximity to ferrous and magnetic materials, and from normal fluctuations in the earth's magnetic field, and
- Inaccuracies in the internal roll and pitch measurement that occur because the accelerometers in the compass cannot differentiate between the acceleration due to gravity (which they are trying to measure) and the superimposed acceleration of the vehicle.

See Appendix F for a more complete discussion on sources of error for compasses and magnetometers. The hard and soft iron effects were mitigated by calibrating the compass once it was mounted onto the vehicle. This was done by suspending the vehicle in the air (using non-ferrous materials) and swinging it roll, pitch and yaw while running the compasses built-in calibration routine. The dynamic accuracy and latency of each of the measurements was then calculated by manually flying the vehicle around with the MOCAP mast in place and comparing the roll, pitch and heading measurements from the compass to the those reported by the MOCAP camera.

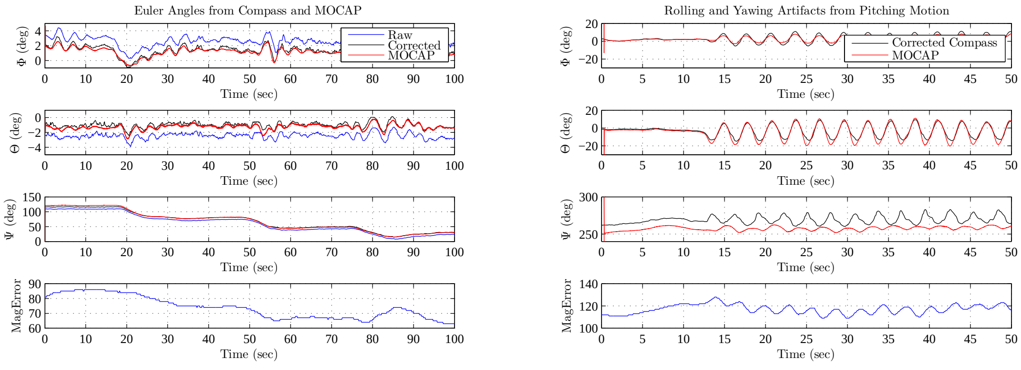

(a) **(b)**

Figure 4.7: Compass: (a) plot showing the sensor measurements compared to the measurements predicted by the MOCAP (b) plot showing the interaction between the degrees of freedom.

Table 4.6: Compass Measurement Summary

Description	Unit	Static Variance	Dynamic Variance	Latency (sec)
Roll (ϕ)	deg	0.02	0.25	0.35
Pitch (θ)	deg	0.02	0.25	0.35
Yaw (ψ)	deg	0.25	0.5625	0.35

Figure 4.7-a shows the angles from the compass compared to the MOCAP system for the vehicle siting stationary at different yaw angles. The output of the compass agrees well with MOCAP predictions. The slight discrepancies that are seen are a cumulation of error in the compass, error in the MOCAP, and also error in measuring the orientation of the HRF with respect to the NRF. This is most evident in the yaw angle which can be out by several degrees depending on the orientation of the vehicle. Figure 4.7-b shows induced yaw measurements from pitching motion. These small fluctuations are due to changes in the orientation of the earth magnetic field with respect to the vehicle. These effects have been minimized through calibration but are none the less still present to some extent. One interesting this to note is that the latency in the compass is 0.35 seconds. The instrument provides data at approximately 10Hz, so the latency crosses more than 3 measurements. This was a repeatable results and is likely due to the extensive amount of filtering that is used with accelerometers and magnetometers to get a clean data signal. A summary of the compass measurement attributes is given in Table 4.6.

The measurement model for the compass is dependant on the vehicle quaternion. Since the compass measurements have already been turned into Euler angles, the measurements can be modelled by:

$$\begin{aligned}
\hat{\phi}\left(\hat{x}\right) &= \text{arctan}\left(\frac{-2\left(s_1 s_3 + s_0 s_2\right)}{-\left(s_0^2 - s_1^2 - s_2^2 + s_3^2\right)}\right) \\
\hat{\theta}\left(\hat{x}\right) &= \text{arcsin}\left(2\left(s_1 s_3 - s_0 s_2\right)\right) \\
\hat{\psi}\left(\hat{x}\right) &= \text{arctan}\left(\frac{-\left(s_0^2 - s_1^2 + s_2^2 - s_3^2\right)}{-2\left(s_1 s_2 - s_0 s_3\right)}\right)
\end{aligned} \tag{4.12}$$

See Appendix D, Eq. D.6 - Eq. D.6 for a more complete derivation of these equations.

Doppler Velocity Log

Teledyne RDI's Explorer DVL is one of the few instruments on the market that is small enough to be used on observation class ROV. It has four transducer heads in a Janus configuration. The Janus configuration, named after a roman god that can look both forward and backward, has the four transducers arranged in a square with each transducer facing out at an angle of 30 degrees [24]. In this configuration the transducers act in pairs looking in opposite directions. With this configuration, the vertical and horizontal velocities in each direction can be differentiated and it is possible to eliminate much of the velocity error associated with pitching and rolling motions. For this work, an OEM version of the Explorer DVL was integrated into a custom housing in the navigation sled as shown in Figure 4.8.

The DVL is mounted as shown in Figure 4.8 with transducer number 3 on the top left at a 45 degree angle from the x-axis of the vehicle. The DVL reports velocity in a special ships frame which happens to be a left hand coordinate system which has the x-axis pointing to the port, the y-axis pointing aft and the z-axis pointing down. Since this reference frame is fixed internally in the sensor, the device driver corrects the output such that it matches the body frame. Therefore, the transformation matrix from the sensor reference frame to the BRF with the DVL in its current orientation is simply the identity matrix. The transformation matrix as well as the location of the DVL in the BRF are shown in Table 4.7.

In the documentation, the quoted accuracy of the velocity measurements are ± 0.02 m/s. As with the other sensors, when the vehicle is moving the variance will be higher. This will be primarily due to three factors:

- Propagation and multi-path errors,
- Errors in estimating the velocity due to vehicle rotation,

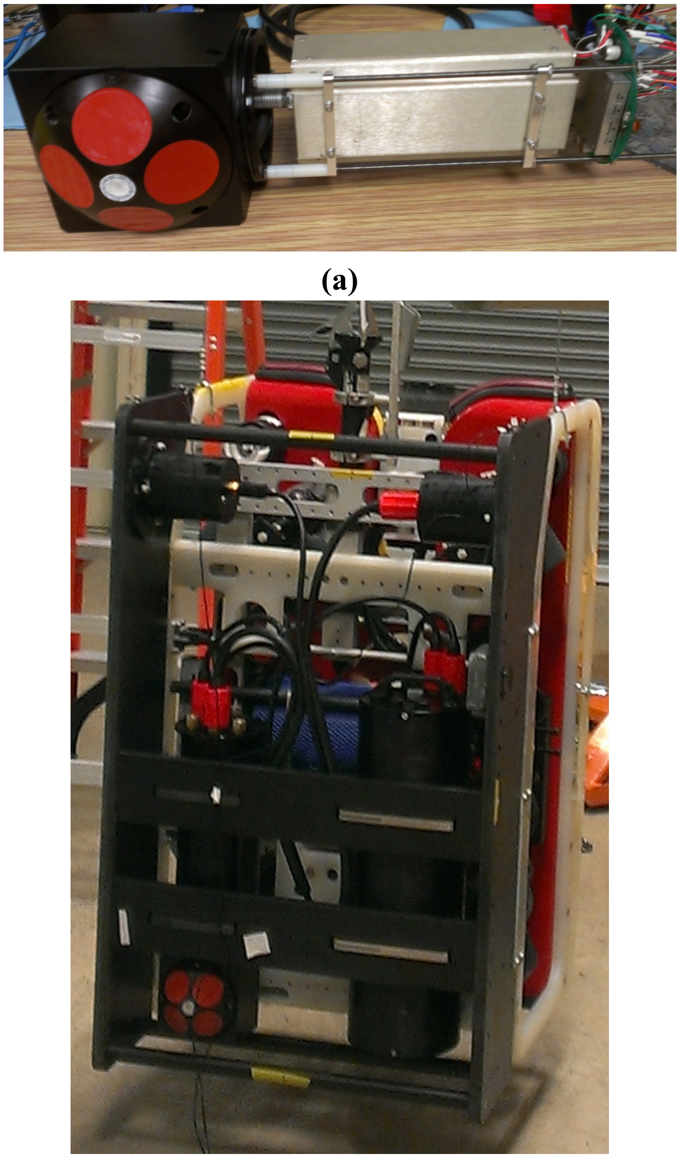
(a)

(b)

Figure 4.8: RDI Explorer DVL: (a) instrument as mounted in the housing (b) DVL in the housing orientated on the navigation sled.

- Changes in water depth.

See Appendix F for a more complete discussion on sources of error for DVLs. The static variance and biases of the DVL was measured by hanging the ROV from a crane in the SWAT facility. Biases can be caused by ringing and should be relatively constant for any given vehicle configuration. In this particular installation the biases are all less than $1 \times$

Table 4.7: DVL Sensor Location Summary

Description	Value	Units
$\mathbf{R}^{S\to B}$	$\begin{bmatrix}1 & 0 & 0\\ 0 & 1 & 0\\ 0 & 0 & 1\end{bmatrix}$	N/A
$\mathbf{X}_d^B$	$\begin{bmatrix}-0.39774\\ 0.12142\\ 0.35123\end{bmatrix}$	m

10^{-5} m/s which for these purposes is negligible.

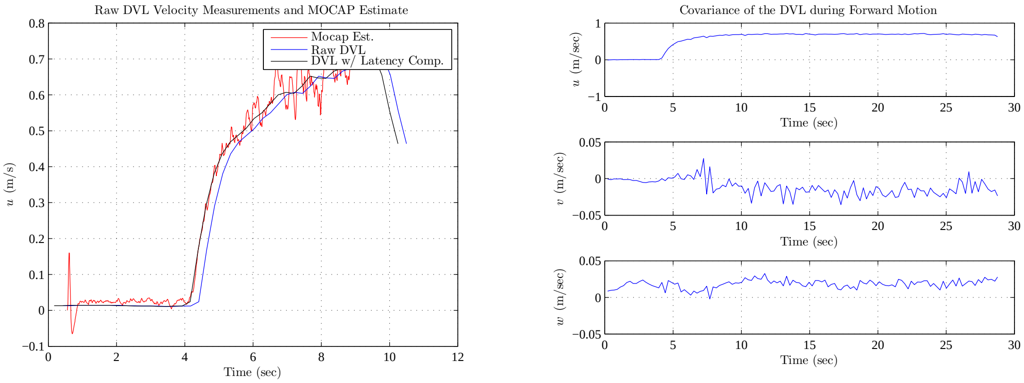

(a) **(b)**

Figure 4.9: DVL: (a) plot showing the sensor measurements compared to the estimated velocities based on the MOCAP measurements (b) Plot showing the variance in the measurements at high speed.

The dynamic accuracy and latency was measured by flying the vehicle with the MOCAP mast in place and comparing the velocities to those recorded by the MOCAP camera, as shown in Figure 4.9. Recall that the MOCAP is recording position in a CRF which is related to the HRF and NRF and these measurements are processed by the mast EKF presented in Appendix C. The mast EKF does not receive any direct velocity measurements; rather the velocities are a byproduct kinematic equations in the process model. This method of estimating the velocities is better than numerical differentiation but will still be noisy and have effectively been put through a low pass filter. Regardless, one can still clearly see

Table 4.8: DVL Measurement Summary

Description	Unit	Biases	Static Variance	Dynamic Variance	Latency (sec)
Forward (u)	m/s	0.000	$1.5e-5$	$1.6e-3$	0.25
Sideways (v)	m/s	0.000	$1.5e-5$	$1.6e-3$	0.25
Vertical (w)	m/s	0.000	$1.5e-5$	$1.6e-3$	0.25

the latency and that the DVL is giving appropriate measurements for the given motion. A summary of the measurement covariances is given in Table 4.8.

The measurement model for the DVL is similar to the model for the accelerometers in that it also includes a rotational term since the DVL is located distal to the CG of the vehicle. The translational velocities experienced by the DVL can be calculated as:

$$\begin{aligned} \boldsymbol{h}_d(\mathbf{x}) &= \mathbf{R}^{B\to S}\dot{\mathbf{X}}^{\boldsymbol{B}}_{\boldsymbol{d}} + \mathbf{B}_d \\ &= \mathbf{R}^{B\to S}\left(\boldsymbol{V} + \boldsymbol{\omega} \times \mathbf{X}^B_d\right) + \mathbf{B}_d \end{aligned} \tag{4.13}$$

where $\mathbf{V} = [u \;\; v \;\; w]^T$ is the translational velocity of the CG, $\boldsymbol{\omega} = [p \;\; q \;\; r]^T$ is a vector of the rotational rates of the rigid body. Figure 4.10 shows the raw DVL measurements and an estimate of the translational velocity of the CG versus the MOCAP estimate of the translational velocity of the CG. The effect is not negligible. Extracting the rotational component can be problematic as the angular rates of the vehicle are measured by the IMU, which has a much faster update rate, and a different latency. Correcting for the instrument latency is critical for properly separating the two velocity components. To correct for errors due to changes in water depth, one must have an accurate estimate of the altitude of the vehicle from the seafloor as well as the depth from the surface, then one can subtract changes in water depth from the w measurement. Altitude information is not available for this research and, therefore, w can not be corrected for this.

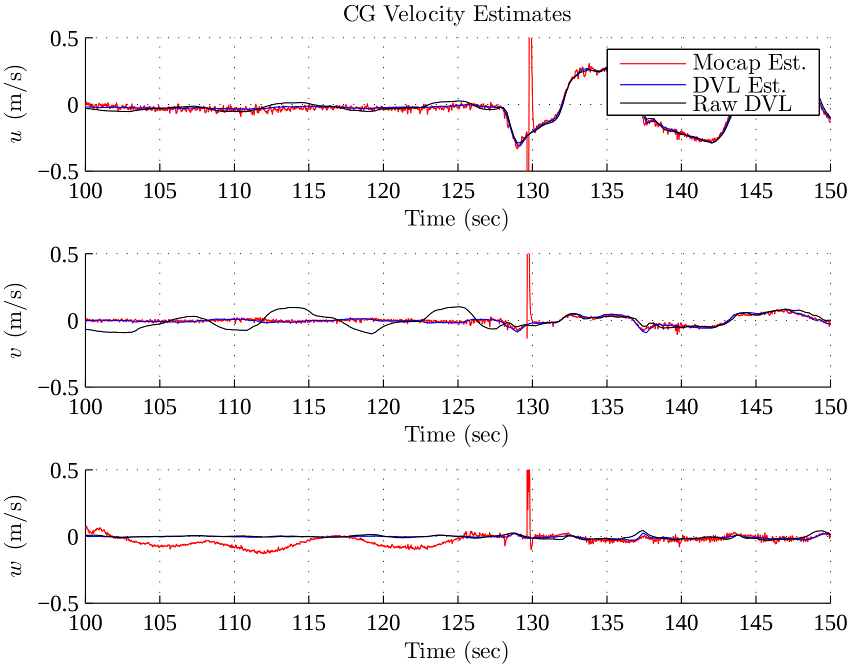

Figure 4.10: Plot showing the raw DVL data, DVL data with the rotational component extracted, and the estimated translational velocity of the vehicle from the MOCAP

Short Baseline Acoustic Positioning System

For position measurements, this system uses the SouthStar SBL system from Desert Star, described in Section 2.2.1, that is installed in the SWAT facility. This SBL system has cm level accuracy and can give position updates at up to 2Hz. The network architecture on this system would allow any acoustic tracking system on the market to be used here. The SouthStar system has excellent accuracy and was used in previous work [78, 61]; a more complete description of acoustic positioning systems can be found in Appendix F.

The SouthStar SBL system is comprised of four fixed tracking transponders and one roving transponder (the rover). The fixed transducers are mounted to poles as shown in Figure 4.11-b and the poles are located at the four corners of the boathouse test area as shown in Figure 2.3-b. The roving transponder is fixed to the vehicle as shown in Figure 4.11-a. For this work, the SBL software is configured to output the range from the rover to each of

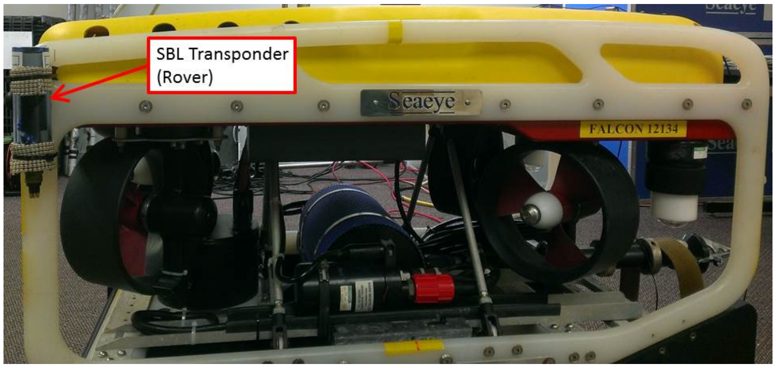

(a)

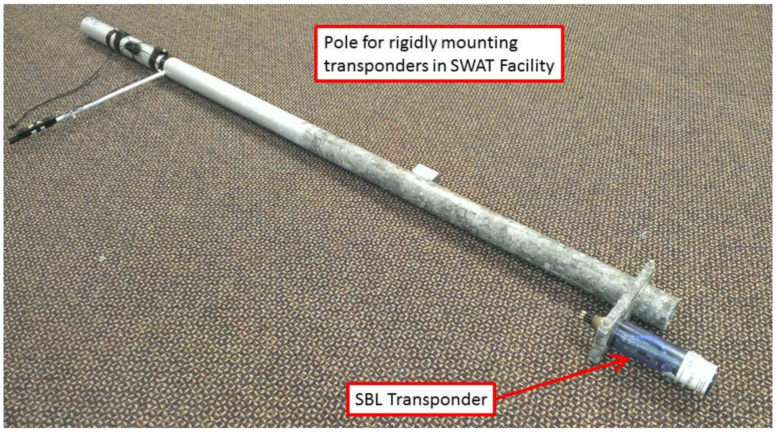

(b)

Figure 4.11: SouthStar SBL System: (a) Roving transponder mounted on the vehicle (b) Fixed transponder mounted to a pole in preparation for installing in the SWAT facility.

the four fixed transponders. The precise location of the fixed transponders must be known to accurately determine the location of the rover from the range data.

The MOCAP system is used to survey the positions of the fixed transponders. The transponder locations in the horizontal plane were determined by putting the roving unit in 12 different known locations and collecting the reported range data; 8 locations were used to calculate the location of the fixed transponders and 4 were used to validate the solution. The rover locations were measured using the MOCAP system. The location of the transponders was then determined by finding a position that minimizes the error between the measured range and the range estimate given by:

$$\boldsymbol{R}_{est_i} = \|\mathbf{T}_i - P\|^2 \tag{4.14}$$

where $\mathbf{T}_i$ is the estimated position of the i_{th} SBL transducer in the HRF and P is the known location of the roving transponder in the HRF. Since the 4 SBL transponders are located in a plane, there is a vertical dilution of precision and the depth of the transducer can't be accurately determined with this method. To circumvent this problem, the depth of the transponders were measured separately using a pole instrumented with LEDs. Accurately measuring the depth of the transponders through measurement is much easier then accurately determining their position in the horizontal plane while they are underwater. Using these two methods the location of the transponders in the HRF were determined with an accuracy of a few centimeters. The locations of each fixed SBL transponder in the NRF as well as the location of the rover in the BRF are in Table 4.9.

In the documentation [65], the quoted accuracy of the range measurements are ± 0.01 m; but the accuracy of the position estimate will depend on both the accuracy of the range measurement and also the accuracy to which the location of the fixed transducers were measured. The static accuracy was measured using the four validation measurements in the location survey. Of these four measurements, the maximum error in the range measurement for transponders 1, 2, 3 and 4 were 2.01, 3.30, 2.01, and 2.91 cm respectively. This measurement would capture errors in locating the roving transponder but does not capture errors due to alignment changes in the camera, errors in the location of the transducer on the vehicle, and errors due to the vehicle motion. The reported errors support the claims in the documentation to within the accuracy that can be measured at the SWAT.

The dynamic accuracy, transponder biases, and latency of the measurements were measured using the vehicle, the mast and the MOCAP system. In these tests, the vehicle was driven around the test area and the ranges reported by the SBL transponders were com-

Table 4.9: SBL Transducer Location Summary

Description	Value	Units
X_{s1}^H	$\begin{bmatrix} 3.09067 \\ 1.40936 \\ 2.28625 \end{bmatrix}$	m
X_{s2}^H	$\begin{bmatrix} -0.03380 \\ 1.48179 \\ -3.05023 \end{bmatrix}$	m
X_{s3}^H	$\begin{bmatrix} 0.00410 \\ 1.40003 \\ 2.33876 \end{bmatrix}$	m
X_{s4}^H	$\begin{bmatrix} 3.09126 \\ 1.42248 \\ -3.07985 \end{bmatrix}$	m
X_r^B	$\begin{bmatrix} -0.48567 \\ 0.31449 \\ -0.27278 \end{bmatrix}$	m

pared with the estimated ranges from the MOCAP measurements. This configuration more accurately reflects the errors in the real system.

The speed of the vehicle is several orders of magnitude slower than the speed of sound in water so that shouldn't have a significant effect. Therefore, the dynamic accuracy should be relatively close to the static accuracy as long as the locations of all the components have been properly surveyed. Figure 4.12 shows a plot where the vehicle was flown inside the test area keeping the same orientation at all times. The error in the range estimate gets significantly larger when the vehicle itself lies between the rover and the fixed SBL transponder; in these situations the transponder is in an acoustic shadow caused by the vehicle and the range measurement is unreliable. The red markers indicate when the transponder lies in the vehicle shadow zone, which extends between between $-112.5°$ and $0°$ relative to the heading of the vehicle. Since removing this error is not realistic, these measurements are

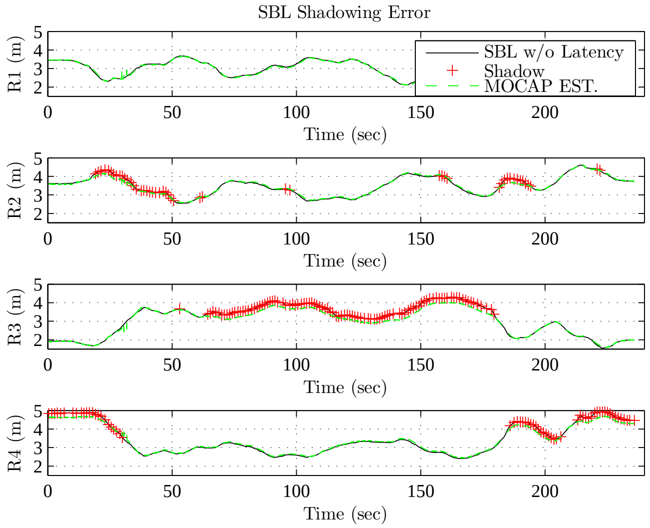

Figure 4.12: Graph showing the SBL measurements compared to the estimated ranges from the MOCAP measurements. Taking into consideration latency and when different SBL transponders are in the shadow of the vehicle.

Table 4.10: SBL Measurement Summary

Description	Unit	Biases	Static Variance	Dynamic Variance	Latency (sec)
SBL1	m	0.0	4.0×10^{-4}	1.2×10^{-3}	0.7
SBL2	m	0.0	4.0×10^{-4}	1.2×10^{-3}	0.7
SBL3	m	0.0	4.0×10^{-4}	1.2×10^{-3}	0.7
SBL4	m	0.0	4.0×10^{-4}	1.2×10^{-3}	0.7

just marked as invalid and not used in the EKF. This issue is an artifact of flying the vehicle close to the surface (as is necessary when using the mast), when the vehicle is deeper and the rover is below the transponders in the water column they will not be shadowed.

Correcting for a latency of 0.7 seconds, the variance for the range measurements when the transponder is not in the shadow of the vehicle is approximately 3.5 cm which is on par with the static accuracy. 0.7 seconds of latency is also reasonable given the way the transponders work. A summary of the measurement performance is given in Table 4.10.

The measurement model for the SBL involves the attitude quaternion, **s**, and the position of the vehicle in the NRF, $\mathbf{X}_{cg}^N = [x\ y\ z]^T$. For each of the fixed transponders, the range from the transponder to the rover is given by:

$$\begin{aligned} \boldsymbol{h}_{si}(\mathbf{x}) &= \| \mathbf{X}_{cg}^N + \mathbf{X}_r^N - \mathbf{X}_{si}^N \| + \mathbf{B}_{si} \\ &= \| \mathbf{X}_{cg}^N + \mathbf{R}^{B \to N}(\mathbf{s}) \mathbf{X}_r^B - \mathbf{X}_{si}^N \| + \mathbf{B}_{si} \end{aligned} \tag{4.15}$$

where i is the transponder number.

4.2.3 Latency Compensation

As shown in the previous section, there is a significant amount of latency in many of the sensors. Latency in the sensor measurements can have two effects: 1) uniform latency can result in a latent state estimate, and 2) differences in the sensor latency can result in instability in the sensor measurements. In this research, there is both cases. Given that the SBL has 0.7 seconds worth of latency, in order for the state estimate to accurately predict the measurement it must also have 0.7 seconds of latency. In addition, since the latencies in the sensors are so different (ranging from 0 to 0.7 seconds), any cross coupling that occurs will generate conflict though the **A** and **H** matrix. While the EKF, as described, is stable without any compensation for latency, the accuracy of the state estimate is degraded and the addition of cross coupling terms to the **H** matrix can cause instability rather than redundancy. One method of handling latency in an EKF, is to utilize the predicted state vector $\hat{\mathbf{x}}^-$ from the time step that the measurement occurred in the measurement model instead of the current one. This ensures that the residual is created from one consistent time step. The consistent but delayed residual is then used at the current time step. This method is one of the better known "tricks" for making EKFs more accurate, but the accuracy can come at the price of stability. While the residual is computed at a consistent time step the Jacobians are from a different one. For this work, latency compensation was used for the SBL measurements only. The SBL has the most latency and because it is related to a position measurement, there is less

Table 4.11: Difference between EKF Estimate and MOCAP estimate

Description	Mean Error	Unit
x	0.045	m
y	0.039	m
z	0.015	m
s_0	0.006	N/A
s_1	0.003	N/A
s_2	0.007	N/A
s_3	0.009	N/A

interaction with the other states in the Jacobians. Compensating for latency in the SBL improved the average accuracy of the horizontal position estimate by approximately 2 cm without sacrificing stability.

4.3 Validation of the State Estimate

Figure 4.13 shows the output of the EKF compared to the MOCAP. The attitude discrepancies are primarily due to the errors in the MOCAP that occur when viewing it from different angles. Overall the mean position error was less than ± 5 cm on all axes. The attitude quaternion had a mean error of ± 0.006 for s_0 which corresponds to an error of approximately 0.7 degrees about the axis of rotation. It should be noted that these errors include errors in the MOCAP system itself. A summary of the differences between the EKF and MOCAP estimates is given in Table 4.11.

4.4 Conclusion

An EKF was created using the process model described in Chapter 3, measurement models described in Section 4.2.2, and Jacobians described in Appendix E. The sensors were characterized using the MOCAP system, and the following parameters were determined

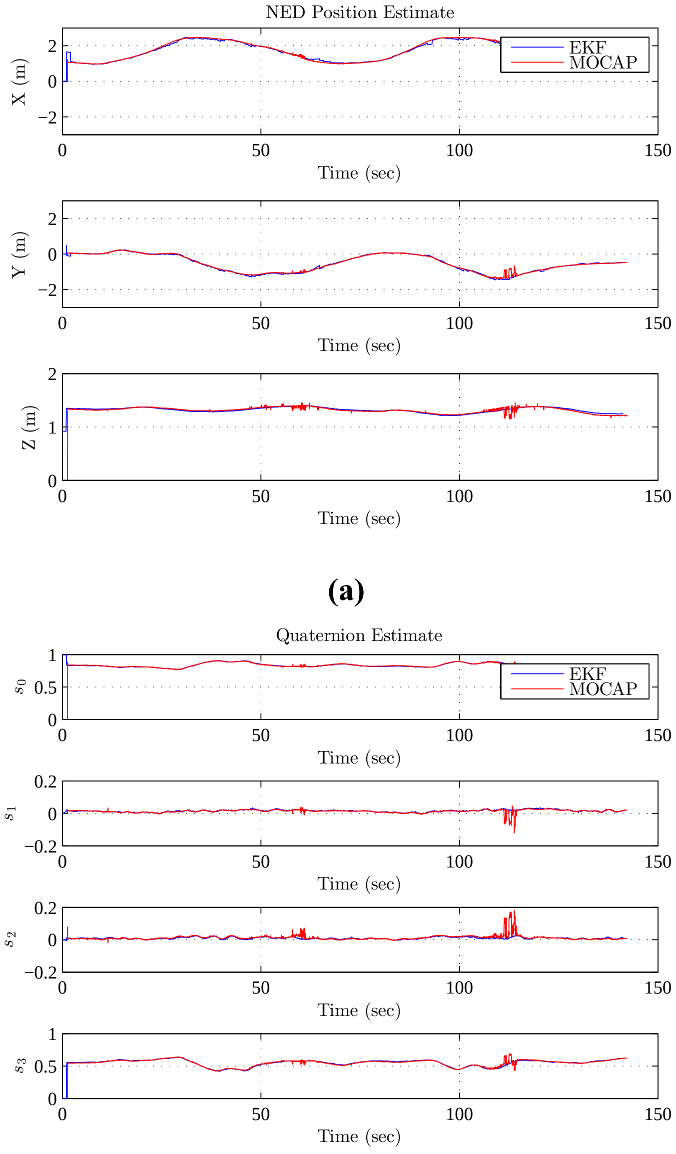

(a)

(b)

Figure 4.13: EKF estimate compared with the MOCAP for a) the NRF positions, b) the attitude quaternion.

for each sensor: position in the BRF, orientation with respect to the BRF, signal latency, and mean dynamic noise variance. The measurement models were validated by comparing sensor measurements to the output of the models using state information obtained with the MOCAP tracking system. The resulting EKF produced a vehicle position estimate with a mean Euclidean error of less than ± 6 cm with respect to the MOCAP position estimate.

Chapter 5

Guidance

This chapter presents a stand-alone guidance system, which, given the vehicle current location and desired destination, produces the desired velocities required to get to the destination. The theory behind the guidance system is presented first, followed by an explanation of how it was implemented. The chapter concludes by presenting some simulation results which highlight the stability of the algorithm and show the performance when applied to this application.

The theory behind the guidance system employed in this research was previously presented in Soylu et al. in [63], which built on the Lyapunov stable guidance system presented by Aicardi, Caiti, Cannata, and Casalino in[2] and was implemented by Caccia and Veruggio in [12]. In this approach, a task function is created using the controllable variables of $\boldsymbol{\eta}$, $\mathbf{e}$ contained in $\Re^4$, is defined such that, by minimizing the function, the ROV will meet its objective. Then by choosing a reference velocity, $\dot{\mathbf{e}} = -\boldsymbol{\lambda}\mathbf{e}$, one can define a Lyapunov function $V(\mathbf{e}) = 1/2\mathbf{e}^T\mathbf{e}$, where $\dot{V} = \dot{\mathbf{e}}$ is negative definite and V has a globally asymptotically stable equilibrium point at $\mathbf{e} = 0$. The task function can then be designed to ensure that the objective is met effectively.

This algorithm is well suited to use on ROVs, because of its stability in the presence of unmodelled dynamics (such as unexpected forces from the tether). This algorithm inherently handles deviations from the planned path; at each time step a new reference velocity along an asymptotically stable path is calculated based on the current position. Since $V \leq 0 \ \forall \ \mathbf{e} \in \Re^4$, every point in the operational space will converge on the equilibrium. The strength of this approach, in contrast to conventional line-of-sight or fixed-path guidance algorithms is that there is no path planning or replanning required. No matter what disturbances happen along the path, the vehicle will just keep trying to meet the objective. The disadvantage of this is that there is no explicit means of controlling the position of the vehicle, rather the velocities. Therefore, it won't specifically avoid out-of-bound areas in space.

5.1 Background

A guidance system provides a planned path to take from a designated starting point to a specified end point. When a driver is planning the path to take from their house to work in the morning, they usually take into account many variables: path length, traffic, drive time, coffee stops, etc. The most simple guidance algorithm uses a line-of-sight behavior, where it points the vehicle at the destination and then moves straight towards it. This algorithm would minimize the path length, but one can imagine that minimizing the path length is not always enough.

Since an ROV is typically controlled by a human pilot, they don't normally have a built-in guidance system. The pilot just naturally figures out where to go. For this work, the ROV is required to exhibit autonomous behaviour and a guidance algorithm is required for path planning. Within the context of Autonomous Underwater Vehicles (AUVs), guidance algorithms are used for many purposes. They can coordinate the behaviors of multiple agents that are acting together to complete a task [19, 54]; they are also be used to manoeuver vehicles around obstacles and command aggressive manoeuvres such that the vehicle arrives safely at its destination [29]. They can also be used to optimize power consumption and many other variables [41].

Most guidance algorithms pre-compute the path for the vehicle to follow. If the vehicle has to deviate from the path for some reason, then another path needs to be generated before the vehicle can continue. The guidance algorithm chosen for this work is simple but runs in real-time, and generates a minimum energy path to the destination point. The algorithm is similar to the Slotine and Li algorithm for manipulator control presented in [56] and further discussed by Fossen in [20]. While this algorithm is stable and ensures that the vehicle will always be given an appropriate path to the destination point, even in the face of disturbances, the development of a new guidance algorithms that can optimize ROV operations is still needed. As shown by Zand in [78], the tether dynamics have a significant effect on transit speeds and a coordinated guidance algorithm that provides a path for the surface vessel, the ROV and the tether could provide significant improvements in the efficiency of operations.

5.2 Task Function and Synthesis of the Guidance Laws

First, define $\boldsymbol{\chi}$ as a subset of $\boldsymbol{\eta}$, such that it is a vector containing the controllable variables of $\boldsymbol{\eta}$. Then $\boldsymbol{\chi}_d$ is the desired value of those state variables. For this work:

$$\boldsymbol{\chi} \triangleq \begin{bmatrix} x \\ y \\ z \\ \psi \end{bmatrix} \tag{5.1}$$

Since neither the roll or pitch are controllable, they don't need to be included in the guidance. Rather we will rely on the inherent stability of the vehicle to ensure that these two states tend towards 0 after a disturbance. Recall that these variables are defined in the NRF, while the velocities, $\boldsymbol{\nu}$, are defined in the BRF. To manage this define the following transformation:

$$\mathbf{L} \triangleq \begin{bmatrix} \mathbf{R}^{N \to B} & 0 \\ 0 & \cos(\theta) / \cos(\phi) \end{bmatrix} \tag{5.2}$$

such that $\boldsymbol{\zeta} = \mathbf{L}\dot{\boldsymbol{\chi}}$ and $\boldsymbol{\zeta}$ is the controllable subset of $\boldsymbol{\nu}$ that correspond to the variables in $\boldsymbol{\chi}$. Note that the $\cos(\theta)\cos(\phi)$ term comes from the mapping between the vectors $[p, q, r]^T$ and $[\dot{\phi}, \dot{\theta}, \dot{\psi}]^T$ (see Appendix D Eq. D.20).

One of the simplest task functions can be defined as: $\mathbf{e} = \mathbf{L}(\boldsymbol{\chi} - \boldsymbol{\chi_d})$, which is essentially a proportional (or P-type) control scheme. Then the reference velocities can be defined as:

$$\begin{aligned} \boldsymbol{\zeta}_d &= \dot{\mathbf{e}} \triangleq -\boldsymbol{\lambda}\mathbf{e} \\ &= -\boldsymbol{\lambda}\mathbf{L}(\boldsymbol{\chi} - \boldsymbol{\chi_d}) \end{aligned} \tag{5.3}$$

where $\boldsymbol{\lambda}$ is a positive definite diagonal matrix of gains for the different variables.

In order to guarantee Lyapunov stability for the command $\boldsymbol{\chi}$, the mapping between $\boldsymbol{\zeta}$ and $\boldsymbol{\chi}$ has to be linear and invertible, which implies that it must be continuous over the entire operational space. Since the command vector $\boldsymbol{\chi}_d$ is defined using the Euler angle ψ then it inherits the singularity at $\theta = \pm 90°$ (see Appendix D).

Remark 1. *In theory, using* $\mathbf{L}$ *to map the error signals into the BRF is a viable means for deriving the reference velocities. However, in practice, this can cause oscillatory heave motion due to the uncontrollable pitching and rolling motion that occur as a natural result of surge and sway motion. When the vehicle is close to the setpoint for Z, and a long way from the setpoint in X then a small pitch angle can change the heave component of the error in the BRF from positive to negative, even though the error in Z has not changed signs.*

To manage this problem, the transformation $\mathbf{L}$ *was not used in the heave direction and the error signal was simply calculated as* $e_z = z - z_d$.

In underwater applications, there are often biases in the velocity estimates which could lead to limit cycles or other instabilities in the guidance loop; an integrator can be added to the task function to mitigate this problem [12]. Defining a PI task function as:

$$\mathbf{e} = \mathbf{L}\left[(\boldsymbol{\chi} - \boldsymbol{\chi_d}) + \boldsymbol{\mu}\int_0^t (\boldsymbol{\chi} - \boldsymbol{\chi_d})\, d\tau\right] \tag{5.4}$$

Then the reference velocities can be defined as:

$$\begin{aligned} \boldsymbol{\zeta}_d &= -\boldsymbol{\lambda}\mathbf{L}\left[(\boldsymbol{\chi} - \boldsymbol{\chi_d}) + \boldsymbol{\mu}\int_0^t (\boldsymbol{\chi} - \boldsymbol{\chi_d})\, d\tau\right] \\ &= -\mathbf{K}_p\mathbf{L}\,(\boldsymbol{\chi} - \boldsymbol{\chi_d}) - \mathbf{K}_i\mathbf{L}\int_0^t (\boldsymbol{\chi} - \boldsymbol{\chi_d})\, d\tau \\ &= \boldsymbol{\zeta}_P + \boldsymbol{\zeta}_I \end{aligned} \tag{5.5}$$

where $\boldsymbol{\lambda}$ and $\boldsymbol{\mu}$ are positive definite diagonal matrix of gains for the different variables, which for clarity sake can be redefined as $\mathbf{K}_p = \boldsymbol{\lambda}$ and $\mathbf{K}_i = \boldsymbol{\lambda\mu}$.

5.3 Implementing Physical Limitations

Given a waypoint sufficiently far away, this algorithm will result in reference velocities that are not achievable by the vehicle. This problem could be managed effectively in many ways; however, in the design philosophy used here, the desired state produced by the guidance algorithms should be achievable by the vehicle. To do this, physical limitations can be imposed on the output of the guidance law. As long as the integral term is properly managed, this will not adversely affect the stability of the overall algorithm. This guidance law does not make any assumptions about where the vehicle should be at a given time, at each iteration it simply generates a new set of reference velocities based on where the vehicle actually is.

5.3.1 Managing the Integral Component

Anytime an integral component is utilized in a real system, it must be managed to ensure it is effective and the magnitude doesn't end up too large. In this work, two mechanisms are employed to manage the integral component. Firstly, the integral portion of the reference velocity is limited so that it can assist in mitigating biases in the estimated velocities but can't grow without bound. Secondly the integral portion is only needed when the vehicle is close to the commanded waypoint; turning the integral portion off when the waypoint is far away and only utilizing the proportional control also helps manage the integral wind-up [12]. Given a set of limits for the integral portion of the reference velocities, $\boldsymbol{\zeta}_{I_{MAX}}$, one may modify the integral component as follows:

$$\text{if } \ \|\zeta_{Ii}\| > \zeta_{I_{MAX_i}} \ \text{ then } \ \zeta_{Ii} = sign\left(\zeta_{Ii}\right)\zeta_{I_{max_i}} \tag{5.6}$$

Secondly, to switch between a P-type task function (described in Eq. 5.3) when the waypoint is far away and a PI-type task function when the waypoint is close, one can simply set $\zeta_{I_{MAX_i}} = 0$ when e_i is large and the integral is not needed. Noise in the state estimate can cause chattering when switching between the two tasks [12]. To mitigate this an anti-chatter mechanism is implemented. Graphically, the mechanism can be represented as shown in Figure 5.1. The P-type task law is used when the error function e_i becomes greater than the upper threshold, however, if the error then decreases the PI-type task law isn't re-engaged until it passes back through the lower threshold.

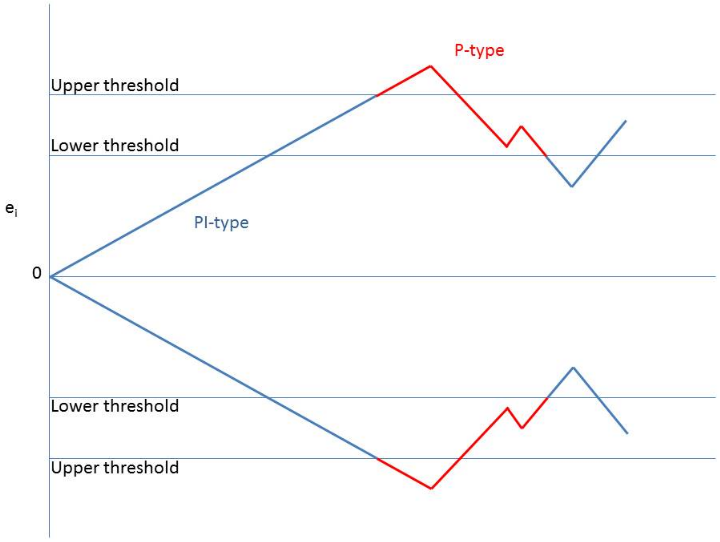

Figure 5.1: Graph showing the anti-chatter mechanism used to switch between the P-type (areas in red) and the PI-type (areas in blue) guidance laws

Logically, this can be described by the following set of conditions:

$$\begin{gathered}\text{if } \ \|e_i\| > T_{U_i} \ \text{ then } \ \text{MODE} = \text{P} - \text{TYPE} \\ \text{if } \ \|e_i\| < T_{L_i} \ \text{ then } \ \text{MODE} = \text{PI} - \text{TYPE} \\ \text{if } \ \text{MODE} = \text{P} - \text{TYPE} \ \text{ then } \ \zeta_{I_i} = 0\end{gathered} \tag{5.7}$$

where T_{U_i} is an upper threshold, T_{L_i} is a lower threshold, and MODE is the mode of the controller. By using only those two conditions and not specifying a state for the area between T_{U_i} and T_{L_i} , MODE will retain it's state until it crosses a threshold line moving in the correct direction.

Since the command, $\boldsymbol{\chi}$ is defined in the NRF, while the guidance parameters, $\mathbf{e}$ and $\boldsymbol{\zeta}$ are defined in the BRF, the horizontal error components (the ones corresponding to the body x-axis and y-axis) are coupled through the heading, ψ. To avoid unexpected switching between the guidance task functions as the vehicle rotates, the task functions for these two axes are switched together. This is done by defining a horizontal error e_h, such that $\|e_h\| = \sqrt{e_x^2 + e_y^2}$. When e_h crosses the thresholds then the task function is switched for both the x-axis and y-axis.

5.3.2 Rate Limits

Once the integral portion of the reference velocities is determined, it is added to the proportional component as described in Eq. 5.5. The sum of these two components may be larger than the maximum attainable velocity for the vehicle. To solve this problem, the desired reference velocities are also limited. Given a set of maximum velocities $\boldsymbol{\zeta}_{MAX}$ for each element in $\boldsymbol{\zeta}$, one can limit the reference velocities as follows:

$$\text{if} \quad \|\zeta_i\| > \zeta_{MAX\,i} \quad \text{then} \quad \zeta_i = sign\left(\zeta_i\right)\zeta_{MAX\,i} \tag{5.8}$$

This assumes that the velocity limits are symmetrical for the positive and negative directions but asymmetric limits could also be used.

5.4 Simulation Results

The robustness of this guidance algorithm is demonstrated through simulation. First, a simplistic simulation is used to highlight how this guidance algorithm adapts to disturbances, then the algorithm is applied to the full vehicle simulation. K_p and K_i were selected experimentally, such that, given vehicle dynamics and the expected amount of noise in the state estimate, the guidance algorithm created a smooth attainable trajectory for the vehicle to follow with minimal overshoot at the destination.

5.4.1 Demonstration of the Features

To demonstrate the features of the guidance system, a simplified simulation was created that is easily manipulated to show different scenarios. This simulation does not contain a controller, instead the vehicle velocities are simply set to the desired value (based on the scenario being discussed) and then integrated to get the vehicle positions; essentially ignoring the vehicle dynamics. This allows the guidance algorithm to be analyzed without extraneous influences from the control system and vehicle model. As a baseline, the algorithm is first run without any impediments, this means that the vehicle tracks the desired velocities perfectly. The results are shown in Figure 5.2.

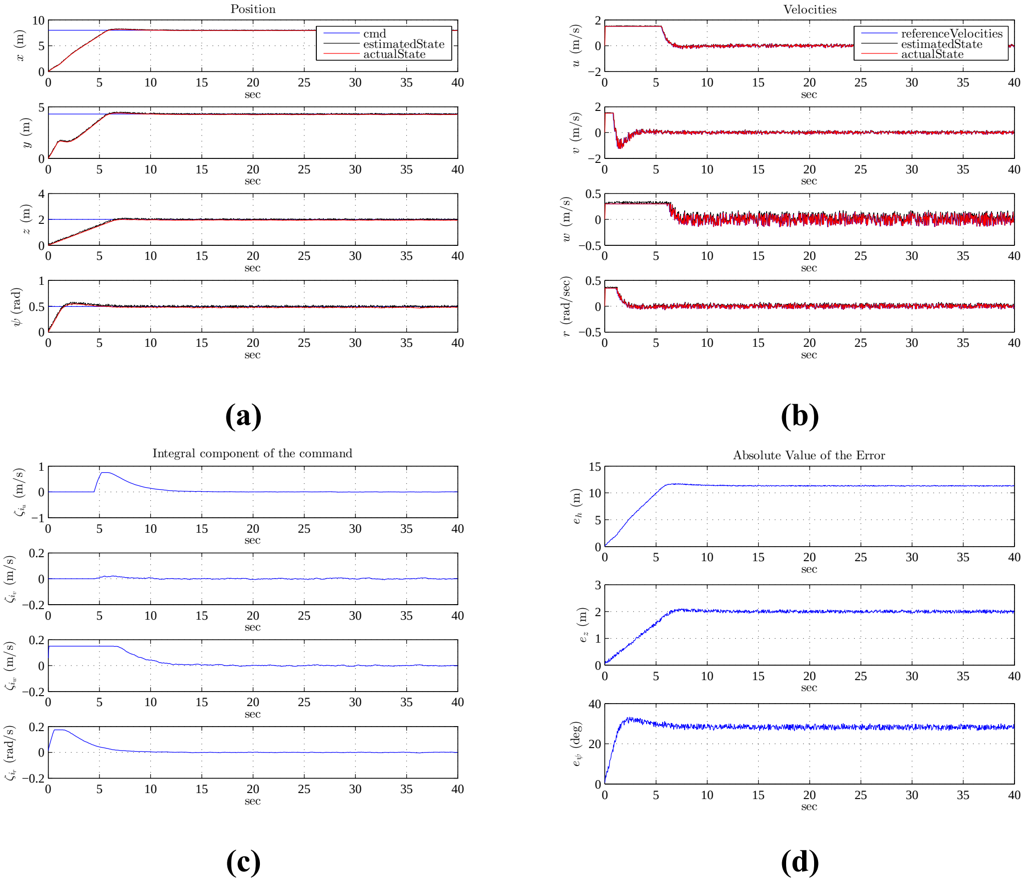

(a) **(b)**

(c) **(d)**

Figure 5.2: Simulation of the guidance algorithm: a) vehicle positions, b) vehicle velocities, c) contribution of the integral component d) position error between the estimated state and the desired trajectory

In Figure 5.2-a, the final destination or command is shown in blue. The estimated plant state and actual plant state are shown in black and red, respectively. In this scenario, the vehicle is commanded to traverse from an initial position of $[0, 0, 0]$, heading of 0.0, and velocities of 0, to a position of $[8.0, 4.3, 2.0]$ with the final heading pointed along the direction of travel. Figure 5.2-b shows the reference velocities from the guidance algorithm in blue, and the estimated and actual plants states in black and red, respectively. In this first scenario, the estimated and actual velocity track the desired velocity perfectly. The vehicle reaches it's velocity limits as it tries to follow the desired trajectory, shown in Figure 5.2-d. In the surge and sway axes the algorithm switches from a P-type to a PI-typle task function after 4.4 seconds once the error function, while the heave and yaw the error is small enough that the PI-type task function is used right from the beginning. The integral component, shown in Figure 5.2-c, increases and reaches it's maximum, set to one half of the velocity limit, on the surge, sway and yaw axes. Once the vehicle reaches the waypoint, the integral component returns to zero, which is what one would expect if there is no bias in the velocity estimate.

In the second scenario, the same starting and termination points are used, but unknown biases are added to the velocity estimates. This could occur, if the measurements from the DVL contained unknown biases. Once again Figure 5.3-a shows the destination, trajectory, position estimate and actual vehicle position. Note that the vehicle still reaches the destination point despite the unknown velocity biases. The biases can be seen in Figure 5.3-b, where the estimated velocity tracks the reference velocity, but the actual velocity is offset by some amount. Once again, the vehicle reaches its velocity limits as it tries to follow the desired trajectory. In this scenario, the integral component, shown in Figure 5.3-c, increases and reaches its maximum as before, but this time once the vehicle reaches the waypoint, the steady state value of the integral is non-zero which compensates for the velocity bias. Without this compensation, the vehicle would not stay at the waypoint as its velocity would

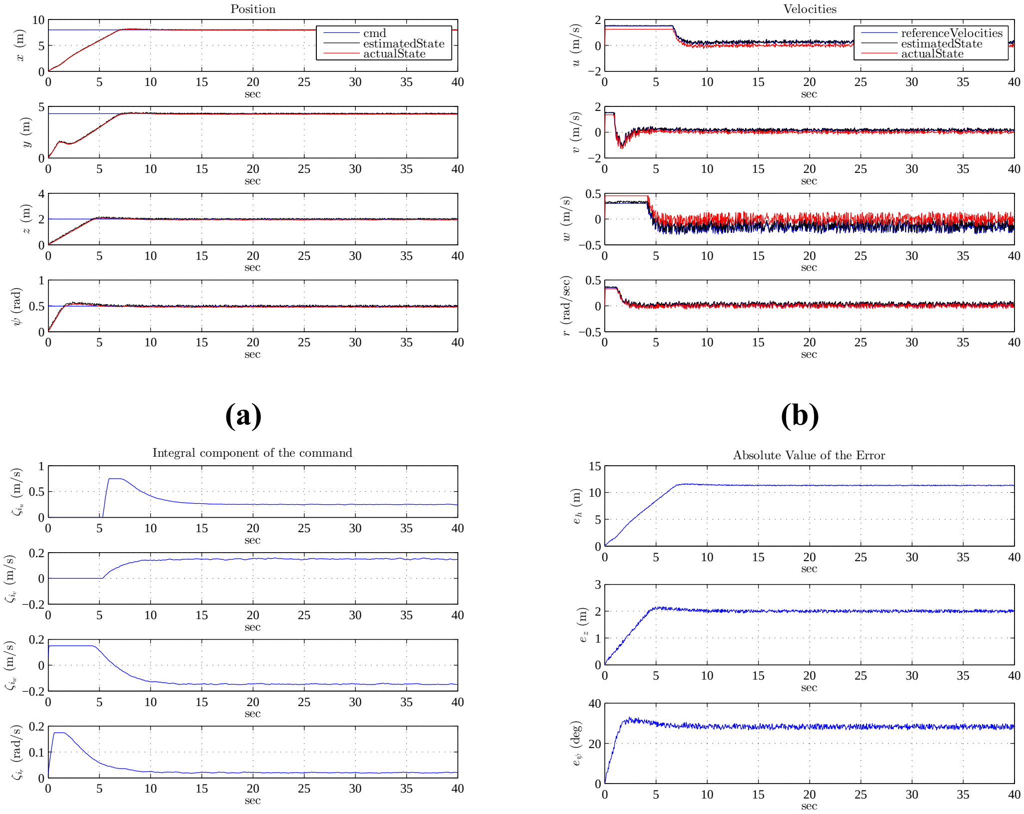

(a) **(b)**

(c) **(d)**

Figure 5.3: Simulation of the guidance algorithm when the estimated velocities have an unmodelled bias: a) vehicle positions, b) vehicle velocities, c) contribution of the integral component d) position error between the estimated state and the desired trajectory

not actually be zero despite the fact that a zero velocity was being commanded. Instead, it would hover in the vicinity of the waypoint, constantly moving in a limit cycle.

In the final scenario, unknown velocity limitations are imposed on the vehicle so that it is unable to achieve the velocities that are requested by the guidance algorithm and significantly lags the desired trajectory, shown in Figure 5.4. This would occur of the thrusters became fouled and the vehicle was suddenly unable to perform to its full capacity. Once again, Figure 5.4-a shows the destination, trajectory, position estimate, and actual vehicle position, and note that the vehicle still reaches the destination point but takes a significantly longer time. Once again, the velocities are seen in Figure 5.4-b. In this scenario, the vehi-

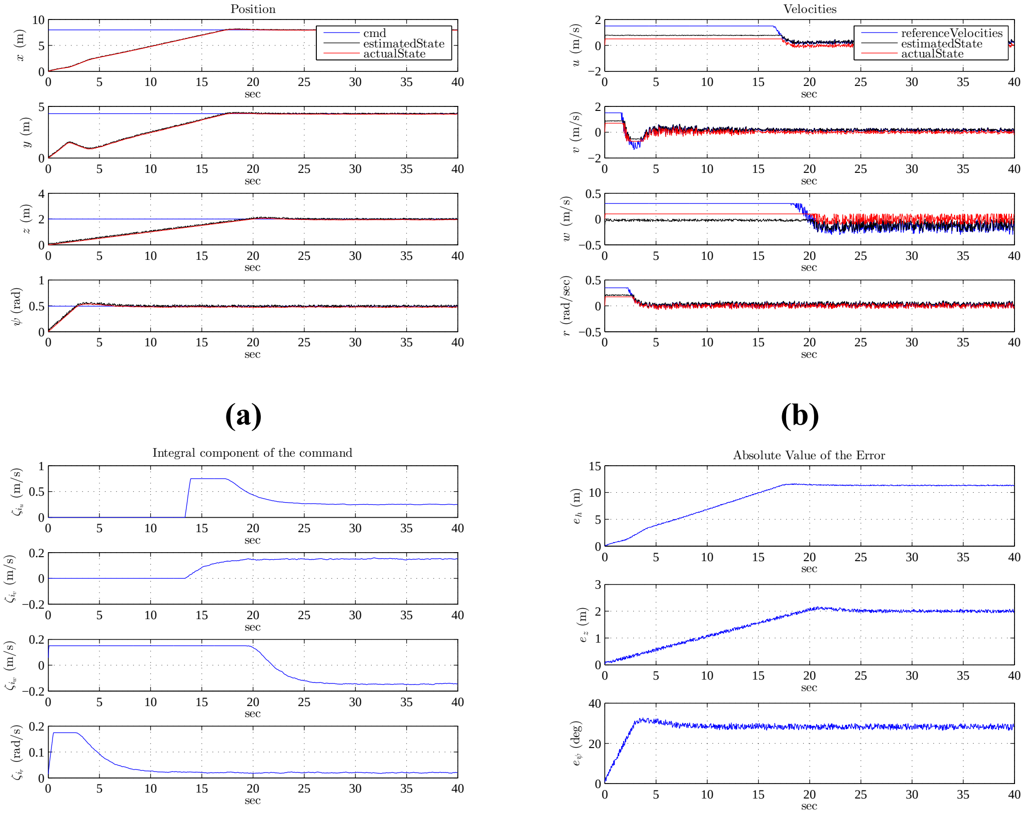

(a) **(b)**

(c) **(d)**

Figure 5.4: Simulation of the guidance algorithm when the estimated velocities have an unmodelled bias and the vehicle velocity is limited such that it can't closely follow the desired trajectory: a) vehicle positions, b) vehicle velocities, c) contribution of the integral component d) position error between the estimated state and the desired trajectory

cle is unable to reach the limiting velocities commanded by the guidance. The estimated velocity varies with the actual velocity but is offset by the bias amount. It is also clear that the vehicle is not able to achieve the desired velocities to track the desired trajectory. Even with imperfect tracking of the desired velocities, the vehicle still reaches the waypoint and remains at it without any oscillatory behavior.

5.4.2 Simulation of Full Vehicle Model

The full vehicle simulation contains: sensor noise, sensor latency, discretization, the vehicle and thruster dynamics as described in Chapter 3, parameter error in the dynamic model (i.e., different system ID parameters for the plant and the navigation system), and environmental disturbances. The simulation runs as follows:

1. The vehicle state is propagated using the dynamic model described in Chapter 3. In this simulation, this is the true state of the vehicle,
2. The measurements including noise, latency and biases are modelled using the state vector produced by the vehicle model,
3. The measurements are used to create an estimate of the vehicle's state using the EKF described in Chapter 4. In experimental studies, this would be the only state information that would be available. This is the state that is used by any subsequent guidance and control algorithms. For this simulation, random modelling error has been added to the plant model so that it differs from the model in the EKF,
4. The estimated state is used as the input to the guidance algorithm. The guidance output is the desired velocities in the BRF,
5. The estimated state and desired velocities are used as the input to the control algorithm. The controller output is a command for each of the 5 thrusters,
6. Return to the first step and propagate the plant forward using the thruster commands from the controller (plus any environmental disturbances).

The simulated results, shown in Figure 5.5, use the adaptive control system that is described in Chapter 6.

Figure 5.5-b shows that the vehicle is unable to track the reference velocities, especially in the sway and yaw motions. This is not an unexpected result; when the vehicle is travelling

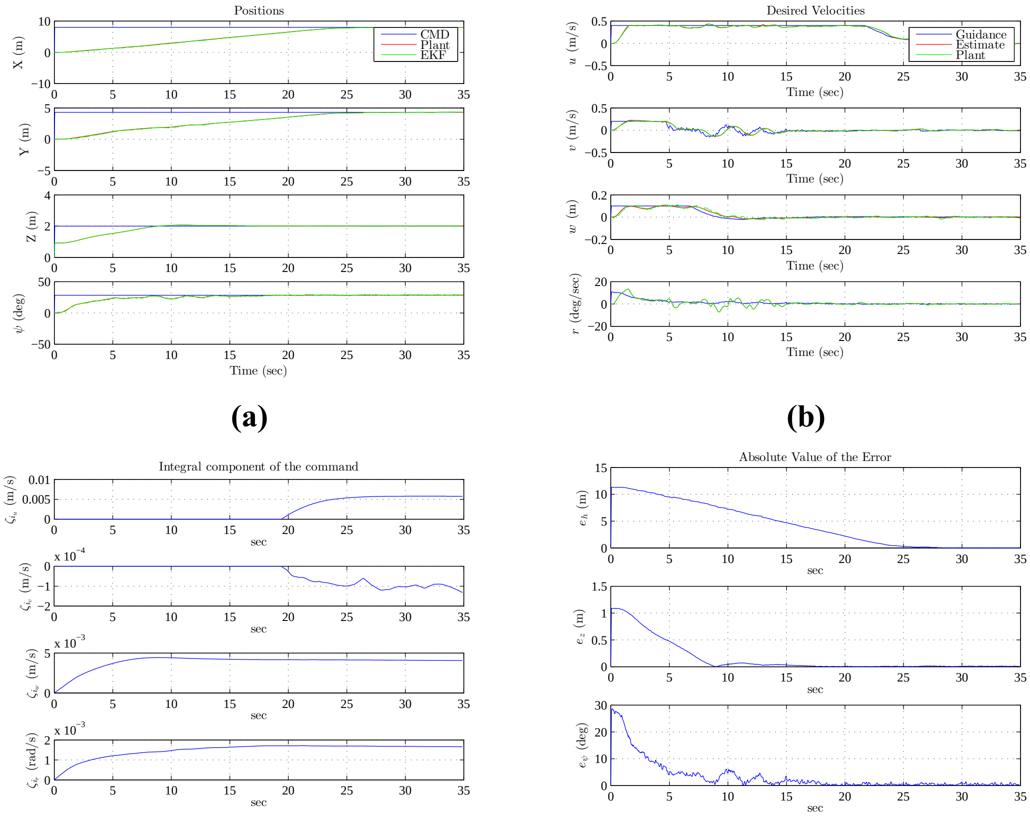

(a) **(b)**

(c) **(d)**

Figure 5.5: Full simulation of the ROV dynamics and the guidance algorithm: a) vehicle positions, b) vehicle velocities, c) contribution of the integral component d) position error between the estimated state and the destination

forward at a high rate of speed and the guidance and control system request more thrust then the thrusters can provide, the command gets truncated by the saturation limit and the vehicle loses the ability to steer. Despite the fact that the vehicle is unable to track the reference velocity at the beginning, it still arrives at the destination, as shown in Figure 5.5-b and Figure 5.5-d. In this simulation, a sinusoidal environmental disturbances are applied to the plant in all 6 DOFs. This means the controller and guidance need to keep working once the vehicle arrives at the destination in order to hold station. Despite the fact that there is noise and uncertainty in the state estimate, there is crisp switching between guidance modes (Figure 5.5-c). This is due to the anti-chattering mechanism presented in Section 5.3.1.

5.5 Modifying the Vehicle Behaviour

Even though the guidance system is stable, it does not always lead to behaviours that are desirable for ROV operations. When the waypoint is far away, the vehicle will be immediately commanded to it's maximum speed, which means a maximum command to the thrusters. In an underwater vehicle this is rarely a desirable behaviour. It will often cause violent pitching or rolling and, when working near the bottom, may disrupt the surrounding sediment and impair visibility. There are many possible solutions to this problem. One solution would be to use a planned trajectory to a waypoint instead of of the waypoint itself. As described previously in Section 5.3, since the guidance algorithm is Lyapunov stable for a path from any starting point to any other attainable state, it will also be stable when presented with a sequence of positions that lead it towards the ultimate waypoint. Further, it will also remain stable if the vehicle deviates from the planned path due to disturbances. In the event of a disturbance, it will simply generate increased desired velocities to attempt to catch up to the place it should be on the desired path. The planned trajectory could include the following special behaviors:

- Lifting off the bottom prior to transiting to a waypoint.
- Rotate to correct heading before transiting.
- Maximum accelerations.
- Maintaining a set altitude during transit.

For this work, the guidance algorithm is left as presented and the distinct behaviours that are desired are created by using multiple waypoints. Using the examples above, the first waypoint in a transit would be to lift off the bottom and hover at a given altitude. The second waypoint, would be to maintain station and rotate to the desired heading, the third waypoint would be the transit and the then fourth waypoint would be to set the ROV down on the bottom. While many of the desired behaviours can be handled this way, limiting the acceleration can not. Instead it will be handled by the local the controller on the vehicle, using a reference model. The reference model will give the vehicle a smooth trajectory between the current and desired velocities that can be tuned to minimize excessive pitching and rolling moments.

5.6 Conclusion

In this chapter, a Lyapunov-based guidance algorithm that runs in real-time, and is stable over the entire operating envelope of the vehicle has been described and implemented. The algorithm was modified to consider the vehicle's velocity limits. An anti-chatter mechanism was implemented to allow the algorithm to switch between a P-Type and PI-Type task function, which helps to mitigate integral wind-up issues. The integral was further managed by limiting it's magnitude. Through simulation, the resulting system was shown to be stable in the face of realistic errors and disturbances, as was predicted by theory.

Chapter 6

Control System

The final component of the system software is the control system. The control system takes the desired velocities from the guidance, the estimated state from the navigation, and determines an appropriate command to the actuators. In general, a control system designer will have to balance performance and robustness to meet the desired design criteria. For this work, the controller has been designed such that the vehicle can perform as a stable work platform, from which a pilot can perform observing and manipulation tasks.

6.1 Performance Criteria and Design Specifications

In order for a controller to effectively make the vehicle into a stable work platform, it must meet the following criteria:

- Be stable in the face of large time varying unmodelled system dynamics and environmental disturbances,
- Be stable over the full performance envelope,
- Be stable with unmodelled thruster deadband,

- provide fine control for station keeping while minimizing limit cycles and excessive thruster fluctuations,
- provide smooth trackable thruster commands.

In this work, the forces and moments from the tether are being considered an environmental disturbance. As was seen in the system identification chapter, when the vehicle is underway pulling the tether through the water can have a significant impact on the steady state velocity of the vehicle. If the tether is not being actively managed by the boat and tether operator, then the tension in the Falcon tether can readily end up at more than 100 N [78]. The hydrodynamic model also contains parameter error. As discussed in Chapter 3, the quadratic drag model is an approximation and will be more accurate in some portions of the performance envelope than others. An effort was made with the system identification to minimize the error across the entire envelope, but it will still likely be less accurate at higher velocities.

One of the goals of this work has been to design a controller that delivers performance and minimizes chattering in the thruster control signal. Given the thruster dynamics shown in Figure 3.3, the thrusters are not capable for following a rapidly changing thruster command. The impact of varying thruster dynamics on control system performance is discussed in [75].

6.2 Background

The vast majority of control papers on underwater vehicles deal with AUV control not ROV control. While both types of vehicle use the same dynamic model, an AUV is typically designed with hydrodynamic characteristics in mind and does not have a tether. As a result the disturbances and parametric uncertainty in an AUV control problem are much smaller. None the less, there is still a substantial body of work on problem of ROV positioning and many different approaches have been employed. In [58], Smallwood and Whitcomb discuss an experimental comparison of a linear proportional-derivative control and a family of fixed and adaptive model-based controllers and H_∞ control schemes are discussed in [38] and [15]. Over the years, sliding mode controllers have been the most common control systems implemented on ROVs [76, 55, 74, 60, 46]. The sliding mode controller is well suited to the ROV problem as it provides a systematic approach to maintaining stability and consistent performance in the face of modelling error [57]. However, the high frequency control action (or chatter) that is often associated with sliding mode controllers has proven to be problematic with this style of controller. The chattering causes losses in electrical power circuits, premature wear in actuators, and can exasperate many of the problems discussed in [75]. This has compelled research into modifications to the traditional sliding mode control that can diminish or eliminate the chattering problem [62].

In this work, a neural network (NN) approach has been chosen; previous work on adaptive control of ROVs using neural networks can be found in [32, 79, 72]. For this work, a single hidden layer NN will be used to approximate the modelling error and augment a simple linear control scheme. The expectation is that this architecture will be as robust to unmodelled dynamics as a sliding mode controller, without the problem of chattering; a similar approach for AUVs was proposed in [44].

6.3 Simulation and Development Environment

To facilitate the testing and development of this control system a full 6 DOF simulation of the vehicle was developed in Matlab. The simulation includes the following:

- Sensor and control system timing,
- Parameter errors,
- Sensor noise,

- Environmental disturbances,
- Discretization of thruster commands,
- Thruster deadband.

In the simulation, the sensor messages are populated discretely at a rate between 2 and 100 Hz depending on the sensor, and the guidance, navigation and control algorithms are run sequentially at 20 Hz. The plant is propagated at 100Hz, using a linear 2-step Adams-Bashford integration method where:

$$x_{k+1} = x_k + (1.5\dot{x}_k - 0.5\dot{x}_{k-1})\Delta T \tag{6.1}$$

This method is substantially more stable than the first order Euler method, but doesn't require the additional computation time required for more advanced algorithms like Runge-Kutta. Runge-Kutta integration methods are most useful on systems with both fast and slow dynamics, which can be distorted and cause instability in first order integration methods. The situation is not applicable to ROV dynamics so the 2-step method above is sufficient.

The output of the sensors are determined using the sensor models from Chapter 4 and white Gaussian noise with the specified standard deviation is added. Modelling errors are also simulated. The controller and EKF use the system model developed in Chapter 3, and the plant is propagated using a model with coefficients that have been randomly changed by up to 20%. The thruster model in the simulation includes, limits, discretization, a randomly generated deadband, and environmental disturbances.

6.4 PID Control with a Reference Model

The first control system has the structure outlined in Figure 6.1. The hardware is shown in green, the control system is shown in blue and the software modules discussed in previous

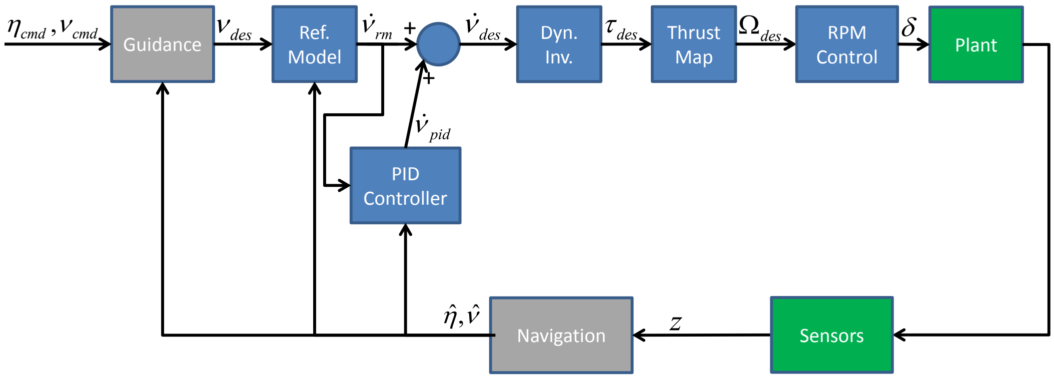

Figure 6.1: Diagram of the PID controller presented in this chapter. All of the software modules shown run on the ROV, with only the command signal (a waypoint) being generated by the pilot.

chapters are shown in grey. All of the software shown in this diagram runs onboard the vehicle on the SSC. The only input coming from the pilot is the desired waypoint. The output of the guidance is first filtered by a reference model which generates desired accelerations based on the input from the guidance command. The reference model addresses the issue of commanding excessively rapid accelerations, described in the conclusion of Chapter 5. A PID controller is used to make the ROV follow the reference model. The desired accelerations, $\dot{\boldsymbol{\nu}}_{des}$, are the sum of the reference model and the PID controller.

$$\dot{\boldsymbol{\nu}}_{des} = \boldsymbol{\nu}_{crm} + \boldsymbol{\nu}_{pid} \tag{6.2}$$

An approximate dynamic inversion is use to turn the desired accelerations into desired forces and moments in the BRF, $\boldsymbol{\tau}_{des}$. These desired forces are then mapped to the thrusters and turned into desired propeller speeds, $\boldsymbol{\Omega}_{des}$. The command vector, $\boldsymbol{\delta}$, is then obtained using one of two methods: an algebraic open loop scheme, or closed-loop control.

6.4.1 Reference Model

The reference model provides a means of specifying the input output dynamics of the system. For this work, four decoupled first order subsystems are used:

$$\dot{\boldsymbol{\nu}}_{crm} = \mathbf{K}_{p_{rm}} \left(\boldsymbol{\nu}_{des} - \boldsymbol{\nu}_{rm} \right) \tag{6.3}$$

where $\dot{\boldsymbol{\nu}}_{crm}$ is the reference model command and $\mathbf{K}_{p_{rm}}$ is a diagonal gain matrix of proportional gains. In this particular control scheme, the dynamics of the reference model are defined simply as:

$$\dot{\boldsymbol{\nu}}_{rm} = \dot{\boldsymbol{\nu}}_{crm} \tag{6.4}$$

The gain for each axis is chosen such that the requested dynamics are trackable by the vehicle. When using the thrust mapping described in Section 6.4.4, it is important to realize that when a large amounts of forward thrust are being commanded from the horizontal thrusters the vehicle has limited residual power for manoeuvering in the yaw and sway directions. As a result, when the thrusters become saturated the heading control is compromised. This issue can be mitigated through the choice of velocity limits in the guidance, $\boldsymbol{\zeta}_{MAX}$, and $\mathbf{K}_{p_{rm}}$. The velocity limits were chosen such that the vehicle can achieve a maximum velocity on all axis at the same time. Then the reference model was designed such that, given a simultaneous step input of the maximum velocities on all axes, only minimal saturation occurs on the thrusters.

6.4.2 PID Component

The PID component is a controller that drives the vehicle to follow the reference model.

$$\dot{\boldsymbol{\nu}}_{pid} = \mathbf{K}_p \mathbf{e} + \mathbf{K}_d \dot{\mathbf{e}} + \mathbf{K}_i \int \mathbf{e} \cdot dt \tag{6.5}$$

where $\mathbf{e} = \boldsymbol{\nu}_{rm} - \hat{\boldsymbol{\nu}}$, and $\mathbf{K}_p$, $\mathbf{K}_d$, and $\mathbf{K}_i$ are diagonal gain matrices. To guarantee that the vehicle tracks the reference model $\mathbf{K}_p$ should be the same for the PID controller and the reference model.

6.4.3 Approximate Dynamic Inversion

Once $\dot{\boldsymbol{\nu}}_{des}$ has been determined, an approximate dynamic inversion can be used to estimate the forces and moments that will be needed to achieve the desired accelerations. From Chapter 3, the vehicle dynamics are given by Eq. 3.9. The inverse of this equation is simply:

$$\boldsymbol{\tau}_{des} = \mathbf{M}\dot{\boldsymbol{\nu}}_{des} + \mathbf{C}\left(\boldsymbol{\nu}\right)\boldsymbol{\nu} + \mathbf{D}\left(\boldsymbol{\nu}\right)\boldsymbol{\nu} + \mathbf{G}\left(\eta\right) \tag{6.6}$$

where $\boldsymbol{\tau}_{des}$ is the estimate of the forces and moments necessary to achieve $\dot{\boldsymbol{\nu}}_{des}$.

6.4.4 Thrust Mapping

Thrust Allocation

Each of the thrusters will impart a force and moment on the CG of the vehicle as described in Eq. 3.23; to determine the thrust required to achieve $\boldsymbol{\tau}_{des}$ this equation must be inverted. Since **B** is not a square matrix, it is not invertible in the traditional sense. This is a common issue in robotics problems, and the generally accepted solution is to use a Moore-Penrose pseudoinverse (called a pseudoinverse from here forward) [59, 48, 21]. The formulation for the pseudoinverse is based on work by E. H. Moore in 1920 and R. Penrose in 1955-56; a comprehensive review of theory behind the pseudoinverse is given in [4]. In short, the pseudoinverse, $A^{\dagger}$, must satisfy the following four criteria:

$$\mathbf{A}\mathbf{A}^{\dagger}\mathbf{A} = \mathbf{A} \quad \mathbf{A}^{\dagger}\mathbf{A}\mathbf{A}^{\dagger} = \mathbf{A}^{\dagger} \quad \left(\mathbf{A}\mathbf{A}^{\dagger}\right)^{*} = \mathbf{A}\mathbf{A}^{\dagger} \quad \left(\mathbf{A}^{\dagger}\mathbf{A}\right)^{*} = \mathbf{A}^{\dagger}\mathbf{A} \tag{6.7}$$

In order for a pseudoinverse to exist, $\mathbf{A}$ must have maximum rank (i.e. $rank\mathbf{A} = min(m, n)$). The pseudoinverse has a different formulation depending on whether $m \geq n$ (the left pseudoinverse) or $m \leq n$ (the right pseudoinverse). If the columns of the matrix $\mathbf{A}$ are linearly independent ($m \geq n$) then $\mathbf{A}^*\mathbf{A}$ will be invertible[1]. In this case, there is at most one solution to the problem, $\mathbf{y} = \mathbf{Ax}$ and the pseudoinverse is chosen to minimize the 2-norm of the vector $\|\mathbf{y} - \mathbf{Ax}'\|$. Hence, in a Euclidean sense, $\mathbf{x}'$ would be the best approximation for $\mathbf{x}$. One can readily derive the left pseudoinverse as follows:

$$\begin{aligned} \mathbf{y} &= \mathbf{Ax} \\ \mathbf{A}^*\mathbf{y} &= \mathbf{A}^*\mathbf{Ax} \\ (\mathbf{A}^*\mathbf{A})^{-1}\mathbf{A}^*\mathbf{y} &= \mathbf{x} \\ \mathbf{A}^\dagger\mathbf{y} &= \mathbf{x} \end{aligned} \tag{6.8}$$

If the rows of the matrix are linearly independent ($m \leq n$) then $\mathbf{AA}^*$ will be invertible[2]. In this case, there are an infinite number of vectors $\mathbf{x}$ that solve the equation $\mathbf{y} = \mathbf{Ax}$, as part of $\mathbf{x}$ will be mapped to the nullspace of $\mathbf{A}$. In this instance, the pseudoinverse sets the null space component to zero, thereby minimizing the Euclidean length of $\mathbf{x}$. In robotics, this is a means of determining a minimum effort solution. To derive the right pseudoinverse, first note that since $\mathbf{AA}^*$ is invertible then $\mathbf{AA}^*(\mathbf{AA}^*)^{-1} = \mathbf{I}$.

$$\begin{aligned} \mathbf{y} &= \mathbf{Ax} \\ \mathbf{AA}^*(\mathbf{AA}^*)^{-1}\mathbf{y} &= \mathbf{Ax} \\ \mathbf{A}^*(\mathbf{AA}^*)^{-1}\mathbf{y} &= \mathbf{x} \\ \mathbf{A}^\dagger\mathbf{y} &= \mathbf{x} \end{aligned} \tag{6.9}$$

---

[1] The left pseudoinverse would be used for an under-actuated system.

[2] The right pseudoinverse would be used for an over-actuated system.

In [4], Barata and Hussein provide proofs that the left and right pseudoinverse as shown above exist and satisfy the criteria in Eq. 6.7.

The Falcon ROV is both an under, and over, actuated system. There are 5 thrusters arranged in such a way that 4 of the 6 DOFs are controllable, which means that overall the system is under-actuated. The vertical thruster controls heave motion and the 4 horizontal thrusters control the surge, sway and yaw motion. Therefore, in the horizontal plane the system is over-actuated, since we have 4 thrusters controlling 3 DOFs.

Setting the desired pitch and roll moment to zero (since those DOFs are uncontrollable), one can split the actuator mapping into an over-actuated horizontal problem and a scalar vertical problem. Therefore, the force required from the vertical thruster is given as:

$$T_5 = -\tau_{des_z} \tag{6.10}$$

where τ_{des_z} is the z component of the desired forces and the negative sign comes from the direction of the 5th thruster as shown in Table 3.1. The forces required from the horizontal thrusters are determined by:

$$\mathbf{T}_H = \mathbf{B}_H^{\dagger} \boldsymbol{\tau}_{des_H} \tag{6.11}$$

where $\mathbf{T}_H$ is the thrust vector for thrusters 1 through 4, $\boldsymbol{\tau}_{des_H} = [\tau_{des_x} \;\; \tau_{des_y} \;\; \tau_{des_\psi}]^T$, and $\mathbf{B}_H^{\dagger}$ is the right pseudoinverse of the horizontal input matrix, $\mathbf{B}_H$, which is formulated by eliminating the 3rd, 4th, and 5th rows and 5th column from **B**.

Determining the Desired Thruster Speed

Once the desired thrust from each thruster is known, then the an approximation for the desired propeller speed, Ω, can be found by inverting (3.1) and (3.4) from Chapter 3. Recall that for this work, it is assumed that J_0 is always positive and this is enforced by taking the absolute value; therefore, the force as a function of Ω is:

$$\begin{aligned} T &= K_T \rho D^4 \left|\Omega\right| \Omega \qquad (6.12) \\ &= \left(\alpha \left|J_0\right|^2 + \beta \left|J_0\right| + \gamma\right) \rho D^4 \left|\Omega\right| \Omega \\ &= \left(\alpha \left(\frac{\left|V_a\right|}{\left|\Omega\right| D}\right)^2 + \beta \left(\frac{\left|V_a\right|}{\left|\Omega\right| D}\right) + \gamma\right) \rho D^4 \left|\Omega\right| \Omega \\ &= \alpha \left(\left|V_a\right|^2 D^2 \rho\right) sign\left(\Omega\right) + \beta \left(\left|V_a\right| D^3 \rho\right) \Omega + \gamma \left(\rho D^4\right) sign(\Omega)\Omega^2 \end{aligned}$$

which can be rewritten as:

$$0 = \alpha_1 - T + \beta_1 \Omega + \gamma_1 \Omega^2 \qquad (6.13)$$

Hence, given the coefficients for K_T that were presented in Eq. 3.25 and V_a as described in Eq. 3.27, Ω_{des} can be found using the quadratic formula. A positive and negative root will be obtained, the one with the correct sign for the direction of the desired thrust is the correct root.

6.4.5 Propeller Speed Control

The simplest way to obtain the command, δ, required to obtain Ω_{des} is to invert the equations for Ω as a function of δ that given in Eq. 3.24. Since Eq. 3.24 is a piecewise quadratic equation, it is simple to invert. This is the method that is used in this controller.

While easy to implement, this method does have a draw back. Tthe equations in Eq. 3.24 are only an empirical approximation based on the propeller speed at $V_a = 0$. As was seen in Figure 3.4, the estimate gets substantially less accurate at higher advance speeds. This means that the error between the propeller speed that is realized for a given command and Ω_{des} will increase when the vehicle is underway. Since the Falcon provides feedback on the speed of the propeller, an alternate way to obtain the desired propeller speed would be to implement a low level controller that uses the feedback to determine the correct command. The disadvantage to this, is that one adds a level of unpredictability in the thruster dynamics which could contribute to unmodelled error in the vehicle dynamics. A low-level controller is currently being developed by the OTL in [7] and will ultimately be tested as part of this control scheme.

6.4.6 Control Signal Smoothing

Noise in the velocity estimate, that comes from the EKF, propagates through the guidance and PID control algorithms to the control signal. If the velocity estimate is sufficiently noisy (as can happen at higher speeds) then this can result in a noisy control signal, which was one of the performance criteria for this control system. Filtering the velocity estimates before they are used in the guidance and control algorithm can have unpredictable results, a better method is to filter the control command, δ.

To achieve the desired smoothness, the following low pass filter was applied to the output of the controller:

$$\delta_{f_k} = \delta_{f_{k-1}} + K_{TH}(\delta - \delta_{f_{k-1}})\Delta T; \tag{6.14}$$

where δ_f is the filtered control command, ΔT is the length of the time step, and K_{TH} is the control gain. In the PID controller, excessive filtering can cause oscillatory behavior in the response as it will introduce latency into the signal. A control gain of 4 was determined to be sufficiently fast to avoid any detrimental effects while still achieving the desired amount of control smoothing.

Table 6.1: Guidance and Control Parameters

Description	Variable	x	y	z	ψ
Guidance Parameters					
Proportional Gain	K_p	0.375	0.375	0.375	0.375
Integral Gain	K_i	0.001	0.001	0.001	0.001
Velocity/Rate Limit	ζ_{MAX}	0.4 m/s	0.2 m/s	0.1 m/s	0.2 rad/s
Integral Limit	$\zeta_{I_{MAX}}$	0.3 m/s	0.15 m/s	0.075 m/s	0.15 rad/s
Upper Switching Threshold	T_U	3 m	3 m	3 m	0.52 rad
Lower Switching Threshold	T_L	2 m	2 m	2 m	0.35 rad
PID Controller Parameters					
Ref Model Proportional Gain	$K_{p_{rm}}$	3.75	3.75	1.25	5
Proportional Gain	K_p	3.75	3.75	1.25	5
Integral Gain	K_i	3.51	3.51	0.39	6.25
Derivative Gain	K_d	0.0	0.0	0.0	0.0
Control Filter Gain	K_{TH}	4.0	4.0	4.0	4.0

6.4.7 Simulation Results for PID Controller

The simulation was set up with the guidance and control parameters shown in Table 6.1. As was previously mentioned, the simulation results contain environmental disturbances, sensor noise, latency, discrete timing, model parameter errors, and thruster deadband. In the simulation, the vehicle is assumed to be at rest at the origin of the NRF and is commanded to go to a waypoint at $\boldsymbol{\chi} = [7.0 \;\; -2.0 \;\; 2.0 \;\; 0.2]^T$, which is expressed in metres for the three translational states and radians for ψ. The results of the simulation are shown in Figure 6.2.

Using the PID controller just described, the vehicle reaches the desired waypoint in approximately 20 seconds (Figure 6.2-a) and is able to maintain station despite continuously applied oscillatory disturbances and parameter errors. It does not track the desired velocities very well (Figure 6.2-b), but the guidance algorithm was still able to provide a trajectory to the waypoint. The guidance and PID integrals, shown in Figure 6.2-c, are both smooth and well behaved. The integral on the PID controller is not constrained by the same measures as the guidance integral. This means that in the event of actuator saturation, integral wind-up could be a problem. This issue was not pursued as it is handled inherently with the more advanced adaptive controller. The control signals are shown in Figure 6.2-d. These signals

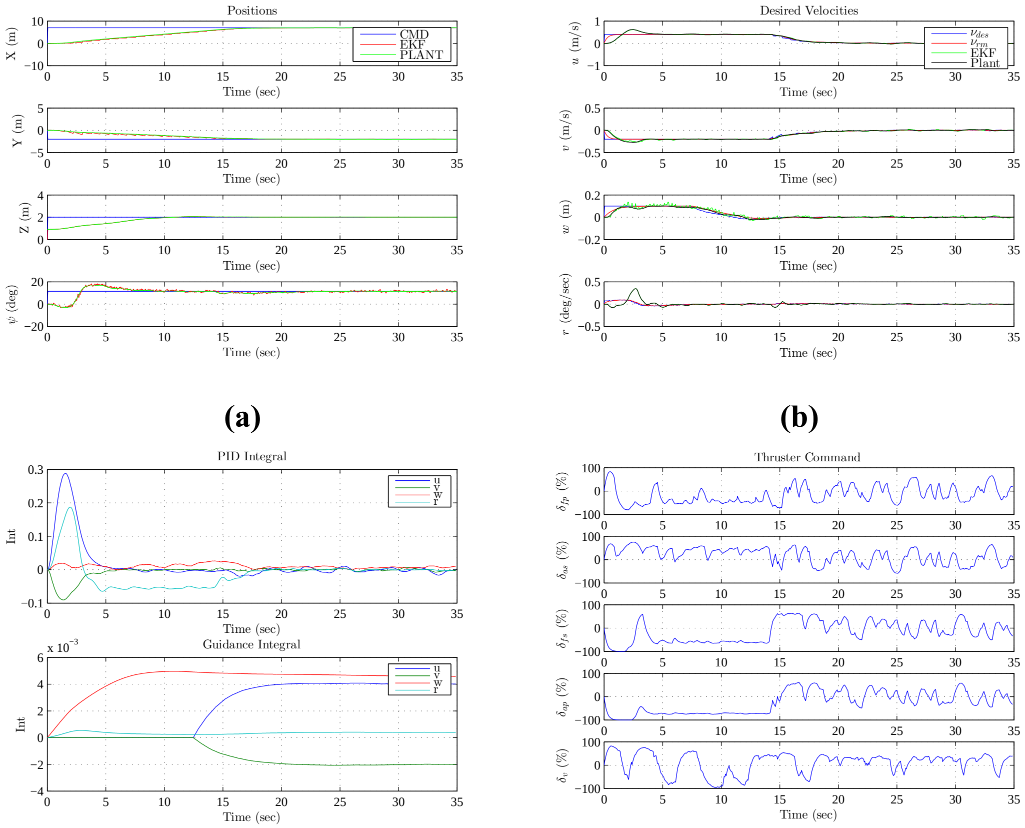

(a) **(b)**

(c) **(d)**

Figure 6.2: Full simulation of the ROV dynamics with PID control system: a) positions, b) velocities, c) contribution of the integral component d) control effort from each thruster (%)

are smooth and trackable by the thrusters. The vertical, aft-port and front-stbd thrusters do saturate for a short period of time, but not for a sustained period. Overall this controller meets the performance objectives, but doesn't track the desired velocities very well and experimental trials have shown it to be sensitive to errors in the model parameters, which result in errors in the inversion.

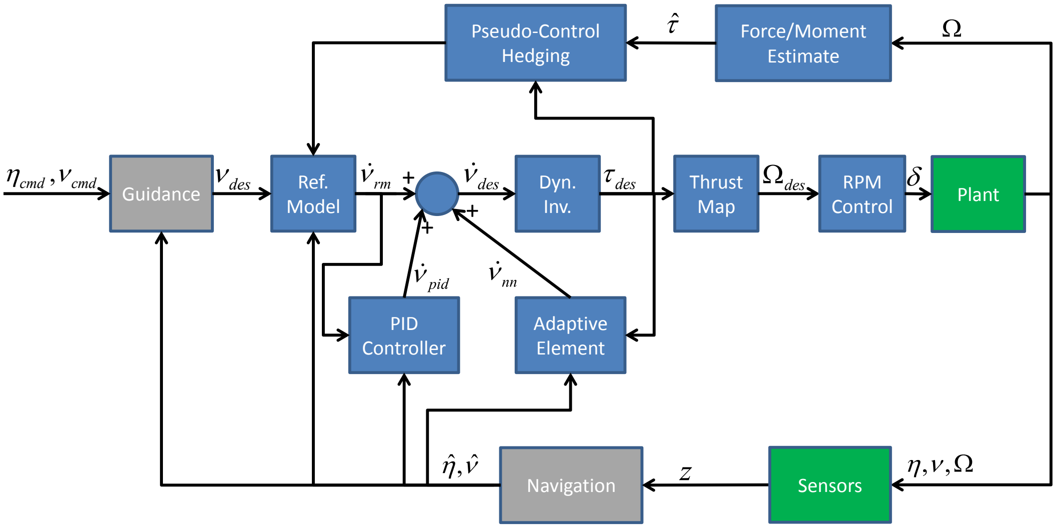

Figure 6.3: Diagram of the adaptive controller presented in this chapter.

6.5 Adaptive Control

The adaptive control system implemented here has the structure outlined in Figure 6.3. It is the same as the baseline controller with the addition of two elements, an adaptive element to compensate for errors in the approximate dynamic inversion and pseudo-control hedging, a method first proposed by Johnson in [35]. This control architecture, dubbed model reference adaptive control (MRAC) in previous work, has been used successfully to control autonomous helicopters [34, 39, 52, 50, 51, 16] and is well suited to handle the level of unmodelled dynamics present with an ROV. The adaptive element will be integrated by modifying the desired acceleration as follows:

$$\dot{\boldsymbol{\nu}}_{des} = \dot{\boldsymbol{\nu}}_{crm} + \dot{\boldsymbol{\nu}}_{pid} - \dot{\boldsymbol{\nu}}_{nn} \tag{6.15}$$

where $\dot{\boldsymbol{\nu}}_{nn}$ is the adaptive contribution. The input to the neural network is restricted to the set of controllable DOFs. From the point forward, $\boldsymbol{\nu}$ can assumed to be the truncated velocity vector $[u \;\; v \;\; w \;\; \psi]^T$.

6.5.1 Pseudo-Control Hedging

Pseudo-Control Hedging (PCH) was proposed by Johnson in [35] as a method for stopping an adaptive element from adapting to select input characteristics of the plant. Specifically, he was interested in preventing a neural network from adapting to actuator saturation and rate limits. Johnson referred to the equivalent of $\dot{\boldsymbol{\nu}}_{des}$ as the "pseudo-control". In a model reference control system, the PCH concept can be described as follows:

> The reference model is moved in the opposite direction (hedged) by an estimate of the amount the plant did not move due to system characteristics the control designer does not want the adaptive control element to see [35].

This same methodology can be applied here to compensate for unmodelled thruster dynamics. The following thruster characteristics would have an adverse effect on the adaptation:

- saturation limits for the control,
- inertial dynamics that differ significantly between a positive (powered) and negative (unpowered) step, as shown in Figure 3.3,
- variations in the mapping between the command and propeller speed that is dependant on the advance speed, Figure 3.4.

For a given $\dot{\boldsymbol{\nu}}_{des}$, the approximate dynamic inversion of the vehicle dynamics, that was previously described, will produce a set of desired forces and moments, $\boldsymbol{\tau}_{des}$, such that:

$$\dot{\boldsymbol{\nu}}_{des} = \hat{\mathbf{f}}\left(\hat{\boldsymbol{\eta}}, \hat{\boldsymbol{\nu}}, \boldsymbol{\tau}_{des}\right) \tag{6.16}$$

where **f** is the dynamic model described in Chapter 3. Since the propeller speeds are being measured, an estimate of the achieved pseudo-control can be obtained and the PCH signal can be calculated as follows:

$$\begin{aligned} \dot{\boldsymbol{\nu}}_{pch} &= \hat{\mathbf{f}}(\hat{\boldsymbol{\eta}}, \hat{\boldsymbol{\nu}}, \boldsymbol{\tau}_{des}) - \hat{\mathbf{f}}(\hat{\boldsymbol{\eta}}, \hat{\boldsymbol{\nu}}, \hat{\boldsymbol{\tau}}) \\ &= \dot{\boldsymbol{\nu}}_{des} - \hat{\mathbf{f}}(\hat{\boldsymbol{\eta}}, \hat{\boldsymbol{\nu}}, \hat{\boldsymbol{\tau}}) \end{aligned} \tag{6.17}$$

where $\hat{\boldsymbol{\tau}}$ is the estimate of what the plant really did given the measured propeller speed. The hedged reference model dynamics are then:

$$\dot{\boldsymbol{\nu}}_{rm} = \dot{\boldsymbol{\nu}}_{crm} - \dot{\boldsymbol{\nu}}_{pch} \tag{6.18}$$

6.5.2 Tracking Dynamics

Define the velocity tracking error as $\mathbf{e_t}$:

$$\mathbf{e}_t = \begin{bmatrix} \mathbf{e}_{t_1} \\ \mathbf{e}_{t_2} \end{bmatrix} = \begin{bmatrix} \int \boldsymbol{\nu}_{rm} - \boldsymbol{\nu} dt \\ \boldsymbol{\nu}_{rm} - \boldsymbol{\nu} \end{bmatrix} \tag{6.19}$$

then a PI compensator for the reference model tracking error would be

$$\dot{\boldsymbol{\nu}}_{pid} = \begin{bmatrix} \mathbf{K}_i & \mathbf{0}^{4\times4} \\ \mathbf{0}^{4\times4} & \mathbf{K}_p \end{bmatrix} \mathbf{e} \tag{6.20}$$

where $\mathbf{K}_p$ and $\mathbf{K}_i$ are diagonal proportional and integral gain matrices.

Differentiating $\mathbf{e}_t$, the dynamics of the tracking error can be found as:

$$\begin{aligned}
\dot{\mathbf{e}}_{t_2} &= \dot{\boldsymbol{\nu}}_{rm} - \dot{\boldsymbol{\nu}} \qquad (6.21)\\
&= \dot{\boldsymbol{\nu}}_{crm} - \dot{\boldsymbol{\nu}}_{pch} - \dot{\boldsymbol{\nu}}\\
&= \dot{\boldsymbol{\nu}}_{crm} - \dot{\boldsymbol{\nu}}_{des} + \hat{\mathbf{f}}\left(\hat{\boldsymbol{\eta}}, \hat{\boldsymbol{\nu}}, \hat{\boldsymbol{\tau}}\right) - \mathbf{f}\left(\boldsymbol{\eta}, \boldsymbol{\nu}, \boldsymbol{\tau}\right)\\
&= -\dot{\boldsymbol{\nu}}_{pid} + \dot{\boldsymbol{\nu}}_{nn} - \Delta\mathbf{f}\left(\hat{\boldsymbol{\eta}}, \hat{\boldsymbol{\nu}}, \hat{\boldsymbol{\tau}}, \boldsymbol{\eta}, \boldsymbol{\nu}, \boldsymbol{\tau}\right)\\
&= -\dot{\boldsymbol{\nu}}_{pid} + \dot{\boldsymbol{\nu}}_{nn} - \Delta\mathbf{f}_{nn}\left(\hat{\boldsymbol{\eta}}, \hat{\boldsymbol{\nu}}, \hat{\boldsymbol{\tau}}, \boldsymbol{\eta}, \boldsymbol{\nu}, \boldsymbol{\tau}\right) - \boldsymbol{\epsilon}\left(\hat{\boldsymbol{\eta}}, \hat{\boldsymbol{\nu}}, \hat{\boldsymbol{\tau}}, \boldsymbol{\eta}, \boldsymbol{\nu}, \boldsymbol{\tau}\right)
\end{aligned}$$

where $\Delta\mathbf{f}$ is the part of the unmodelled dynamics that can be cancelled by the neural network and $\boldsymbol{\epsilon}$ is the part that the neural network can't correct for, which is primarily unmodelled thruster dynamics. The overall tracking dynamics can then be expressed as:

$$\begin{aligned}
\dot{\mathbf{e}}_t &= \mathbf{Ae} + \mathbf{Bu} \qquad (6.22)\\
&= \begin{bmatrix} \mathbf{0}^{4\times4} & \mathbf{I}^{4\times4} \\ -\mathbf{K_i} & -\mathbf{K_p} \end{bmatrix} \mathbf{e} + \begin{bmatrix} \mathbf{0}^{4\times4} \\ \mathbf{I}^{4\times4} \end{bmatrix} \left(\dot{\boldsymbol{\nu}}_{nn} - \Delta\mathbf{f}_{nn} - \boldsymbol{\epsilon}\right) \qquad (6.23)
\end{aligned}$$

6.5.3 Adaptive Element

It has been proven by Hornik, Stinchcombe, and White in [28] that "standard multilayer feedforward networks are capable of approximating any measurable function to any desired degree of accuracy", and that "these “mapping” networks can be considered to be universal approximators". Single hidden layer neural networks have been successfully used to approximate unmodelled dynamics in vehicle control applications [30, 52, 50, 39, 35]. The network architecture proposed here uses state feedback to train a single hidden layer perceptron neural network (NN) online to approximate the modelling error in $\Delta\mathbf{f}_{nn}$ and produce a control contribution, $\dot{\boldsymbol{\nu}}_{nn}$ that cancels the modelling error. It is based on the control system described by Johnson in [35], which uses NN that is based on the control system developed

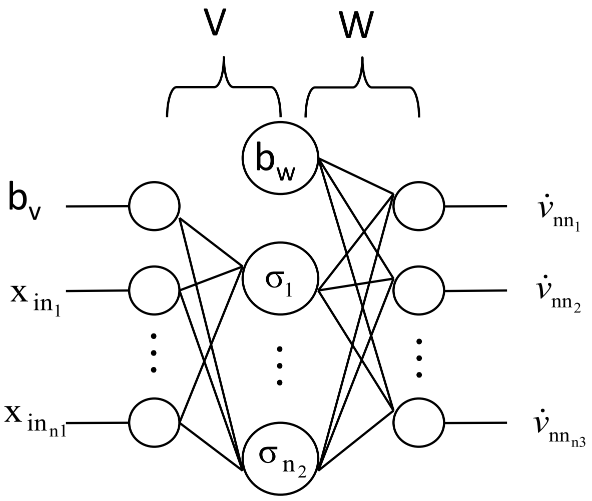

Figure 6.4: Neural Network with a Single Hidden Layer.

by Yeşildirek and Lewis in [73].

The structure of the NN is shown in Figure 6.4. The input vector, $\bar{\mathbf{x}}$, is comprised of of the velocity estimates, $\hat{\boldsymbol{\nu}}$, and the desired forces and moments, $\boldsymbol{\tau}_{des}$. Since the desired forces and moments are a function of the complete command in the current time step, which is a function of the output of the NN, there is an algebraic loop. Using $\dot{\boldsymbol{\nu}}_{des}$ from the last time step has been found to be adequate to address this [51].

An input bias, b_v, is added to the beginning of the input vector to allow thresholds, Θ_v, to be included in the weight matrix V. Similarly, the value of the first hidden layer neuron is defined as a strictly positive constant b_w to allow for thresholds, Θ_w, to be included in the weight matrix $\mathbf{W}$; for this work b_v and b_w are set to 0.5. Assuming there are n_1 input variables, and $n_2 + 1$ hidden layer neurons, then the weight matrix $\mathbf{V}$ is a $(n_1 + 1) \times n_2$

matrix that maps the input vector, $\bar{\mathbf{x}}$, to the input for the hidden layer neurons.

$$\mathbf{V} = \begin{bmatrix} \Theta_{v_1} & \dots & \Theta_{v_{n_2}} \\ v_{1,1} & \dots & v_{1,n_2} \\ \vdots & \ddots & \vdots \\ v_{n_1,1} & \dots & v_{n_1,n_2} \end{bmatrix} \tag{6.24}$$

The weight matrix **W** then maps the output of the activation function to the output of the NN, where **W** is defined as a $(n_2 + 1) \times n_3$ matrix.

$$\mathbf{W} = \begin{bmatrix} \Theta_{w_1} & \dots & \Theta_{w_{n_3}} \\ w_{1,1} & \dots & w_{1,n_2} \\ \vdots & \ddots & \vdots \\ w_{n_2,1} & \dots & w_{n_2,n_3} \end{bmatrix} \tag{6.25}$$

The input to the hidden layer neurons is defined as $\mathbf{z} = \mathbf{V}^T\bar{\mathbf{x}}$ and the input-output map for the hidden layer is a sigmoidal activation function.

$$\sigma(z_i) = \frac{1}{1 + e^{-a_i z_i}} \tag{6.26}$$

where the variable a_i is the activation potential of the neuron. The activation potentials are distinct for each of the hidden layer neurons. For this work, 5 hidden layer neurons are used and the activation potentials are $[0.2 \quad 0.4 \quad 0.6 \quad 0.8 \quad 1.0]$. Combining the output of the activation function and b_w yields a vector $\boldsymbol{\sigma}(z) = [b_w, \sigma_{z_1}, \dots, \sigma_{z_{n_2}}]^T$. Then, the output vector of the NN is simply:

$$\dot{\boldsymbol{\nu}}_{nn} = \mathbf{W}^T\boldsymbol{\sigma}(z) \tag{6.27}$$

The update dynamics for the network weight matrices **V** and **W** use a learning law based on a filtered error signal. The learning law controls the rate of adaptation and allows the

NN to track the modelling error. Defining the filtered error as:

$$\begin{aligned} \bar{\mathbf{r}}(\mathbf{e}) &= (\mathbf{e}^T\mathbf{P}\mathbf{B})^T && (6.28)\\ &= \mathbf{e}^T\begin{bmatrix} \frac{1}{2}(\mathbf{K}_i\mathbf{K}_p) \\ \mathbf{K}_i \end{bmatrix}\left[\frac{1}{0.25n_2+b_w^2}\right] && (6.29)\end{aligned}$$

P is a solution to the Lyapunov equation $\mathbf{A}^T\mathbf{P}+\mathbf{P}\mathbf{A}+\mathbf{Q}=\mathbf{0}$, where **A** comes from the tracking dynamics presented in Eq. 6.22 [39]. Since **A** is Hurwitz, the existence of a unique **P** is guaranteed for any positive definite choice of **Q**. $\mathbf{K}_p$ and $\mathbf{K}_i$ are diagonal matrices containing the proportional and integral gains for each set of states in the error vector. The dynamics of **V** and **W** are defined by the learning law presented in [73], where

$$\begin{aligned} \dot{\mathbf{W}} &= -\left[\left(\boldsymbol{\sigma}-\boldsymbol{\sigma}'\mathbf{V}^T\bar{\mathbf{x}}\right)\bar{\mathbf{r}}^T+\kappa\|\bar{\mathbf{r}}\|\mathbf{W}\right]\boldsymbol{\Gamma}_{\boldsymbol{w}}\\ \dot{\mathbf{V}} &= -\boldsymbol{\Gamma}_v\left[\bar{\mathbf{x}}\left(\bar{\mathbf{r}}^T\mathbf{W}^T\boldsymbol{\sigma}'\right)+\kappa\|\bar{\mathbf{r}}\|\mathbf{V}\right] && (6.30)\end{aligned}$$

In Eq. 6.30, $\boldsymbol{\Gamma}_w$ and $\boldsymbol{\Gamma}_v$ are the learning rates, which, for this work have been set to $0.2\times\mathbf{I}^{n_3\times n_3}$ and $2\times\mathbf{I}^{n_1\times n_1}$ respectively. The rate of change of the sigmoidal activation function is denoted by $\boldsymbol{\sigma}'\in\Re^{n_2+1\times n_2}$. The final term in both equations is the e-modification term, κ, which is a strictly positive constant, set at 0.1 for this work. A proof of boundedness on $\dot{\boldsymbol{\nu}}_{nn}$ using these update laws is given by Kannan and Johnson in [39].

6.5.4 Simulation Results for Adaptive Controller

The contribution of the neural network to the control system is to cancel out the errors that occur in the dynamic inversion from inaccurate modelling. The effectiveness of the neural network is best seen using a simplified simulation. Figure 6.5 shows a simulation that only includes errors in the model parameters. Starting from rest, the vehicle is being asked to track a step input in reference velocities, followed by a second step input of twice the

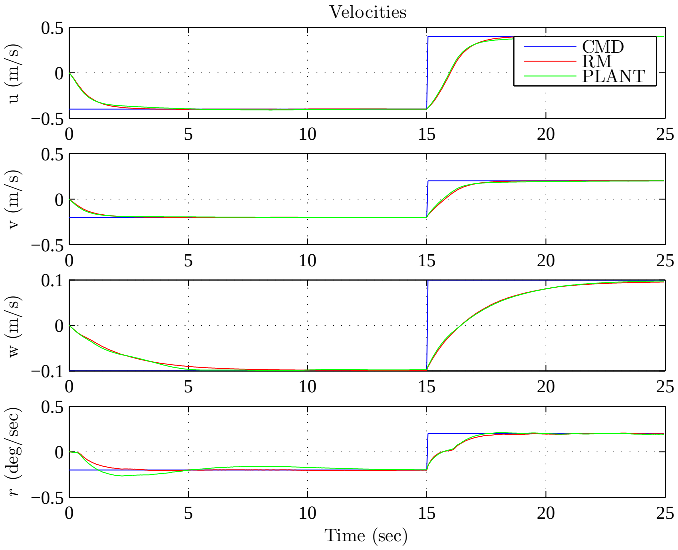

Figure 6.5: Plot showing the contribution of the neural network to the control system.

Table 6.2: Neural Network Control Parameters

Description	Variable	value
# of inputs	n_1	9
# of hidden layer neurons	n_2	5
# of outputs	n_3	4
activation potentials	$\mathbf{a}$	$[0.20.40.60.81.0]^T$
e-modification terms	κ	0.1
input bias	b_v	0.5
hidden layer bias	b_w	0.5
learning rate for **V**	$\mathbf{\Gamma}_v$	$2 \times \mathbf{I}^{n_1 \times n_1}$
learning rate for **W**	$\mathbf{\Gamma}_w$	$0.2 \times \mathbf{I}^{n_3 \times n_3}$

magnitude. During the first step the network is learning the parameter errors and the vehicle doesn't track the reference model very well. The tracking on the second step, however, is significantly better despite the fact that the step is twice the magnitude.

To test this control sytem in the full vehicle simulation, the same scenario was used here as was used for the PID controller in Section 6.4.7. The parameters used for the NN are listed in Table 6.2. All of the PID and trajectory parameters from Table 6.1 in Section 6.4.7 were also used. The only difference between the two control systems is the addition of the

NN and PCH.

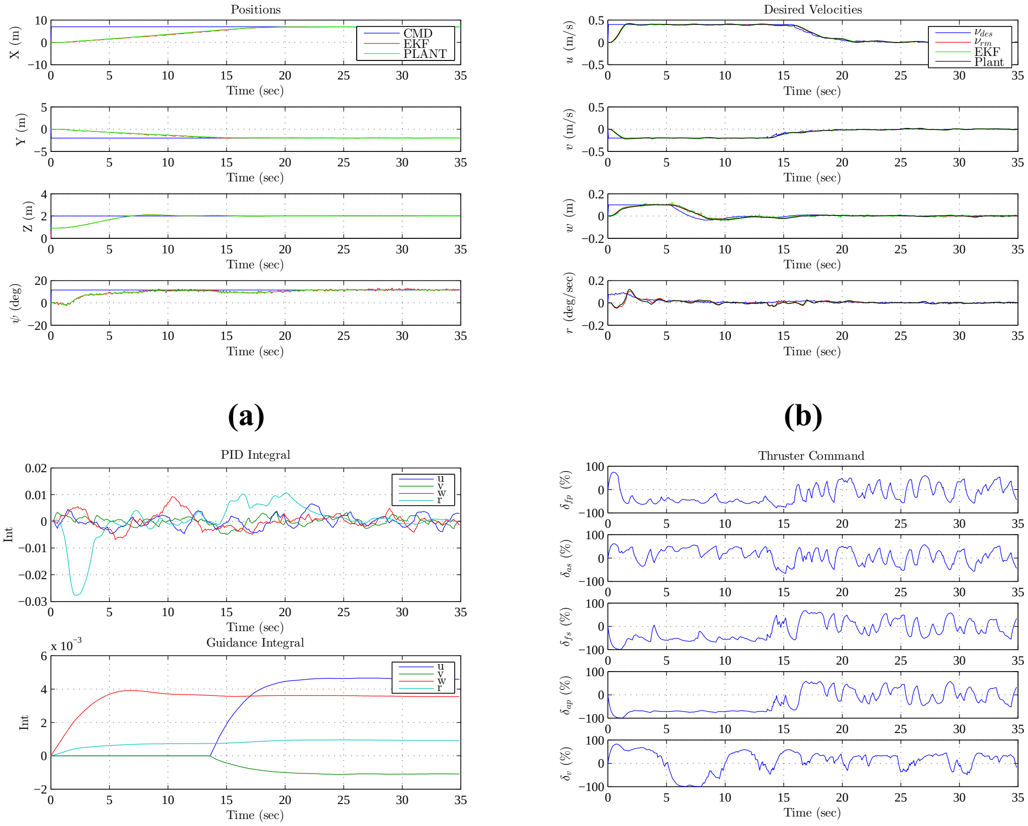

(a) (b)

(c) (d)

Figure 6.6: Full simulation of the ROV dynamics with adaptive control system: a)positions, b) velocities, c) contribution of the integral component d) control effort from each thruster (%)

The results of the simulation are shown in Figure 6.6. As with the PID controller, the vehicle was able to reach the destination point in approximately 20 seconds and hold station once it arrived (Figure 6.6-a). One of the biggest differences is in the desired velocities shown in Figure 6.6-b; the adaptive controller tracks the desired velocities much better, which resulted in less overshoot in the positions. This is especially true with the yaw control. A second thing of note is the size of the integral term for the PID compensator, shown in Figure 6.6-c. The integral term is several orders of magnitude smaller than it was with the previous controller; this is because the modelling error is being handled by the NN and the PID compensator doesn't see it. The control signal, shown in Figure 6.6-d, is also trackable by the thrusters. The mean thrust demanded by the two control systems have no statistical differences. The biggest difference in the neural network controller is the ability to accurately track the reference velocities, which is an important trait for many underwater applications[3]. The network weights from **W** and **V** are shown in Figure 6.7; they are stable and converge on steady-state values within a few seconds.

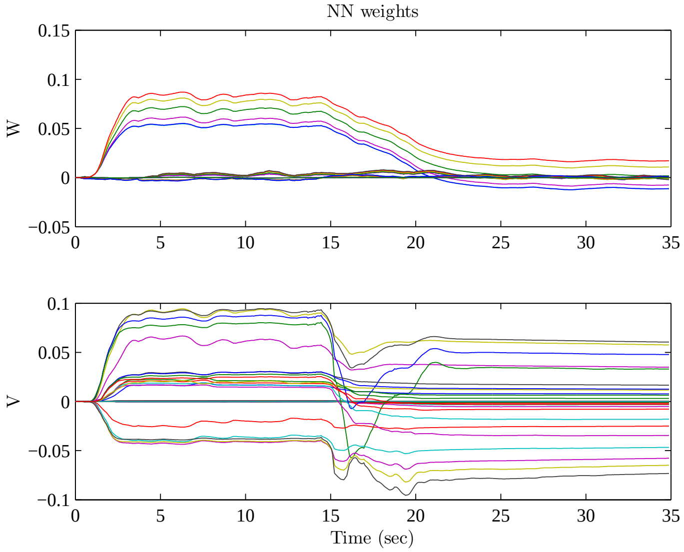

Figure 6.7: Plot showing the neural network weights

6.6 Conclusion

In this chapter, two different control schemes were presented. The first was a baseline PID controller that used a nonlinear dynamic inversion and a reference model. The reference model was a set of first order sub-systems that provided an trackable trajectory to the desired velocities from the guidance algorithm. The vehicle tracked the reference model though

---

[3] For Example: If the vehicle is being used as an observing platform, it is important that the camera stays pointed at the object of interest is the transect is performed. If the vehicle is yawing the camera will not be pointed at the subject.

the PID controller and approximate nonlinear inversion. In the second control scheme, an adaptive element was added that used an online learning algorithm to cancel the errors in the approximate nonlinear inversion, and PCH was used to prevent the NN from adapting to the thruster dynamics. Both control systems were able to manage error and get the vehicle to the destination, but there was a significant decrease in the velocity tracking error with the addition of the NN to the controller.

Chapter 7

Conclusion

Semi-autonomous functionality is necessary, if ROV operators are going to meet the growing demand from the underwater industry. The challenges faced by pilots will continue to increase as the underwater oil and gas, and mining industries venture into deeper and deeper water. Science tasks for ROVs have also increased in complexity over the last decade. More and more countries are installing permanent seafloor observing stations (or observatories). These installations require ROVs with precise position control that can gently manipulate instruments and connectors using hydraulic arms with force feedback.

In this work, a complete guidance, navigation, and control system was implemented on the Saab Sea-Eye Falcon ROV. The Falcon was modified to incorporate a navigation sled, which contained an IMU, a Compass, a Pressure Sensor, and a DVL. This sled was used in conjunction with an SBL positioning system to estimate the position of the vehicle with an overall error, in a Euclidean sense, of less than 6 cm. The output of the navigation system was validated using a high-speed motion capture camera system that acted as an independent observer and provided data about the position and attitude of the vehicle while it was inside the SWAT facility. The guidance algorithm, which was also used in previous work, was shown to be a stable and provide a reliable trajectory to a given destination point.

Lastly, two control systems were considered. The first system was a simple PID controller contained in an architecture with a reference model. The second control system added an adaptive element to cancel out the errors in the approximate dynamic inversion. Both control systems produced control signals that met all the stability criteria, but the adaptive controller showed an increase in tracking performance. Successful field tests of the vehicle, guidance, navigation, and control systems presented in this document have been conducted; the results will be published in a future paper.

7.1 Future Work

The Falcon ROV used for this research has been developed as an experimental research platform. The onboard software uses a combination of Labview by National Instruments and code generated by Matlab Coder (Mathworks). All of the development for the guidance, navigation, and control algorithms was done completely in Matlab and ported directly over to the actual hardware without any intermediate steps. The SWAT facility is a valuable asset for testing underwater vehicles and related research. While working on this research, there were many areas of investigation that were not explored but could be easily pursued using the SWAT and OTL's Falcon ROV:

System Identification: Further investigation into the cross coupled pitch and roll dynamics should be performed. The results in Chapter 3 contradict the current theory that at low speeds the DOFs of an ROV can be considered uncoupled and addressed separately. The SWAT facility could be used to perform additional system ID testing that could expand on the findings in this work.

Navigation: During this research the following items were identified as topics of interest for future work with this vehicle.

- It has been shown that other non-linear estimators can out perform conventional

EKFs in both stability and accuracy. While the results of this research are adequate for most applications, improved accuracy would be needed to implement an ROVM system or other advanced research,

- Using a highly accurate short range vision-based navigation system in conjunction with a less precise long range navigation could enable very precise positioning at a work site. This concept has been realized, to some extent, with SeaBytes latest software, the CoPilot. However, there are still many potential research problems that could be investigated at the SWAT,
- Simultaneous localization and mapping is always an interesting topic. The SWAT is a perfect location for this type of work as one can install features at precise locations and observe the progress of the ROV during trials using the MOCAP camera system.

Guidance: The guidance algorithm presented here provides a stable trajectory of velocities that will get the vehicle to the destination, but does not do it very elegantly. Improved high-level path planning techniques could be investigated. These techniques could use fuzzy logic or other rule-based methods for determining trajectories that are more suitable for a working ROV.

Control: There are many potential controls projects that could be pursued. Firstly, the controller presented in this work should be subjected to sea trials to determine how robust it actually is. Once that is complete, there are a number of ways it could be improved or further investigated:

- Developing an adaptive inner layer control system to manage the thrusters in a fault tolerant manner,
- Incorporate the latency compensation algorithms presented in [51],

- Do an indepth comparison between the controller presented here and a sliding mode controller.

These are only a few suggestions for future work that could be done using these facilities; there are many more potential avenues of research that could be followed.

Appendix A

Mathematical Notation

The following mathematical notation is used throughout this text.

A scalar is depicted by normal text n.

A vector or matrix is depicted by boldface $\mathbf{n}$.

A vector expressed in frame a is denoted as $\mathbf{n}^a$.

The rotation matrix from frame a to frame b is denoted as $\mathbf{R}^{a\to b}$

Identity matrix with n rows and n columns

$$\mathbf{I}^{n\times n} \triangleq \begin{bmatrix} 1 & 0 & \cdots & 0 \\ 0 & 1 & \cdots & 0 \\ \vdots & & & \vdots \\ 0 & 0 & \cdots & 1 \end{bmatrix} \tag{A.1}$$

Zero matrix with n rows and m columns

$$\mathbf{0}^{n\times m} \triangleq \begin{bmatrix} 0 & 0 & \cdots & 0 \\ 0 & 0 & \cdots & 0 \\ \vdots & & & \vdots \\ 0 & 0 & \cdots & 0 \end{bmatrix} \tag{A.2}$$

A diagonal matrix is defined by

$$diag(\mathbf{n}) \triangleq \begin{bmatrix} n_1 & 0 & 0 \\ 0 & n_2 & 0 \\ 0 & 0 & n_3 \end{bmatrix} \tag{A.3}$$

Skew symmetric matrix operator

$$\widetilde{\mathbf{n}} \triangleq \begin{bmatrix} 0 & -n_3 & n_2 \\ n_3 & 0 & -n_1 \\ -n_2 & n_1 & 0 \end{bmatrix} \tag{A.4}$$

Appendix B

Supplemental ROV Hardware

In its nominal configuration, the OTL's ROV is a stock Saab SeaEye Falcon with a 350m copper tether. The vehicle is rated to 300m and is controlled by joystick through the SCU. The vehicle comes equipped with a camera, compass, rate gyro for heading, and depth sensor. These nominal navigation sensors are insufficient for generating a position estimate accurate enough for this work. To address this the vehicle was augmented with a positioning system, navigation sensors, and several other upgrades, as shown in Figure B.1. To facilitate this new configuration, three major modifications were made to the vehicle:

1. An "In-Control" switch was added to the junction box to allow the pilot to switch between the traditional manual control mode and the computer-aided dynamic positioning mode,
2. An auxiliary interface container, or AIC, was added to the main vehicle to enable support for auxiliary equipment and additional communication protocols,
3. A navigation sled with additional sensors was added to the bottom of the vehicle.

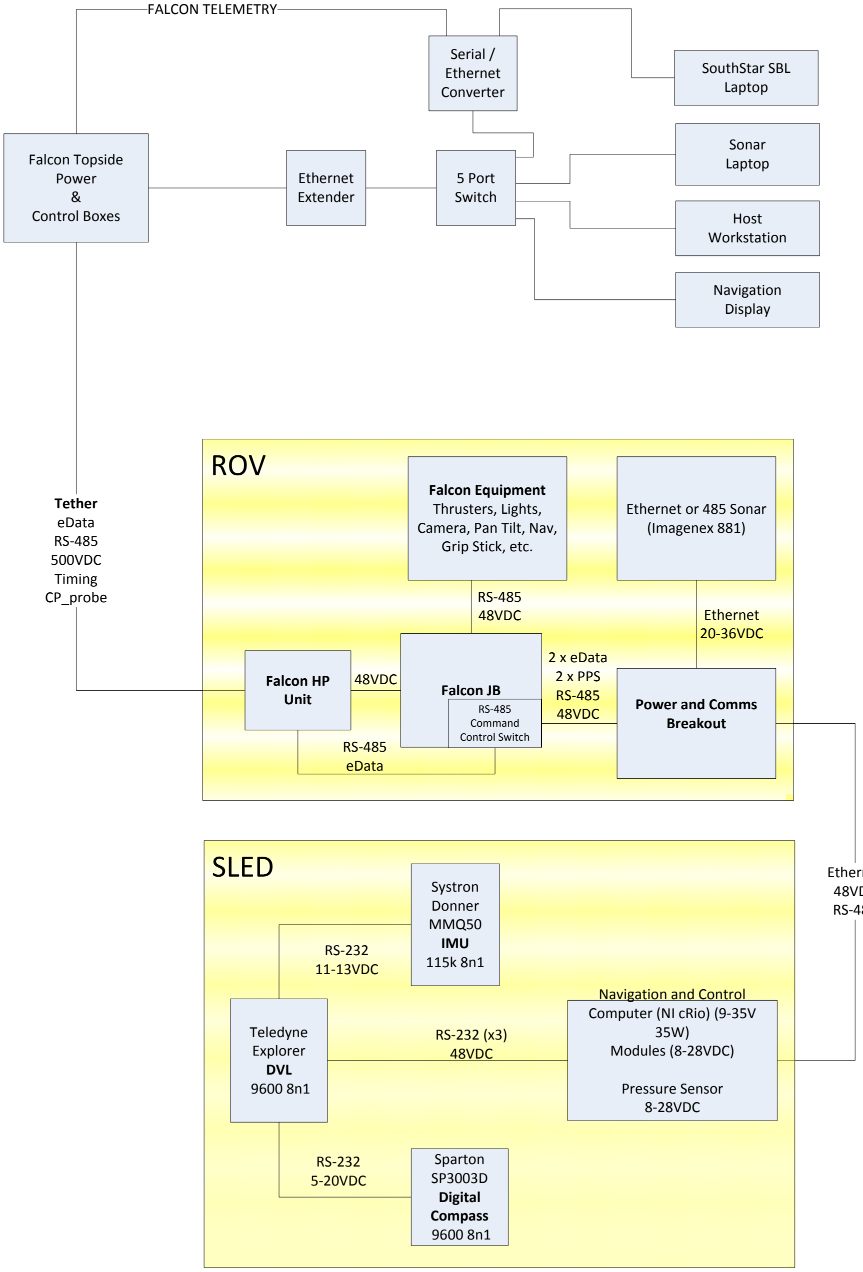

Figure B.1: Schematic showing the layout of all the equipment used to support this research

B.1 Vehicle Modifications

The upgraded Falcon is shown in Figure B.2. These major upgrades, as well as some other minor ones, are described in detail in the following sections.

Figure B.2: The modified OTL Falcon with navigation skid

B.1.1 In-Control Switch

A small but important detail for this research was adding a reliable way of switching between the human pilot and the computer control. This provides a level of safety for the vehicle and operating area by allowing a human supervisor to assume control of the vehicle quickly in case the automatic controller does something unexpected. This was accomplished using a spare conductor in the cable that is normally used for a Cathodic Protection (CP) Probe. This conductor is connected to the black banana plug shown in Figure B.3, with the green plug being connected to reference ground (also known as Earth). To use this interface as the "In-Control" switch, a small IC board was added in the vehicle junction box. When the two plugs are connected together with a shorting cable, a relay is powered on the IC and the RS-485 telemetry lines from the vehicle are diverted from the tether to the computer on the navigation sled. When the shorting cable is removed the relay reverts to its default state and the vehicle telemetry lines are connected back to the tether so that the surface control unit is once again in control.

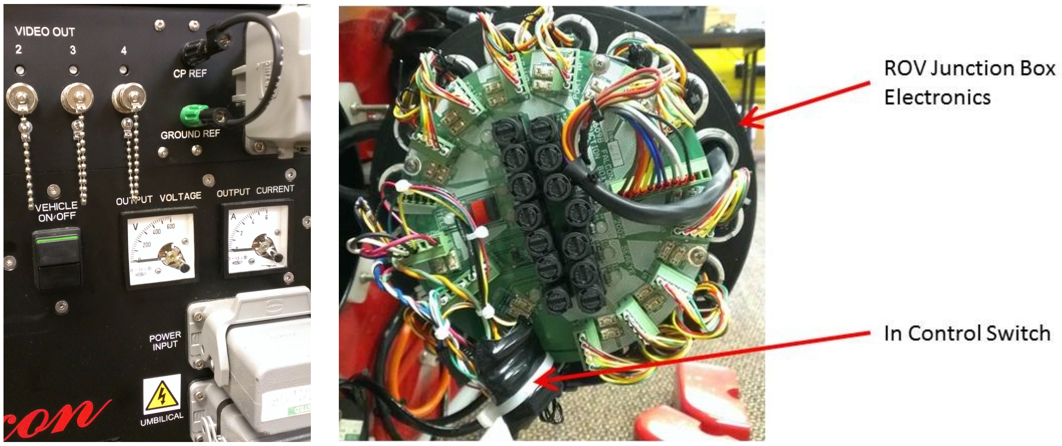

(a) **(b)**

Figure B.3: In-Control Switch: (a) The In-Control plug on the SCU shown connected putting the unit in computer aided mode) (b) IC for the In-Control switch located in the vehicle junction box

B.1.2 Auxiliary Interface Can (AIC)

The vehicle was also equipped with a small housing containing electronics that can provide power and communications to auxiliary instruments. This housing, referred to as the Auxiliary Interface Can, or AIC, is shown in Figure B.4. The AIC takes the 48VDC available from the Falcon and powers internal and external electronics and instrumentation. For communications, the AIC works in conjunction with topside equipment to provide Ethernet connectivity to instruments on the ROV. This is done using the Patton 2172 Ethernet Extender and an ADAM-6520 Industrial Ethernet Switch. The Patton ethernet extender can transmit up to 25Mbps over a single set of twisted pair conductors in the tether. 10/100 ethernet normally requires two sets of twisted pair conductors and there is only one spare set of conductors in the falcon tether. Ethernet extenders work by having a transmit/receive unit at both ends of a wire that is to be transmitted over. The units convert ethernet packets into a proprietary communication algorithm at one end of the and then decode them and turn them back into ethernet packets at the other end. For this work, there is one unit on the surface and one unit in the AIC. This allows the subsea infrastructure to communicate with the surface equipment over ethernet and vice versa. Lastly the AIC also provides an access point to the Falcon RS-485 communication buss when the In-Control switch is in computer aided mode.

(a) **(b)**

Figure B.4: Auxiliary Interface Can: (a) Front Side (b) Back Side

There are two devices connected to the AIC, an Imagenex 881L Ethernet based forward looking sonar system and the SSC. The AIC can also support additional Ethernet instruments or legacy RS-485 instruments using an ADAM-4570 serial server. This device can be used to transmit and receive serial data over Ethernet. The serial server is required, since all of the spare conductors in the tether, that would have otherwise been used for serial communication, have been repurposed to provide the Ethernet service.

B.2 Surface Unit (SCU) Modifications

The SCU is shown in Figure B.5. SeaEye uses a small 12 unit 19 inch rack to house all of the surface electronics, including a power supply unit, processing unit, keyboard, and monitor. The keyboard and monitor are used for debugging the vehicle, and the monitor is also used for displaying the image from the onboard video camera and the overlay with the basic

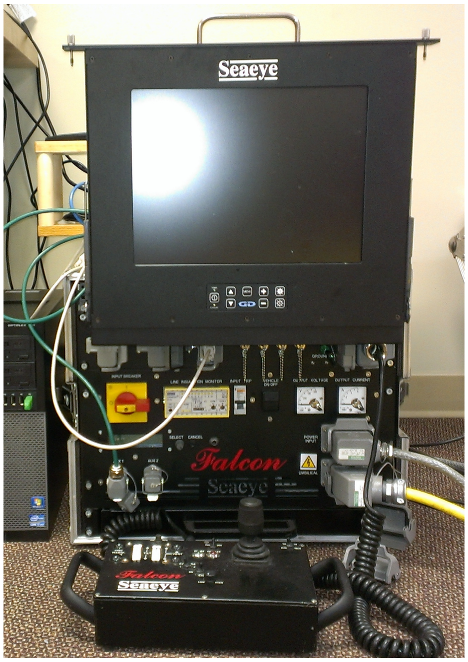

Figure B.5: Falcon Surface Equipment - deck equipment including power supply, processing unit, and monitor.

vehicle telemetry. The power supply unit takes in the AC power and outputs 500VDC to the tether for the vehicle. The power supply compensates for the tether resistance to ensure that the vehicle receives a consistent 500VDC regardless of which tether is being used or the amount of current being drawn by the vehicle.

For this research, the surface equipment was augmented with a host workstation, a tracking system laptop, a serial/ethernet converter, and a 5-port ethernet switch. The host workstation is the primary operating and development platform for the Labview software. The tracking system laptop runs the SBL or USBL software and then transmits the output to the rest of the system over the serial/ethernet converter. All of the surface equipment uses ethernet communication and communicates with the subsea infrastructure via the ethernet extenders.

The state of the In-Control switch determines whether or not the SCU or the SSC is in control. When the SCU is in control, the SSC does not have access to the Falcon's

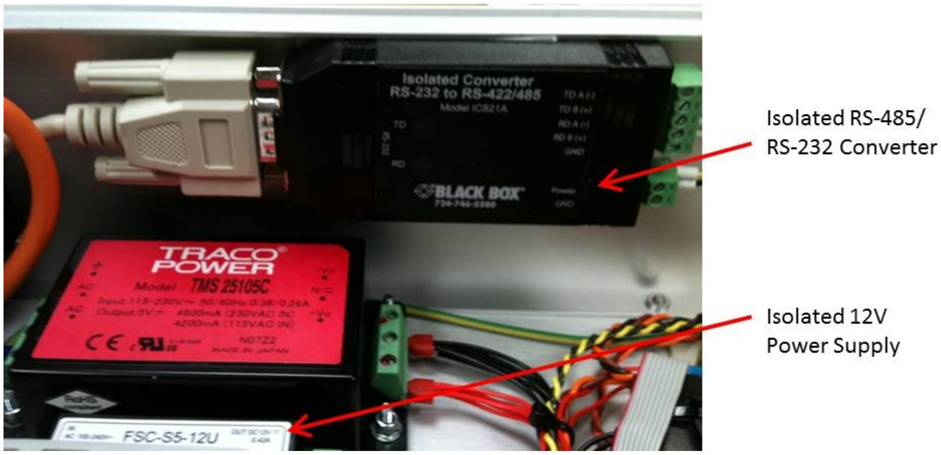

Figure B.6: Falcon Surface Equipment - the isolated RS-232/485 transceiver and isolated power supply that were added to the CPU box.

RS-485 communication buss; so the only way to view the commands being sent, is on the surface through the SCU. In order to run the navigation algorithm with the SCU in charge, it is necessary to be able to monitor the commands being sent to the thrusters. To facilitate this, the SCU was modified by adding an isolated power supply and isolated RS-232/485 transceiver to the processing unit. This feed is connected to a serial server (shown in Figure B.1) on the surface through one of the auxiliary ports on the front of the SCU. The transceiver and power supply inside of the processing unit are shown in Figure B.6.

B.3 Navigation and Control Sled

The navigation and control sled, holds all of the extra navigation sensors and the SSC. Unlike the rest of the modifications described here, the sled is not permanently attached to the vehicle and can be removed and replaced as necessary. This is important, as the sled is quite large and could be a detriment for ROV missions that don't require the augmented navigation and control provided by the SSC. Most of the navigation sensors on the sled have been used in previous graduate work by Zand in [78] and Soylu in [61], and are well understood.

B.3.1 SubSea Controller (SSC)

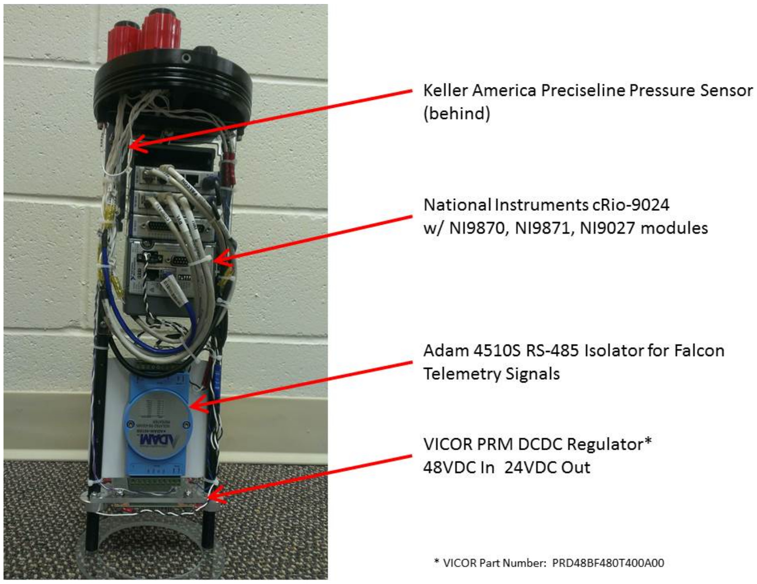

Figure B.7: The SubSea Controller (SSC) showing the National Instruments compactRio industrial computer and Keller America Pressure Sensor

The SSC, shown in Figure B.7 is the nerve centre of the onboard vehicle control system. It contains a National Instruments cRio computer and runs all of the Labview control software. The data from all the navigation sensors are fed into the cRio via Ethernet or through integrated modules that support RS-232 and RS-485 communication. The SSC also contains a pressure sensor and an ADAM 4510S RS-485 isolator. The pressure sensor provides a more accurate depth estimate than is provided by the Falcon depth sensor and the ADAM isolator is used to electrically isolate the RS-485 telemetry signals going to and from the main Falcon telemetry buss.

B.3.2 Doppler Velocity Log (DVL)

The DVL housing contains an OEM version of the Teledyne Benthos Explorer DVL and a power distribution board that acts as a power and communication hub for the compass and and IMU. The DVL transducer head mounts into the lower end section of the housing and

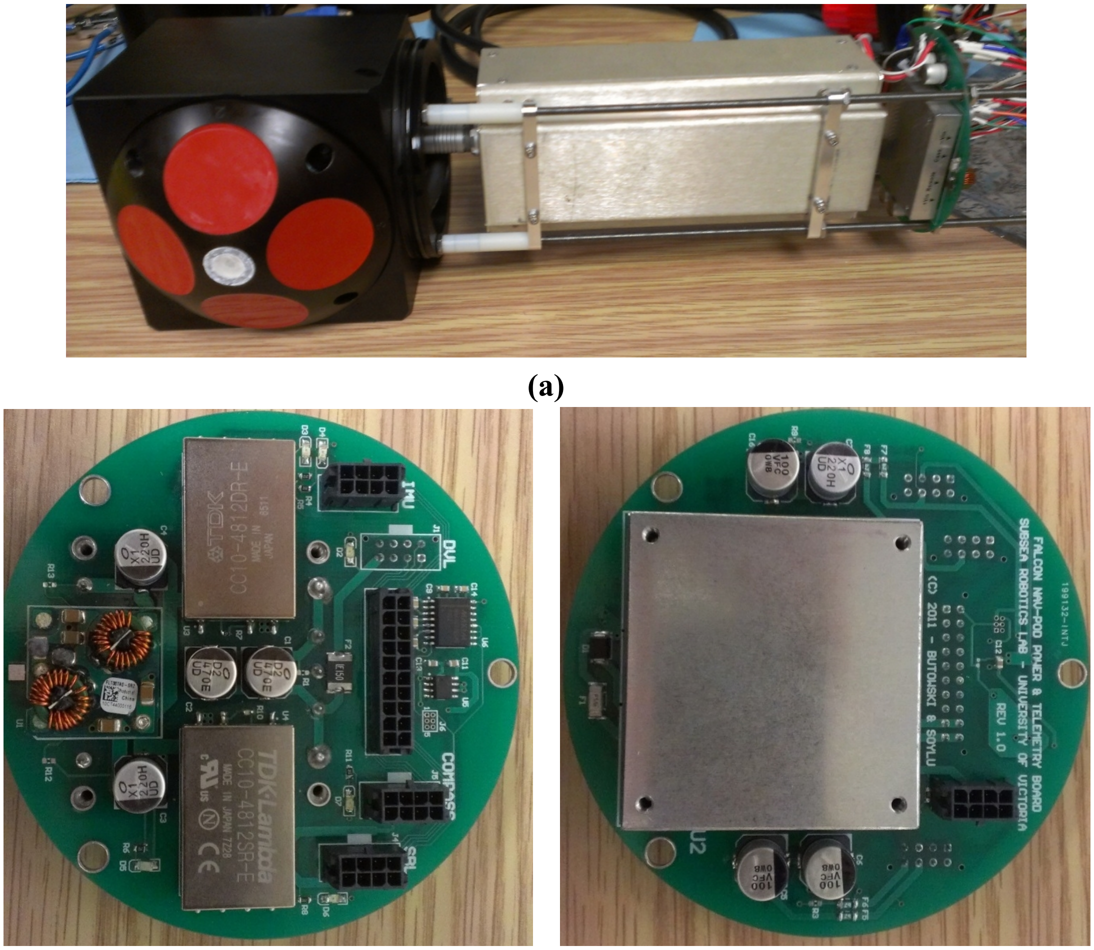

(a)

(b)

(c)

Figure B.8: The Doppler Velocity Log: (a) DVL assembly (b) power distribution board (c) power distribution board

the rest of the electronics go in the upper tube section. The transducer is arranged at a 45 degree angle to the x-axis of the vehicle, this is the optimal orientation for error rejection and mitigating the effects of ringing [31]. The DVL electronics, in the gold metal box, are attached to the DVL head with two cables, shown in Figure B.8-a. The power distribution board, shown in Figure B.8-b and Figure B.8-c, is located above the DVL electronics. This custom-built circuit board takes the nominal 48VDC from the Falcon and provides 24VDC and RS-232 communication to the DVL, as well as 12V and RS-232 communication for the IMU and compass, which are housed in separate enclosures and connected to the DVL enclosure by subsea cabling. The DVL enclosure is connected to the SSC via underwater cable and the three sets of RS-232 communication lines are connected directly to an RS-232 module in the cRio control computer.

B.3.3 Inertial Measurement Unit (IMU)

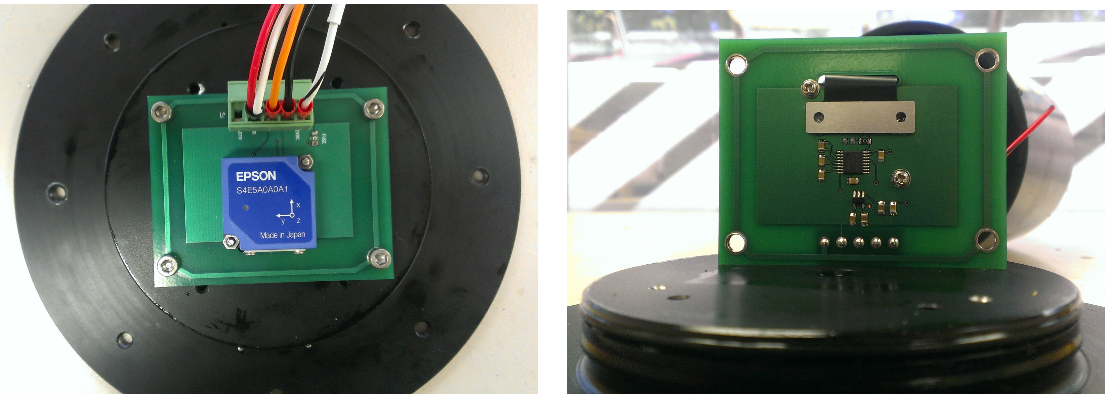

(a) **(b)**

Figure B.9: Inertial Measurement Unit: (a) sensor as mounted in the housing (b) custom interface board

The Epson M-G350-PD11 IMU (shown in Figure B.9) was purchased to replace the Systron Donner MMQ50 IMU that was used in previous work. A custom interface board, shown in Figure B.9-b, with a TTL/RS-232 level shifter and DCDC power supply, was built to integrate the IMU into the existing architecture. The IMU is mounted in the housing as shown in Figure B.9-a and connects to the rest of the infrastructure through the DVL enclosure.

B.3.4 Compass

The Honeywell Spartan SP3003D compass, which was used in previous work, is also on the navigation sled. It is mounted inside the compass housing, as shown in Figure B.10. The compass provides heading as well as a roll and pitch measurement. Power and communication for the compass are provide via the DVL enclosure.

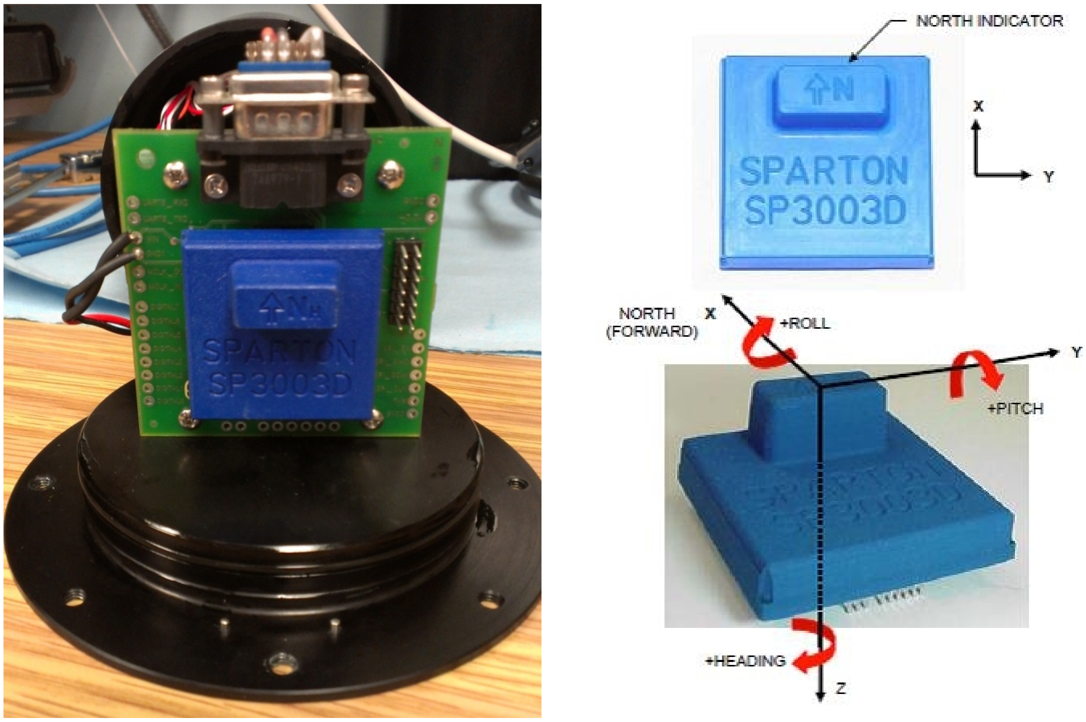

(a) **(b)**

Figure B.10: Spartan Compass: (a) sensor as mounted in the housing (b) sensor orientation diagram

Appendix C

Mast EKF Derivation

The EKF for analyzing the mast information is similar in structure to the EKF described in Chapter 4 and Appendix E. It estimates 13 states $\mathbf{X}^N$, $\mathbf{s}$, $\mathbf{v}$, and $\boldsymbol{\omega}$. The measurements are the LED locations in the boathouse frame. The measurement model is simply:

$$\hat{z} = \mathbf{X}^N + \mathbf{R}^{B\rightarrow N}\mathbf{X}^B_{Li} \tag{C.1}$$

where $\mathbf{X}^N$ is the position of the vehicle in the NRF, $\mathbf{R}^{B\rightarrow N}$ is the rotation matrix from the BRF to the NRF, and $\mathbf{X}^B_{Li}$ is the location of LED i in the BRF.

The process model used the kinematics from Chapter 3, but assumed the velocities and rates were constant (ie. $\dot{\boldsymbol{\nu}} = 0$). Therefore, the A matrix contains the partial derivatives of $\dot{\boldsymbol{\eta}}$ from Appendix E but the partial derivatives for $\dot{\boldsymbol{\nu}}$ are all zeros. Therefore, $\mathbf{A}$ is comprised of two components: the partial derivatives for $\dot{\boldsymbol{\eta}}$ with respect to $\boldsymbol{\nu}$,

$$\begin{aligned} \frac{\partial\dot{\boldsymbol{\eta}}}{\partial\boldsymbol{\nu}} &= \frac{\partial\mathbf{J}(\mathbf{s})\boldsymbol{\nu}}{\partial\boldsymbol{\nu}} \\ &= \mathbf{J} \end{aligned} \tag{C.2}$$

and the partial derivative of $\dot{\boldsymbol{\eta}}$ with respect to s_i,

$$\begin{aligned} \frac{\partial \dot{\boldsymbol{\eta}}}{\partial s_i} &= \frac{\partial \mathbf{J}(\mathbf{s})}{\partial s_i}\boldsymbol{\nu} \\ &= \begin{bmatrix} \frac{\partial \mathbf{R}^{B\to N}}{\partial s_i} & \mathbf{0}^{3\times 3} \\ \mathbf{0}^{4\times 3} & \frac{\partial \mathbf{J}_2}{\partial s_i} \end{bmatrix} \boldsymbol{\nu} \end{aligned} \tag{C.3}$$

H also borrows from the EKF described in Appendix E, and has two components. The partial derivative of with respect to $\mathbf{X}^N$, and **s**. The first is simply:

$$\frac{\partial \mathbf{h}_a}{\partial \mathbf{s}_i} = \mathbf{I}^{3\times 3}; \tag{C.4}$$

The second is the following familiar equation:

$$\begin{aligned} \frac{\partial \mathbf{h}_a}{\partial \mathbf{s}_i} &= \frac{\partial}{\partial \mathbf{s}_i}\mathbf{R}^{B\to N}\mathbf{X}^B_{Li} \\ &= \frac{\partial \mathbf{R}^{B\to N}}{\partial \mathbf{s}_i}\mathbf{X}^B_{Li} \end{aligned} \tag{C.5}$$

where $\frac{\partial \mathbf{R}^{N\to B}}{\partial \mathbf{s}_i}$ can be obtained from Eq. E.3.

The $\mathbf{x}_0$ and $\mathbf{P}_0$ from Appendix E are used. This is reasonable as the same vehicle location is being estimated. The $\mathbf{Q}_P$, matrix values are as follows:

$$\begin{array}{llll} \mathbf{Q}_{P_{xx}} = 0.01 & \mathbf{Q}_{P_{yy}} = 0.01 & \mathbf{Q}_{P_{zz}} = 0.01 & \\ \mathbf{Q}_{P_{s_0 s_0}} = 0.0025 & \mathbf{Q}_{P_{s_1 s_1}} = 0.0025 & \mathbf{Q}_{P_{s_2 s_2}} = 0.0025 & \mathbf{Q}_{P_{s_3 s_3}} = 0.0025 \\ \mathbf{Q}_{P_{uu}} = 0.25 & \mathbf{Q}_{P_{vv}} = 0.25 & \mathbf{Q}_{P_{ww}} = 0.25 & \\ \mathbf{Q}_{P_{pp}} = 0.09 & \mathbf{Q}_{P_{qq}} = 0.09 & \mathbf{Q}_{P_{rr}} = 0.09 & \end{array} \tag{C.6}$$

Note that the values for the states in $\boldsymbol{\eta}$ have been kept small while the values for $\boldsymbol{\nu}$ are large. This allows the velocity information to propagate backwards from the position information obtained through the measurements. Since the measurements are all the same and the MOCAP has a variance for each LED measurement of approximately 0.0001, $\mathbf{R}_M$ is simply:

$$\mathbf{R}_M = 0.0001 \cdot \mathbf{I}^{13\times13} \tag{C.7}$$

Appendix D

Representing Orientation of Vehicles in 3D Space

A reference frame is a mathematical abstraction used for defining an observers point of view of an object; for example: two people sitting on opposite sides of a table looking at a pencil will each see the pencil differently, to one person the pencil will be pointing towards them, to the other it will point away. Both people see the same pencil, but they are viewing it from different frames of reference. By definition, a reference frame has an origin and n basis vectors, where n is the dimension of the space in question. A reference frame is typically used as the basis for a coordinate system, which allows one to quantitatively describe points and objects in space.

When considering the forces and moments on an underwater vehicle, some are fixed to the earth's reference frame, like gravity and buoyancy, others are fixed to the vehicle reference frame, like propulsion, and still others which are fixed to the direction of velocity, like hydrodynamic forces and moments. When creating a dynamic model of a vehicle it is often helpful to be able to work with quantities in their native frame and then transform the results. There are two reference frames in particular that are universally used in guidance, navigation and control applications:

Inertial frame: The reference frame where Newton's Laws are valid.

Body Frame: A reference frame that is fixed to the vehicle body.

This raises the question of how to best describe the relationship between different reference frames, and transform vector quantities between them.

D.1 Transformation Matrices

There are two types of transformation matrices used in this work, the direction cosine matrix (DCM) and the homogenous transformation matrix (HTM). The DCM is a 3x3 orthonormal matrix, that is made up of the cosines between the different axes of the two reference frames. The fundamental method for obtaining the DCM is by taking the dot product of the vectors that make up the axes for each reference frame:

$$\mathbf{DCM}^{1\to 2} \triangleq \begin{bmatrix} e_{1x}\cdot e_{2x} & e_{1x}\cdot e_{2y} & e_{1x}\cdot e_{2z} \\ e_{1y}\cdot e_{2x} & e_{1y}\cdot e_{2y} & e_{1y}\cdot e_{2z} \\ e_{1z}\cdot e_{2x} & e_{1z}\cdot e_{2y} & e_{1z}\cdot e_{2z} \end{bmatrix} \tag{D.1}$$

D.2 Euler Angles

Geometric representations of transformations are most common as they are easily visualised. Leonard Euler, an 18th century mathematician, presented the following theorem:

> Any two independent orthonormal coordinate frames, whose origins are coincident, can be related by a sequence of rotations (not more than three) about coordinate axes, where no two successive rotations may be about the same axis.

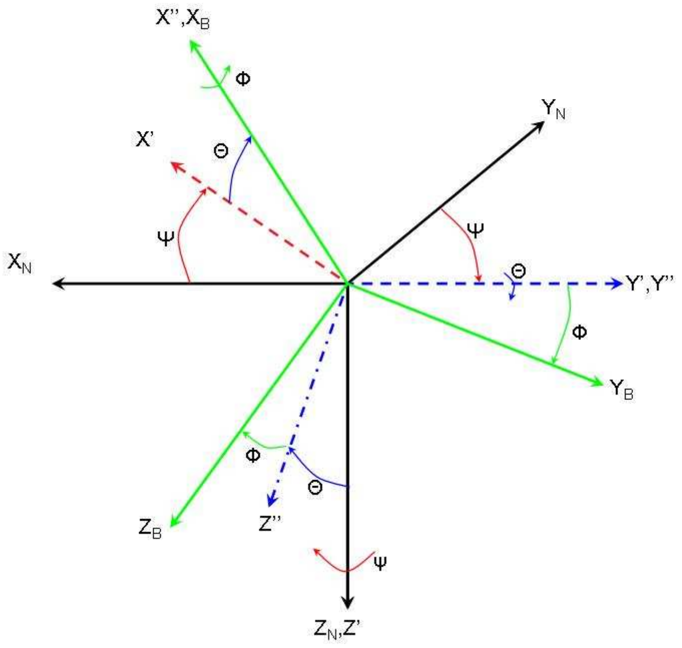

Figure D.1: Euler Angle Sequence ZYX

This theorem is the basis for the Euler Angle Sequences, which are used to describe a sequence of rotations which transforms the observer from one coordinate system to another, Figure D.1. These sequences are not unique; there are 12 different choices of axes that can be used to move between coordinate systems. In guidance and control applications, it is conventional to use the ZYX transformation to go from the inertial to the body frame, shown in Figure D.1, where X_N, Y_N, Z_N is the inertial frame, X_B, Y_B, Z_B is the body fixed frame and X', Y', Z' X'', Y'', Z'' are intermediate sets of axes. In this transformation, the first rotation is about the z-axis, the second rotation is about the new y-axis and the final rotation is about the new x-axis.

Euler angle sequences provide a intuitive method of transforming vectors from one reference frame to another, because they are composed of a sequence of planar rotations about one axis of the reference frame. Planar rotations are easy to visualise as they are easily described by simple geometry. From Figure D.2, it can be seen that the representation of

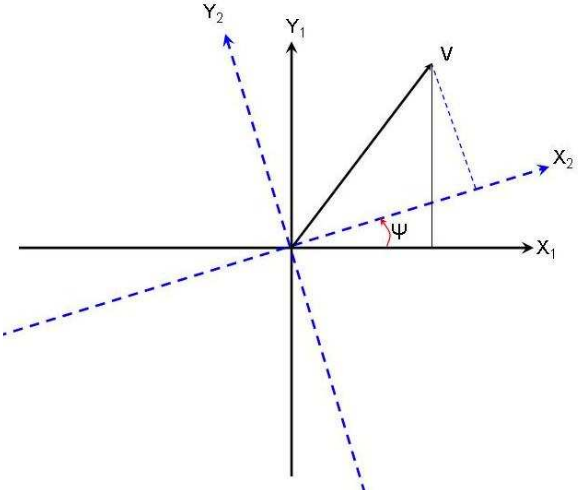

Figure D.2: Geometry of a Planar Rotation

vector **n** in reference frame 1 will be related to the representation in reference frame 2 by a planar rotation about the z-axis that can be expressed as follows:

$$\begin{aligned}\mathbf{n}^2 &= \mathbf{R}_z(\psi)\mathbf{n}^1 \\ &= \begin{bmatrix} cos(\psi) & sin(\psi) & 0 \\ -sin(\psi) & cos(\psi) & 0 \\ 0 & 0 & 1 \end{bmatrix}\mathbf{n}^1\end{aligned} \tag{D.2}$$

The transformation, $\mathbf{R}_z$ is also a DCM. By extension, rotations about the x-axis and y-axis can be expressed by the following matrices:

$$\mathbf{R}_x(\phi) = \begin{bmatrix} 1 & 0 & 0 \\ 0 & cos(\phi) & sin(\phi) \\ 0 & -sin(\phi) & cos(\phi) \end{bmatrix} \tag{D.3}$$

$$\mathbf{R}_y(\theta) = \begin{bmatrix} cos(\theta) & 0 & -sin(\theta) \\ 0 & 1 & 0 \\ sin(\theta) & 0 & cos(\theta) \end{bmatrix} \tag{D.4}$$

Since an euler angle sequence is just a set of sequential planar rotations the DCM for the complete ZYX sequence that rotates a vector from the inertial to the body frame, otherwise denoted as $\mathbf{R}^{i\to b}$, can be calculated as follows:

$$\begin{aligned} \mathbf{R}^{i\to b} &\triangleq \mathbf{R}_x(\phi)\mathbf{R}_y(\theta)\mathbf{R}_z(\psi) \\ &= \begin{bmatrix} 1 & 0 & 0 \\ 0 & cos(\phi) & sin(\phi) \\ 0 & -sin(\phi) & cos(\phi) \end{bmatrix} \begin{bmatrix} cos(\theta) & 0 & -sin(\theta) \\ 0 & 1 & 0 \\ sin(\theta) & 0 & cos(\theta) \end{bmatrix} \cdots \\ & \begin{bmatrix} cos(\psi) & sin(\psi) & 0 \\ -sin(\psi) & cos(\psi) & 0 \\ 0 & 0 & 1 \end{bmatrix} \end{aligned} \tag{D.5}$$

The biggest draw back to Euler angle sequences is illustrated when trying to reversing the process. It is possible to obtain the Euler angles from the DCM itself; for the ZYX sequence, shown in Eq. D.5 the following equations can be used to obtain the Euler angles:

$$\phi = atan\left(\frac{\mathbf{R}^{i\to b}(2,3)}{\mathbf{R}^{i\to b}(3,3)}\right) \quad \text{(D.6)}$$

$$\theta = -asin\left(\mathbf{R}^{i\to b}(1,3)\right) \quad \text{(D.7)}$$

$$\psi = atan\left(\frac{\mathbf{R}^{i\to b}(1,2)}{\mathbf{R}^{i\to b}(1,1)}\right) \quad \text{(D.8)}$$

From Eq. D.6 and Eq. D.6 it is clear that if $\theta = \pm n\pi/2 \quad n = 0,1,2,3...$ that $cos(\theta) = 0$ and both the numerator and denominator will be zero leaving ϕ and ψ undefined. To see exactly why this occurs substitute $\theta = \pi/2$ back into Eq. D.5.

$$\mathbf{R}^{i\to b}|_{\theta=\frac{\pi}{2}} \quad \text{(D.9)}$$

$$= \begin{bmatrix} 0 & 0 & -1 \\ sin(\phi)cos(\psi) - cos(\phi)sin(\psi) & sin(\phi)sin(\psi) + cos(\phi)cos(\psi) & 0 \\ sin(\phi)sin(\psi) + cos(\phi)cos(\psi) & -\left(sin(\phi)cos(\psi) - cos(\phi)sin(\psi)\right) & 0 \end{bmatrix}$$

$$= \begin{bmatrix} 0 & 0 & -1 \\ sin(\phi-\psi) & cos(\phi-\psi) & 0 \\ cos(\phi-\psi) & -sin(\phi-\psi) & 0 \end{bmatrix}$$

$$= \begin{bmatrix} 1 & 0 & 0 \\ 0 & cos(\phi-\psi) & sin(\phi-\psi) \\ 0 & -sin(\phi-\psi) & cos(\phi-\psi) \end{bmatrix} \begin{bmatrix} 0 & 0 & 1 \\ 0 & 1 & 0 \\ -1 & 0 & 0 \end{bmatrix}$$

From Eq. D.9 it is easy to see that this condition is reduces to a mirroring operation plus a single rotation about the Z-axis, making it impossible to retrieve ϕ and ψ independently. This singularity is analogous to gimbal lock, and is unavoidable with any three variable representation of orientation. This is the major draw back to using euler angles to represent orientation for vehicles with six degrees of freedom.

D.3 Quaternions

The following section presents the aspects of quaternions and quaternion math that are relevant to this paper; an in depth treatment of quaternions is available in [42]. Quaternions are another way of representing orientation. A quaternion is a four element representation based on Euler's Law of Finite Rotations which states:

> Any arbitrary finite rotation that leaves a point fixed can be viewed as a single rotation of magnitude Φ about a unit vector **n**.

Note: in this quotation **n** represents the axis of rotation not a generic vector as it is used elsewhere in this work. The rotation of a vector using a quaternion can be seen graphically in Figure D.3.

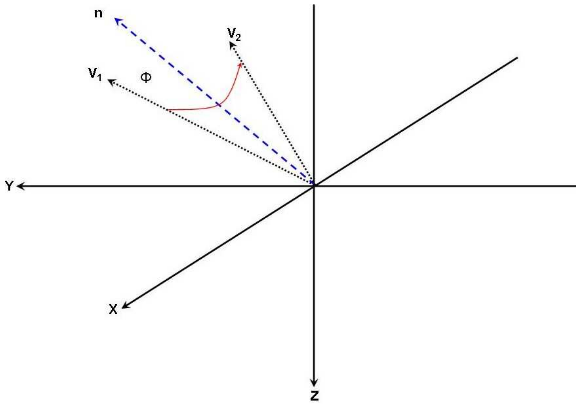

Figure D.3: A Graphical representation of a quaternion rotation Φ about a specific axis **n**

The set of quaternions makes up a non-commutative division ring with two operators, addition and multiplication. A quaternion can be viewed as a concatenation of a scalar and vector in $\Re^3$.

$$\begin{aligned} \mathbf{s} &= s_0 + s_1\mathbf{i} + s_2\mathbf{j} + s_3\mathbf{k} \\ &= \begin{bmatrix} s_0 \\ \mathbf{s} \end{bmatrix} \end{aligned} \tag{D.10}$$

where s_0 is the scalar part and **i**, **j**, and **k** are the usual orthonormal basis vectors. This definition provides a convenient framework for defining quaternion mathematics.

The identity quaternion is defined as $\mathbf{s}_I \triangleq [1, 0, 0, 0]^T$, and quaternion addition is analogous to vector addition with the four components adding separately. Additionally, quaternions must obey the following law, which was originally proposed by William Rowan Hamilton:

$$\mathbf{i}^2 = \mathbf{j}^2 = \mathbf{k}^2 = \mathbf{ijk} = -1 \tag{D.11}$$

This law does not conform to the laws of multiplication for real numbers, but rather provides a new law of multiplication, which is the basis for quaternion multiplication. In quaternion multiplication, similar to multiplying polynomials, each element of the first quaternion is multiplied through each element of the second. The result of a quaternion multiplication is as follows:

$$\begin{aligned} \mathbf{ps} \;=\; & p_0 s_0 + p_0 s_1 \mathbf{i} + p_0 s_2 \mathbf{j} + p_0 s_3 \mathbf{k} \\ & + p_1 s_0 \mathbf{i} + p_1 s_1 \mathbf{i}^2 + p_1 s_2 \mathbf{ij} + p_1 s_3 \mathbf{ik} \\ & + p_2 s_0 \mathbf{j} + p_2 s_1 \mathbf{ji} + p_2 s_2 \mathbf{j}^2 + p_2 s_3 \mathbf{jk} \\ & + p_3 s_0 \mathbf{k} + p_3 s_1 \mathbf{ki} + p_3 s_2 \mathbf{kj} + p_3 s_3 \mathbf{k}^2 \end{aligned} \tag{D.12}$$

then by applying Hamilton's law (Eq. D.11), this is reduced to:

$$\begin{aligned}
\mathbf{ps} &= p_0 s_0 + p_0 s_1 \mathbf{i} + p_0 s_2 \mathbf{j} + p_0 s_3 \mathbf{k} \\
&\quad + p_1 s_0 \mathbf{i} - p_1 s_1 + p_1 s_2 \mathbf{k} - p_1 s_3 \mathbf{j} \\
&\quad + p_2 s_0 \mathbf{j} - p_2 s_1 \mathbf{k} - p_2 s_2 + p_2 s_3 \mathbf{i} \\
&\quad + p_3 s_0 \mathbf{k} + p_3 s_1 \mathbf{j} - p_3 s_2 \mathbf{i} - p_3 s_3 \qquad \text{(D.13)} \\
&= p_0 s_0 - \mathbf{p} \cdot \mathbf{s} + p_0 \mathbf{s} + s_0 \mathbf{p} + \mathbf{p} \times \mathbf{s} \qquad \text{(D.14)} \\
&= \begin{bmatrix} p_0 & -p_1 & -p_2 & -p_3 \\ p_1 & p_0 & -p_3 & p_2 \\ p_2 & p_3 & p_0 & -p_1 \\ p_3 & -p_2 & p_1 & p_0 \end{bmatrix} \mathbf{s} \qquad \text{(D.15)}
\end{aligned}$$

Finally, the inverse to a quaternion (a requirement of a division ring) is simply $\mathbf{s}^{-1} = \mathbf{s}^*$, where $\mathbf{s}^* \triangleq s_0 - s_1\mathbf{i} - s_2\mathbf{j} - s_3\mathbf{k}$. This can be shown simply be expanding the quaternion product $\mathbf{ss}^*$ to verify that it does equal the identity quaternion.

The mathematical notion of a quaternion can be related to a physical rotation in 3D space as follows:

$$\mathbf{s} = \begin{bmatrix} s_0 \\ s_1 \\ s_2 \\ s_3 \end{bmatrix} = \begin{bmatrix} cos(\Phi/2) \\ sin(\Phi/2) \cdot n_0 \\ sin(\Phi/2) \cdot n_1 \\ sin(\Phi/2) \cdot n_2 \end{bmatrix} ; |\mathbf{s}| = 1 \qquad \text{(D.16)}$$

Notice that this definition of the quaternion provides an additional property $\| \mathbf{s} \| = 1$.

Rotation operators, analogous to the direction cosine matrices described above, can be created using quaternions [42]. The following double quaternion multiplication will transform a vector from the inertial frame to the body frame:

$$\mathbf{n}'^{b} = \mathbf{s}^{*}\mathbf{n}'^{i}\mathbf{s} \tag{D.17}$$

where the $\mathbf{n}'$ denotes the vector $\mathbf{n}$ being expressed as a quaternion with a scalar part of 0, $\mathbf{n}' = [0 \;\; n_1\mathbf{i} \;\; n_2\mathbf{j} \;\; n_3\mathbf{k}]^T$. Note that if one were to rotate the vector $\mathbf{n}$ a second time Eq. D.17 would become:

$$\begin{aligned} \mathbf{n}'^{x} &= \mathbf{p}^{*}\mathbf{s}^{*}\mathbf{n}'^{i}\mathbf{s}\mathbf{p} \\ &= (\mathbf{s}\mathbf{p})^{*}\mathbf{n}'^{i}(\mathbf{s}\mathbf{p}) \end{aligned} \tag{D.18}$$

where $\mathbf{p}$ is a second quaternion. Therefore, quaternion multiplication can be used to represent a sequence of rotations.

Through extensive manipulation, which is available for review in [42], Eq. D.17 can be rewritten as follows:

$$\begin{aligned} \mathbf{n}^{b} &= \begin{bmatrix} 1-2(s_2^2+s_3^2) & 2(s_1s_2-s_0s_3) & 2(s_1s_3+s_0s_2) \\ 2(s_1s_2+s_0s_3) & 1-2(s_1^2+s_3^2) & 2(s_2s_3-s_0s_1) \\ 2(s_1s_3-s_0s_2) & 2(s_2s_3+s_0s_1) & 1-2(s_1^2+s_2^2) \end{bmatrix}\mathbf{n}^{i} \\ &= \begin{bmatrix} s_0^2+s_1^2-s_2^2-s_3^2 & 2(s_1s_2-s_0s_3) & 2(s_1s_3+s_0s_2) \\ 2(s_1s_2+s_0s_3) & s_0^2-s_1^2+s_2^2-s_3^2 & 2(s_2s_3-s_0s_1) \\ 2(s_1s_3-s_0s_2) & 2(s_2s_3+s_0s_1) & s_0^2-s_1^2-s_2^2+s_3^2 \end{bmatrix}\mathbf{n}^{i} \\ &= Q\mathbf{n}^{i} \end{aligned} \tag{D.19}$$

where Q is the quaternion rotation operator, and will perform the same function as $R^{N\rightarrow B}$ from Eq. D.5 without being effected by the singularity that is associated with Euler angles.

D.4 Rotational Rate Equations

In this work, a vehicle is described as a rigid body that is free to move in six degrees of freedom, three translational degrees and three rotational degrees. The rotational rates are typically measured using sensors that are rigidly mounted to the vehicle. Therefore, the sensors are measuring rotational rates about axes that are fixed to the vehicle body, $\boldsymbol{\omega} \triangleq [p, q, r]^T$. Euler angles, on the other hand, are defined as rotations in three different reference frames, one rotation from the initial frame, and two more rotations in intermediate frames, before arriving at the final reference frame. Therefore, the time derivative of the Euler angles and the measured angular rates are not equal.

Since the Euler angles are each defined in their own reference frame, the transformation between the time derivative of the euler angles $[\dot{\phi}, \dot{\theta}, \dot{\psi}]$ and $\boldsymbol{\omega}$ is not just the rotational matrix **R** defined in the previous section. Rather, the two are related by the following equation:

$$\begin{aligned}
\boldsymbol{\omega} &= \mathbf{T} \begin{bmatrix} \dot{\phi} \\ \dot{\theta} \\ \dot{\psi} \end{bmatrix} \qquad \text{(D.20)} \\
&= \begin{bmatrix} \dot{\phi} \\ 0 \\ 0 \end{bmatrix} + \mathbf{R}_x(\phi) \begin{bmatrix} 0 \\ \dot{\theta} \\ 0 \end{bmatrix} + \mathbf{R}_x(\phi)\mathbf{R}_y(\theta) \begin{bmatrix} 0 \\ 0 \\ \dot{\psi} \end{bmatrix} \\
&= \begin{bmatrix} 1 & 0 & -\sin(\theta) \\ 0 & \cos(\phi) & \cos(\theta)\sin(\phi) \\ 0 & -\sin(\phi) & \cos(\theta)\cos(\phi) \end{bmatrix} \begin{bmatrix} \dot{\phi} \\ \dot{\theta} \\ \dot{\psi} \end{bmatrix}
\end{aligned}$$

The transformation from the rotational rates $\boldsymbol{\omega}$ to $[\dot{\phi}, \dot{\theta}, \dot{\psi}]$ can be found by taking the inverse:

$$\begin{aligned}\begin{bmatrix}\dot{\phi}\\ \dot{\theta}\\ \dot{\psi}\end{bmatrix} &= \mathbf{T}^{-1}\begin{bmatrix}p\\ q\\ r\end{bmatrix} \\ &= \begin{bmatrix}1 & \sin(\phi)\tan(\theta) & \cos(\phi)\tan(\theta)\\ 0 & \cos(\phi) & -\sin(\phi)\\ 0 & -\sin(\phi)/\cos(\theta) & \cos(\phi)/\cos(\theta)\end{bmatrix}\begin{bmatrix}p\\ q\\ r\end{bmatrix}\end{aligned} \tag{D.21}$$

Note that T is not a DCM and that $T^T \neq T^{-1}$ and that it is not defined at the singularity point where $\theta = \pm 90^\circ$.

When dealing with quaternions, one is looking for a similar transformation such that one can calculate $\dot{\mathbf{s}}$ as a function of $[p, q, r]^T$. A derivations of this function can be found in both [42] and [20]; since the notation used here is different from these two sources, the derivation is repeated for clarity.

First recall that a sequence of rotations can be represented through quaternion multiplication. Therefore, with the following steps we can construct a quaternion difference equation.

$$\mathbf{s}(t + \Delta t) = \mathbf{s}(t)\boldsymbol{\Delta}\mathbf{r}(t) \tag{D.22}$$

where $\boldsymbol{\Delta}\mathbf{r}(t)$ is a transitional quaternion with a rotation of $\Delta\alpha$ about an axis $\mathbf{n}_r$. If we assume that Δt is small then one can also assume that $\boldsymbol{\Delta}\mathbf{r}(t)$ is small. Therefore, from

Eq. D.16 $\mathbf{\Delta r}(t)$ can be represented as:

$$\mathbf{\Delta r}(t) = \begin{bmatrix} cos\left(\frac{\Delta\alpha}{2}\right) \\ sin\left(\frac{\Delta\alpha}{2}\right) \cdot n_{r0} \\ sin\left(\frac{\Delta\alpha}{2}\right) \cdot n_{r1} \\ sin\left(\frac{\Delta\alpha}{2}\right) \cdot n_{r2} \end{bmatrix} = \begin{bmatrix} 1 \\ \frac{\Delta\alpha}{2} \cdot n_{r0} \\ \frac{\Delta\alpha}{2} \cdot n_{r1} \\ \frac{\Delta\alpha}{2} \cdot n_{r2} \end{bmatrix} \tag{D.23}$$

Therefore,

$$\begin{aligned} \mathbf{s}(t+\Delta t) &= 2 \begin{bmatrix} s_0 & -s_1 & -s_2 & -s_3 \\ s_1 & s_0 & -s_3 & s_2 \\ s_2 & s_3 & s_0 & -s_1 \\ s_3 & -s_2 & s_1 & s_0 \end{bmatrix} \begin{bmatrix} 1 \\ \frac{\Delta\alpha}{2} \cdot n_{r0} \\ \frac{\Delta\alpha}{2} \cdot n_{r1} \\ \frac{\Delta\alpha}{2} \cdot n_{r2} \end{bmatrix} \\ &= \begin{bmatrix} 1 & -\frac{\Delta\alpha}{2} \cdot n_{r0} & -\frac{\Delta\alpha}{2} \cdot n_{r1} & -\frac{\Delta\alpha}{2} \cdot n_{r2} \\ \frac{\Delta\alpha}{2} \cdot n_{r0} & 1 & \frac{\Delta\alpha}{2} \cdot n_{r2} & -\frac{\Delta\alpha}{2} \cdot n_{r1} \\ \frac{\Delta\alpha}{2} \cdot n_{r1} & -\frac{\Delta\alpha}{2} \cdot n_{r2} & 1 & \frac{\Delta\alpha}{2} \cdot n_{r0} \\ \frac{\Delta\alpha}{2} \cdot n_{r2} & \frac{\Delta\alpha}{2} \cdot n_{r1} & -\frac{\Delta\alpha}{2} \cdot n_{r0} & 1 \end{bmatrix} \begin{bmatrix} s_0 \\ s_1 \\ s_2 \\ s_3 \end{bmatrix} \end{aligned} \tag{D.24}$$

Pulling the identity matrix out, one can rewrite the above equation as:

$$\begin{aligned}
\mathbf{s}(t+\Delta t) &= \left[I + \frac{\Delta\alpha}{2} \begin{bmatrix} 0 & -n_{r0} & -n_{r1} & -n_{r2} \\ n_{r0} & 0 & n_{r2} & -n_{r1} \\ n_{r1} & -n_{r2} & 0 & n_{r0} \\ n_{r2} & n_{r1} & -n_{r0} & 0 \end{bmatrix} \right] \begin{bmatrix} s_0 \\ s_1 \\ s_2 \\ s_3 \end{bmatrix} \\
&= \mathbf{s}(t) + \frac{\Delta\alpha}{2} \begin{bmatrix} 0 & -n_{r0} & -n_{r1} & -n_{r2} \\ n_{r0} & 0 & n_{r2} & -n_{r1} \\ n_{r1} & -n_{r2} & 0 & n_{r0} \\ n_{r2} & n_{r1} & -n_{r0} & 0 \end{bmatrix} \mathbf{s}(t) \\
&= \mathbf{s}(t) + \begin{bmatrix} s_0 & -s_1 & -s_2 & -s_3 \\ s_1 & s_0 & -s_3 & s_2 \\ s_2 & s_3 & s_0 & -s_1 \\ s_3 & -s_2 & s_1 & s_0 \end{bmatrix} \begin{bmatrix} 0 \\ n_{r0} \\ n_{r1} \\ n_{r2} \end{bmatrix} \frac{\Delta\alpha}{2}
\end{aligned} \tag{D.25}$$

moving $\mathbf{s}(t)$ to the left hand side, dividing by Δt leads to:

$$\frac{\mathbf{s}(t+\Delta t) - \mathbf{s}(t)}{\Delta t} = \frac{1}{2}\mathbf{s}(t)\mathbf{n}_r(t)\frac{\Delta\alpha}{\Delta t} \tag{D.26}$$

taking the limit at $\Delta t \rightarrow 0$ yields:

$$\begin{aligned}
\dot{\mathbf{s}}(t) &= \frac{1}{2}\mathbf{s}(t)\mathbf{n}_r(t)\dot{\alpha} \\
&= \mathbf{C}(t)\boldsymbol{\omega}(t)
\end{aligned} \tag{D.27}$$

where

$$\mathbf{C}(t) = \frac{1}{2}\begin{bmatrix} -s_1 & -s_2 & -s_3 \\ s_0 & -s_3 & s_2 \\ s_3 & s_0 & -s_1 \\ -s_2 & s_1 & s_0 \end{bmatrix} \tag{D.28}$$

and $\boldsymbol{\omega}(t)$ is the angular rate vector of the transition quaternion $\mathbf{\Delta r}$. Since **s** was post-multiplied by $\mathbf{\Delta r}$ in Eq. D.22, then in a physical system where the quaternion, **s**, represents a rotation between the navigation frame and the body frame $\boldsymbol{\omega}(t)$ will be the angular rate vector $[p, q, r]^T$ expressed in the body frame.

Appendix E

Navigation EKF Jacobians and Matrices

A complete discussion on Kalman Filters is contained in [70]; the following is a short discussion on the fundamental components of the Discrete Extended Kalman Filter which is used throughout this work.

E.1 Derivation of the A Matrix

Given a system described by Eq. 3.9, the $\mathbf{A}_k$ matrix from the Kalman Equations shown in Figure 4.1 is the Jacobian of the process model with respect to the states, and defined as:

$$\begin{aligned} A_k &\triangleq \left.\frac{\partial \mathbf{f}}{\partial \mathbf{x}}\right|_{\mathbf{x}=\hat{\mathbf{x}}_k} \\ &= \mathbf{I} + \left.\frac{\partial \dot{\mathbf{x}}}{\partial \mathbf{x}}\right|_{\mathbf{x}=\hat{\mathbf{x}}_k} dt \end{aligned} \tag{E.1}$$

The state vector has three components, the positions expressed in the NRF, the attitude quaternion, and the velocities and rates expressed in the BRF. The dynamics for the positions and attitude quaternion come from the kinematic equation, Eq. 3.5, and are a function of $\boldsymbol{\nu}$ and $\mathbf{s}$. The first set of partial derivatives for $\dot{\boldsymbol{\eta}}$ is the partial derivative with respect to $\boldsymbol{\nu}$ and is simply:

$$\begin{aligned} \frac{\partial \dot{\boldsymbol{\eta}}}{\partial \boldsymbol{\nu}} &= \frac{\partial \mathbf{J}(\mathbf{s})\boldsymbol{\nu}}{\partial \boldsymbol{\nu}} \\ &= \mathbf{J} \end{aligned} \tag{E.2}$$

The second set of partial derivatives, with respect to **s**, are a little more complicated. Since **J** is comprised of $\mathbf{J}_1 = \mathbf{R}^{B\to N}$ and $\mathbf{J}_2$, one can first note that the partial derivatives of $\mathbf{R}^{B\to N}$ with respect to the elements of the attitude quaternion are given by the following four derivative matrices:

$$\begin{aligned} &\frac{\partial \mathbf{R}^{B\to N}}{\partial s_0} = 2\begin{bmatrix} s_0 & -s_3 & s_2 \\ s_3 & s_0 & -s_1 \\ -s_2 & s_1 & s_0 \end{bmatrix} \quad \frac{\partial \mathbf{R}^{B\to N}}{\partial s_1} = 2\begin{bmatrix} s_1 & s_2 & s_3 \\ s_2 & -s_1 & -s_0 \\ s_3 & s_0 & -s_1 \end{bmatrix} \\ &\frac{\partial \mathbf{R}^{B\to N}}{\partial s_2} = 2\begin{bmatrix} -s_2 & s_1 & s_0 \\ s_1 & s_2 & s_3 \\ -s_0 & s_3 & -s_2 \end{bmatrix} \quad \frac{\partial \mathbf{R}^{B\to N}}{\partial s_3} = 2\begin{bmatrix} -s_3 & -s_0 & s_1 \\ s_0 & -s_3 & s_2 \\ s_1 & s_2 & s_3 \end{bmatrix} \end{aligned} \tag{E.3}$$

Similarly, the partial derivatives of the $\mathbf{J}_2$ with respect to the elements of $\mathbf{s}$, are as follows:

$$\frac{\partial \mathbf{J}_2}{\partial s_0} = \begin{bmatrix} 0 & 0 & 0 \\ 1 & 0 & 0 \\ 0 & 1 & 0 \\ 0 & 0 & 1 \end{bmatrix} \quad \frac{\partial \mathbf{J}_2}{\partial s_1} = \begin{bmatrix} -1 & 0 & 0 \\ 0 & 0 & 0 \\ 0 & 0 & -1 \\ 0 & 1 & 0 \end{bmatrix}$$
$$\frac{\partial \mathbf{J}_2}{\partial s_2} = \begin{bmatrix} 0 & -1 & 0 \\ 0 & 0 & 1 \\ 0 & 0 & 0 \\ -1 & 0 & 0 \end{bmatrix} \quad \frac{\partial \mathbf{J}_2}{\partial s_3} = \begin{bmatrix} 0 & 0 & -1 \\ 0 & -1 & 0 \\ 1 & 0 & 0 \\ 0 & 0 & 0 \end{bmatrix} \tag{E.4}$$

Therefore, the partial derivative of $\dot{\boldsymbol{\eta}}$ with respect to s_i would be given by:

$$\begin{aligned} \frac{\partial \dot{\boldsymbol{\eta}}}{\partial s_i} &= \frac{\partial \mathbf{J}(\mathbf{s})}{\partial s_i}\boldsymbol{\nu} \\ &= \begin{bmatrix} \frac{\partial \mathbf{R}^{B\rightarrow N}}{\partial s_i} & \mathbf{0}^{3\times 3} \\ \mathbf{0}^{4\times 3} & \frac{\partial \mathbf{J}_2}{\partial s_i} \end{bmatrix}\boldsymbol{\nu} \end{aligned} \tag{E.5}$$

The dynamics for $\boldsymbol{\nu}$ are given by Eq. 3.9. Since the coriolis force is small and contributes a lot of cross coupling, the overall effect of it's inclusion in $\mathbf{A}$ was deemed to be detrimental and as such it is neglected. Therefore, the simplified dynamics is given by:

$$\dot{\boldsymbol{\nu}} = \mathbf{M}^{-1}\left(\boldsymbol{\tau}\left(\boldsymbol{\delta}\right) - \mathbf{D}\left(\boldsymbol{\nu}\right)\boldsymbol{\nu} - \mathbf{g}\left(\mathbf{s}\right)\right) \tag{E.6}$$

which is a function of $\mathbf{s}$ and $\boldsymbol{\nu}$.

The first set of partial derivatives is respect to $\mathbf{s}$. Since only the gravitational component is a function of $\mathbf{s}$, the partial derivatives with respect to the elements of the quaternion are given by:

$$\begin{aligned}\frac{\partial \mathbf{g}\left(\eta\right)}{\partial s_i} &= -\frac{\partial}{\partial s_i}\begin{bmatrix} \mathbf{R}^{N\to B}\begin{bmatrix}0\\0\\W-B\end{bmatrix} \\ \mathbf{r}_{CG}\times\mathbf{R}^{N\to B}\begin{bmatrix}0\\0\\W\end{bmatrix}+\mathbf{r}_{CB}\times\mathbf{R}^{N\to B}\begin{bmatrix}0\\0\\-B\end{bmatrix}\end{bmatrix} \\ &= -\begin{bmatrix} \frac{\partial\mathbf{R}^{N\to B}}{\partial s_i}\begin{bmatrix}0\\0\\W-B\end{bmatrix} \\ \mathbf{r}_{CG}\times\frac{\partial\mathbf{R}^{N\to B}}{\partial s_i}\begin{bmatrix}0\\0\\W\end{bmatrix}+\mathbf{r}_{CB}\times\frac{\partial\mathbf{R}^{N\to B}}{\partial s_i}\begin{bmatrix}0\\0\\-B\end{bmatrix}\end{bmatrix}\end{aligned} \tag{E.7}$$

where the partial derivatives of the rotation matrix are given in Eq. E.3. The second, and last partial derivative, is with respect to $\boldsymbol{\nu}$, and is simply.

$$\begin{aligned}\frac{\partial\dot{\boldsymbol{\nu}}}{\partial\nu} &= \frac{\partial}{\partial\nu}-\mathbf{M}^{-1}\mathbf{D}\left(\boldsymbol{\nu}\right)\boldsymbol{\nu} \\ &= -\mathbf{M}^{-1}\left(\mathbf{D}_L+2\begin{bmatrix}\left|\boldsymbol{\nu}\right|^T\mathbf{D}_{Q_u}\\ \left|\boldsymbol{\nu}\right|^T\mathbf{D}_{Q_v}\\ \left|\boldsymbol{\nu}\right|^T\mathbf{D}_{Q_w}\\ \left|\boldsymbol{\nu}\right|^T\mathbf{D}_{Q_p}\\ \left|\boldsymbol{\nu}\right|^T\mathbf{D}_{Q_q}\\ \left|\boldsymbol{\nu}\right|^T\mathbf{D}_{Q_r}\end{bmatrix}\right)\end{aligned} \tag{E.8}$$

Since the biases are assumed to be a constant in the model, their partial derivatives are all zero.

E.2 Derivation of the H Matrix

The H_k matrix from the Kalman Equations shown in Figure 4.1 is the Jacobian of the measurement model with respect to the states and defined as:

$$H_k \triangleq \left. \frac{\partial \mathbf{h}}{\partial \mathbf{x}} \right|_{\mathbf{x}=\hat{\mathbf{x}}_k} \tag{E.9}$$

Organizing the measurement vector by instrument allows one to divide the H_k matrix up into strips as follows:

$$H_k = \begin{bmatrix} \frac{\partial \mathbf{h}_{IMU}}{\partial \mathbf{x}} \\ \frac{\partial \mathbf{h}_{Pressure}}{\partial \mathbf{x}} \\ \frac{\partial \mathbf{h}_{Compass}}{\partial \mathbf{x}} \\ \frac{\partial \mathbf{h}_{DVL}}{\partial \mathbf{x}} \\ \frac{\partial \mathbf{h}_{SBL}}{\partial \mathbf{x}} \end{bmatrix} \tag{E.10}$$

The derivatives for each sensor are derived in the sections below.

E.2.1 IMU

The measurement model for the IMU accelerometers given in Eq. 4.4 is a function of **s**, **v**, $\boldsymbol{\omega}$ and $\mathbf{B}_a$.

Using Eq. D.19 for $\mathbf{R}^{N\to B}$ and the sensor to body rotation matrix from Table 4.1, the first set of partial derivatives is with respect to **s** can be found as:

$$\begin{aligned}
\frac{\partial \mathbf{h}_a}{\partial \mathbf{s}_i} &= \frac{\partial \mathbf{R}^{N\to S}}{\partial \mathbf{s}_i}\begin{bmatrix} 0 \\ 0 \\ -g \end{bmatrix} \\
&= \mathbf{R}^{B\to S}\frac{\partial \mathbf{R}^{N\to B}}{\partial \mathbf{s}_i}\begin{bmatrix} 0 \\ 0 \\ -g \end{bmatrix}
\end{aligned} \tag{E.11}$$

where $\frac{\partial \mathbf{R}^{N\to B}}{\partial \mathbf{s}_i}$ can be obtained from Eq. E.3.

The second set of partial derivatives is with respect to the velocity vector $\mathbf{v} = [u\ v\ w]$. This one is slightly simpler and can be left in matrix notation.

$$\begin{aligned}
\frac{\partial \mathbf{h}_a}{\partial \mathbf{v}} &= \mathbf{R}^{B\to S}\frac{\partial}{\partial \mathbf{v}}2\boldsymbol{\omega}\times\mathbf{v} = \mathbf{R}^{B\to S}\frac{\partial}{\partial \mathbf{v}}2\tilde{\boldsymbol{\omega}}\mathbf{v} \\
&= 2\mathbf{R}^{B\to S}\tilde{\boldsymbol{\omega}}
\end{aligned} \tag{E.12}$$

The third set of partial derivatives is with respect to the angular rate vector $\boldsymbol{\omega} = [p\ q\ r]$.

$$\begin{aligned}
\frac{\partial \mathbf{h}_a}{\partial \boldsymbol{\omega}} &= \mathbf{R}^{B\to S}\frac{\partial}{\partial \boldsymbol{\omega}}\left(2\boldsymbol{\omega}\times\mathbf{v} + \boldsymbol{\omega}\times\boldsymbol{\omega}\times\mathbf{r}_{IMU}\right) \\
&= \mathbf{R}^{B\to S}\frac{\partial}{\partial \boldsymbol{\omega}}\left(-2\tilde{\mathbf{v}}\boldsymbol{\omega} + \tilde{\boldsymbol{\omega}}\tilde{\boldsymbol{\omega}}\mathbf{r}_{IMU}\right) \\
\frac{\partial \mathbf{h}_a}{\partial \omega_i} &= \mathbf{R}^{B\to S}\left(-2\tilde{\mathbf{v}} + \frac{\partial \tilde{\boldsymbol{\omega}}\tilde{\boldsymbol{\omega}}}{\partial \omega_i}\mathbf{r}_{IMU}\right) \\
&= \mathbf{R}^{B\to S}\left(-2\tilde{\mathbf{v}} + \frac{\partial}{\partial \omega_i}\begin{bmatrix} -(r^2+q^2) & qp & pr \\ qp & -(r^2+p^2) & qr \\ pr & qr & -(p^2+q^2) \end{bmatrix}\mathbf{r}_{IMU}\right)
\end{aligned} \tag{E.13}$$

where $\mathbf{r}_{IMU}$ is the position vector of the IMU in the BRF and the partial derivatives of $\tilde{\boldsymbol{\omega}}\tilde{\boldsymbol{\omega}}$

are:

$$\frac{\partial \tilde{\boldsymbol{\omega}}\tilde{\boldsymbol{\omega}}}{\partial p} = \begin{bmatrix} 0 & q & r \\ q & -2p & 0 \\ r & q & -2p \end{bmatrix} \quad \frac{\partial \tilde{\boldsymbol{\omega}}\tilde{\boldsymbol{\omega}}}{\partial q} = \begin{bmatrix} -2q & p & 0 \\ p & 0 & r \\ 0 & r & -2q \end{bmatrix}$$

$$\frac{\partial \tilde{\boldsymbol{\omega}}\tilde{\boldsymbol{\omega}}}{\partial q} = \begin{bmatrix} -2r & 0 & p \\ 0 & -2r & q \\ p & q & 0 \end{bmatrix} \tag{E.14}$$

Lastly, the fourth set of partial derivatives is with respect to the biases. Since the biases are calculated in the sensor frame they do not need to be rotated. Hence

$$\frac{\partial \mathbf{h}_a}{\partial \mathbf{B}_\mathbf{a}} = \mathbf{I}^{3\times 3} \tag{E.15}$$

The measurement model for the IMU rate gyros given in Eq. 4.5 is much simpler and only a function of $\boldsymbol{\omega}$ and $\mathbf{B}_g$. For $\mathbf{B}_g$ the partial derivatives are given by:

$$\frac{\partial \mathbf{h}_g}{\partial \boldsymbol{\omega}} = \mathbf{R}^{B\to S}\frac{\partial}{\partial \boldsymbol{\omega}}\boldsymbol{\omega} = \mathbf{R}^{B\to S}\mathbf{I}^{3\times 3} \tag{E.16}$$

For the biases, similar to the accelerometers, the partial derivatives are simply given by

$$\frac{\partial \mathbf{h}_g}{\partial \mathbf{B}_g} = \mathbf{I}^{3\times 3} \tag{E.17}$$

E.2.2 Pressure

The measurement model for the pressure sensors is given in Eq. 4.6 is a function of z and $\mathbf{s}$. Using the chain rule, the partial derivative of the pressure with respect to z and $\mathbf{s}$ will be:

$$\frac{\partial P}{\partial z} = \frac{\partial P}{\partial z_p}\frac{\partial z_p}{\partial z}, \quad \frac{\partial P}{\partial \mathbf{s}} = \frac{\partial P}{\partial z_p}\frac{\partial z_p}{\partial \mathbf{s}} \tag{E.18}$$

If Φ is the latitude in radians, the partial derivative with respect to z_p are:

$$\begin{aligned}
\frac{\partial k}{\partial z_p} &= \frac{2\times 10^{-5}\,(g-9.80612)}{(9.80612-2\times 10^{-5} z_p)^2} \qquad \text{(E.19)}\\
\frac{\partial h_{45}}{\partial z_p} &= 1.00818\times 10^{-2} + 2\cdot 2.465\times 10^{-8} z_p - 3\cdot 1.25\times 10^{-13} z_p^2 + 4\cdot 2.8\times 10^{-19} z_p^3\\
\frac{\partial \delta h}{\partial z_p} &= \frac{1}{(z_p+100)^2} + 6.2\times 10^{-6}\\
g &= 9.7803(1+5.3\times 10^{-3} sin(\Phi)^2)\\
\frac{\partial P}{\partial z} &= 10\left(\frac{\partial h_{45}}{\partial z_p}k + h_{45}\frac{\partial k}{\partial z_p}\right) - \frac{\partial \delta h}{\partial z_p}
\end{aligned}$$

Then using Eq. D.19 one can derive the partial derivatives of z_p to be:

$$\begin{aligned}
\frac{\partial z_p}{\partial z} &= 1 \qquad \text{(E.20)}\\
\frac{\partial z_p}{\partial s_0} &= 2\left(-s_2X^B_{p_1} + s_1X^B_{p_2} + s_0X^B_{p_3}\right)\\
\frac{\partial z_p}{\partial s_1} &= 2\left(s_3X^B_{p_1} + s_0X^B_{p_2} - s_1X^B_{p_3}\right)\\
\frac{\partial z_p}{\partial s_2} &= 2\left(-s_0X^B_{p_1} + s_3X^B_{p_2} - s_2X^B_{p_3}\right)\\
\frac{\partial z_p}{\partial s_3} &= 2\left(s_1X^B_{p_1} + s_2X^B_{p_2} + s_3X^B_{p_3}\right)
\end{aligned}$$

E.2.3 Compass

The compass measurements are based solely on the quaternion, **s**. Recall that derivatives for the trig functions $atan(x)$ and $asin(x)$ are:

$$\frac{d}{dx}asin(x) = \frac{1}{\sqrt{1-x^2}},\quad \frac{d}{dx}atan(x) = \frac{1}{1+x^2} \qquad \text{(E.21)}$$

Therefore, using the chain rule the partial derivatives of the measurements can be obtained as follows

$$\frac{\partial}{\partial s_i}\phi = -\frac{1}{1+\left(\frac{2(s_1s_3+s_0s_2)}{s_0^2-s_1^2-s_2^2+s_3^2}\right)^2}\frac{\partial}{\partial s_i}\left(\frac{2\left(s_1s_3+s_0s_2\right)}{s_0^2-s_1^2-s_2^2+s_3^2}\right) \tag{E.22}$$

$$\frac{\partial}{\partial s_i}\theta = \frac{1}{\sqrt{1-\left(2\left(s_1s_3-s_0s_2\right)\right)^2}}\frac{\partial}{\partial s_i}2\left(s_1s_3-s_0s_2\right) \tag{E.23}$$

$$\frac{\partial}{\partial s_i}\psi = -\frac{1}{1+\left(\frac{2(s_1s_3+s_0s_2)}{s_0^2-s_1^2-s_2^2+s_3^2}\right)^2}\frac{\partial}{\partial s_i}\left(\frac{2\left(s_1s_3+s_0s_2\right)}{s_0^2-s_1^2-s_2^2+s_3^2}\right) \tag{E.24}$$

E.2.4 DVL

The measurement model for the DVL given in Eq. 4.13 is a function of the velocities, **V**, and the angular rates, ω. For **V** the partial derivatives are given by:

$$\frac{\partial \mathbf{h}_d}{\partial \mathbf{V}} = \mathbf{R}^{B\to S}\frac{\partial}{\partial \mathbf{V}}\mathbf{V} = \mathbf{R}^{B\to S}\mathbf{I}^{3\times 3} \tag{E.25}$$

For ω the partial derivatives are simply:

$$\begin{aligned}\frac{\partial \mathbf{h}_d}{\partial \boldsymbol{\omega}_i} &= \mathbf{R}^{B\to S}\frac{\partial}{\partial \boldsymbol{\omega}_i}\tilde{\boldsymbol{\omega}}\mathbf{X}_D^B \\ &= \mathbf{R}^{B\to S}\tilde{\mathbf{e}}_i\mathbf{X}_D^B\end{aligned} \tag{E.26}$$

where $\mathbf{e}_i$ is the unit vector along the axis of rotation.

E.2.5 SBL

The measurement model for the SBL given in Eq. 4.15 is a function of the position in the NRF, $\mathbf{X}_{CG}^N$ and the attitude quaternion **s**. For $\mathbf{X}_{CG}^N$ the partial derivatives in matrix notation are given by:

$$\frac{\partial \mathbf{h}_{si}}{\partial \mathbf{X}_{CG}^{N}} = \frac{\left(\mathbf{X}_{cg}^{N} + \mathbf{X}_{r}^{N} - \mathbf{X}_{si}^{N}\right)^{T}}{\| \mathbf{X}_{cg}^{N} + \mathbf{X}_{r}^{N} - \mathbf{X}_{si}^{N} \|} \tag{E.27}$$

For **s** the partial derivatives in matrix notation are given by:

$$\begin{aligned} \frac{\partial \mathbf{h}_{si}}{\partial \mathbf{s}_{j}} &= \frac{\left(\mathbf{X}_{cg}^{N} + \mathbf{X}_{r}^{N} - \mathbf{X}_{si}^{N}\right)^{T}}{\| \mathbf{X}_{cg}^{N} + \mathbf{X}_{r}^{N} - \mathbf{X}_{si}^{N} \|} \cdot \frac{\partial \mathbf{X}_{r}^{N}}{\partial \mathbf{s}_{j}} \\ &= \frac{\left(\mathbf{X}_{cg}^{N} + \mathbf{X}_{r}^{N} - \mathbf{X}_{si}^{N}\right)^{T}}{\| \mathbf{X}_{cg}^{N} + \mathbf{X}_{r}^{N} - \mathbf{X}_{si}^{N} \|} \cdot \frac{\partial \mathbf{R}^{B\to N}}{\partial \mathbf{s}_{j}} \mathbf{X}_{r}^{B} \end{aligned} \tag{E.28}$$

where the partial derivatives of the rotation matrix $\mathbf{R}^{B\to N}$ are the partial derivatives described in Eq. E.3 and $\mathbf{X}_{r}^{B}$ is the position of the SBL rover in the BRF.

E.3 Initial Values for $\mathbf{x}_0$, $\mathbf{P}_0$, $\mathbf{Q}_P$, and $\mathbf{R}_M$ Matrix Values

E.3.1 $\mathbf{x}_0$ Vector

$\mathbf{x}_0 \in \Re^{19}$ is the initial state estimate. The EKF is always started with the vehicle in the water, typically with the vehicle on the surface (which put the CG of the vehicle at approximately 0.92 m in the NRF. This leads to the following initial guess:

$$\begin{array}{llll} \mathbf{x}_{0_x} = 0 \ \ m & \mathbf{x}_{0_y} = 0 \ \ m & \mathbf{x}_{0_z} = 0.92 \ \ m & \\ \mathbf{x}_{0_{s_0}} = 1 & \mathbf{x}_{0_{s_1}} = 0 & \mathbf{x}_{0_{s_2}} = 0 & \mathbf{x}_{0_{s_3}} = 0 \\ \mathbf{x}_{0_u} = 0 \ \ m/s & \mathbf{x}_{0_v} = 0 \ \ m/s & \mathbf{x}_{0_w} = 0 \ \ m/s & \\ \mathbf{x}_{0_p} = 0 \ \ rad/s & \mathbf{x}_{0_q} = 0 \ \ rad/s & \mathbf{x}_{0_r} = 0 \ \ rad/s & \\ \mathbf{x}_{0_{ba_x}} = 0 \ \ mG/s^2 & \mathbf{x}_{0_{ba_y}} = 0 \ \ mG/s^2 & \mathbf{x}_{0_{ba_z}} = 0 \ \ mG/s^2 & \\ \mathbf{x}_{0_{bg_x}} = 0 \ \ {}^\circ/s^2 & \mathbf{x}_{0_{bg_y}} = 0 \ \ {}^\circ/s^2 & \mathbf{x}_{0_{bg_z}} = 0 \ \ {}^\circ/s^2 & \end{array} \tag{E.29}$$

where $\mathbf{x}_{0_i}$ is the initial estimate error covariance for state variable i.

E.3.2 $\mathbf{P}_0$ Matrix

$\mathbf{P}_0 \in \Re^{19\times 19}$ captures the uncertainty in the initial state estimate. Tuning the EKF resulted in the following non-zero entries for $\mathbf{P}_0$:

$$\begin{aligned}
&\mathbf{P}_{0_{xx}} = 9 && \mathbf{P}_{0_{yy}} = 9 && \mathbf{P}_{0_{zz}} = 9 && \\
&\mathbf{P}_{0_{s_0 s_0}} = 1 && \mathbf{P}_{0_{s_1 s_1}} = 1 && \mathbf{P}_{0_{s_2 s_2}} = 1 && \mathbf{P}_{0_{s_3 s_3}} = 1 \\
&\mathbf{P}_{0_{uu}} = 1 && \mathbf{P}_{0_{vv}} = 1 && \mathbf{P}_{0_{ww}} = 1 && \\
&\mathbf{P}_{0_{pp}} = 1 && \mathbf{P}_{0_{qq}} = 1 && \mathbf{P}_{0_{rr}} = 1 && \\
&\mathbf{P}_{0_{ba_x ba_x}} = 10000 && \mathbf{P}_{0_{ba_y ba_y}} = 10000 && \mathbf{P}_{0_{ba_z ba_z}} = 10000 && \\
&\mathbf{P}_{0_{bg_x bg_x}} = 100 && \mathbf{P}_{0_{bg_y bg_y}} = 100 && \mathbf{P}_{0_{bg_z bg_z}} = 100 &&
\end{aligned} \tag{E.30}$$

where $\mathbf{P}_{0_{ik}}$ is the initial estimate error covariance for state variable i as a result of errors in state variable k. The values in $\mathbf{P}_0$ are not critical to the ultimate convergence of the EKF, but smart choice will help it converge faster. The units on the entries are the units of state variable i multiplied by the unit of state variable k.

E.3.3 $\mathbf{Q}_P$ Matrix

$\mathbf{Q}_P \in \Re^{19\times 19}$ captures the uncertainty in the process model. Tuning the EKF resulted in the following non-zero entries for $\mathbf{Q}_P$:

$$\begin{array}{llll}
\mathbf{Q}_{P_{xx}} = 9 & \mathbf{Q}_{P_{yy}} = 9 & \mathbf{Q}_{P_{zz}} = 9 & \\
\mathbf{Q}_{P_{s_0s_0}} = 0.25 & \mathbf{Q}_{P_{s_1s_1}} = 0.25 & \mathbf{Q}_{P_{s_2s_2}} = 0.25 & \mathbf{Q}_{P_{s_3s_3}} = 0.25 \\
\mathbf{Q}_{P_{uu}} = 0.25 & \mathbf{Q}_{P_{vv}} = 0.25 & \mathbf{Q}_{P_{ww}} = 0.25 & \\
\mathbf{Q}_{P_{pp}} = 0.25 & \mathbf{Q}_{P_{qq}} = 0.25 & \mathbf{Q}_{P_{rr}} = 0.25 & \\
\mathbf{Q}_{P_{ba_xba_x}} = 1 & \mathbf{Q}_{P_{ba_yba_y}} = 1 & \mathbf{P}_{Q_{ba_zba_z}} = 1 & \\
\mathbf{Q}_{P_{bg_xbg_x}} = 0.01 & \mathbf{Q}_{P_{bg_ybg_y}} = 0.01 & \mathbf{Q}_{P_{bg_zbg_z}} = 0.01 & \\
\mathbf{Q}_{P_{xs_1}} = 0.25 & \mathbf{Q}_{P_{xs_2}} = 0.25 & \mathbf{Q}_{P_{xs_3}} = 0.25 & \mathbf{Q}_{P_{xs_4}} = 0.25 \\
\mathbf{Q}_{P_{ys_1}} = 0.25 & \mathbf{Q}_{P_{ys_2}} = 0.25 & \mathbf{Q}_{P_{ys_3}} = 0.25 & \mathbf{Q}_{P_{ys_4}} = 0.25 \\
\mathbf{Q}_{P_{zs_1}} = 0.25 & \mathbf{Q}_{P_{zs_2}} = 0.25 & \mathbf{Q}_{P_{zs_3}} = 0.25 & \mathbf{Q}_{P_{zs_4}} = 0.25 \\
\mathbf{Q}_{P_{xu}} = 0.25 & \mathbf{Q}_{P_{xv}} = 0.25 & \mathbf{Q}_{P_{xw}} = 0.25 & \\
\mathbf{Q}_{P_{yu}} = 0.25 & \mathbf{Q}_{P_{yv}} = 0.25 & \mathbf{Q}_{P_{yw}} = 0.25 & \\
\mathbf{Q}_{P_{zu}} = 0.25 & \mathbf{Q}_{P_{zv}} = 0.25 & \mathbf{Q}_{P_{zw}} = 0.25 & \\
\mathbf{Q}_{P_{s_1p}} = 0.09 & \mathbf{Q}_{P_{s_1q}} = 0.09 & \mathbf{Q}_{P_{s_1r}} = 0.09 & \\
\mathbf{Q}_{P_{s_2p}} = 0.09 & \mathbf{Q}_{P_{s_2q}} = 0.09 & \mathbf{Q}_{P_{s_2r}} = 0.09 & \\
\mathbf{Q}_{P_{s_3p}} = 0.09 & \mathbf{Q}_{P_{s_3q}} = 0.09 & \mathbf{Q}_{P_{s_3r}} = 0.09 & \\
\mathbf{Q}_{P_{s_4p}} = 0.09 & \mathbf{Q}_{P_{s_4q}} = 0.09 & \mathbf{Q}_{P_{s_4r}} = 0.09 &
\end{array} \tag{E.31}$$

where $\mathbf{Q}_{P_{ik}}$ is the error covariance for state variable i as a result of errors in state variable k. The values in $\mathbf{Q}_P$ will determine how much weight the model has compared to the measurements in the state estimate. The units on the entries are the units of state variable i multiplied by the unit of state variable k.

E.3.4 $\mathbf{R}_M$ Matrix

$\mathbf{R}_M \in \Re^{17\times 17}$ captures the uncertainty in the measurements. Comparison of the sensor output to known states in a dynamic environment resulted in the following non-zero values for $\mathbf{R}_M$:

$$\begin{array}{llll}
\mathbf{R}_{IMU_{axax}} = 900 & \mathbf{R}_{IMU_{ayay}} = 900 & \mathbf{R}_{IMU_{azaz}} = 900 & \\
\mathbf{R}_{IMU_{gxgx}} = 0.56 & \mathbf{R}_{IMU_{gygy}} = 0.56 & \mathbf{R}_{IMU_{gzgz}} = 0.56 & \\
\mathbf{R}_{P_{pp}} = 6.25e-8 & & & \\
\mathbf{R}_{C_{\phi\phi}} = 0.25\left(\frac{\pi}{180}\right)^2 & \mathbf{R}_{C_{\theta\theta}} = 0.25\left(\frac{\pi}{180}\right)^2 & \mathbf{R}_{C_{\psi\psi}} = 0.56\left(\frac{\pi}{180}\right)^2 & \\
\mathbf{R}_{DVL_{uu}} = X.X & \mathbf{R}_{DVL_{vv}} = X.X & \mathbf{R}_{DVL_{ww}} = X.X & \\
\mathbf{R}_{SBL_{r1}} = 0.0016 & \mathbf{R}_{SBL_{r2}} = 0.0016 & \mathbf{R}_{SBL_{r3}} = 0.0016 & \mathbf{R}_{SBL_{r4}} = 0.0016
\end{array} \tag{E.32}$$

where $\mathbf{R}_{M_{ik}}$ is the error covariance for measurement i as a result of errors in measurement k. While in theory there can be cross coupled errors in the measurements it is unlikely, so for this work we assume that the measurements are all independent and $\mathbf{R}_M$ is a diagonal matrix. The units on the entries are the unit of measurement i multiplied by the unit of measurement k.

Appendix F

Sensing Systems

Most underwater positioning systems have the same basic components. For example, a typical Ultra Short Base Line (USBL) system is comprised of an acoustic transceiver and transponder for obtaining range and bearing from the boat to the underwater vehicle, a system for determining the position of the vessel (and therefore the transceiver) such as the Global Positioning System (GPS) or the LOng RAnge Navigation system (LORAN), and a Motion Reference Unit (MRU) for determining the orientation (roll, pitch, and yaw) of the vessel. The following section discusses the different types of sensors available to perform these functions and the errors associated with each.

F.1 Acoustic Tracking Systems

Acoustic tracking systems are the most commonly used instruments for estimating the position of ROVs and other subsea vehicles. Acoustic positioning systems are typically divided into the following types: Long BaseLine (LBL), Short BaseLine (SBL) and USBL) systems. A brief comparison of the different types of systems is provided below; in depth discussions on Acoustic tracking systems can be found in [67] and [23].

LBL systems use multiple (3 or more) acoustic transponders on the seafloor, whose positions have been carefully surveyed, to estimate the position of a remote transceiver, attached to the underwater vehicle. The transponders each emit an acoustic pulse in response to an initiating pulse from the transceiver on the vehicle. The system on the vehicle uses time of flight of the response to trilaterate the position of the vehicle; with an LBL system the position information is calculated on the vehicle and must be transmitted to the surface to the pilot. LBL systems are typically the most accurate type of underwater positioning but are difficult to install and calibrate. Each transponder must be deployed and surveyed before the system can be used. This type of system is most appropriate on a long term underwater installation; the deployment challenges typically make this LBL systems inappropriate for small ROVs that are operating in new areas all the time.

SBL systems use multiple (3 or more) acoustic transceivers attached to the ship's hull and a transponder on the vehicle. Like LBL, SBL systems use time of flight and trilateration to determine the position of the vehicle; unlike LBL systems, the position of the vehicle is calculated on the surface equipment, and the vehicle doesn't have any knowledge of where it is. The accuracy of the solution will be dependent on how far apart the transceivers are spaced on the ship's hull. Therefore, SBL systems are typically only used with larger vessels. Similarly to LBL systems, the position of the transceivers must be very well known with respect to each other. However, this only provides a tracking solution for the vehicle relative to the vessel. In order to know the absolute position of the vehicle, the attitude and position of the vessel must also be known. Therefore, SBL systems also require a MRU and vessel positioning system such as LORAN or GPS.

USBL systems are the most popular type of acoustic positioning systems with ROV operators who utilise vessels of opportunity. A USBL system uses a single transponder to estimate the position of the vehicle. Unlike LBL and SBL systems, USBL systems have only one transceiver which has an array of acoustic elements. This transceiver computes both the direction of arrival and range to the pinger on the vehicle. The ranging data comes from time of flight and the direction of arrival is calculated through the difference in phase of the received ping across the acoustic array. USBL systems have the advantage of being relatively easy to deploy as, unlike LBL and SBL systems, they don't rely on the precise localisation of transducers to establish a highly accurate solution. Like the SBL system the USBL system requires knowledge of the position and attitude of the vessel in order to know the absolute position of the vehicle.

While the advantages of USBL systems are clear, it is often costly to build a system which can provide a precision tracking solution as the accuracy of the underwater tracking solution is dependant on the accuracy of the MRU on the vessel. This is especially difficult on small vessels of opportunity that experience a lot more motion due to sea state than larger vessels. ROV operators operating in such conditions often use traditional dead reckoning for navigation and only use the USBL tracking systems to give then a general idea of where the vehicle is in case of emergency.

F.2 Compasses and Inertial Sensors

Inertial measurement systems are often comprised of an IMU or Attitude Heading Reference System (AHRS), and an observer (Kalman filter, particle filter, etc) to optimally combine the measurements. High-end systems often have the observer contained in the sensor itself. These devices are often called an Inertial Navigation Systems (INS). However, as with this research, the observer can also be separate software that uses the raw output of the inertial sensors. In this work, an IMU refers to an instrument which contains a 3-axis accelerometer and a 3-axis rate gyro and an AHRS is an instrument that contains a 3-axis accelerometer, a 3-axis rate gyro, and a 3-axis magnetometer. A compass typically focuses on measuring heading and will usually contains a 3-axis magnetometer and accelerometers for measuring the inclination of the instrument. Accelerometers are used to measure the acceleration vector, magnetometers are used to measure the magnetic field vector, and rate gyros are used to measure the angular rate on each axis.

There isn't an agreed upon standard for classifying the quality of inertial sensors. However, in general, modern inertial sensors can be loosely classified into the following categories: Marine grade, Navigation grade, Tactical Grade, Industrial Grade, and Automotive or Consumer Grade. Marine grade are the highest accuracy systems and are used on submarines, spacecraft and other systems where navigational accuracy is absolutely critical. An INS built with marine grade sensors can expect to have an unaided navigational accuracy of less than 2 km over a 24 hour period but can cost upward of a million dollars. Navigation grade sensors are the next best for navigational stability and are typically used in commercial aircraft and on ships. An INS built with navigation grade sensors would typically cost a few hundred thousand dollars and have an unaided navigational accuracy of less than 1.5km over an hour. These systems, when coupled with a Military grade GPS, can provide navigation solutions that are accurate to within a few centimetres [26].

Tactical and Industrial grade inertial systems are the high-end consumer products. These systems cost between one thousand dollars for a low-end industrial grade IMU to thirty thousand dollars for a high-end tactical grade. A tactical and industrial grade INSs can provide a reasonable unaided navigation solution for a few minutes and few seconds, respectively. These two grades of system typically contain similar accelerometers, but differ in the quality of the rate gyro. The lowest category is the automotive or consumer grade sensors. These sensors are often sold individually rather than in an integrated IMU or AHRS package and typically they are used in airbags, anti-lock brakes, entertainment systems, and other non-navigation related applications. Often the consumer grade sensing devices are the same products as those used in an industrial grade system and the primary difference between the two categories is the sensor calibration [26].

F.2.1 Accelerometers

Accelerometers measure the specific force on the instrument along a given axis. Historically, accelerometers were large mechanical devices and had one of two main designs: the pendulous mass or the vibrating beam. Although there are other more complex precision accelerometer designs, such as the Pendulating Integrating Gyroscopic Accelerometer, this type of instrument is typically used for military operations and not readily available for mainstream applications. Pendulous mass designs have a hinged beam, perpendicular to the axis of sensitivity, with a proof mass on the end. Pendulous mass accelerometers can either be open or closed loop designs. Open loop pendulous mass accelerometers suspend the beam with springs and then measure the deflection of the mass to obtain the specific force. Closed loop designs use either a magnetic or electrostatic torquer coil to keep the beam centred, using the position of the mass for feedback. In closed loop designs, the specific force is function of the current in the torquer coil rather than the position of the mass.

Vibrating beam designs still use the hinged beam with a mass on the end, but in this type of instrument, the hinged beam is supported top and bottom by a stiff beam parallel to the axis of sensitivity. These stiff beams are driven to vibrate at their resonant frequencies. Under acceleration, the hinged beam will push on one vibrating beam and pull on the other changing their lengths slightly and, therefore, changing their resonant frequencies. The specific force will be a function of the change in resonant frequency.

Traditional open loop pendulous mass devices suffered from several draw backs: 1) The force exerted by a spring is not actually linear and usually exhibits hysteresis, 2) Since the mass is swinging about a pivot as the arm moves so does the axis of sensitivity - this leads to nonlinearity and sensitivity to specific forces on orthogonal axes, 3) the motion of the mass makes it necessary to be able to measure the position of the mass over a large area. The closed loop designs mitigated these issues by keeping the mass stationary, but are more complex mechanically and when unpowered they are highly susceptible to shock damage. High precision vibrating beam devices are typically manufactured using quartz suspension beams. Since this mechanism is essentially static, with the hinged beam fixed between the vibrating beams, this type of device does not exhibit the issues seen with either of the pendulous designs. However, temperature sensitivity and instability in the crystals can cause drift in the measurement.

Micro-Electro-Mechanical Systems (MEMS) technology has allowed sensor manufacturers to use these same basic mechanical principals but make the devices smaller and more robust. MEMS accelerometers are much cheaper to manufacture and generally out perform the equivalent conventionally manufactured sensor, showing improved robustness, temperature characteristics, repeatability, and bias stability. In these sensors, the force on or deflection of the proof mass can be measured by a differential capacitor, piezoresistive element, piezoelectric element, hall-effect sensor, magnetoresistive element or optical sensor. Different sensing structures can combine with variations in mechanical design to tailor accelerometers to a wide range of applications and price points. MEMS has also enabled new accelerometer designs, including devices that: 1) detect acceleration related changes in the temperature profile around a heating element, and 2) measure the changes in capacitance due to the movement of a liquid bubble in a capillary tube [68]. Marine and navigational grade accelerometers are typically still manufactured conventionally using piezoelectric elements, but tactical, industrial and consumer grade accelerometers are predominantly MEMS sensors.

In the rest of this section, errors found in accelerometers are discussed. The significance of the error depends on the type and quality of sensor. While it is possible to characterise all of these error sources, it is not always practical, so a designer must decide which elements are most important for a given application.

Alignment Errors: Mounting alignment errors occur in two places: 1) alignment of the instrument on the vessel, and 2) alignment of the accelerometers with respect to each other in the triad. The first problem results in a steady state angular error and the second results in non-orthogonality of the sensitive axes.

Bias Errors: For accelerometers that use a proof mass, bias errors typically arise from the null position of the proof mass (or bubble) being different from the null position of the pick-off sensor. This bias can change with temperature, or over longer periods, from fatigue. Minimising changes in the startup bias is an important consideration for accelerometers used in strapdown systems which cannot be recalibrated before each use. Hysteresis of the mechanical and electrical components will contribute to bias variations during operations.

Scale Factor Errors: Machining imperfections in the sensor will cause the sensitivity on each axis to be slightly different. One example of this would be minute variations in thickness of polysilicon springs in a MEMS pendulous mass accelerometer. The scale factor may even differ between positive and negative accelerations.

Non-linearities: G-squared terms (terms depending on the square of the acceleration or the product of two orthogonal accelerations) or G-cubed terms arise from non-linearities in the accelerometer. These effects typically show up in mechanical accelerometers at higher accelerations when the proof mass is highly deflected. Large deflections can also cause cross-coupling, by changing the orientation of the axis of sensitivity. Lastly, orthogonal accelerations can cause changes in the properties of the accelerometer. For example, in pendulous mass accelerometers, a large acceleration along the axis of the pendulum can cause compression on the hinge altering its dynamic performance.

Dynamic Errors: Constant angular velocity, angular acceleration, and the internal separation of the accelerometers in the triad can lead to anisonertia, output axis coupling, and size effects respectively. The first two errors occur predominantly in mechanical accelerometers, while the third is an issue with all accelerometer designs. Anisonertia effects are torques that arise in the beam or pendulum hinge due to centripetal acceleration; thereby changing the measurable effect of the acceleration. Output axis coupling occurs when a similar torque develops due to angular acceleration of the system. The size effect, which is much less important in MEMS accelerometers, occurs when the individual accelerometers in the triad are not exactly co-located. This means that angular motion will cause accelerations that are a function of the distance separating the sensors.

F.2.2 Rate Gyros

A rate gyro is a device that measures angular velocity. Historically, rate gyros were large spinning disks which would precess when forced to rotate about an axis orthogonal to the spin axis. These devices were typically large and difficult to handle. Modern rate gyros use a variety of solid state technologies that range from very low to very high in cost. The following section describes some of the different types of rate gyros and the errors that are commonly seen with these devices.

In a spinning mass rate gyro, a motor driving a spinning mass is mounted to a pivot. The mass spins about the spin axis. The motor and spinning mass are constrained to rotate with the instrument on one axis, known as the input axis, but is free to rotate about a pivot (the output axis), which is perpendicular to both the input and spin axes. Rotating the spinning mass about the input axis introduces a torque on the assembly about the output axis. The motor assembly is typically suspended by springs that resist the induced torque. Then the deflection of the motor assembly is proportional to the induced torque which is related to the angular rate about the input axis. The deflection of the motor assembly can be measured through capacitive, magnetic, piezoresistive, or piezoelectric means as seen with the accelerometers.

Vibratory gyroscopes work on the same principle as the Foucault pendulum which was invented in 1851 by Jean Bernard Leon Foucault to measure the rotation of the earth. Foucault's pendulum measured the rate of the earths rotation by observing the affects of the resulting coriolis force on the pendulum. Vibratory gyroscopes use the same principal, deriving the rate of rotation by observing the affects of the coriolis force, which induces harmonic motion orthogonal to both the axis of vibration and the axis of rotation, on the vibrating element. The amplitude of the induced motion is proportional to the angular rate. This style of gyro comes in many shapes and sizes, where the vibratory element may be a string, one or more beams, a tuning fork, a ring, a cylinder, or a hemisphere. The method of detection depends on the design of the rate gyro, but typically uses some arrangement of pick offs to measure the vibration or a resulting torque. Vibratory gyroscopes tend to be low cost, low performance, MEMS devices. The exception is the hemispherical resonator gyro that can provide navigation grade performance. Since vibratory gyroscopes are detecting an induced acceleration, they can be affected by the relative orientation of gravity or the acceleration vector of the instrument.

Ring Laser Gyros (RLG) create a closed loop light path inside the sensor chamber using mirrors. A laser creates two counter propagating beams of light that are compared using a photo detector. When the instrument is stationary the beams of light interfere constructively. When the instrument is rotating in the plane of the light rings one beam will have a shorter path length to the detector than the other (the Sagnac effect). This will cause a change in the beam interference pattern; the beat frequency of the beams will be proportional to the angular rate of the instrument. In a ring laser gyro the ring, laser, and detectors are all an integral unit and the measured phase shift is proportional to the accumulated rotation. RLGs are very precise instruments, but at low frequencies scattering in the chamber causes coupling between the two beams, which prevents the photo detector from measuring the rotation. This is called lock-in and is usually mitigated by dithering the optical chamber thereby keeping the instrument out of the lock-in zone.

Fiber Optic Gyros (FOG) also utilise the Sagnac effect to measure angular rotation, but instead of using an integrated light chamber with mirrors, the light path is created from fiber optics. In a FOG, beam splitters are used to allow a laser to inject counter propagating beams into a coil of optical fiber and then recombine the beams back at a detector. When the FOG is rotated in the plane of the coil the distance travelled by the two beams will change and the detector will observe a phase change proportional to the angular velocity and the total path length of the beams. Therefore the sensitivity of the instrument can be increased by using a fiber coil with more wraps. FOGs were originally introduced as a low cost alternative to RLGs but the technology has now matured to a point where FOGs are the most reliable and accurate rate gyros available and are no longer a low cost alternative.

Optical rate gyros are very robust, stable, and highly accurate measuring devices. FOGs and RLGs are usually the cornerstone instruments in medium and high end INSs. They are still prone to mounting alignment errors, but since these devices are usually found in high end systems, care is taken to ensure that they are well aligned to minimise any alignment issues. Mechanical rate gyros (spinning mass and vibratory) have many of the same sources of error as described for accelerometers, specifically alignment errors, bias errors, scale factor errors, non-linearities, and dynamic errors from external accelerations.

F.2.3 Magnetometers

The Earth's magnetic field has been a cornerstone of navigation for centuries. There is evidence that the Chinese developed magnetic direction finding devices as early as 200 BC, but these devices were used for mystical purposes, and it was many centuries before people started using magnets for navigation. Sometime between the 9th and 13th century, magnetic compasses became common navigational tools on ships in both Eastern and Western cultures. These early compasses were made using small iron needles that were magnetised using loadstones, a naturally occurring permanent magnet [45, 6]. Even back then, compass calibration was an important part of navigation, and early explorers carried a large loadstone with them on voyages so that they could remagnetise their compass needle along the way. The following is a brief review of some key points about magnetism relevant to the use of magnetic sensors, more in-depth discussions on magnetic theory and it's application to navigation can be found in [45, 27, 9, 6].

The same theory can be used to explain both electromagnetics and ferromagnetics. While the magnetic force from an electromagnet is generated by a current carrying wire, the magnetic force inside of a ferromagnet is generated by electrons spinning around their atomic nuclei, and the strength of the magnetic field depends on how well aligned the atoms are with each other. Ferromagnetic substances such as iron or rare earth alloys contain microscopic regions called domains. In each domain the magnetic fields from the individual atoms are aligned. In a piece of demagnetised iron, the direction of the domains will be random, whereas in a magnetised piece the domains will have a dominant direction.

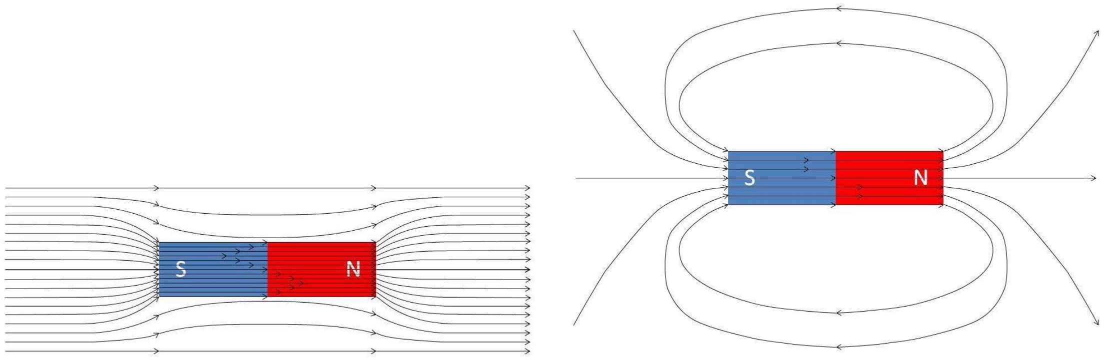

(a) **(b)**

Figure F.1: Visualization of the magnetic force lines for: a ferromagnetic substance exposed to (a) an external magnetic field and (b) a permanent magnet.

When a ferromagnetic material is placed in a weak magnetic field, the domains that are nearly aligned with the external field rotate into alignment, causing the ferromagnetic material to have a net magnetic field. If the external magnetic field is strong enough, all the domains will rotate into alignment, saturating the material, and creating the strongest field. Magnetism which is present only under the influence of an external field is called **induced** magnetism and that which remains after the magnetising force is removed is called **residual** magnetism. A ferromagnetic substance, which retains its domain alignment after the external field is removed, is called a permanent magnet and is said to have a high **retentivity**. The strength of the reverse field that is required to reduce the magnetism back to zero is called the **coercivity** of the magnet. In materials with low retentivity, the domains reorient themselves in a random fashion after the external forces are removed. Hard iron is a material with high retentivity and soft iron is a material with low retentivity.

All practical magnets have a north and south pole. The lines of magnetic force (or flux) inside of a magnet point from the south to the north pole, and the density of the lines represents the intensity of the field in that area. When a ferromagnetic material is placed in a uniform magnetic field, the lines of flux tend to get sucked in towards the material, as shown in Figure F.1-a [6]. If the iron becomes permanently magnetised then after the external field is removed then the lines of flux of the external field of the permanent magnet will circle around from the north pole and to the south pole, as shown in Figure F.1-b.

The source of the Earth's magnetic field is still widely debated. However, one point not debated is that it exists and, on average, the field looks as if there is a short but very powerful bar magnet in the Earth's core and the overall field has a dipole shape that is similar to Figure F.1-b. Although the dipole model provides a convenient means of picturing the Earth's magnetic field, when one studies the Earth's magnetic field up close, it is far more complex than that of a simple dipole magnet. Not only is it constantly changing, but locally the Earth's magnetic field is affected by many local factors and can point in almost any conceivable direction. The direction of the Earth's magnetic field at a particular location is described by the declination, or magnetic variation, and inclination, or dip, angles. Declination is the angle between the horizontal component of the magnetic flux vector and a vector pointing towards true North. Inclination is the vertical angle between the vector and the horizontal plane. Since the Earth's magnetic field is approximated by a bar magnet, then in general the inclination of the field will increase from 0 degrees at the equator to 90 degrees near the poles. The magnitude of the Earth's magnetic field also sees considerable variation, ranging from 0.3 to 0.6 gauss.

When using the Earth's magnetic field for navigation, it is important to use a locally accurate magnetic reference for navigation. The Canadian National Research Council runs a number of magnetic observatories around Canada. These observatories can provide precise details about the local magnetic field. For other regions, a detailed model of the Earth's magnetic field, called the World Magnetic Model (WMM), is available from the National Geophysical Data Centre. In practice, local variations due to ferrous deposits and other highly localised anomalies must still be accounted for, but in this work it is assumed that the direction and magnitude of the local magnetic field is known and the operations are in a sufficiently small area that the magnetic field can be considered constant through out the operating area. It should be noted when discussing the Earth's magnetic field - the North Pole was so named because it attracts the north magnetic pole of a magnet. Therefore, the Earth's North Pole has south magnetism and the Earth's South Pole has north magnetism. This means that the lines of force flow out of the Earth's South Pole and into the Earth's North Pole.A complete discussion on the variations in the Earth's magnetic field and how to navigate using the local magnetic field can be found in [6].

In contrast to a compass, which traditionally measures the horizontal component of the earth's magnetic field and provides a heading, magnetometers measures the magnetic flux density of the Earth's magnetic field, commonly measured in Gauss or Tesla (1 Gauss is equivalent to 10^{-5} Tesla). A 3-axis magnetometer provides the the measured flux density in all three directions, and this information can be used for navigation or for many other purposes ranging from finding anomalies in the local magnetic field to medical imaging.

There are many different magnetometer designs. Fluxgate magnetometers, first introduced in the 1930 and still widely used today, has one or more cores of highly permeable material wrapped in two coils of wire. The first coil carries an alternating electrical current which drives the core through a cycle of magnetic saturation with reversing polarity. The changing magnetic field induces a current in the second coil. When the system is exposed to an external magnetic field an imbalance is created in the cycle and the induced current becomes out of step with the driving current. The magnitude of the cycle variation is dependant on the magnitude of the external field.

Hall Effect and magnetoresistive sensors are the most common low cost magnetometers today. They are both solid state devices, making them suitable for a multitude of commercial applications. Hall Effect sensors pass current through a conducting element. When the element is exposed to a magnetic field perpendicular to the flow of current, the path of the moving charges is deflected by the Lorentz Force resulting in a net potential, called the hall voltage, which develops on an axis perpendicular to both the current and the magnetic field. This voltage is proportional to the magnitude of the field. Magnetoresistive sensors on the other hand change impedance in the presence of an external field. These sensors are typically constructed using a nickel-iron magnetic alloy called Permalloy, which changes resistance as the magnetic domains swing around in response to external fields.

There are also many high precision magnetometers that measure the effects of magnetic fields on atomic elements. This type of sensor is used when precise measurements are required or for sensing very small changes in magnetic fields; they are used in magnetic observatories, geophysical surveys, medical testing, and other precision applications. Atomic magnetometers are used in Marine grade and Navigation grade navigation solutions, but aren't typically found in consumer level products. Examples of atomic magnetometers are the Proton Precession, Caesium Vapor, Spin-exchange relaxation-free (SERF), and superconducting quantum interference devices (SQUID) magnetometers.

Magnetometers have all the same error sources as accelerometers (alignment errors, measurement bias and scale factor errors, and non-linearities) and a few more. Many low cost magnetic sensors rely on measuring changes in the direction and magnitude of magnetisation in ferromagnetic element. While these elements have very low retentivity, they still require some finite change in the magnetic field before the domains begin to reorganise, this is referred to as the magnetic inertia of the material. In a dynamic environment, this leads to latency in the sensor which manifests itself as path-dependance or hysteresis.

A magnetometer measures the total magnetic field, which is the sum of the Earth's magnetic field and any locally generated magnetic fields. The locally generated magnetic fields can come from nearby hard and soft iron as well as electric devices generating electromagnetic fields. Estimating the Earth's magnetic field from the measurement requires knowledge of all the locally generated magnetic fields. In a strap-down system, sources that move rigidly with the sensor can be removed but sources that move independently from the sensor or are time-varying (and can't be modelled) can not be removed and will result in measurement errors. The effect of this type of source can often be mitigated by magnetic shielding or careful selection of the instrument location.

F.3 Pressure Sensors

The concept of pressure, defined as force per unit area, wasn't really understood until the 1640's when Blaise Pascal correctly hypothesised that the height of a column of mercury inside of an evacuated tube would vary with altitude and that one could calculate the weight of the air from the height of the mercury. It was 200 years before the first mechanical pressure sensor, which didn't rely on fluid displacement, was built, and almost another century, before the first electric pressure sensing mechanisms were developed in the 1930's.

Modern pressure sensors come in 3 types; displaying either absolute, differential or gauge pressure. Absolute pressure is the pressure relative to a vacuum. Differential pressure is the difference in pressure between two distinct locations and gauge pressure is the pressure relative to ambient atmospheric pressure. Differential or absolute pressure sensors are most often used for subsea applications, measuring the ambient water pressure or measuring pressure in hydraulic cylinders.

Most pressure sensors use a diaphragm that is exposed to a specified pressure on one side (vacuum, ambient pressure, etc.) and a different pressure on the other. The deformation of the diaphragm will be relative to the difference in the two pressures. The primary difference in the types of pressure sensors in how that deformation is measured. There are many different kinds of pressure sensors and the market is continually changing with improvements to existing products and the introduction of new ideas. The following is a list of some of the common sensor types and the style of measurement to which the are most suited.

Strain Gauge: In this type of sensor, a thin film strain gauge is bonded to the diaphragm. As the diaphragm moves due to changing pressure on its face, the resistance of the strain gauge changes. The change in resistance can be measured using a wheatstone bridge, which then outputs a voltage that is proportional to the change in resistance and, hence, the pressure. Strain gauge are the simplest and most inexpensive type of pressure sensor, but they are sensitive to temperature and the bonding process can cause nonlinearities. Strain gauges are still one of the preferred sensors for measuring high pressures.

Piezoelectric: Piezoelectric sensors use a quartz crystal to detect pressure. When pressure, force or acceleration is applied to a quartz crystal an electric charge proportional to the force develops across the face of the crystal; this charge develops rapidly but diminishes with time and, therefore, cannot be used to measure static pressures. This type of sensor is also very sensitive to environmental conditions. It is most often used for measuring transient pressure phenomenon such as explosions.

Piezoresistive: Piezoresistive sensors work in a similar fashion to the strain gauge sensors, except that they utilize the resistive dependence of silicon on stress to measure applied pressure. In these sensors, a silicon diaphragm with integrated silicone resisters is used with a wheatstone bridge. This type of sensor is sensitive to changes in temperature, but has benefitted greatly from advances in silicone manufacturing over the last few decades. It can provide stable and accurate measurements at a reasonable price.

Capacitive: Capacitive sensors use a diaphragm as one half of a parallel capacitor. In this case, the diaphragm is separated from a fixed plate. As the diaphragm flexes inwards it gets closer to the fixed plate, changing the capacitance. Capacitive pressure sensors are more stable than piezoresistive ones, but require a more complicated circuit. These sensors are slightly more expensive than piezoresistive sensors with comparable performance.

Optical: Optical pressure sensors use a diaphragm to move an opaque shield between a light source and a sensor. As the pressure increases, the shield moves further into the light beam and blocks more of the light. This type of sensor is very stable, with minimal temperature effects, minimal hysteresis, and excellent repeatability. This type of sensor can be combined with fiber optics to create extremely small rugged sensors.

The term pressure sensor usually refers to the sensing mechanism, as described in the list above. A pressure transducer usually includes a sensor, a housing and electronics to condition the analog output signal (filtering, temperature compensation, etc.) such that it can be easily interpreted by an end-user. A pressure transmitter is even more complex, digitizing the analog signal from the sensor and transmitting the results through a common communication standard such as ethernet or serial. The measurements from a pressure transducer will be more susceptible to transmission losses and noise than a pressure transmitter, as it minimizes the distance that the analog signal is required to travel.

In underwater work, ambient water pressure is closely related to depth. Seawater is a complex mixture of minerals, salts, and organic materials. In 1980, the international community agreed on a set of empirical equations called the "International Equation of State of Seawater" or EOS-80 to describe the density of seawater as a function of temperature, salinity and pressure. This equation has only recently been replaced by a new equation of state based on thermodynamic laws TEOS-10 [47]. EOS-80 is sufficiently accurate for this work so the new standard was not adopted. In 1983, a procedure (UNESCO 83) was developed to calculate depth from pressure given the temperature and salinity of the water. In the 1990's, the French Research Institute for Exploitation of the Sea (IFREMER) further worked with these equations to make them more suitable for use in ROV work where temperature and salinity are not always known. This group developed a set of temperature and salinity profiles for different regions of the world and built a new set of empirical equations based on Fofonoff and Millard's work that would simply calculate depth given pressure and latitude and the inverse, pressure from depth and latitude [43]. Assuming that UNESCO 83 calculates pressure exactly, these equations have an absolute accuracy of less than ± 0.2 m over 80% of the world and ± 0.8 m in the remaining 20%.

F.4 Doppler Velocity Logs

Nautical instruments that measure the speed of a vehicle through the water are known as logs. The word log dates back to the 16th century when mariners used a "common log" for measuring speed [6]. The common log consisted of a piece of wood tied to a rope and an hour glass. The rope had knots tied in it at regular intervals. Mariners would throw the wood into the water, pay out the line, and count the number of knots that passed during the length of time measured by the hour glass; this would give them a measurement of the vessel's speed. The technology has improved but the terms "log" and "knots" have remained, with "log" meaning nautical instrument for measuring a vessel's speed and "knots" being a unit of speed equal to 0.514 m/s.

A DVL uses the doppler effect to measure velocity. Single frequency DVLs emit an acoustic signal at a fixed frequency and listen for the frequency shift in the signal that is reflected back to it. DVLs can typically be set to listen for signals reflected from the bottom or from sound scatterers in the water column. Scatterers are small particles or plankton that are floating in the water column and reflect small amounts of sound back to the DVL.

Broadband DVLs use a different approach but the same basic concepts. A broadband DVL emits a packet of pulses that are very close together. The propagation delay or the time it takes the signal to travel outward and get reflected back to the transmitter, can be measured by noting the time of arrival of the first pulse. Since the pulses in the packet are very close together, neither the sensor or reflective object will have the chance to move very far while the packet is being reflected. Therefore, the range to the reflecting object can be considered constant over the packet and any spreading in the arrival of the reflected pulses will be due to the relative velocity of the instrument and reflecting object and the doppler effect. DVLs typically have multiple transducers or a phased array of transducers to enable the measurement of velocity on all three axes, and allow for the cancellation of effects due to pitching and rolling of the instrument. Pitching and rolling will cause the swath from the instrument beams to sweep across the bottom, which can be misinterpreted as translational velocity in systems without .

If the reflections comes from a fixed location, such as the sea floor, then the measured velocity will be the velocity of the instrument (or vehicle it is attached to) over ground. If the reflection comes from scatterers in the water column, then the measured velocity will be with respect to the water around the vehicle. Most DVLs can operate in either bottom following or water column mode. The preceding description is a highly simplified description of how DVLs work. Obtaining an accurate and robust velocity measurement requires a lot of complex signal processing and analysis. As such, DVLs are a highly specialized and expensive piece of equipment.

The error sources for a DVL can also be complex:

Acoustic Interference: The DVL transmits and receives acoustic signals, as such it is susceptible to acoustic noise from other acoustic instruments operating in the same frequency range. It is also susceptible to ringing, where the transmitted acoustic pulse reverberates in the vehicle for an extended period of time and is then picked up by the receiver instead of the reflected pulse.

Multipath: Acoustic signals can be reflected by the surface of the water as well as by the sea floor and mid column scatterers. This means that acoustic signals can act much like a pinball and bounce around between the surface and bottom taking many different paths back to the receiver. Multipath problems are especially challenging in shallow water or confined water environments, for example, the Explorer DVL does not work in the MTC test tank because there are too many reflected signals.

Sea Floor Variations: The DVL looks for specific characteristics in the reflected signal to decide if the reflection comes from the bottom. Since there are extensive variations in the reflectivity of the seafloor, the reflections from some bottom types (such as very fine deep silt) may not be detected by the instrument.

Vehicle Dynamics: Rapid roll and pitch rates can also affect the instruments ability to detect and process pings, especially when the instrument approaches the maximum operating angle with respect to the seafloor (20 degrees).

A DVL is an important component of a complete navigation suite but an understanding of the instrument limitations is important to ensure that the measurements are accurate.

Bibliography

[1] Sonardyne and oceaneering demonstrate ROV dynamic positioning capabilities. *Sea Technology*, 54(1):59, January 2013.

[2] Michele Aicardi, Andrea Caiti, Giorgio Cannata, and Giuseppe Casalino. Stability and robustness analysis of a two layered hierarchical architecture for the closed loop control of robots in the operational space. In *Proceedings of the IEEE International Conference on Robotics and Automation*, pages 2771--2778, 1995.

[3] R. Bachmayer, L.L. Whitcomb, and M.A. Grosenbaugh. An accurate four-quadrant nonlinear dynamical model for marine thrusters: theory and experimental validation. *Oceanic Engineering, IEEE Journal of*, 25(1):146--159, Jan 2000.

[4] João Carlos Alves Barata and Mahir Saleh Hussein. The moore-penrose pseudoinverse: A tutorial review of the theory. *Brazilian Journal of Physics*, 42(1-2):146--165, 2012.

[5] V. E. Beneš. Exact finite-dimensional filters for certain diffusions with nonlinear drift. *Stochastics*, 5(1-2):65--92, 1981.

[6] Nataniel Bowditch. *American Practical Navigator - An Epitome of Navigation*. U.S. Naval Oceanographic Office, 1966.

[7] Amos Buchanan. Experimental work for master's thesis. Flume tank experiments, 2014.

[8] Bradley J. Buckham. *Dynamics modelling of low-tension tethers for submerged remotely operated vehicles*. Phd thesis, University of Victoria, 2003.

[9] Harry E. Burke. *The handbook of magnetic phenomena*. Van Nostrand Reinhold, New York, 1986.

[10] M Caccia. *Advances in Unmanned Marine Vehicles*, chapter Low-cost high-precision motion ontrol for ROVs, pages 187--215. Control Engineering. Institution of Engineering and Technology, 2006.

[11] M. Caccia, G. Indiveri, and G. Veruggio. Modeling and identification of open-frame variable configuration unmanned underwater vehicles. *IEEE Journal of Oceanic Engineering*, 25(2):227--240, April 2000.

[12] M. Caccia and G. Veruggio. Guidance and control of a reconfigurable unmanned underwater vehicle. *Control Engineering Practice*, 8(1):21 -- 37, 2000.

[13] Robert D. Christ and Robert L. Wernli Sr. *The ROV manual a user guide for observation class remotely operated vehicles*. Elsevier Ltd., 1st edition, 2007.

[14] Linton Clark, Kevin R. Goheen, and D.R. Yoerger. Practical experiments in rov system identification. In *American Control Conference, 1993*, pages 575--579, June 1993.

[15] Giuseppe Conte and Andrea Serrani. Robust control of a remotely operated underwater vehicle. *Automatica*, 34(2):193 -- 198, 1998.

[16] Johann Dauer, Timm Faulwasser, Sven Lorenz, and Rolf Findeisen. Optimization-based Feedforward Path Following for Model Reference Adaptive Control of an Unmanned Helicopter. In *AIAA Guidance, Navigation and Control Conference*, 2013.

[17] F. Daum. Nonlinear filters: beyond the kalman filter. *Aerospace and Electronic Systems Magazine, IEEE*, 20(8):57--69, Aug 2005.

[18] Frederick E. Daum. Exact finite-dimensional nonlinear filters. *Automatic Control, IEEE Transactions on*, 31(7):616--622, Jul 1986.

[19] E. Fiorelli, N. E. Leonard, P. Bhatta, D. Paley, R. Bachmayer, and D. M. Fratantoni. Multi-AUV control and adaptive sampling in Monterey Bay. *IEEE Journal of Oceanic Engineering*, 31:935--948, October 2006.

[20] Thor Fossen. *Guidance and Control of Ocean Vehicles*. John Wiley and Sons, 1994.

[21] T.I. Fossen and T.A. Johansen. A survey of control allocation methods for ships and underwater vehicles. In *Control and Automation, 2006. MED '06. 14th Mediterranean Conference on*, pages 1--6, June 2006.

[22] Gene F. Franklin, J. David Powell, and Abbas Emami-Naeini. *Feedback control of dynamic systems*. Addison-Wesley, 3rd edition, 1994.

[23] Emmett D. Gamroth. Design implementation and testing of an underwater global positioning system. Master's thesis, University of Victoria, August 2009.

[24] Lee R. Gordon. Acoustic Doppler Current Profiler Principles of Operation - A Practical Primer. Technical report, 1996.

[25] N.J. Gordon, D.J. Salmond, and A. F M Smith. Novel approach to nonlinear//non-gaussian bayesian state estimation. *IEE Proceedings of Radar and Signal Processing*, 140(2):107--113, Apr 1993.

[26] Paul D Groves. *Principles of GNSS, Inertial, and Multi-sensor Integrated Navigation Systems*. Artech House, 2008.

[27] P. Hammond. *Electromagnetism for engineers : an introductory course*. Pergamon Press, Oxford [Oxfordshire] ; New York, 3rd ed edition, 1986.

[28] Kurt Hornik, Maxwell Stinchcombe, and Halbert White. Multilayer feedforward networks are universal approximators. *Neural Networks*, 2(5):359 -- 366, 1989.

[29] S.E. Houts, S.M. Rock, and R. McEwen. Aggressive terrain following for motion-constrained auvs. In *Autonomous Underwater Vehicles (AUV), 2012 IEEE/OES*, pages 1--7, Sept 2012.

[30] N. Hovakimyan, Hungu Lee, and A. Calise. On approximate nn realization of an unknown dynamic system from its input-output history. In *American Control Conference, 2000. Proceedings of the 2000*, volume 2, pages 919--923 vol.2, 2000.

[31] RD Instruments. Explorer DVL Operation Manual. Technical report, 2006.

[32] Kazuo Ishii and Tamaki Ura. An adaptive neural-net controller system for an underwater vehicle. *Control Engineering Practice*, 8(2):177 -- 184, 2000.

[33] Matt R. Jardin and Eric R. Mueller. Optimized measurements of unmanned-air-vehicle mass moment of inertia with a bifilar pendulum. *Journal of Aircraft*, 46(3):763 -- 775, 2009.

[34] E.N. Johnson and A.J. Calise. Neural network adaptive control of systems with input saturation. In *American Control Conference, 2001. Proceedings of the 2001*, volume 5, pages 3527--3532, 2001.

[35] Eric N. Johnson. *Limited Authority Adaptive Flight Control*. PhD thesis, Georgia Institute of Technology, School of Aerospace Engineering, Atlanta, GA,30332, Dec 2000.

[36] Simon J Julier and Jeffrey K Uhlmann. A new extension of the kalman filter to nonlinear systems. *International symposium aerospace/defense sensing, simululation and controls*, 3(26), 1997.

[37] R. E. Kalman. A new approach to linear filtering and prediction problems. *ASME Journal of Basic Engineering*, 1960.

[38] I. Kaminer, A.M. Pascoal, C.J. Silvestre, and P.P. Khargonekar. Control of an underwater vehicle using h infin; synthesis. In *Decision and Control, 1991., Proceedings of the 30th IEEE Conference on*, pages 2350--2355 vol.3, Dec 1991.

[39] S.K. Kannan and E.N. Johnson. Adaptive trajectory based control for autonomous helicopters. In *Digital Avionics Systems Conference, 2002. Proceedings. The 21st*, volume 2, 2002.

[40] Jinhyun Kim and Wan Kyun Chung. Accurate and practical thruster modeling for underwater vehicles. *Ocean Engineering*, 33(5□6):566 -- 586, 2006.

[41] D. Kruger, R. Stolkin, A. Blum, and J. Briganti. Optimal auv path planning for extended missions in complex, fast-flowing estuarine environments. In *Robotics and Automation, 2007 IEEE International Conference on*, pages 4265--4270, April 2007.

[42] Jack B. Kuipers. *Quaternions and rotation sequences: a primer with applications to orbits, aerospace , and virtual reality*. Princeton University Press, 1998.

[43] Claude C. Leroy and Fran□ois Parthiot. Depth-pressure relationships in the oceans and seas. *The Journal of the Acoustical Society of America*, 103(3):1346--1352, 1998.

[44] Ji-Hong Li, Pan-Mook Lee, and Sang-Jeong-Lee. Neural net based nonlinear adaptive control for autonomous underwater vehicles. In *Robotics and Automation, 2002. Proceedings. ICRA '02. IEEE International Conference on*, volume 2, pages 1075--1080, 2002.

[45] James D. Livingston. *Driving force : the natural magic of magnets*. Harvard University Press, Cambridge, Mass, 1996.

[46] A. R. Marzbanrad, M. Eghtesad, and R. Kamali. A robust adaptive fuzzy sliding mode controller for trajectory tracking of rovs. In *Decision and Control and European Control Conference (CDC-ECC), 2011 50th IEEE Conference on*, pages 2863--2870, Dec 2011.

[47] F. J. Millero. History of the equation of state of seawater. *Oceanography*, 23(3):18 --33, 2010.

[48] Tristan Perez and Alejandro Donaire. Constrained Control Design for Dynamic Positioning of Marine Vehicles with Control Allocation. *Modeling, Identification and Control*, 30(2):57--70, 2009.

[49] Juan Pomárico-Franquiz, Sanowar H Khan, and Yuriy S Shmaliy. Combined extended fir/kalman filtering for indoor robot localization via triangulation. *Measurement*, 50(April):236--243, 2014.

[50] Alison A. Proctor, B. Gwin, Suresh Kannan, Adrian Koller, Henrik Christophersen, and Eric N. Johnson. Ongoing development of an autonomous aerial reconnaissance system at georgia tech. In *Proceedings of the AUVS International Symposium*, 2004.

[51] Alison A. Proctor and Eric N. Johnson. Latency compensation in an adaptive flight controller. In *AIAA Guidance, Navigation and Control Conference*, August 2003.

[52] Alison A. Proctor, Suresh Kannan, C. Raabe, Henrik Christophersen, and Eric N. Johnson. Development of an autonomous aerial reconnaissance system at georgia tech. In *Proceedings of the AUVS International Symposium*, 2003.

[53] S. Reed, J. Evans, B. Privat, and J. Wood. Automated visual servoing for close inspection using low-cost, man-portable vehicles. In *Oceans - San Diego, 2013*, pages 1--6, Sept 2013.

[54] Bryan Schulz, Brett Hobson, Mathieu Kemp, Jim Meyer, Ryan Moody, Heather Pinnix, and Mathew St. Clair. Field results of multi-UUV missions using ranger micro-UUVs. In *The Proceedings of IEEE OCEANS*, volume 2, pages 956 -- 961, Sept. 22-26 2003.

[55] J.-J. E. SLOTINE and J. A. COETSEE. Adaptive sliding controller synthesis for nonlinear systems. *International Journal of Control*, 43(6):1631--1651, 1986.

[56] J.-J.E. Slotine and W. Li. Adaptive manipulator control a case study. In *Robotics and Automation. Proceedings. 1987 IEEE International Conference on*, volume 4, pages 1392--1400, Mar 1987.

[57] J.J.E. Slotine and W.A. LI. *Applied Nonlinear Control*. Prentice Hall, 1991.

[58] D. A. Smallwood and L. L. Whitcomb. Model-based dynamic positioning of underwater robotic vehicles: theory and experiment. *IEEE Journal of Oceanic Engineering*, 29(1):169--186, January 2004.

[59] S. Soylu, B.J. Buckham, and R.P. Podhorodeski. A fault-tolerant fuzzy-logic based redundancy resolution method for underwater mobile manipulators. In *OCEANS 2007*, pages 1--9, Sept 2007.

[60] S. Soylu, B.J. Buckham, and R.P. Podhorodeski. Dynamics and control of tethered underwater-manipulator systems. In *OCEANS 2010*, pages 1--8, Sept 2010.

[61] Serdar Soylu. *Coordinated Control of Small, Remotely Operated and Submerged Vehicle-ManipulatorSystems*. Doctor of Philosophy, University of Victoria, 2011.

[62] Serdar Soylu, Bradley J. Buckham, and Ron P. Podhorodeski. A chattering-free sliding-mode controller for underwater vehicles with fault-tolerant infinity-norm thrust allocation. *Ocean Engineering*, 35(16):1647 -- 1659, 2008.

[63] Serdar Soylu, Alison A. Proctor, Ron P. Podhorodeski, Colin Bradley, and Bradley J. Buckham. Precise trajectory control for the falcon - an inspection class rov. *Ocean Engineering*, page Submitted, 2013.

[64] Dean Steinke. Design and simulation of a kalman filter for rov navigation. Master's thesis, University of Victoria, December 2009.

[65] Desert Star Systems. *Southstar ShipHull Operator's Manual*, 1 edition, Dec 2009.

[66] I. Tena. A new ROV DP. In *Dynamic Positioning Conference*, Houston, TX, October 9-10th 2007.

[67] Keith Vickery. Acoustic positioning systems - a practical overview of current systems. *Proceedings of the IEEE Symposium on Autonomous Underwater Vehicle Technology*, pages 5 -- 17, 1998.

[68] Xu Wang. Design and Analysis of Liquid-drop Accelerometer. Master of Applied Science, Simon Fraser University, 2009.

[69] Greg Welch and Gary Bishop. An introduction to the Kalman filter. In Computer Graphics, Annual Conference on Computer Graphics & Interactive Techniques. ACM Press, Addison-Wesley, Los Angeles, CA, USA, SIGGRAPH 2001 course pack edition, course No. 8, Aug 12-17 2001.

[70] Greg Welch and Gary Bishop. An introduction to the kalman filter. In *SIGGRAPH*, volume Course 8, 2001.

[71] R. Wernli and J. Jaeger. ROV technology update from an international perspective. *The Proceedings of IEEE OCEANS*, 16:639--645, September 1984.

[72] Guoqing Xia, Chengcheng Pang, Hongjian Wang, and Yu Le. Adaptive neural network controller applied to dynamic positioning of a remotely operated vehicle. In *OCEANS - Bergen, 2013 MTS/IEEE*, pages 1--6, June 2013.

[73] A. Yeşildirek and F.L. Lewis. Feedback linearization using neural networks. *Automatica*, 31(11):1659 -- 1664, 1995.

[74] D. R. Yoerger and J.-J. E. Slotine. Adaptive sliding control of an experimental underwater vehicle. In *IEEE Robotics and Automation Magazine*, volume 3, pages 2746--2751, 9-11 April. 1991.

[75] D.R. Yoerger, J.G. Cooke, and J.-J.E. Slotine. The influence of thruster dynamics on underwater vehicle behavior and their incorporation into control system design. *Oceanic Engineering, IEEE Journal of*, 15(3):167--178, Jul 1990.

[76] D.R. Yoerger and J.-J.E. Slotine. Robust trajectory control of underwater vehicles. *Oceanic Engineering, IEEE Journal of*, 10(4):462--470, Oct 1985.

[77] D.R. Yoerger, R. Weiman, and T. Somers. Remote control of a telerobotic underwater vehicle via satellite. In *Telesystems Conference, 1991. Proceedings. Vol.1., NTC '91., National*, pages 331--336, Mar 1991.

[78] Jonathan Zand. Enhanced Navigation and Tether Management of Inspection Class Remotely Operated Vehicles. Master of Science, University of Victoria, 2009.

[79] Yan zeng Gao, Jia wei Ye, Xin Song, and Ping an Shi. A reinforcement learning algorithm based neural network used for course angle control of remotely operated vehicle. In *Intelligent Computation Technology and Automation, 2009. ICICTA '09. Second International Conference on*, volume 1, pages 31--34, Oct 2009.